UNIVERSITAT POLITÈCNICA DE CATALUNYA BARCELONATECH

Study of the dynamic behavior of Pelton turbines

by

Mònica Egusquiza Montagut

ADVERTIMENT La consulta d'aquesta tesi queda condicionada a l'acceptació de les següents condicions d'ús: La difusió d'aquesta tesi per mitjà del repositori institucional UPCommons (http://upcommons.upc.edu/tesis) i el repositori cooperatiu TDX (http://www.tdx.cat/) ha estat autoritzada pels titulars dels drets de propietat intel·lectual **únicament per a usos privats** emmarcats en activitats d'investigació i docència. No s'autoritza la seva reproducció amb finalitats de lucre ni la seva difusió i posada a disposició des d'un lloc aliè al servei UPCommons o TDX. No s'autoritza la presentació del seu contingut en una finestra o marc aliè a UPCommons (*framing*). Aquesta reserva de drets afecta tant al resum de presentació de la tesi com als seus continguts. En la utilització o cita de parts de la tesi és obligat indicar el nom de la persona autora.

ADVERTENCIA La consulta de esta tesis queda condicionada a la aceptación de las siguientes condiciones de uso: La difusión de esta tesis por medio del repositorio institucional UPCommons (http://upcommons.upc.edu/tesis) y el repositorio cooperativo TDR (http://www.tdx.cat/?locale-attribute=es) ha sido autorizada por los titulares de los derechos de propiedad intelectual **únicamente para usos privados enmarcados** en actividades de investigación y docencia. No se autoriza su reproducción con finalidades de lucro ni su difusión y puesta a disposición desde un sitio ajeno al servicio UPCommons No se autoriza la presentación de su contenido en una ventana o marco ajeno a UPCommons (*framing)*. Esta reserva de derechos afecta tanto al resumen de presentación de la tesis como a sus contenidos. En la utilización o cita de partes de la tesis es obligado indicar el nombre de la persona autora.

WARNING On having consulted this thesis you're accepting the following use conditions: Spreading this thesis by the institutional repository UPCommons (http://upcommons.upc.edu/tesis) and the cooperative repository TDX (http://www.tdx.cat/?locale-attribute=en) has been authorized by the titular of the intellectual property rights **only for private uses** placed in investigation and teaching activities. Reproduction with lucrative aims is not authorized neither its spreading nor availability from a site foreign to the UPCommons service. Introducing its content in a window or frame foreign to the UPCommons service is not authorized (framing). These rights affect to the presentation summary of the thesis as well as to its contents. In the using or citation of parts of the thesis it's obliged to indicate the name of the author.

Study of the dynamic behavior of Pelton turbines

Doctoral thesis

Submitted by

Mònica Egusquiza Montagut

Universitat Politècnica de Catalunya
Dept. of Fluid Mechanics
Doctorate program in Mechanical and Aeronautical Engineering

Thesis Supervisor

Prof. Eduard Egusquiza Estevez

December 2019
Barcelona

Acknowledgements

I would like to start these acknowledgements by expressing my most sincere gratitude towards my thesis supervisor and father, Prof. Eduard Egusquiza, and towards my mother, Carme Montagut, for their unconditional support. Their advice and encouragement over the course of this thesis, inside and outside the technical field, have made it possible for me to reach this end.

Next, I would like to acknowledge the assistance provided by my colleagues Dr. Eng. David Valentín, Dr. Eng. Carme Valero and Dr. Eng. Alex Presas. Thank you very much for sharing your knowledge and experience with me, especially at the beginning. I really appreciate your support and I wish we can keep on sharing many good moments together. My thanks to David Castañer, Paloma Ferrer, Dr. Eng. Alfredo Guardo and the rest of members of the CDIF, who have also contributed to an enjoyable stay. I would also like to acknowledge the support received from Prof. Jesús Álvarez during the last stage of the thesis.

Needless to mention the good experiences shared with the doctoral students Eng. Zhao Weiqiang, Eng. Geng Linlin, Eng. Chen Jian and Dr. Eng. Zhang Ming. I would like to make a special mention to my dear friend Dr. Eng. He Lingyan, whose company I cherished the most in my first doctoral year.

I would also like to show my gratitude and appreciation towards the colleagues of VOITH Hydro, who gave me their support during my stay in Heidenheim, especially to Eng. Nagore San José and Eng. Christian Probst. I want to thank them, as well as all the other colleagues, for making my stay so memorable. Thank you very much to Dr. Eng. Jiri Koutnik for giving me the opportunity to have this experience and to Eng. Reiner Mack for his time and advice on Pelton turbines.

Thanks to Prof. François Avellan and the colleagues of the LMH for the short but nice stay in Lausanne.

Finally, I would like to express my gratitude to Oscar, who has always supported and encouraged me in the distance. Thanks also to my family and friends, whose understanding and support I have always appreciated. Special thanks to Dr. Paula Garcia for the time spent together over so many years and for her always-good advice.

Abstract

The future of hydropower is tied to the rapid increase of new renewable energies, such as photovoltaic and wind energy. With the growing share of intermittent electricity production, the operation of hydropower installations must be more flexible in order to guarantee the balance between supply and demand. As a result, turbines must increase their operating range and undergo more starts and stops, what leads to a faster deterioration of the turbine components, especially the runner. In the current scenario, condition monitoring constitutes an essential procedure to assess the state of the turbines while in operation and can help preventing major damage.

Pelton turbines are used in locations with high heads and low discharges. The runner is composed by a disk with several attached buckets, which periodically receive the impact of high speed water jets. Buckets must thus endure large tangential stresses that can lead to fatigue problems and, in case the natural modes of the runner are excited, this problem can be severely aggravated. Therefore, a deep comprehension of the modal behavior and dynamics of Pelton turbines is required in order to keep track of the runner condition with monitoring systems.

In this thesis, the dynamic behavior of Pelton turbines during different operating conditions has been studied in detail and the knowledge acquired has been used to upgrade the present condition monitoring. The first part of the document comprises the study of the modal behavior of Pelton turbines. A systematic approach has been followed with such purpose; first a single bucket has been analyzed, second the runner and then the whole turbine. With the help of numerical models and experimental tests the natural frequencies and mode shapes have been identified and classified. The effect of the mechanical design and the boundary conditions has also been discussed.

The second part of the thesis is focused on determining the transmission of the runner vibrations to the monitoring locations. It is proved that these can be detected from the bearings and that the transmission depends on the mode type.

In the third and last part the analysis of Pelton turbines in operation is carried out. Two different machines have been studied during start-up and under different load conditions to determine which modes are excited, how the frequencies change in operation with respect to the still machine and how they are detected from different positions. The spectrum frequency bands corresponding to the runner modes and the overall vibration levels have been analyzed. Finally, the information obtained has been used to propose an upgrade of the current practice in condition monitoring. A case of damage has been analyzed with a numerical model and with historic data to illustrate the strategy.

Resum

El futur de l'energia hidràulica està lligat al ràpid creixement de les noves energies renovables, tals com l'energia fotovoltaica i l'eòlica. A mesura que la porció d'energia intermitent que es produeix creix, el funcionament de les instal·lacions hidroelèctriques es veu forçat a ser més flexible per tal de garantir el balanç entre el subministrament i la demanda d'energia. Això es tradueix en un increment del rang de funcionament de les turbines i en més parades i arrancades, fet que contribueix a un deteriorament més ràpid dels seus components, especialment del rodet. En la situació actual, la monitorització de l'estat de les turbines és essencial per tal d'assegurar-ne les bones condicions de funcionament i evitar danys majors.

Les turbines Pelton s'utilitzen en emplaçaments amb salts elevats i cabals reduïts. El rodet està compost per un disc amb diverses culleres que reben periòdicament l'impacte de raigs d'aigua a molta velocitat. Com a conseqüència, les culleres han de suportar grans tensions en direcció tangencial, les quals comporten seriosos problemes de fatiga a l'estructura. En cas que els modes naturals del rodet també s'excitin pels rajos d'aigua, aquest problema és altament agreujat. Així, és necessari tenir un coneixement profund del comportament modal i dinàmic de les turbines Pelton per tal de controlar l'estat del rodet amb sistemes de monitorització.

En aquesta tesi s'ha estudiat en detall el comportament dinàmic de turbines Pelton en diferents condicions d'operació. El coneixement adquirit s'ha utilitzat per a millorar el sistema de monitorització actual. La primera part del document comprèn l'estudi del comportament modal de turbines Pelton. Amb tal propòsit s'ha abordat el problema de manera sistemàtica: primer s'han analitzat els modes d'una sola cullera, després els del rodet sencer i per últim els de tota la turbina. Amb l'ajuda de models numèrics i de proves experimentals s'han identificat i classificat les corresponents freqüències naturals i formes modals. A més a més s'ha estudiat l'efecte del disseny mecànic i de les condicions de contorn.

La segona part d'aquesta tesi està centrada en determinar la transmissió de les vibracions del rodet a les posicions de monitorització. S'ha demostrat que aquestes es poden detectar des dels coixinets i que la qualitat de la transmissió depèn del tipus de mode.

A la tercera i última part s'ha dut a terme l'anàlisi de turbines Pelton en funcionament. S'han estudiat dues màquines diferents durant el transitori de posta en marxa i sota diferents càrregues per tal de determinar quines modes s'exciten, com canvien les freqüències de la turbina en funcionament respecte la màquina parada i com es detecten des de les diferents posicions. Les bandes de freqüència de l'espectre de vibració corresponents als diferents modes del rodet i els nivells de vibració s'han analitzat. Finalment, la informació obtinguda ha estat utilitzada per a fer una proposta de millora de l'actual procediment de

monitorització. Un cas de dany en un rodet ha estat analitzat amb un model numèric i amb l'històric de vibracions per tal d'il·lustrar l'estratègia a seguir en un futur.

Resumen

El futuro de la energía hidráulica está relacionado con el rápido crecimiento de las nuevas energías renovables, tales como la energía fotovoltaica y la eólica. A medida que la porción de energía intermitente que se produce crece, el funcionamiento de las instalaciones hidroeléctricas se ve obligado a ser más flexible con tal de garantizar el balance entre el suministro y la demanda de energía. Esto se traduce en un incremento del rango de operación de las turbinas y en más paradas y arranques, hecho que contribuye a un deterioro más rápido de sus componentes, especialmente del rodete. En la situación actual, la monitorización del estado de las turbinas es esencial para asegurar sus buenas condiciones de funcionamiento y evitar daños mayores a medio y largo plazo.

Las turbinas Pelton se utilizan en emplazamientos con saltos elevados y caudales reducidos. El rodete está compuesto por un disco con varias cucharas que reciben periódicamente el impacto de chorros de agua a velocidad muy alta. Como consecuencia, las cucharas tienen que aguantar tensiones muy elevadas en dirección tangencial, las cuales conllevan serios problemas de fatiga a la estructura. En caso que los modos naturales del rodete también se exciten por los chorros de agua, este problema es empeora notablemente. Así, es necesario tener un conocimiento profundo del comportamiento modal y dinámico de las turbinas Pelton por tal de controlar el estado del rodete con sistemas de monitorización.

En esta tesis se ha estudiado en detalle el comportamiento dinámico de turbinas Pelton en diferentes condiciones de operación. El conocimiento adquirido se ha utilizado para mejorar el sistema de monitorización actual. La primera parte del documento comprende el estudio del comportamiento modal de turbinas Pelton. Con tal propósito se ha abordado el problema de manera sistemática: primero se han analizado los modos de una sola cuchara, después los de todo el rodete y por último los de toda la turbina. Con la ayuda de modelos numéricos y de pruebas experimentales se han identificado y clasificado las correspondientes frecuencias naturales y formas modales. Además, se ha estudiado el efecto del diseño mecánico y de las condiciones de contorno.

La segunda parte de esta tesis está centrada en determinar la transmisión de las vibraciones del rodete a las posiciones de monitorización. Se ha demostrado que estas se pueden detectar desde los cojinetes y que la calidad de la transmisión depende del tipo de modo.

En la tercera y última parte se ha llevado a cabo el análisis de turbinas Pelton en funcionamiento. Se han estudiado dos máquinas diferentes durante el transitorio de puesta en marcha y bajo diferentes cargas con tal de determinar qué modos se excitan, como cambian las frecuencias de la turbina en funcionamiento respecto la máquina parada y como se detectan desde las diferentes posiciones. Las bandas de frecuencia del espectro de vibración correspondientes a los diferentes modos del rodete y los niveles de vibración se han analizado. Finalmente, la información obtenida ha sido utilizada para hacer una propuesta de mejora

del actual procedimiento de monitorización. Un caso de daño en un rodete ha sido analizado con un modelo numérico y con el histórico de vibraciones con tal de ilustrar la estrategia a seguir en un futuro.

Table of contents

List of figures

List of tables

Nomenclature

a	Bucket height	mm
b	Bucket width	mm
C	Damping coefficient	$\mathrm{kg \cdot s^{-1}}$
C_c	Critical damping coefficient	$\mathrm{kg \cdot s^{-1}}$
C_0	Water jet velocity	$\mathrm{m \cdot s^{-1}}$
D_1	Pitch diameter	mm
D_s	Specific diameter	
d_o	Nozzle diameter	mm
E	Specific energy	$\mathrm{m^2 \cdot s^{-2}}$
F	External force	N
f	Natural frequency	Hz
f_b	Bucket passing frequency	Hz
f_f	Rotation frequency	Hz
f_p	Pole passing frequency	Hz
g	Gravitational acceleration	$\mathrm{m \cdot s^{-2}}$
H	Head	m
K	Stiffness constant	$\mathrm{kg \cdot s^{-2}}$
k_{Cm}	Nozzle loss coefficient	
k_u	Peripheral velocity coefficient	
M	Mass	kg
n	Integer number	
N	Rotational speed	$\mathrm{min^{-1}}$
N_{11}	Unit speed	
N_s	Specific speed	
P	Rated output	kW
Q	Discharge	$\mathrm{m^3 \cdot s^{-1}}$
Q_{11}	Unit discharge	
S	Power spectrum	
T	Time period	s

U_1	Peripheral velocity	$\mathrm{m} \cdot \mathrm{s}^{-1}$
u	Position	m
$\dot{u}$	Velocity	$\mathrm{m} \cdot \mathrm{s}^{-1}$
$\ddot{u}$	Acceleration	$\mathrm{m} \cdot \mathrm{s}^{-2}$
z_0	Number of nozzles	
z_b	Number of buckets	

Greek symbols

Δ	Sampling interval	s
κ	Coherence	
ξ	Damping ratio	
ϕ	Phase angle	°
$\{\phi\}$	Eigenvector	
ω	Angular frequency	$\mathrm{rad} \cdot \mathrm{s}^{-1}$
ω_n	Angular natural frequency	$\mathrm{rad} \cdot \mathrm{s}^{-1}$

Abbreviations

AI	Artificial Intelligence
CAD	Computer Assisted Design
DFT	Discrete Fourier Transform
DOF	Degrees of Freedom
EMA	Experimental Modal Analysis
FEA	Finite Element Analysis
FFT	Fast Fourier Transformation
FRF	Frequency Response Function
FT	Fourier Transform
ND	Nodal Diameter
ODS	Operational Deflection Shape
RMS	Root Mean Square

Chapter 1 Introduction

1.1. Introduction

1.1.1. The future of hydropower

Hydropower is one of the most important renewable energies. It has been used since the 19th century to generate electricity by means of rotational machines called turbines, which convert the potential energy of the water into mechanical energy. The technology and design of hydraulic turbines has been developed and optimized to the extent of providing efficiencies of over 90%, which is one of the largest among all power generation machines. The future of hydropower is closely tied to the evolution of the so-called new renewable energies (NRE), like solar and wind. These technologies have been largely developed in the last years and are characterized by its low environmental impact compared to other established technologies like nuclear or thermic energy. Due to the increasing concern about the environmental effects of power generation, NRE are taking the lead to a more sustainable future and are experiencing a rapid increase [1]. Nevertheless, the energy generated depends on the atmospheric conditions and it is random. This is translated into a growing share of electricity production that comes from intermittent sources, and cannot be adapted to the actual electricity demand. In order to ensure the balance between supply and demand, hydropower installations are required to fill the fluctuating gap. This requires power plant operators to increase the operating range of hydraulic turbines and to undergo more starts and stops, what leads to a faster deterioration of the turbine components, especially the runner.

This new scenario enhances the action of the forces applied on the rotating equipment and can put at risk its structural integrity. Since hydropower machines are designed to be a reliable and profitable investment for the power utility and its owners, it is therefore essential to understand the dynamics of the machine and to use this knowledge to track and monitor their performance during its service life. In doing so, faulty operating conditions or

deterioration of the machine can be detected and power plant operators can take convenient action.

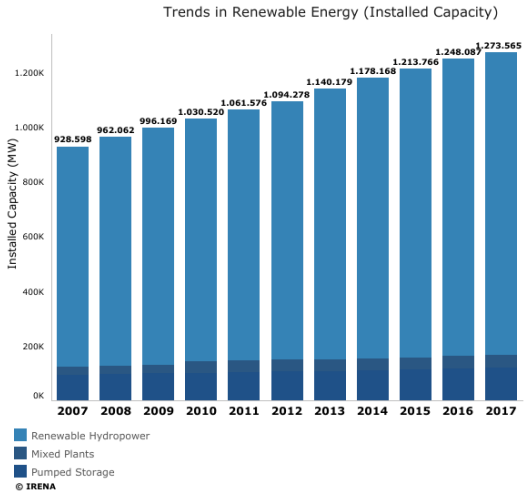

Figure 1.1. Evolution of installed worldwide hydropower capacity [2]

1.1.2. Operation of Pelton turbines

The Pelton turbine is one of the most efficient types of turbines. It is used in power stations where the hydraulic head is high, usually above 400 m, and operates with low discharges. Pelton turbines have efficiencies that exceed 90% for a wide operating range, thus being one of the most efficient and flexible type of hydraulic turbine [3]. There is a wide range of capacities and dimensions of Pelton runners and the most powerful ones are those housed in the Bieudron power station in Switzerland, with a rated output of 423 MW each [4], [5].

The invention of the Pelton turbine dates back to the end of the 19th century. In the late 1870's, Lester Allan Pelton (1829-1908), a fortune seeker who was established in California during the Gold Rush, found that the performance of a water wheel could be improved by adding a middle ridge to the buckets. In that way, the water flow was split and deflected, what caused a stronger impulse on the buckets due to a better utilization of the energy of the water. In addition, Pelton found that the performance of the machine was increased when the water flow impinged the buckets at maximum velocity. At present, a Pelton runner consists of a casted stainless steel disk with a series of metal cups divided in halves attached along its periphery (see Figure 1.2). They are classified as impulse turbines because they have no pressure difference between the inlet and the outlet, what means only the kinetic energy of the water is employed to impulse the runner. In consequence, all the potential energy of the water (hydraulic head) must be converted into velocity before entering the turbine. This is attained by means of a nozzle, which is installed at the end of the penstock and directed in the tangential direction of the wheel (see Figure 1.3). By doing so, the high speed water jet ejected from the nozzle impinges the buckets of the runner perpendicularly.

Figure 1.2. Pelton wheel

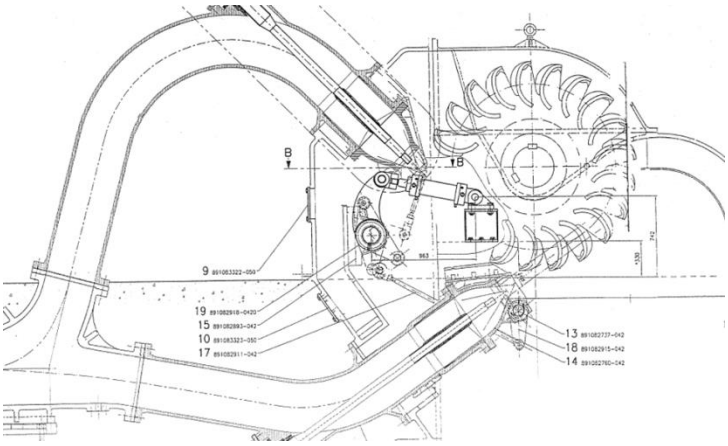

Figure 1.3. Cross section of a Pelton turbine

Pelton turbines are subjected to strong pulsating forces coming from the action of the water jets. The most critical parts are the buckets, which resemble a cantilever beam and have to transmit the torque to the wheel. For this reason, the fatigue of the material on the bucket area is one of the most common causes of failure in this type of turbines. In case of wrong design or faulty casting of the buckets (which can leave imperfections in the material), the service life can be significantly reduced. In some cases, damage can be catastrophic. In addition, the effect of the impact of the jets is intensified when the frequency of the excitation force is near a natural frequency; in such case the deformation of the structure is amplified and the stress state severely aggravated. Therefore, it is of utmost importance to understand the dynamics of the machine before and after the commissioning of the power station. During operation, knowledge on the dynamics of the structure provides the means to evaluate the operational and structural state of the runner without the need to disassemble.

1.2. Interest of the study

The study proposed is of great interest in the industrial field. With the surge of new renewables, Pelton turbines are required to work under harsher operating conditions, which put at risk the integrity of the runner. Apart from the efforts performed in the stage of design to reduce the effect of the pulsating forces on the structure, several factors can compromise the Remaining Useful life (RUL) of the machine that cannot be predicted beforehand. Scenarios such as a damaged runner or abnormalities in the jet quality can remain unnoticed for as much time it requires undergoing a machine inspection. Having a deep understanding of the dynamics of the machine and knowing how this is affected by the aforementioned undesired conditions opens the door to surveilling what is happening inside the machine in real time and provides facility operators a major control on their assets.

1.3. State of the art

First records on the dynamic behavior of Pelton turbines can be tracked back to the start of the 20th century. In 1937, Fulton [6] stated that with the steady increase in output of Pelton turbines, there had been an outbreak of cracks due to bucket vibration, which caused designers to reinforce their designs. In the 1950s, many catastrophic failures caused by fatigue fracture took place due to the trend of increasing size and power of Pelton turbines [7]. In the following years, bolted buckets started being replaced by new designed one piece casted runners. Even though the existence of bucket vibration was acknowledged, mainly the static stresses coming from centrifugal forces and the jet impact were considered being important [8].

In the following years, the attention to the alternating stresses coming from the dynamic excitation of the buckets started to rise. One of the most important publications was written by Grein et al. [9], who remarked the importance of the dynamic stresses as a controlling parameter for fatigue failure and considered the bucket vibration in circumferential direction to be the most dangerous natural vibration, whose amplification factor in case of resonance could reach up to x1000. The buckets of Pelton turbines had to be designed carefully to limit the maximum value of alternating stresses due to dynamic excitation to 45 MPa in order to avoid fatigue and to guarantee the minimum service life requirements [10]. Before the development of numerical methods, the design criteria to ensure long lifetime regarding the fatigue problem was established by performing laboratory tests and crack propagation calculations based on theory of fracture mechanics [11]. The use of strain gauges was also a spread practice in order to study the vibrations of the buckets [12].

With the development of Finite Element Methods, the dynamic behavior of the buckets could be more accurately studied. The structural analysis of Pelton turbines is nowadays an indispensable procedure to be followed during the manufacturing of Pelton turbines. Many publications mention the study of the natural frequencies in such stage [13][14]. In the upgrading and the maintenance of Pelton turbines also many publications can be found addressing the study of the stress fluctuations [15][16]. Failure analyses can also be found

[17]. A better knowledge of the stress state of the Pelton turbines also lead to the development of new technologies which have allowed optimizing the fabrication of Pelton runners [18][19][20], and new designs in order to decrease the effect of alternating stresses [21][22].

The traditional method in the analysis of the vibration of the runners was based on the classical beam theory, which consisted in treating the bucket as a beam clamped at its base. With the increase in size an output, the development of more sophisticated models are necessary, such as in the case of Bieudron power plant [23].

Due to the discrepancies between the natural frequencies in the theoretical design and the real runner, Schmied et al. [24] developed a method to detune a Pelton runner by finding the optimal bucket mass removal required. In this article, other modes of a Pelton bucket are briefly described: torsional mode, axial mode and radial mode. It is also stated that as the number of nodal diameters increases, so does the resemblance to a pure bucket mode. Sick et al. [25] highlight the difficulties in performing quasi-static stress analysis nowadays and divides the general practice in structural analysis of Pelton turbines in two steps: first the deformation and stress in the bucket as a response to the dynamic load and second the analysis of natural modes and frequencies and evaluation of safety limits with respect to resonance.

In the last years, some authors performed test measurements with strain gauges [26], [27] and pressure sensors [28]–[32] on reduced models to determine the pressure distribution, the values of the jet force and the stresses at the critical locations of the buckets in case of resonance. The natural frequencies of the buckets were determined by experimental testing with accelerometers and were analyzed with FEM analysis.

On his review on dynamic problems of Francis and Pelton turbines, Brekke [33] still alerted of the appearance of superimposed high frequency bucket oscillations, which can put at risk the whole turbine even before damage can be detected in an inspection.

Sanvito et al. [34] developed a new method for identifying the dynamic stresses of Pelton turbines, which consisted in decoupling the load on the bucket into different harmonic analyses and then reconstructing the 'stress vs. time' trace. This was performed on the reduced geometry of a Pelton bucket, which consisted of one half constrained by its contact surfaces, for no description of the runner modes was available.

In 2007, Pesatori et al. [35] performed a numerical and experimental analysis of a two jets Pelton turbine. A FEM model consisting of a single bucket was studied with different boundary conditions on the periodic surfaces. Experimental tests showed that the behavior of a runner bucket was best defined by a bucket whose periodic surfaces were clamped. In this publication, also the first five modes of the bucket were described. However, the behavior of the whole runner is not described.

The vibration and mechanical effects on Pelton turbines are well documented by Dörfler [36]. In his book, the author warns about the important role of the harmonics of the excitation frequency on the dynamic stresses due to the low damping ratio of the natural oscillations of the runner/bucket assembly. With this, taking into account the effect of the added mass and the precision in the machining are indispensable to avoid resonances. Dörfler also explains

in detail the importance of a proper choice of jet distribution and the number of buckets due to its effect on the vibrations of the whole machine, in transient and normal operation. Special attention is put on the torsional modes of the rotor, which are highly excited during startup.

Records on monitoring of Pelton turbines are difficult to find. One relevant publication is written by Karacolcu et al. [37], who explain the procedure followed in the rehabilitation of a two jet horizontal Pelton turbine, which suffered from strong vibrations at certain output (30 MW), even though its rated power was of 38 MW. In the mechanical assessment of the existing turbine, vibration data was analyzed, finding a strong vibration in the axial bearings at 150 Hz. After performing bump tests on the buckets and turbine casing and doing a FEM analysis, a rotor-bending mode was found near the problematic frequency. Even though the most important rotor modes were showed in the paper, runner modes were not described.

1.4. Objectives

The main objective of this thesis is to obtain a deeper understanding of the dynamic behavior of horizontal Pelton turbine prototypes in operation. The ultimate purpose is to use the research results to improve the capability to monitor the condition of the turbines in real time.

To accomplish this, the first goal is to have a better understanding of the structural (modal) response of Pelton runners when still and in operating conditions (mounted in the machine and rotating). The purpose is also to check the ability to extrapolate the results to different Pelton turbines.

The second goal is to study the feasibility to monitor the runner vibrations from typical monitoring positions in the bearings. For that purpose, the propagation of the runner vibrations to the monitoring positions have to be evaluated.

Finally, to improve the existing monitoring procedures, it is necessary to analyze the data from monitoring several Pelton units and to determine the main types of damage found in these machines and the symptoms observed in the spectra.

1.5. Outline

This thesis is organized in three parts. The first part contains a deep modal analysis of Pelton turbines, the second shows the study of the transmissibility of runner vibrations to the monitoring positions and the third part is focused on the study of the dynamic behavior of these turbines with a proposal to improve condition monitoring.

The first part consists of two chapters. In chapter two the modal behavior of a Pelton runner without constraints (free vibrating body) is studied numerically and experimentally. Then a discussion on the parameters that influence on the natural frequencies and modal shapes is performed. In chapter three, three modal analyses are carried out for whole Pelton machines.

The first analysis is performed numerically with the geometry of the runner of the previous section. The second and the third are made experimentally on two different Pelton turbines. Finally, all the results are brought together with data obtained from other Pelton turbines to define general trends in the modal behavior of Pelton turbines.

The second part is developed in chapter four. In this chapter the excitability of the runner modes and the transmissibility of the bucket vibrations to the monitoring positions is studied in the same Pelton machines whose modal behavior was studied in the previous section.

The third part comprises chapter five and six. In chapter five the dynamic behavior of both Pelton turbines is studied during the startup transient and under different loads. In chapter six, the vibration signatures of different Pelton turbines are analyzed in order to extract the symptoms of common types of damage. Then an update on the spectral bands and vibration amplitudes is proposed as condition indicators for a possible improvement of condition monitoring of Pelton turbines.

Chapter 2 Modal behavior of Pelton runners

To perform the dynamic analysis of a Pelton turbine it is essential to understand its modal characteristics. This chapter is devoted to analyzing numerically and experimentally the natural frequencies and mode shapes of a Pelton runner without constraints. To do so, the numerical model of a real suspended runner has been created. First, the mode shapes of a single bucket have been identified and classified. After that, the frequencies and mode shapes have been analyzed for the whole structure. An Experimental Modal Analysis (EMA) has been performed on the runner to check the validity of the numerical model. Finally, the results have been discussed and the influence of different geometrical parameters on the modal behavior of the runner has been analyzed.

2.1. Theoretical background

The modal analysis of a structural system consists in determining its inherent vibration properties, such as its natural frequencies and mode shapes. Modal analysis is fundamental when studying any dynamic system because it allows determining how it responds to external excitations and helps preventing it from reaching resonance.

2.1.1. Free vibration of a structural system

To introduce the basics of modal analysis, we will consider a dynamic system with a single degree of freedom (DOF) composed by a mass attached to a spring and a damper. The vibration of this system is governed by the second law of Newton, which is expressed as follows [38]

$$M\ddot{u} + C\dot{u} + Ku = F(t) \qquad \text{Eq. 2.1}$$

The first term on the left side of the equation represents the inertial forces of the system, the second term the friction forces (dissipation of energy) and the third the elastic forces, where M is the mass, C is the damping coefficient and K is the stiffness constant. $\ddot{u}$, $\dot{u}$ and u represent the acceleration, the velocity and the position of the mass, at every instant respectively. The term on the right side of the equation, $F(t)$, represents an external force applied on the system as a function of time.

When the force applied on the system is removed, the motion of the system is described as a free vibration, and is written as follows

$$M\ddot{u} + C\dot{u} + Ku = 0 \qquad \text{Eq. 2.2}$$

The solution to this equation allows obtaining the natural frequency of the system ω_n. If we consider that the friction forces are negligible, then we obtain the following expression

$$\omega_n = \sqrt{K/M} \qquad \text{Eq. 2.3}$$

There are three possible solutions to Eq. 2.3 depending on whether the system is underdamped $(C/2M < K/M)$, critically damped $(C/2M = K/M)$ or overdamped $(C/2M > K/M)$. The value of C when the system is critically damped is called the coefficient of critical damping C_c. The damping ratio is written as

$$\xi = C/C_c \qquad \text{Eq. 2.4}$$

The previous equations describe the motion of a single DOF dynamic system. However, any real structural system has infinite DOF's. This can also be represented in a simplified way as multiple masses connected between them with springs and dampers. The motion of such structural system with an applied loading is governed by the following equation:

$$[M]\{\ddot{u}\} + [C]\{\dot{u}\} + [K]\{u\} = F(t) \qquad \text{Eq. 2.5}$$

Where $[M]$ is the mass matrix, $[C]$ is the damping matrix and $[K]$ the stiffness matrix. $\{\ddot{u}\}$,$\{\dot{u}\}$ and $\{u\}$ are respectively the acceleration vector, velocity vector and the position vector. F(t) is the external force applied on the system. All vectors vary as a function of time.

The natural frequencies and mode shapes of the system can be found if Eq. 2.5 is formulated supposing zero damping and no applied loading. In such case, the equation of motion reduces to:

$$[M]\{\ddot{u}\} + [K]\{u\} = 0 \qquad \text{Eq. 2.6}$$

This is known as the free vibration equation of motion. In this case, only the inertial and the elastic forces are significant.

To solve the equation, we assume a harmonic solution of the following form:

$$\{u\} = \{\phi\} \sin \omega t \qquad \text{Eq. 2.7}$$

Where $\{\phi\}$ is the eigenvector or mode shape and ω is the circular frequency. This solution means that the inertial forces are equal to the elastic forces and that all the degrees of freedom of the vibrating structure move in a synchronous manner. When this solution is differentiated and substituted in Eq. 2.7, the following is obtained:

$$-\omega^2[M]\{\phi\} \sin \omega t + [K]\{\phi\} \sin \omega t = 0 \qquad \text{Eq. 2.8}$$

Which is simplified to the following form:

$$([K] - \omega^2[M])\{\phi\} = 0 \qquad \text{Eq. 2.9}$$

There are two possible solutions for Eq. 2.9. The first one implies that $\{\phi\} = 0$, which does not provide any valuable information from the physical point of view. The second one is obtained by solving the following expression:

$$det([K] - \omega^2[M]) = 0 \qquad \text{Eq. 2.10}$$

And provides a set of discrete ω^2 values and their corresponding eigenvectors $\{\phi_i\}$. These values describe the free vibration of the dynamic system. Each eigenvalue represents one natural frequency of the system by the following relationship:

$$f_i = \frac{\omega_i}{2\pi} \qquad \text{Eq. 2.11}$$

Where f_i is the i-th natural frequency of the system. The natural frequencies are those at which the elastic forces counterbalanced the inertial forces, and the mode shapes describe the deflection shape of the system at each natural frequency.

2.1.2. Forced vibration of a structural system

When studying the forced vibration of a structural system with a single DOF, we consider that the force applied is oscillating harmonically, leaving Eq. 2.1 in the following way:

$$M\ddot{u} + C\dot{u} + Ku = F_0 \sin(\omega t + \varphi) \qquad \text{Eq. 2.12}$$

Where F_0 is the amplitude of the force and φ is the phase angle difference between the frequency of the excitation force and the frequency of the system. The steady-state solution of the equation is as follows:

$$u = \frac{F_0/K}{\sqrt{\left[1-\left(\omega_s/\omega_n\right)^2\right]^2+\left(2\xi\omega_s/\omega_n\right)^2}} \qquad \text{Eq. 2.13}$$

When the frequency of the force is lower than the frequency of the system, elasticity controls the motion, and when the frequency is higher, the inertial forces control it. However, when the frequencies are the same, the system enters in resonance, and the only force that opposes the motion is the damping force, because the terms of elasticity and mass cancel each other out. In such case, the amplitude of the movement is maximum, and the angle between the force and the system response is 90 degrees.

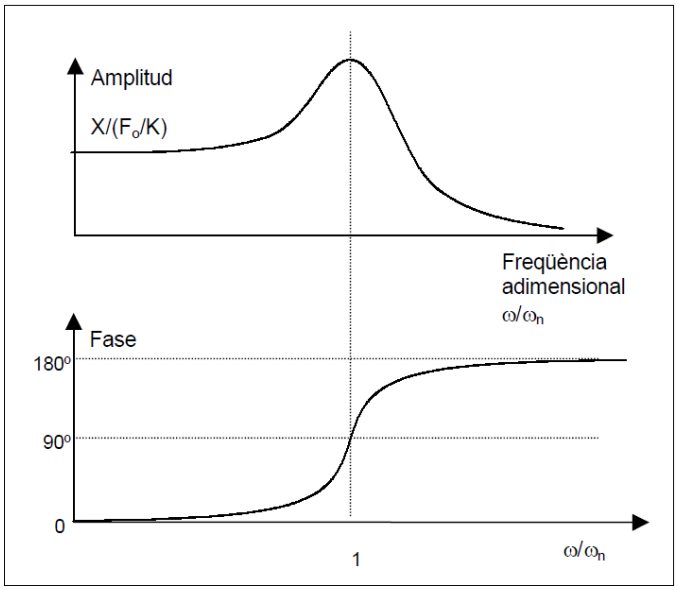

Figure 2.1. Bode plot when the system enters in resonance with an external force [38]

2.2. Structure of a Pelton runner

2.2.1. Geometry

The geometry of a Pelton turbine runner is very different from reaction turbines. It is composed by a wheel with a series of buckets attached to its periphery. The buckets are the components that receive the impact of the water jet and where the hydraulic energy is converted into mechanical energy. The shape of a Pelton bucket must meet a compromise between a hydraulic and a structural optimal shape; one the one hand, they must be dimensioned and contoured to have maximum hydraulic efficiency and on the other hand they must guarantee enough structural resistance to bear the forces applied to them during operation. The main dimensions of a Pelton runner are showed in Figure 2.2. The pitch diameter D_1 is defined as double the distance between the jet axis and the runner centerline, b is the bucket width and a is the bucket height. The main parts of the buckets are the cutout, the splitter and the rim. The cutout is where the jet first enters the bucket, the splitter divides the jet into two streams, and the rim is where the water last interacts with the turbine and is considered the outlet of the bucket. Between the splitter and the rim, the water jet is deflected almost 180 degrees to deliver the maximum available power to the turbine.

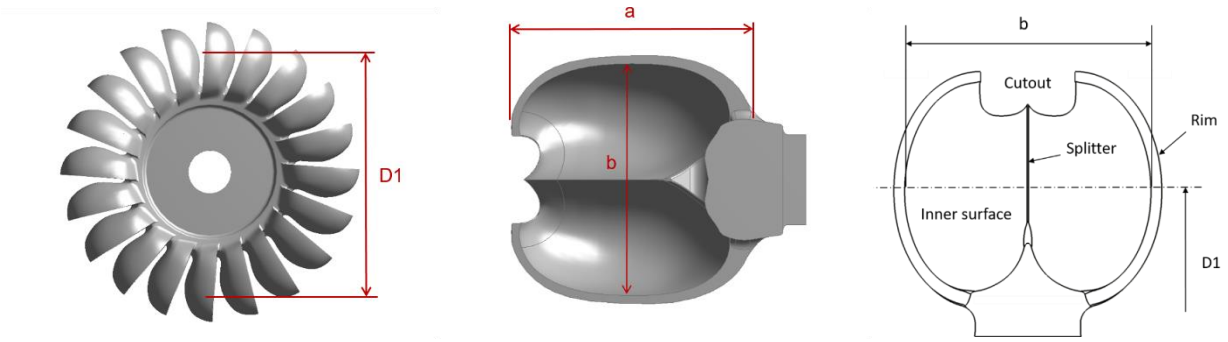

Figure 2.2. Main dimensions of a Pelton runner

2.2.2. Specific speed and dimensions

The dimensions of the wheel and the buckets of a Pelton turbine are related to its specific speed. The specific speed N_s of a turbine is a non-dimensional number that represents the speed at which a geometrically similar turbine that delivers an output of 1 kW rotates under a head of 1 m. It is a widely used parameter to classify hydraulic turbines and to define their compactness. Over the years, there has been a trend to increase the specific speed of Pelton turbines due to economic reasons [39]: minimizing the dimensions of the runner leads to a reduced cost on electro-mechanical equipment and on civil works. Nevertheless, factors such as cavitation and the maximum allowable peripheral velocity of the runner define the upper limit of the specific speed value [10]. These effects are dramatized with increasing head

because of the increasing velocity of the jet. It is possible to correlate the head of the turbine to its specific speed, as shown in the chart of Figure 2.3.

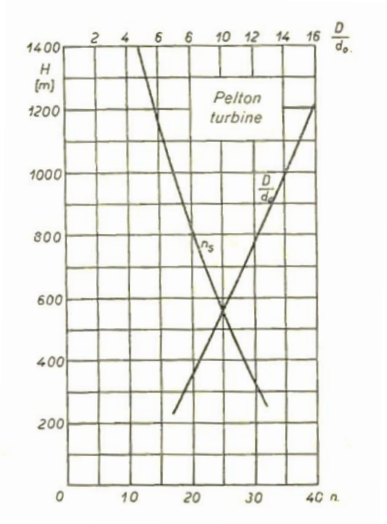

Figure 2.3. Correlation between head H and specific speed N_s [8]

The main dimensions of the runner can be related to the specific speed by the following procedure. The equation of specific speed N_s for a one jet Pelton runner is expressed as follows

$$N_s = NP^{0,5}H^{-1,25} \quad \text{Eq. 2.14}$$

In this equation, N_s represents the specific speed in min^{-1}, N the rotational speed in min^{-1}, P is the rated output in kW and H is the net head in m. These values can be directly related to the dimensions of the nozzle and of the wheel when some assumptions are made. Since almost all the potential energy in a Pelton turbine is converted into kinetic energy, the velocity C_0 of the water at the exit of the nozzle can be defined as

$$C_0 = k_{Cm}\sqrt{2gH} \quad \text{Eq. 2.15}$$

Where k_{Cm} is the loss coefficient of the nozzle and amounts to 0,95 to 0,98, g is the gravitational acceleration in m · s^{-2} and H is the net head in m. To obtain maximum power from the water jet, the peripheral velocity of the buckets U_1 at the pitch diameter must be half the absolute velocity C_0 of the water jet. In practice, this value can range from 0,44 to 0,46 and it is defined by k_u.

$$U_1 = k_u C_0 = k_u k_{Cm}\sqrt{2gH} \quad \text{Eq. 2.16}$$

For simplification purposes we will consider k_{Cm}=1 and k_u=0,5.

$$U_1 \cong \sqrt{gH/2} \quad \text{Eq. 2.17}$$

We can say then that the velocity U_1 of the bucket only depends on the net head. The diameter of the runner is related to the rotational speed N and the velocity of the bucket U_1 by the following equation

$$D_1 = \frac{U_1 60}{\pi N} \qquad \text{Eq. 2.18}$$

Where N is the rotational speed in min^{-1} and can only take synchronous values, which usually are 1000, 750, 600, 500 and 428 min^{-1}. The discharge of the Pelton runner can be obtained from the area of the cross-section of the jet and the jet velocity

$$Q = \frac{\pi {d_0}^2 C_0}{4} \qquad \text{Eq. 2.19}$$

where Q is the turbine discharge in $m^3 \cdot s^{-1}$ and d_0 is the diameter of the water jet in m. Substituting the terms N, P and H in the Eq. 2.14, we have the following equation

$$n_s = \left(\frac{U_1 60}{\pi D_1}\right)\left(\gamma \frac{\pi {d_0}^2 C_0}{4} \frac{2{U_1}^2}{g}\right)^{0,5} \left(\frac{2{U_1}^2}{g}\right)^{-1,25} \qquad \text{Eq. 2.20}$$

If we consider that $C_0 = 2 \cdot U_1$ we have

$$n_s = const. \frac{d_0}{D_1} \qquad \text{Eq. 2.21}$$

It can be seen that the ratio of the diameter of the jet d_0 to the diameter of the runner D_1 is of major importance. From these two parameters, all the other design parameters can be deduced from geometrical relationships that are limited by efficiency and/or structural resistance reasons. For example, the centripetal stresses increase with the mass of the bucket (which is proportional to d_0) and with the centripetal acceleration (which is inversely proportional to D_1) for a given head. The bending stresses also increase with increasing bucket size and decreasing pitch diameter, so the ratio d_0/D_1 must be decreased with increasing head.

2.3. Numerical study of a Pelton runner

2.3.1. Characteristics of Arties Pelton turbine

The Pelton runner used to perform this modal analysis belongs to a power plant called Arties located near a mountainous site in Catalonia (Spain). The machine is a horizontal Pelton turbine with two runners. Each one of them is operated by one jet, which impinges the lower buckets horizontally. Two bearings support the structure between the runners and the alternator (see Figure 2.4). The main characteristics of the runner are listed in Table 2.1.

Table 2.1. Characteristics of Arties Pelton turbine

Name	Arties	**Pitch diameter D_1**	1900 mm
Head	770,5 m	**Jet diameter d_0**	170 mm
Output	35 MW	**Bucket width b**	595 mm
Speed	600 min^{-1}	**Nozzles**	1
N_s	19	**Buckets**	22

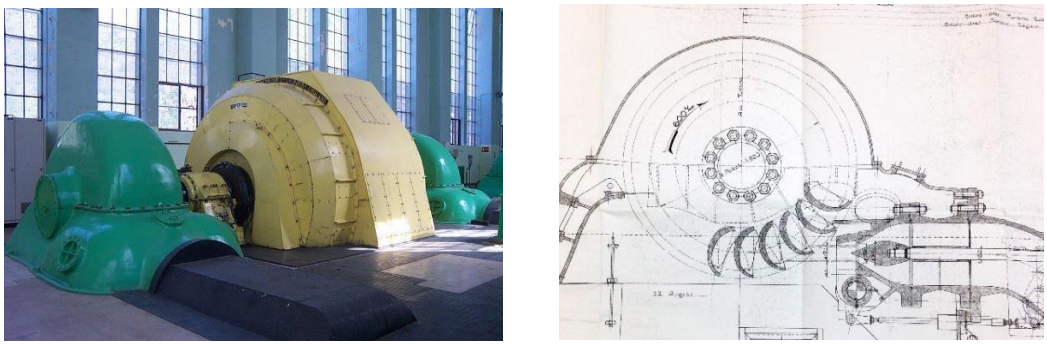

Figure 2.4. Views of the Pelton unit

To perform the numerical modal analysis, one runner of recent design that was still not installed in the machine was scanned with a 3D scanner (see Figure 2.5). Later, this runner was also used for the experimental analysis.

Figure 2.5. Left, view of the runner and right, CAD geometry of the runner

2.3.2. Finite Element Analysis (FEA)

The numerical study of the Pelton turbine has been performed by means of Finite Element Analysis (FEA). FEA is a powerful computational technique that allows simulating the physical behavior of any structure by decomposing its domain into a finite number of subdivisions and converting it into a mathematical model. These subdomains, called elements, are connected to each other by nodes, which specify the location in space where degrees of freedom and interaction between the elements exist. The interaction between the elements is defined by systematic approximate solutions of the governing physical equations that affect the structure, which are constructed by applying variational or weighted residual methods.

The program used to perform this analysis is the commercial software ANSYS®. It provides a wide range of modules, suitable to perform different kinds of structural analysis. For this study, the Modal Analysis module was used to obtain the natural frequencies and mode shapes of the turbine.

The first step when performing a FEA is to discretize the domain of the structure into a finite number of elements. Such procedure is known as meshing and largely defines the quality of the results of the simulation. Increasing the amount of elements and nodes (what is known as a refined mesh) usually improves the accuracy of the simulation. However, having a large number of mesh elements implies a greater computational effort. Therefore, it is convenient to perform a mesh sensitivity analysis in order to find a balance between result stability and reasonable computational time. Equally important is to assess a proper mesh refinement depending on the characteristics of the geometry. Those areas of the solid that have high curvatures require a finer mesh than those with small geometric variations.

After meshing the geometry, the boundary conditions of the body must be determined. For structural analysis, this usually means to fix one or more areas of the body. When performing a free vibration analysis, no boundary conditions are considered.

2.3.3. Numerical analysis of a single bucket

The geometry of the Pelton runner was imported to ANSYS®. From the original geometry, one of the buckets was cut off and treated as a separate body to perform the following analysis. The meshing of the bucket was carried out with tetrahedral elements, which were smaller in the areas of the cut-out and the ridge of the bucket due to their high curvature. The purpose of this study is to know which are the typical mode shapes of a bucket when it is attached to the runner. Hence the model of the bucket wasn't treated as a free body. Instead, the body was constrained (zero displacement) on the areas that are attached to the rest of the runner (see green surfaces in Figure 2.6). The x-direction corresponds to the tangential direction of the pitch diameter of the runner, y-direction to the radial direction and z-direction to the axial direction. The mesh had 25000 tetrahedral elements. The mesh density was increased in the sharp edges and the locations were typically a high concentration of stresses occur, which are the cutout and the ridge.

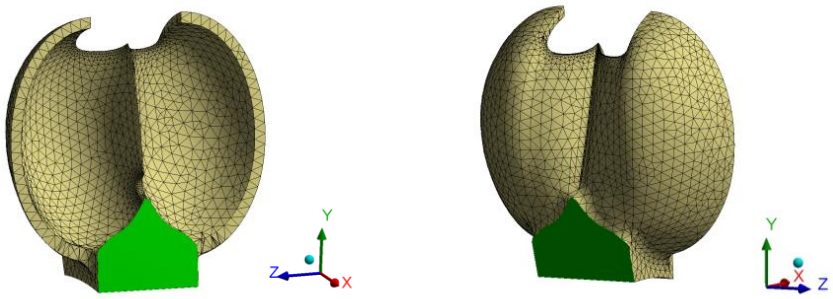

Figure 2.6. Front and rear view of the meshed bucket

Next, the pure mode shapes of the bucket have been analyzed. Although the number of modes is infinite for any structure, only the eight modes at the lowest frequencies have been considered for this study. Since the main dimensions of a bucket are standardized in relation to the jet diameter, we can take the results as representative for most Pelton runners. In Figure 2.7 front and side views of the first four modes of the bucket are displayed. The regions that vibrate with maximum amplitude are represented in red while the regions with minimum or zero displacement are represented in blue. It is worth noting that the color scale is not the same for all the modes, since the program takes as a reference the maximum and minimum values of every mode. The shape of the bucket without deformation is depicted with the light-wired figure.

The first two modes (top left and top right of Figure 2.7) can be compared to the first natural mode of a cantilever beam, in which the structure tilts over a clamped base. The first one is known as axial mode, because the bucket bends in the same direction as the axis of the runner. The second mode is referred to as tangential mode (or bending mode in circumferential direction in some publications [24]) and is considered the most dangerous mode in a Pelton runner since it is the most excited by the impact of the water jet. The bucket axial mode is found at the lowest frequency because the stiffness of the bucket is lower in the axial direction than in the tangential direction. For both mode shapes, the tips of the bucket deform in phase.

In the second group of modes (bottom left and bottom right of Figure 2.7), both halves of the bucket oscillate with opposite phases. In the third mode, which has been named counter-phase tangential mode but it is also known as torsional mode, the bucket halves bend tangentially in opposite phases, thus giving certain torsion around the radial axis of the bucket. In this mode shape, we can also see that the splitter is deforming. The fourth natural mode, called counter-phase axial mode or rim mode, involves the axial deformation of the rims of the bucket in opposite directions, with a periodic spreading and contracting motion.

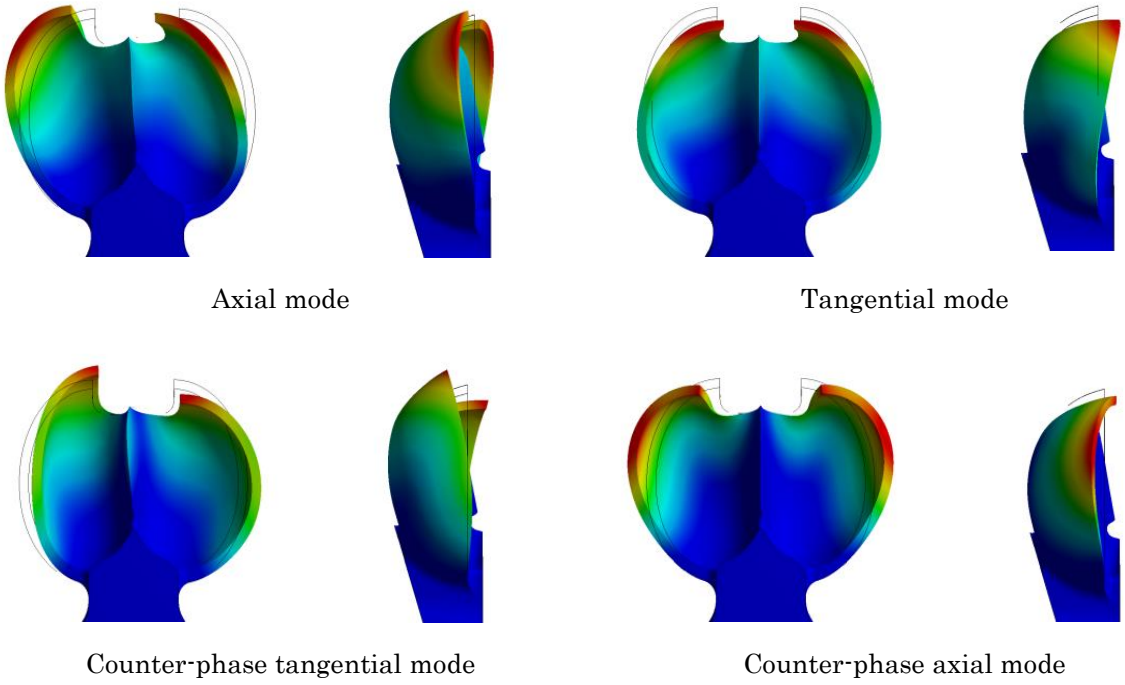

Figure 2.7. Pure bucket modes

In Figure 2.8 the fifth, sixth, seventh and eighth natural modes of the bucket have been represented. All of them are featured by the appearance of transversal nodes on the bucket, what increases the stiffness, and thus the frequency. In the fifth and sixth modes (top left and top right of Figure 2.8, respectively) the tips of the bucket are stretched in the radial direction, with equal and opposed phases on both halves, respectively. Consequently, they have been named radial and counter-phase radial. The deformation of the rims in the axial direction is also relevant in these modes.

The seventh mode (bottom left of Figure 2.8) is similar to the counter-phase radial mode, although the tips of the bucket do not have a pure radial deformation. Instead, they have a combination of axial and radial deformation. Thus, this mode has been named counter-phase axial-radial mode. At this frequency, the splitter also shows a large deformation. In the eighth mode, called 2-ND radial mode, two transversal nodes appear in the bucket and the tips stretch radially.

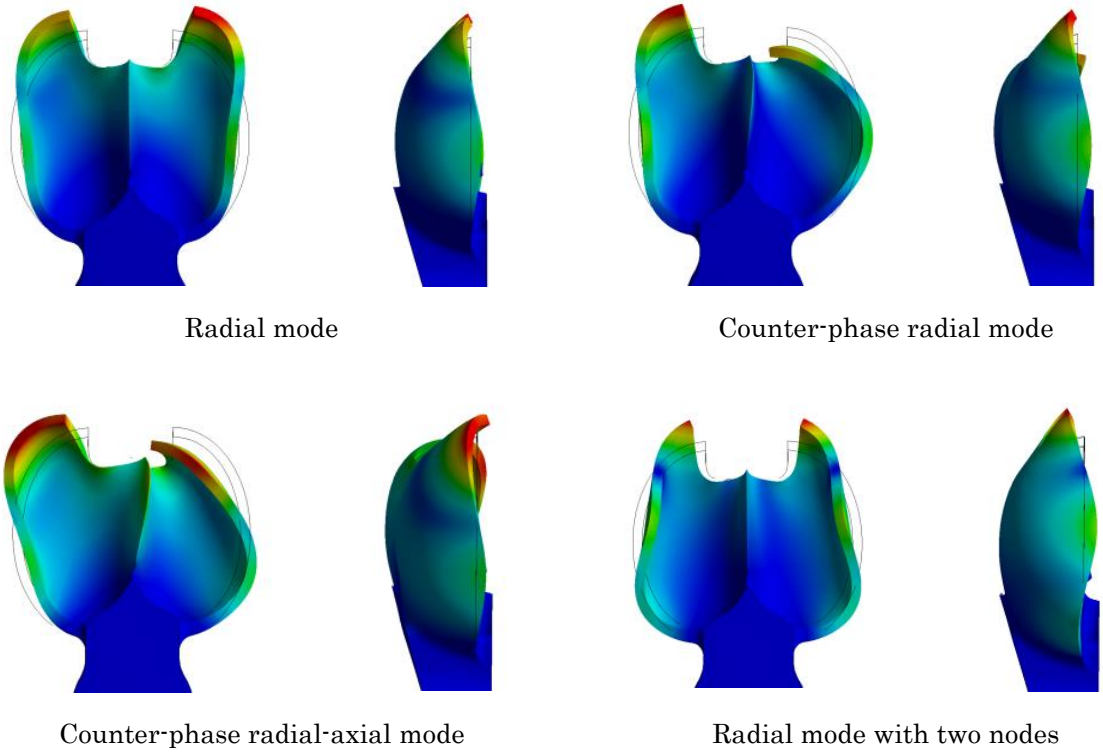

Figure 2.8. Pure bucket modes

2.3.4. Numerical analysis of the whole runner

After representing the pure modes of a bucket, the modal simulation of the whole structure was carried out. A mesh sensitivity analysis was done prior to the analysis to determine an acceptable number of mesh nodes, which didn't require too much time and computational resources, and guaranteed stable results. As seen in Figure 2.9, the values of the first natural frequencies obtained with different mesh refinements were compared. From 400000 elements on, the values converged. The main characteristics of the final simulation are listed in Table 2.2. Two views of the mesh are displayed in Figure 2.10. The mesh properties at the buckets were the same as in the single bucket model.

Table 2.2. Information about the FEM simulation of the runner

Boundary conditions	Free body
Material	Stainless steel
Density	7500 $kg \cdot m^{-3}$
Young's modulus	2×10^{11}
Mesh element type	Tetrahedral
Number of mesh elements	400000

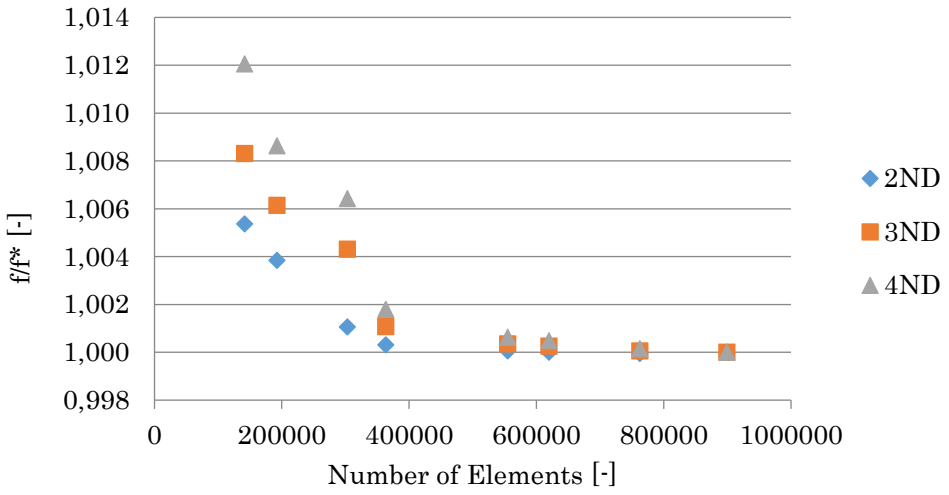

Figure 2.9. Mesh sensitivity analysis

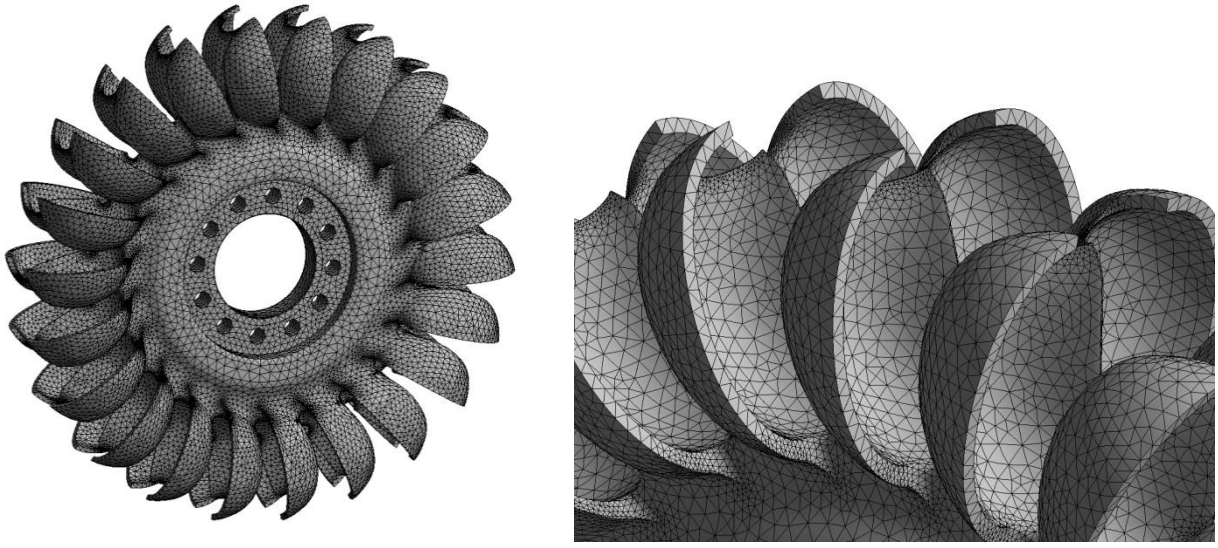

Figure 2.10. Left: Mesh of the whole runner, right: detailed mesh of the buckets

Next, the modal shapes of the Pelton runner, which are displayed in Figure 2.11 and Figure 2.12, will be analyzed. The order of appearance of the mode shapes is the same as in the pure bucket modes. The simulation shows that for every mode shape found in the single bucket, several variants of the same mode appear in the runner. Each variant of the same bucket mode appears at a different frequency and combines the oscillation of the buckets and the wheel in different ways. These can be classified by the number of nodal diameters of the wheel. The nodal diameters delimit circumferentially consecutive regions oscillating in opposite phases and have minimum or zero displacement. The areas that are the furthest from the nodal lines show the maximum deformation amplitude. The number of buckets determine the total sum of variants of the same bucket mode shape. This Pelton turbine has 22 buckets, thus there is a total amount of 22 modal shapes for every bucket mode, which reach a maximum number of 11 nodal diameters. For simplicity purposes only the modal shapes of the Pelton runner with two (2-ND), five (5-ND) and ten (10-ND) nodal diameters have been displayed for each bucket mode.

The axial, tangential and counter-phase tangential are displayed in Figure 2.11. The color scale is fixed for every mode to see the differences in amplitude between the different variants. At the lowest frequencies, one finds the axial modes, where wheel and buckets are deforming in the axial direction (top of Figure 2.11). When the number of nodes increases (left to right), the deformation of the disk is minimized and only a deformation in the area of the buckets is noticed. In that case, the maximum deformation, which is found at the tip of the buckets, is increased with respect to lower ND modes. The second group (middle of Figure 2.11) corresponds to the tangential modes. The disk deforms in the radial direction for the first ND modes, while for higher ND only the bending of the buckets is significant, just like in the axial case. In the third group (bottom of Figure 2.11), the counter-phased tangential mode involves the movement of the bucket tips in opposite phases. In this case, there is no deformation of the disk in the 2-ND (only the buckets are oscillating), and the maximum deformation of the tips of the buckets is kept almost constant for different ND, unlike the previous cases.

In Figure 2.12, the following modes of the Pelton runner are displayed also for 2-ND, 5-ND and 10-ND. One can clearly identify the 2-ND runner deformation in all of them, except in the radial mode, in which the oscillation amplitude of the disk is much lower than the buckets. In the counter-phase axial modes, the deformation of the disk is in the radial direction, like in the tangential modes. However, in the counter-phase radial mode, the disk deforms in the axial direction. In all of them, the deformation of the tip/rim of the buckets increases with the number of nodal diameters.

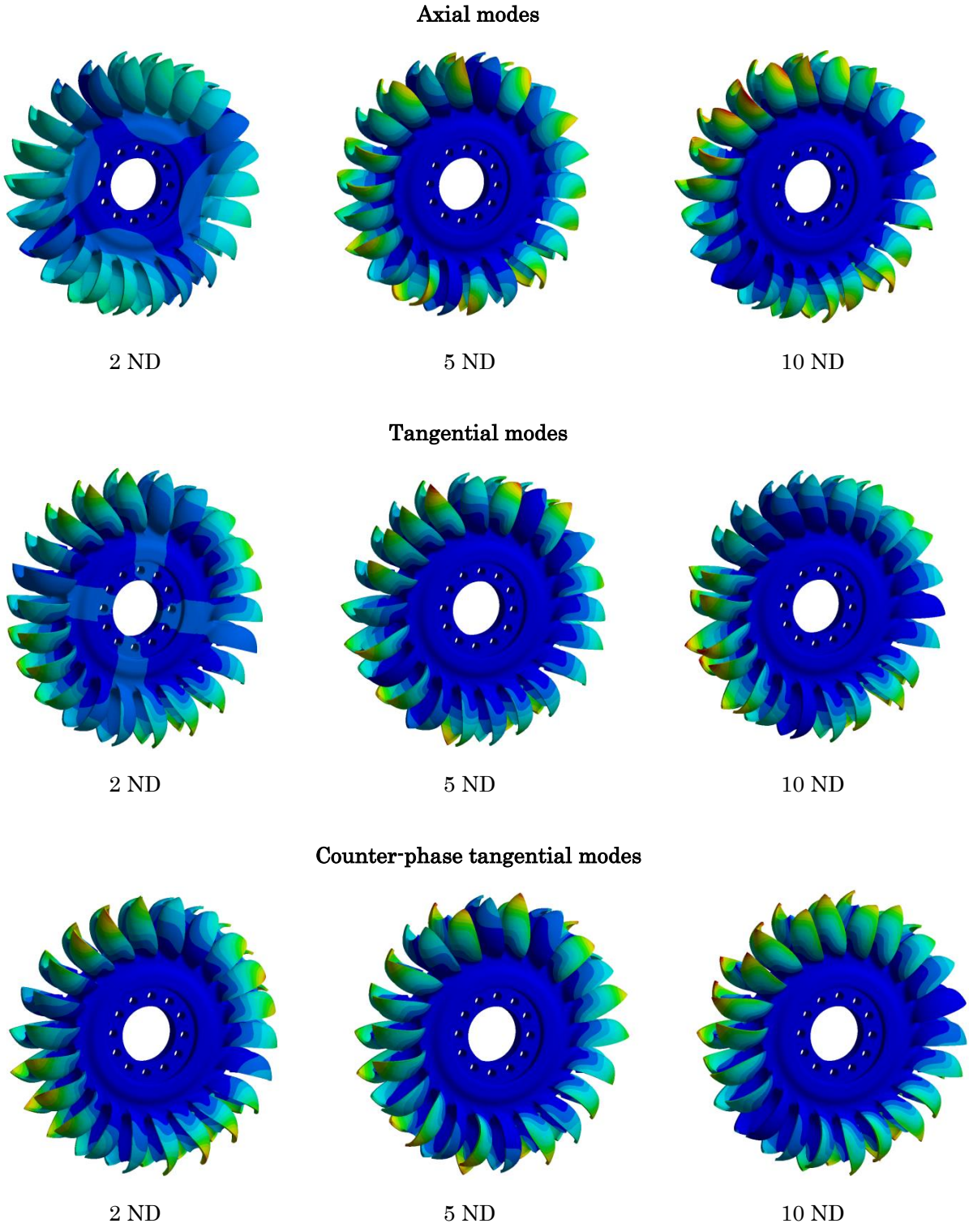

Figure 2.11. Runner modes

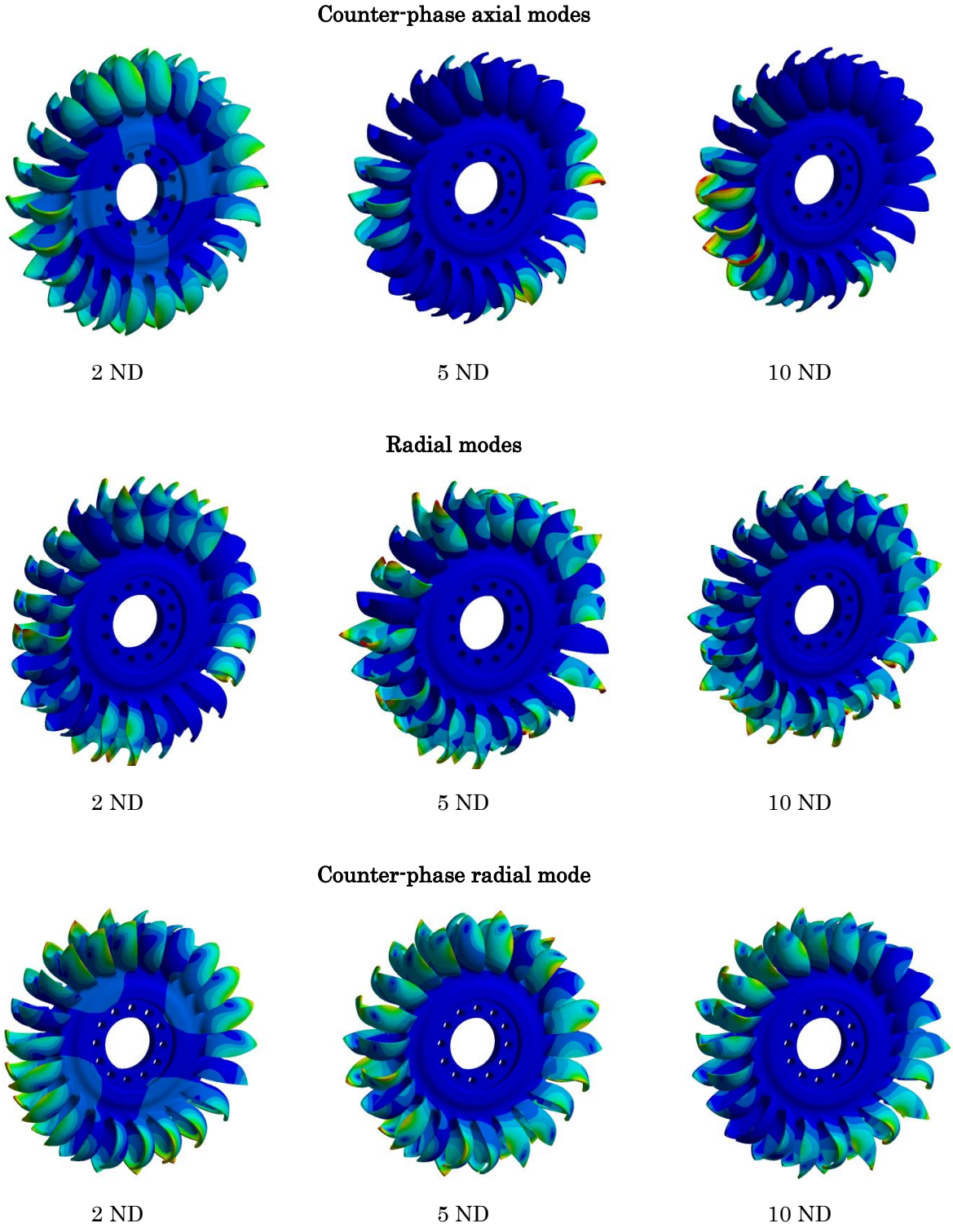

Figure 2.12. Runner modes 2

2.4. Experimental Modal Analysis (EMA)

The aim of the experimental tests was to study the pure mode shapes and frequencies of the Pelton runner, without the influence of the rotor. Therefore, the runner was suspended with a rope and placed in an accessible location of the power station to carry out impact tests. This was equivalent to considering the runner as a free body (without any constraint) due to the small influence of the rope on the vibration of the runner.

2.4.1. Impact testing

The object of an Experimental Modal Analysis (EMA) is to determine the frequencies and mode shapes of a structure experimentally. The procedure consists in executing a series of impacts to the structure in order to excite its natural frequencies, and in recording the resulting vibration with accelerometers. Tests can be performed either by placing several accelerometers on different locations of the structure or by executing several impacts on different locations. The latter is known as roving hammer method and the results obtained are the same as if using many accelerometers due to the reciprocity principle. Following any of these procedures, the natural frequencies and mode shapes of the structure can be determined.

The instrumentation used during an EMA typically includes an instrumented hammer, accelerometers and a recording module (Figure 2.13). The hammer is used to excite the natural frequencies of the structure and, due to an internal sensor, also measures the magnitude of the force exerted. Accelerometers convert the mechanical motion of the structure into an electrical signal. The force and the acceleration signals are then recorded by an acquisition module as a function of time for further analysis.

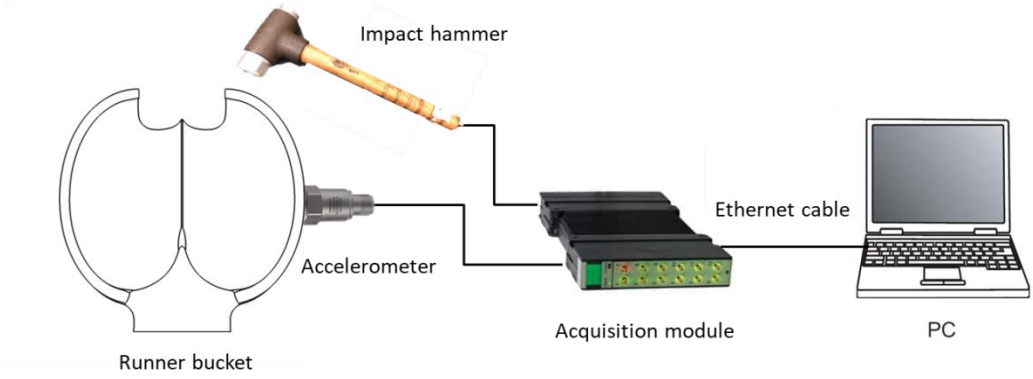

Figure 2.13. Impact test setup

The sensors used were industrial K-Shear® accelerometers from KISTLER type 8752A50. Their sensitivity was 100 mV/g and the acceleration range ± 50 g. They were mounted on clean and flat locations of the runner to ensure reliable and accurate measurements. The

sensitivity of the hammer was 223 μV/N. The acquisition module was a LAN-XI Data Acquisition Hardware from Brüel & Kjær. The model had 12 channels to connect the sensors.

To perform the EMA it was important to choose the location of the sensors accurately to represent the main mode shapes of the runner. For this reason, four accelerometers were placed on the surface of the disk (axial direction) with approximately 90 degrees between them and the same radial position. In addition, four accelerometers were placed on different locations of the buckets to detect the axial, tangential and radial modes. The axial accelerometers were adhered on the outer surface of the bucket rim, approximately in the middle section, and the tangential and radial accelerometers were placed on the tip of the bucket, on perpendicular surfaces. Since the vibration of a runner is complex, different series of impacts were carried out. In each series, the accelerometers were relocated in different parts of the buckets. One distribution to detect tangential modes of the runner is displayed in Figure 2.14.

Figure 2.14. Accelerometers disposition on the hanged runner

2.4.2. Signal processing

After performing the impact tests, the recorded data is analyzed in order to obtain the information.

The Fourier transform (FT) is a powerful tool that decomposes a signal into a series of frequencies by which it is formed [40]. The FT of a function $f(x)$ is the function $F(\omega)$, where

$$F(\omega) = \int_{-\infty}^{\infty} f(x) e^{-i\omega x} dx \qquad \text{Eq. 2.22}$$

And the inverse Fourier transform is

$$f(x) = \frac{1}{2\pi}\int_{-\infty}^{\infty} F(\omega)e^{i\omega x}d\omega \qquad \text{Eq. 2.23}$$

When we think of $f(x)$ as a signal, then the function $F(\omega)$ is called the signal's spectrum. The spectrum represents the energy of vibration in the frequency domain.

Since the signals obtained from the impact tests are discrete and periodic, it is not necessary to perform the FT. Instead, we use the Fast Fourier Transform (FFT), which is a fast algorithm for computing the Discrete Fourier Transform (DFT). The DFT is written as

$$A_k = \sum_{n=0}^{N-1} e^{-i\frac{2\pi}{N}kn}a_n \qquad \text{Eq. 2.24}$$

Where the analyzed signal is a_n for $n = 0 \ldots N-1$, and $a_n = a_{n+jN}$ for all n and j. The FFT computes the DFT at a lower cost. Once the spectrum of a signal is obtained, the natural frequencies are easily detected by peak picking.

The Frequency Response Function (FRF) gives the magnitude ratio and phase difference between the vibration of the structure and the excitation force. It can be thought of as the transfer function between the output (structure vibration) and the input (excitation force) of a dynamic system. With FRF the resonant frequencies, the damping and the mode shapes can be obtained [41].

The FRF are obtained from the steady-state solution of the equation of the forced vibration (section 2.1.2) and can be expressed in terms of magnitude and phase angle ϕ in the following manner:

$$\left|\frac{X(\omega)}{F(\omega)}\right| = \left[\frac{1}{k}\right]\left[\frac{\omega_n^2}{\sqrt{(\omega_n^2-\omega^2)^2+(2\xi\omega\omega_n)^2}}\right] \qquad \text{Eq. 2.25}$$

$$\phi = \tan^{-1}\left[\frac{2\xi\omega\omega_n}{\omega_n^2-\omega^2}\right] \qquad \text{Eq. 2.26}$$

The coherence function compares the content of two different signals to assess which frequencies are of the same origin. To define the coherence, it is necessary to first introduce the concept of power spectrum and cross-spectrum [42].

The power spectrum $S_{xx,j}$ of a signal x indicates the amplitude of a periodic oscillation in the frequency domain. It is defined by the following equation:

$$S_{xx,j} = (2\Delta^2/T)X_jX_j^* \qquad \text{Eq. 2.27}$$

Where X_j is the Fourier transform of x at frequency $f_j(X_j)$, X_j^* is its complex conjugate, Δ is the sampling interval and T is the total duration of the recording.

In a similar fashion, the cross-spectrum between two signals x and y is defined in the following way:

$$< S_{xy,j} >= \frac{2\Delta^2}{T}\frac{1}{K}\sum_{k=1}^{K} X_{j,k}Y_{j,k}^* \qquad \text{Eq. 2.28}$$

In this case, we replace the conjugate of the FT of signal $, X_j^*$, with the conjugate of the FT of signal y, $Y_{j,k}^*$. The subscript k and letter K represent the number of trials. Finally, the coherence can be expressed in the following way:

$$< \kappa_{xy,j} >= \frac{| < S_{xy,j} > |}{\sqrt{< S_{xx,j} >}\sqrt{< S_{yy,j} >}} \qquad \text{Eq. 2.29}$$

The coherence measures the relationship between two signals x and y at the same frequency and ranges between 0 and 1 at every frequency, in which 0 means there is no coherence between both signals, and 1 means absolute coherence between them at that frequency.

2.4.3. Results

An example of the FRF's obtained after performing hammer impacts to one runner bucket in the tangential and axial direction is shown in the top plot of Figure 2.15. The coherence between the hammer signal (excitation) and the accelerometers (response) is shown in the bottom plot of Figure 2.15.

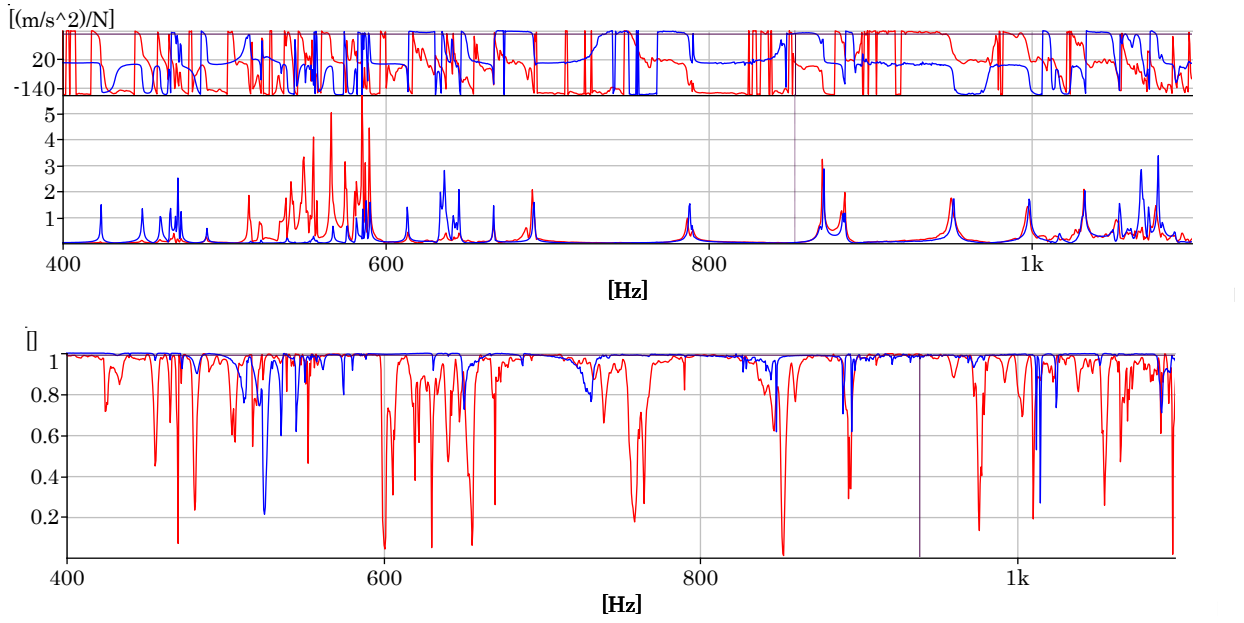

Figure 2.15. FRF's and coherence after impacts in the tangential (red) and axial (blue) directions

To identify the modal shapes of the structure, it is necessary to compare the signals from the different accelerometers (or different impacts) in terms of magnitude and phase. For complex structures it is common to create a simplified virtual model known as Operating Deflection Shapes (ODS), which offers a dynamic representation of the vibration pattern of the structure. Many nodes compose this model and each one of them represents the motion detected from one accelerometer. Some runner modes are represented in the ODS model in Figure 2.16.

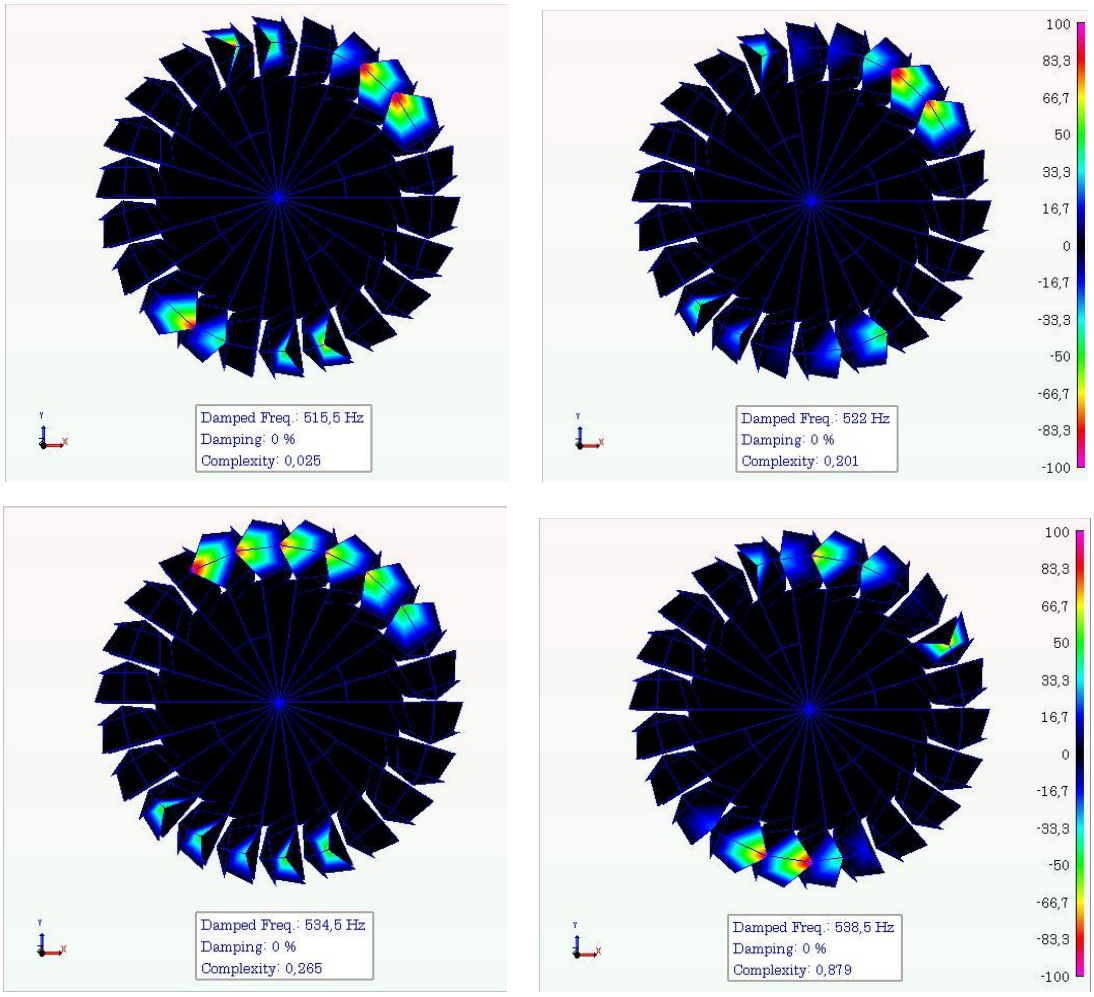

Figure 2.16. ODS of some tangential modes of the suspended runner

2.5. Analysis and discussion of results

This section attempts to analyze the modes of a Pelton runner by comparing the vibrational modes of the wheel with those of a single bucket. The interaction between both elements will be studied in order to have a better understanding of the modal behavior of the turbine. In Figure 2.17, the frequencies obtained from the numerical model (upper chart) can be compared with the experimental results (lower chart). Every type of bucket mode shape is attributed a color to relate more easily the peaks from the experimental tests with the numerical modes. The modes studied are located in a range between 0 and 1200 Hz. The first modes found are the axial modes between 195 Hz and 473 Hz. They are followed by the tangential modes (in-phase and counter-phase), which appear between 519 and 591 Hz and overlap each other. Next, the counter-phase axial modes are found in a very narrow frequency range between 618 and 648 Hz. The counter-phase radial modes and the radial modes are found in the next frequency band, being the former ones spread over a wide range of frequencies and the latter concentrated in a narrow band (1017 to 1077 Hz). Similar to the counter-phase axial modes, the counter-phase radial-axial modes have small differences between them.

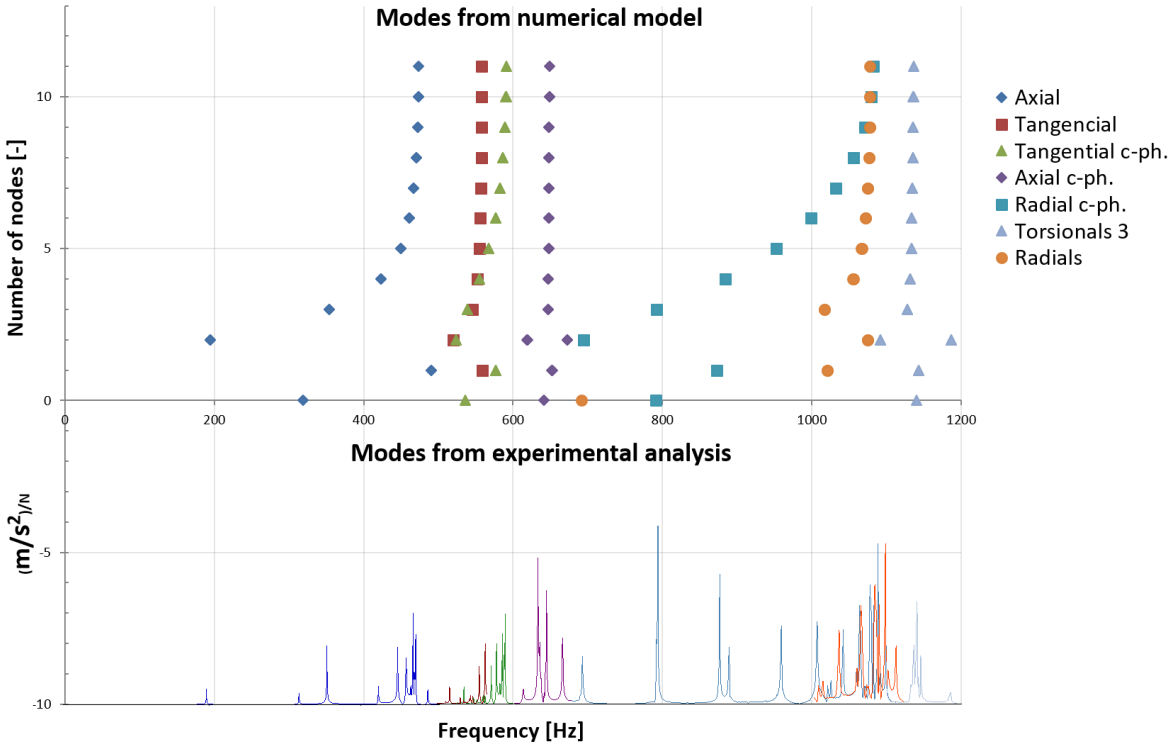

Figure 2.17. Numerical and experimental modes of a Pelton runner. Top, numerical results and bottom, response spectrum after the impacts

A noticeable fact is the nonlinear increase of the frequencies of each mode, which are distributed in a similar way to an asymptote. The modes in lower frequencies are those with a fewer number of runner nodal diameters. As the number of nodal lines increases, so does

the frequency, but at a decreasing rate. For instance, the axial mode with 2 ND has a frequency of 194,3 Hz and the one with 3 ND a frequency of 353,9 Hz, which is about 82% of increase. However, the 4-ND mode is found at 423,1 Hz, which is less than 20% increase with respect to the 3-ND mode. After 5 ND, frequencies converge in a small range, with a frequency variation lower than 3%. This effect is caused by the interaction between the modal shapes of the disk and the modal shapes of the buckets.

2.5.1. Analysis of the coupling between the disk and the buckets

To appreciate the contribution of every component (disk and buckets) to the global modal shapes of the structure, three simplified models have been studied: a disk (model 1), a disk with a single peripheral mass (model 2) and a disk with separated peripheral masses (model 3). The geometries and the distribution of frequencies can be seen in Figure 2.18. In model 1, the frequencies increase steadily with the number of nodal diameters. This is attributed to the fact that the mass oscillating between the nodal diameters becomes more restricted, thus having an increase in the stiffness. Attaching a peripheral mass to the disk (model 2) increases the overall stiffness of the modes, but the behavior is similar. However, when it comes to the disk with attached masses (model 3) the frequencies change their distribution. The maximum frequency is lowered. We can say that for a fewer number of nodal diameters the modes are governed by the disk (the frequencies are very similar for the three models) while for an increased number of nodal diameters, the modes become more dominated by the masses.

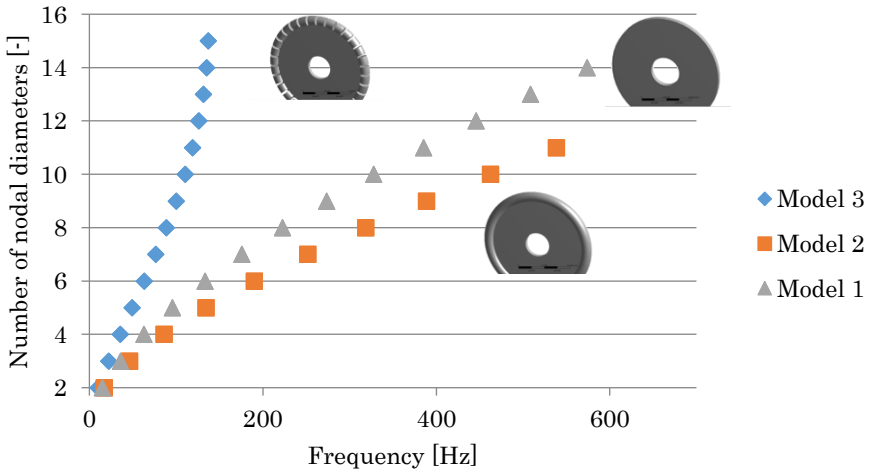

Figure 2.18. Frequencies of a disk and of a disk with masses

To see the progression from a disk-dominated mode to a bucket-dominated mode the deformation of the outer diameter of the disk in the axial direction in model 1 and model 3 has been represented in Figure 2.19. It can be seen that in model 1 the maximum displacement is kept almost constant. This fits the behavior observed in the distribution of frequencies: the modal mass is kept almost constant, and the frequency increases steadily

due to the stiffness increase. However, in model 3 the deformation of the disk decreases largely between 2 ND and 4 ND. From 5 ND the deformation barely shows a reduction. Some conclusions can thus be extracted from the chart. First, the increase in disk nodal diameters from 2 ND to 4 ND happens to reduce largely the vibrating mass of the disk, which explains the large difference between the first frequencies. Second, for modes with more than 5 ND the deformation of the disk is very small and shows almost no variation, even if the number of nodal diameters is increased. It can be thus said that in the higher modes almost all the vibration is performed by the buckets, and that their base is similarly restricted. This allows explaining why all the frequencies are so similar. Therefore, when studying the runner, the mode in the highest frequency, which corresponds to 11 ND, has the most resemblance to a pure bucket mode. The base of the bucket has the smallest angle between nodal diameters, being the most rigid one.

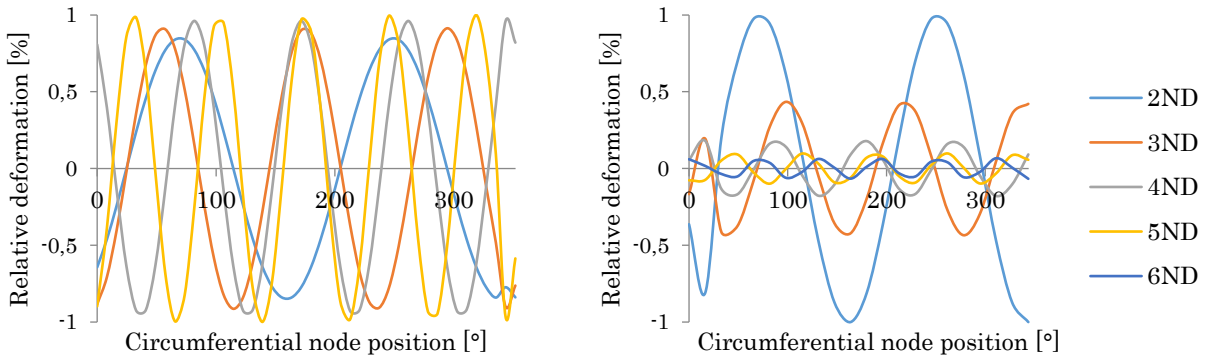

Figure 2.19. Relative deformation of the outer periphery modes in: left, the disk and right, the disk with masses

To check the similarity of the 11-ND mode to a simple bucket vibration, another analysis has been performed. The natural frequencies of a single bucket and the natural frequencies obtained in the 11-ND runner mode are indicated in Table 2.3. Comparing both columns, it can be seen that the bucket-dominated frequencies of the runner are 1-4.5% lower than the constrained bucket, which means that the nodal diameter provides more flexibility than a rigid surface. It is worth noting, though, that the variation in the frequencies differs from one mode shape to another. The axial and the counter-phase radial mode shapes are the most affected by the change in the boundary conditions of the disk.

Table 2.3. Variation in the bucket frequencies for different modes

	Single bucket [Hz]	**Runner 11 ND [Hz]**
Axial	487,8	473,7
Tangential	564,9	558,2
Tangential c-ph.	590,9	591,2
Axial c-ph.	635,0	648,6
Radial c-ph.	1120,4	1082,3
Radial	1091,9	1077,9

2.5.2. Effect of the bucket mode shapes

As already indicated, the effect of the coupling to the disk affects differently on every bucket mode. Some of them converge in a small range, like tangential and counter-phase axial modes. Such behavior can be attributed to the nature of the deformation of the bucket and its interaction with the disk. Some modes require a low contribution of the disk, for example the counter-phase axial modes, which are local and only affect the rim of the buckets. For these types of modes, a change in the stiffness of the coupling to the disk has a small effect on the vibration of the buckets. On the other hand, it is also important to mention that the increase in the number of nodal diameters affects the stiffness in the axial direction. In circumferential and radial direction, the disk is very stiff and the increase in nodal diameters does not entail a big change. Therefore, the modes with a large axial deformation of the disk (see axial and counter-phase radial in Figure 2.11 and Figure 2.12) are more sensitive to the variation in the disk stiffness. Tangential and counter-phase axial modes have a significant deformation of the disk but in the radial direction. In Figure 2.20, the deformation of the runner of 2-ND mode shapes at the base of the buckets in the axial direction has been plotted for all the modes. It is clear that the axial and counter-phase radials are the mode shapes most influenced by the axial stiffness of the disk.

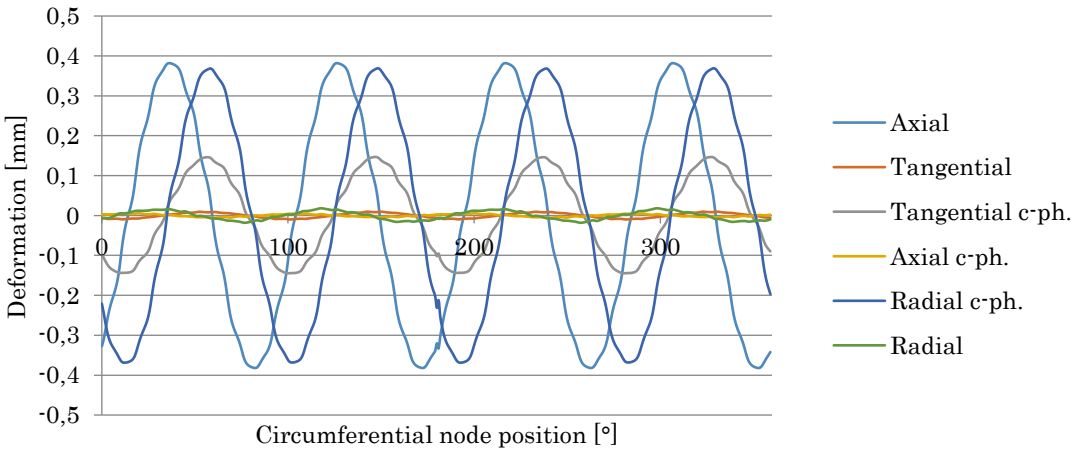

Figure 2.20. 2-ND axial deformation of the base of the buckets for every mode shape

2.6. Conclusions

The modal behavior of an existing Pelton turbine runner has been performed numerically and experimentally. A CAD of the runner was available from a scanning of the real runner. A numerical model using FEM was created and validated with an experimental modal analysis (EMA).

First, the modes of a single bucket have been studied numerically assuming it is rigidly connected (to disregard the effect of the disk). In this way, the pure bucket modes have been identified and, depending on the direction of the deformation, they have been classified as axial, tangential and radial modes. Depending on the phase between the bucket halves, these modes are considered in-phase or counter-phase. The first modes found are axial in-phase followed by tangential in-phase and counter-phase modes (also called torsional modes). After them, axial counter-phase (or rim modes) and radial modes appeared.

Second, the analysis of the complete runner was performed. The results showed that for every type of basic bucket mode, the runner has several multiples, which are coupled to the modes of the disk (n nodal diameters). For each group of bucket modes, the frequencies increase with the number of nodal diameters of the disk. It was noticed that in lower frequencies the vibration is global to all the runner (behaves like a disk) and in higher frequencies the vibration is more restricted and is dominated by the vibration of the buckets. The displacement of the buckets is larger in bucket-dominated modes than in disk-dominated modes. In addition, the influence of the stiffness of the disk is different for every bucket mode and this affects the distribution of frequencies. For example, tangential modes gather in a small frequency range, while axial modes spread over a wider range of frequencies. Finally, it has been proved that the bucket-dominated natural frequencies of the whole runner are lower than the ones obtained with a fixed single bucket.

Because runners are attached to the turbine rotor, the influence of this connection is analyzed in the next chapter.

Chapter 3 Modal behavior of Pelton machines

In the previous chapter, the modal behavior of a Pelton runner was comprehensively studied with the support of numerical models and experimental data. In the real machine, though, the runner is attached to the shaft, and this has an influence on its natural frequencies. Moreover, a Pelton turbine comprises the runner, the shaft and the alternator, which behave as a single body and have their own modal shapes and eigenfrequencies. All of these must be studied, since they are prone to be excited during the operation of the turbine. For such purpose, the modal behavior of the real turbine is analyzed in this chapter with the help of impact tests on the installed machine and with a numerical model of the whole rotor.

Next, to check if the distribution of runner modes obtained previously is similar between different Pelton turbines, two machines with different specific speeds are studied experimentally.

After that, the effect of the mechanical and hydraulic design on the modal behavior of Pelton turbines is studied. Two machines with the same characteristics and specific speed but different structural design are analyzed to see which influence this has on its natural frequencies. The effect of hydraulic design is then studied with three turbines with different specific speed but similar hydraulic design.

Finally, the feasibility to estimate the natural frequencies of Pelton turbines is evaluated. To that end, Pelton runners are geometrically characterized as function of its operational features, and the location of their natural frequencies analyzed.

3.1. Modal analysis of Arties Pelton turbine

The modal behavior of the whole Arties Pelton turbine has been studied in this section. Two Pelton runners, two shafts and one alternator comprise the rotor. Two bearings support the rotating structure between each runner and the alternator. The sketch and the main dimensions are shown in Figure 3.1.

3.1.1. Experimental analysis

The experimental tests were aimed at detecting the rotor modes of the turbine. For that purpose, accelerometers were placed on bearing 2 in the radial direction, horizontally and vertically (A31 and A34). In addition, four accelerometers were installed on the shaft: two between the runner and the bearing (E1V and E4V), and two between the bearing and the alternator (E2V and E3V). The distribution of the sensors is represented in Figure 3.1. The accelerometers were the same used in the hanged runner tests. The positions of the accelerometers on bearing 2 are shown in Figure 3.2.

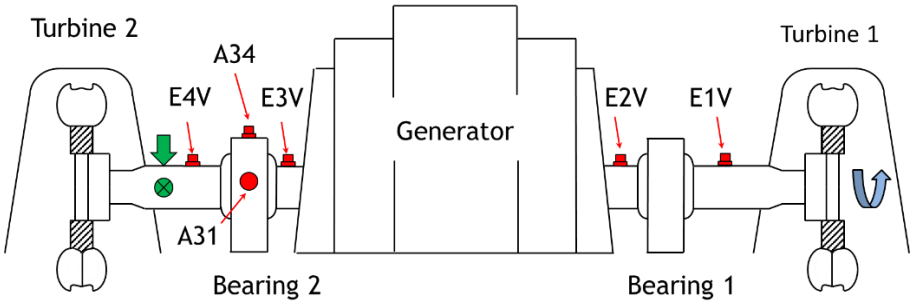

Figure 3.1. Sketch of the impact tests performed on the machine

Figure 3.2. Position of the accelerometer A31, A34 (left) and A35 and A38 (right)

In order to excite the rotor modes, a series of impacts was carried out between runner 2 and bearing 2 with the hammer. The impacts were made horizontally and vertically. The FRF of the frequencies excited are represented in Figure 3.3. There are three main groups of rotor modes and all of them appear after horizontal and vertical impacts. However, it is worth noting that the frequencies detected by the sensors differ a little depending on the direction of the impacts. All the frequencies excited after horizontal impacts are lower than the frequencies in the vertical direction due to the variation in the stiffness of the bearings. This means that there are four different variants for every group of modes, two where the rotor vibrates horizontally and two, vertically.

The modal shapes of the frequencies found can be described approximately looking at the magnitude and phase of the signals. In the first group of modes, found around 35 Hz, the accelerometers near the runner have a larger vibration than the ones between the bearing and the alternator. The same happens in the modes around 115 Hz. The phase, though, indicates that all the points of the rotor vibrate in the same direction in the first group of modes, while in the last group the alternator and the rotor move in opposite directions. The modes around 75 Hz involve a larger vibration between the bearing and the alternator and a higher damping. These indications will be useful to identify the modes on the numerical model.

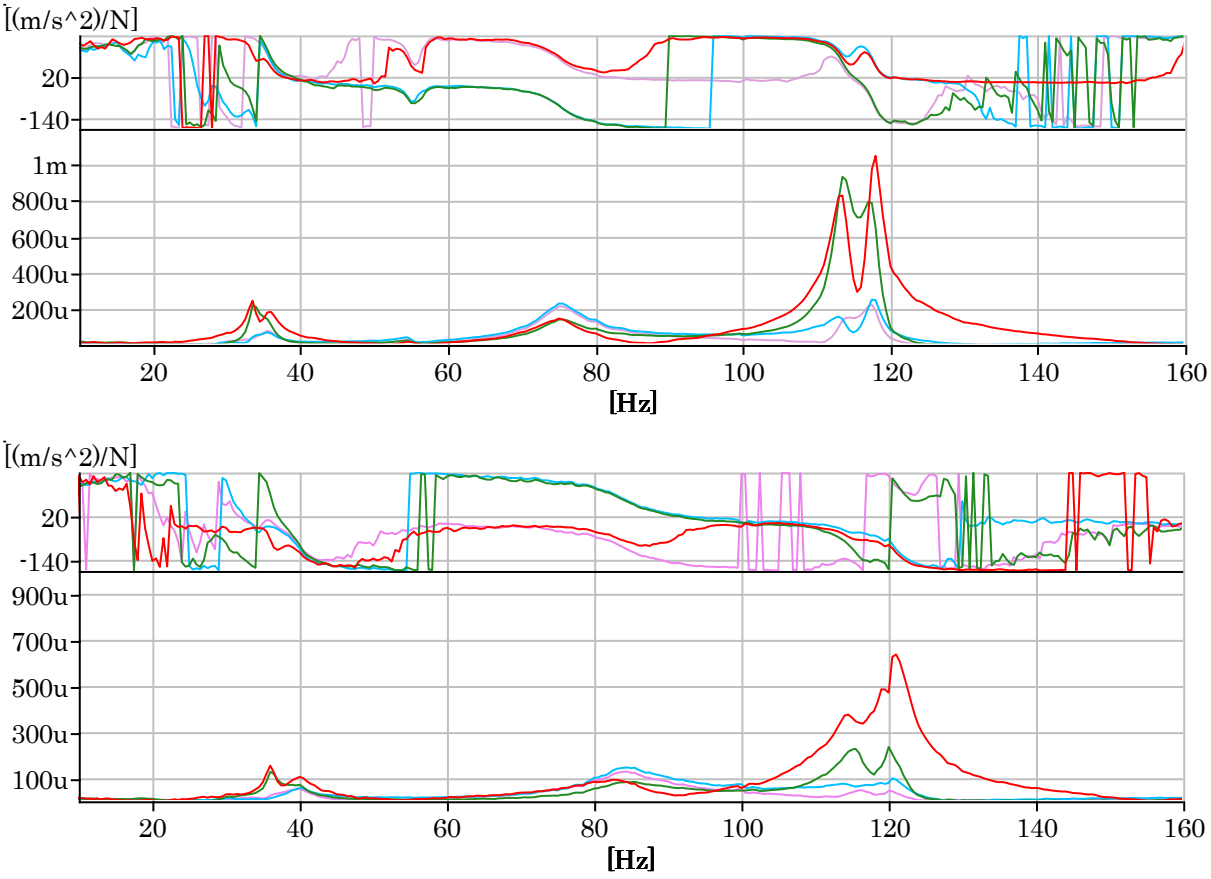

Figure 3.3. FRF of the response of accelerometers E1V (green), E2V (blue), E3V (pink) and E4V (red) to horizontal (top) and vertical (bottom) impacts

3.1.2. Numerical simulation

A numerical model was developed in order to analyze in detail the modal behavior of a Pelton turbine. The alternator and the shaft were created by computer assisted design (CAD) representing the same distribution and dimensions of the real machine. Two models of the same runner studied in the previous chapter were attached to the tip of the shaft. The design runner buckets used in the numerical model (from turbine A-1) was different from the ones installed in the machine (turbine A-2), but the effect of this variance has very low effect on the modes of the rotor, because it behaves almost as a rigid body.

The numerical model of the turbine (see Figure 3.4) consisted of two runners, two shafts and the alternator (core and poles). The meshing of the runner geometry had the same characteristics as the model developed in Chapter 2. The characteristics of the shaft and the runner are listed in Table 3.1. Two types of connections were used as boundary conditions in the different components. To attach the runners to the shaft, and the shaft to the alternator, the contact surfaces were set as bonded connections. These ensure that no translation takes place between the respective mesh nodes. To emulate the stiffness of the bearings, elastic connections to the ground (springs) were created in the horizontal and vertical directions.

Table 3.1. Mesh characteristics of the shaft and the alternator

	Shaft 1 / Shaft 2	Alternator
Boundary conditions	Elastic connect. to ground Bonded to runner 1 / runner 2 Bonded to alternator	Bonded to shaft 1 and shaft 2
Material density	7850 $kg \cdot m^{-3}$	7000 $kg \cdot m^{-3}$
Young's modulus	2×10^{11}	2×10^{11}
Mesh element type	Tetrahedral	Hexahedral
Number of mesh elements	82300	24800

The procedure followed to know the stiffness of the bearings consisted in varying the connection elasticities of the FEM model and comparing the resultant frequency values with the experimental values. The speed dependent oil film elasticity and damping were not considered. After some calculations, the values listed in Table 3.2 were selected. The maximum error between experiment and FEM model was under 20% (Table 3.3). The elasticity values are consistent with results obtained from other studies [43].

Table 3.2. Elasticity of the bearings in every direction

	Bearing 1	Bearing 2
Vertical stiffness	$5\times10^{9}\ N \cdot m^{-1}$	$5\times10^{9}\ N \cdot m^{-1}$
Horizontal stiffness	$3\times10^{9}\ N \cdot m^{-1}$	$3\times10^{9}\ N \cdot m^{-1}$

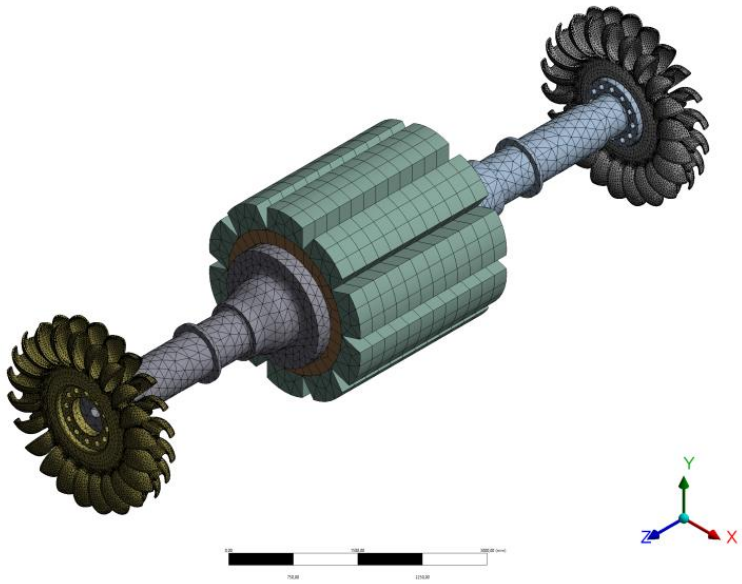

Figure 3.4. Numerical model of Pelton rotor

The rotor modes appear in the lowest frequencies and involve all the components of the turbine, which behave as a single body. In Figure 3.5, the views of the first two horizontal bending modes of the turbine are shown. Each mode has also a variant in the vertical direction, at a higher frequency. In the first bending mode the nodes are located by the bearings, which are the most rigid points of the structure, and the rest of the structure oscillates around these points. In the second bending mode all the area comprised between the two bearings acts a node, with a very small oscillation. In fact, the maximum deformation in this mode shape is found at the tips of the rotor, where the runners are attached. In this case, the runners behave as a stiff body. There are four variants of this mode depending on the direction of the deformation (horizontal or vertical), and on the symmetry between both sides (in-phase and counter-phase).

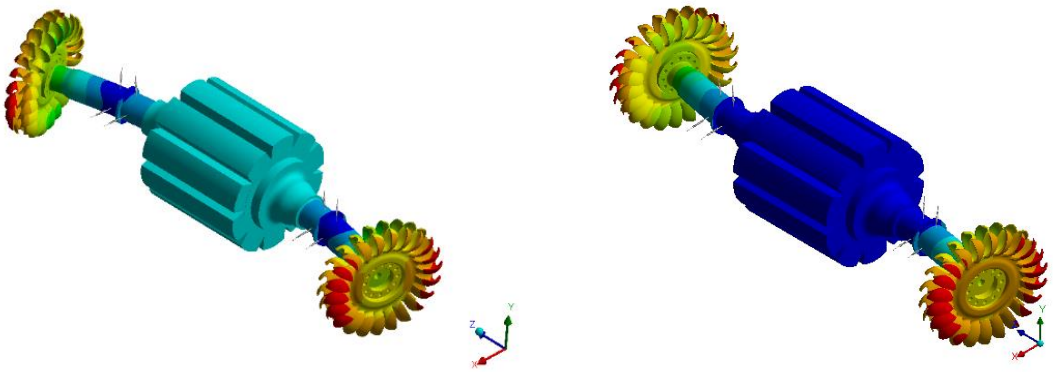

Figure 3.5. First (left) and second (right) horizontal bending modes

The next modes found in the model are the torsional and the third bending mode (Figure 3.6). The torsional mode is not excited by the impacts on the shaft and has not been detected in the experiment. There are two variants of the torsional mode, one with both runners twisting in phase and another in counter-phase. In the third bending mode three nodal lines can be discerned. One crosses transversally the core of the alternator, and the other two cross diametrically both runners. The modal mass displaced is large. This also has a variant in the vertical direction and another in the vertical direction.

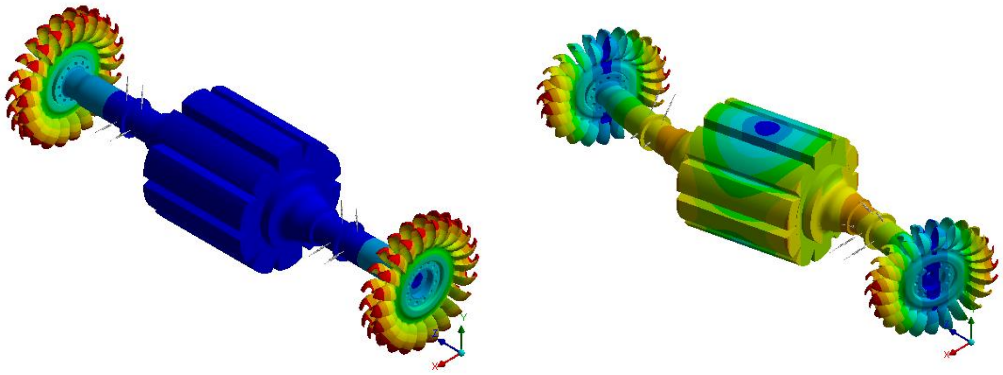

Figure 3.6. Torsional (left) and third bending (right) modes

At higher frequencies, the modes are a combination between rotor and runner modes. The shapes are displayed in Figure 3.7. The first resembles a 1-ND runner mode, and still has some deformation of the shaft. Again, four variants appear, depending on whether both runners move in-phase or in counter-phase, and on the direction of the deformation (horizontal or vertical). The following shape is also a runner-rotor combination, in this case for an axial 0-ND mode. All the buckets in each runner move in phase in the direction of the shaft axis. The shaft has a certain elongation with the motion of the runners. There are two variants, one is with the runners moving in-phase and another in counter-phase.

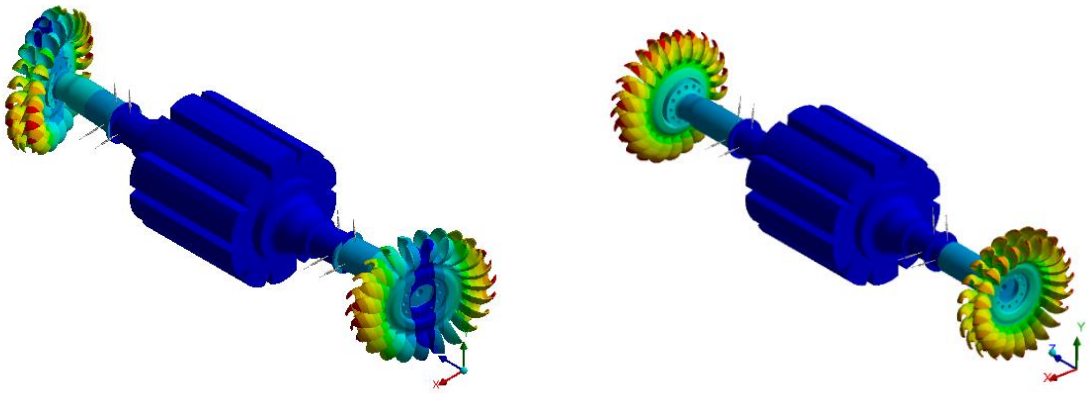

Figure 3.7. 1-ND (left) and 0-ND (right) rotor/runner modes

Finally, all the rotor modes have been identified and the frequencies checked with experimental results (Table 3.3 and Figure 3.8).

Table 3.3. Comparison between experimental and numerical rotor modes

	Horizontal			Vertical		
	Exp. [Hz]	Num. [Hz]	Error [%]	Exp. [Hz]	Num. [Hz]	Error [%]
2nd bending	33,5	31,54	5,85	36	30,39	15,58
3rd bending	75	79,84	6,45	84	69,0	17,86
4th bending	118	118,22	0,19	120,5	119,57	0,77

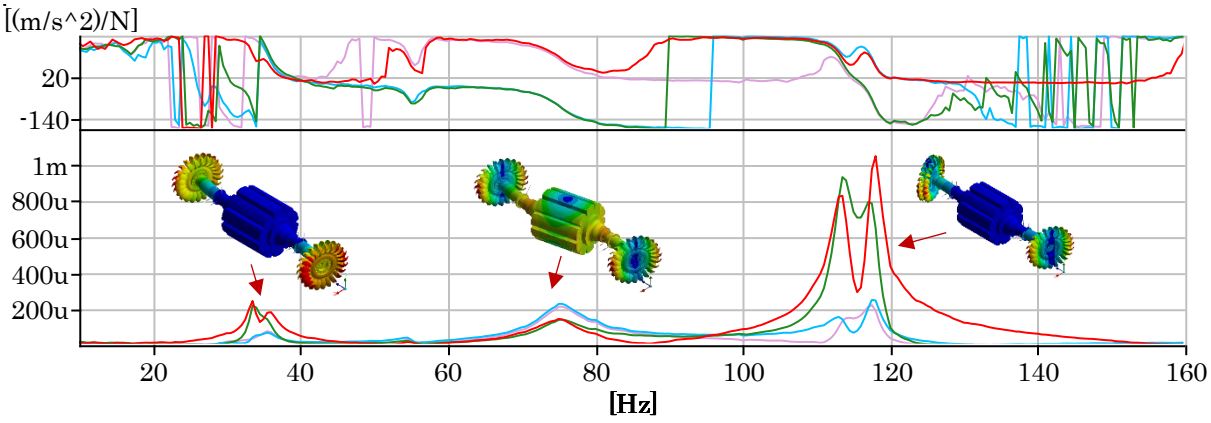

Figure 3.8. Identification of the modal shapes excited by the hammer impacts

3.1.3. Runner modes (effect of attachment to the rotor)

In this section, the vibration of the runner when it is attached to the shaft is compared to its oscillation as a free-vibrating body. In Figure 3.10, the distribution of frequencies of the axial and the tangential modes are compared between both models. It can be seen that the frequencies of the runner when it is fixed are higher than when unconstrained, due to the increased stiffness. Another noticeable fact is that the frequency does not increase in the same way in all the mode shape variants. The stiffness of the connection affects more the modes with a lower number of diametrical nodes. This is attributed to the fact that in modes with less number of ND, the disk dominates the motion, while in modes with higher number of ND the oscillation is located in the buckets.

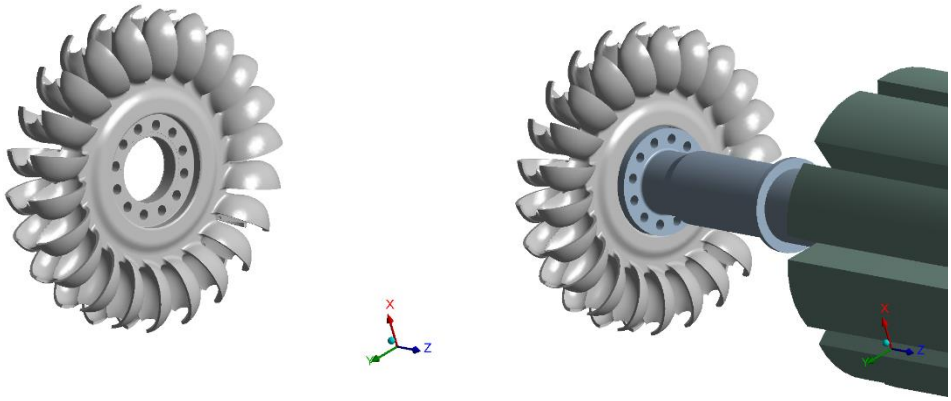

Figure 3.9. Runner without constraint (left) and runner attached to the shaft (right)

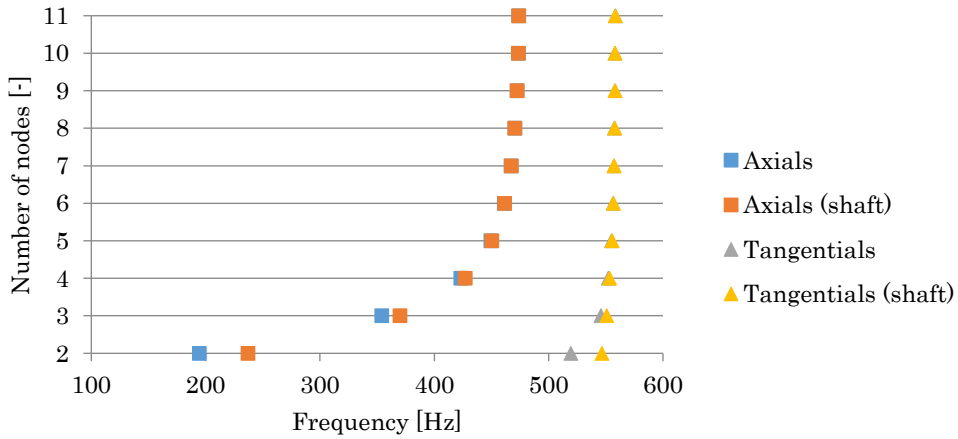

Figure 3.10. Distribution of axial and tangential frequencies for free vibrating and for attached runner

3.2. Influence of mechanical design (same N_s)

The main geometrical features of a Pelton turbine are related to its head H, discharge Q and the number of nozzles. The specific speed is a non-dimensional number used to classify hydraulic machines, which is defined as

$$n_{sq} = \frac{NQ^{0.5}}{E^{0.75}} \qquad \text{Eq. 3.1}$$

where N is the rotational speed of the turbine, Q the discharge and E the specific energy. The specific speed n_{sq} is related to the head of the turbine and, for Pelton, this is connected to the ratio between the runner diameter and the jet diameter D/d_j. In like manner, the discharge of the turbine is related to the dimensions of the bucket. Thus the dimensions of a Pelton

runner (from the hydraulic point of view) are characterized by the specific speed N_s. However, even for the same N_s, runners may bear some differences, especially in the structural design, depending on the manufacturer and on the year of construction.

In this section, two runners from the same power plant in Arties will be analyzed (turbine A-1 and turbine A-2). The specific speed N_s is the same for both (head, discharge, speed and output), what means they have the same hydraulic design. However, the mechanical design is different, since they were not produced in the same time, and some mechanical variances can be discerned. One of the most visible ones is the back shape of the buckets (Figure 3.11). In the older runner (on the right), the buckets are reinforced with ribs. This was a typical design feature to make the buckets more resistant to the load of the water jet. In recent designs (left), the back shape is slimmer. In recent designs, ribs are only to be found in runners with very high heads.

Figure 3.11. Left, runner A-1 attached to the machine and left, A-2 buckets with back supports

The modal behavior of turbine A-1 was studied in previous sections. An EMA was carried out in the installed machine as described next to identify the natural frequencies and mode shapes of the runner A-2.

3.2.1. Experimental tests

The tests were performed systematically on one side of the turbine. The casing of the runner 2 was removed in order to place the sensors and perform the impacts on the buckets (Figure 3.12 left). Three accelerometers were placed on bucket number 21 in the axial, tangential and radial direction on one side of the bucket, as indicated in Figure 3.12 right and Figure 3.13. Two accelerometers were placed on buckets 16 and 11 in the axial direction. The accelerometers used were The procedure consisted in performing impacts on the opposite side of the buckets, in the axial, tangential and radial directions. Buckets from number 21 to number 10 were impinged in a row. In this way, most of the modal shapes and natural frequencies of the runner were identified.

Figure 3.12. Left, view of the turbine with open housing and right, view of impacts in the buckets

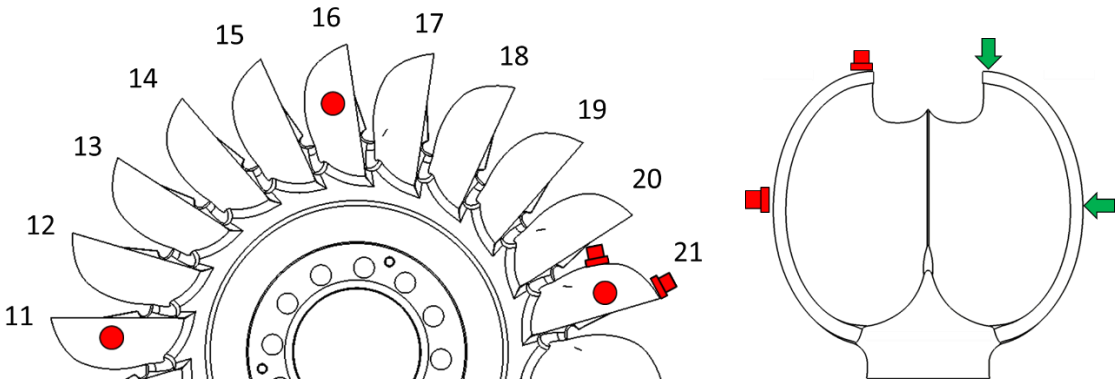

Figure 3.13. Location of the accelerometers on the runner A-2 and the impacts

3.2.2. Results

The natural frequencies were detected by peak picking the signals from all the buckets. Figure 3.14 shows the FRF and the coherence between one accelerometer signal and the hammer signal after axial and tangential impacts on the buckets. The ranges corresponding to every type of mode can be clearly identified, because axial impacts excite the axial in-phase modes axial counter-phase modes and radial modes. On the contrary, tangential impacts mainly excite tangential in-phase and counter-phase modes.

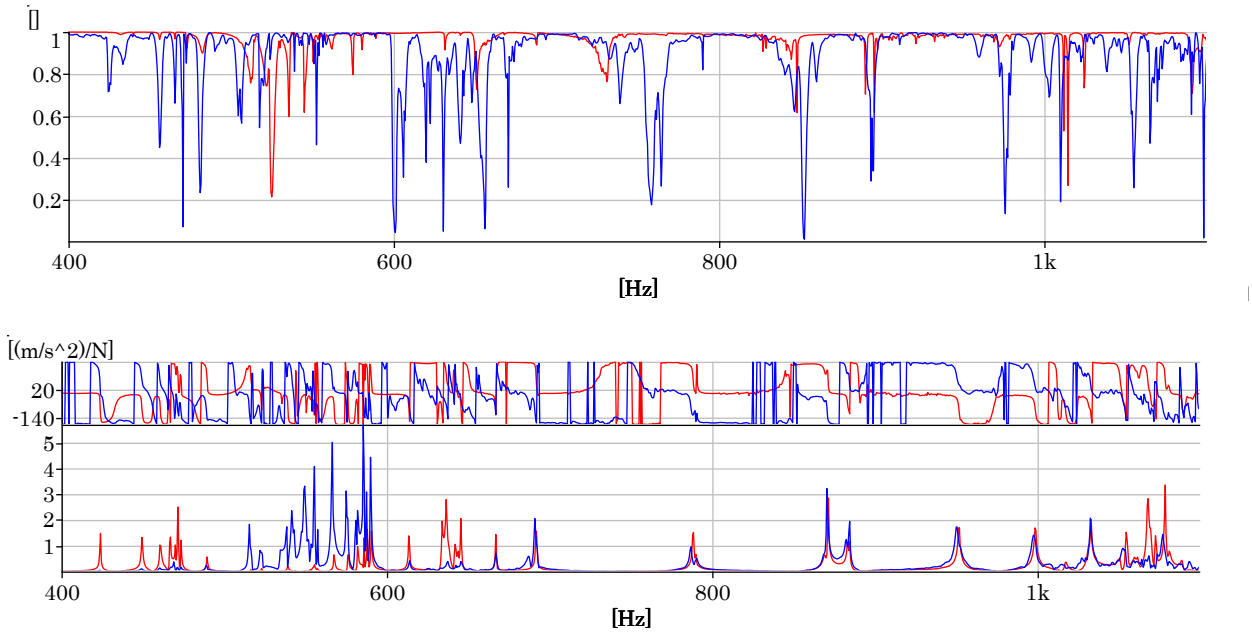

Figure 3.14. Axial (red) and tangential (blue) impacts to a bucket of the installed runner. Top: coherence, bottom: FRF's (amplitude and phase)

When representing the frequencies of turbine A-2 with respect to the number of nodes (Figure 3.15), the distribution is very similar to the one of turbine A-1. The order of appearance of the modes is the same. The axial in-phase and radial counter-phase are still the ones which are more spread, while the tangential and the axial counter-phase modes are gathered in a narrow range. However, the values of the frequencies are different, especially the mode shapes involving a tangential deformation.

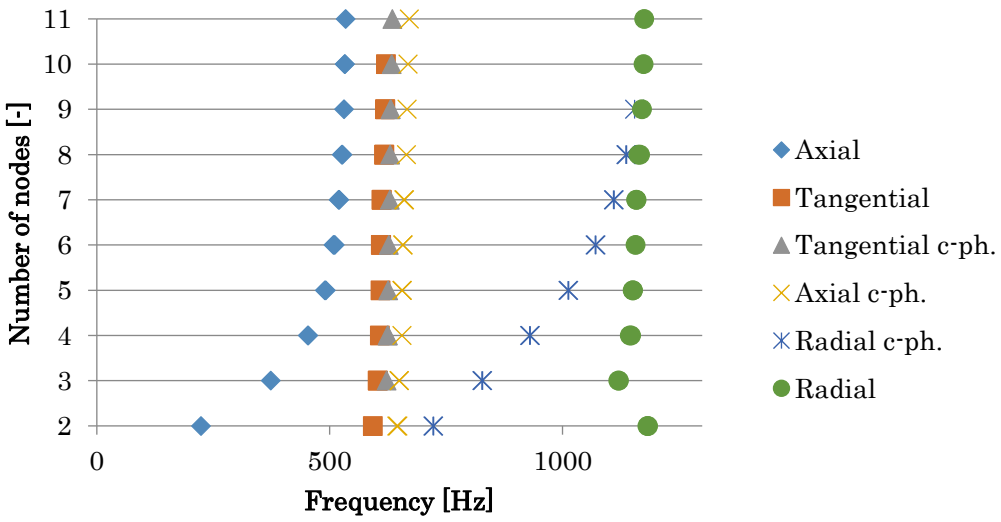

Figure 3.15. Mode distribution for the experimental Pelton turbine

In Table 3.4, the axial frequencies are listed with the percentage of difference between the old design and the new design. It can be seen that the frequencies for disk-dominated modes are similar, while the bucket-dominated modes show an important difference. It can thus be deduced that the change in the design affects mostly the bucket modes, which in the old design are stiffer due to the back support. The same behavior can be found in the counter-phase radial modes. When the tangential modes are analyzed (Table 3.5), it can be seen that all the modes are affected similarly by the design variation. All of them have around a 9% of difference between the old and the new prototype. Torsional modes and counter-phase axial modes show a similar behavior.

Table 3.4. Axial frequencies in the old runner and the new runner

	3 ND	4 ND	5 ND	6 ND	7 ND	8 ND	11 ND
Old design [Hz]	373,5	453,5	489,8	508	519,3	526,3	534,3
New design [Hz]	369,8	426,9	450,3	461,3	467,2	470,5	473,7
Rel. diff. [%]	1,0	5,8	8,1	9,2	10,0	10,6	11,0

Table 3.5. Tangential frequencies in the old runner and the new runner

	3 ND	4 ND	5 ND	6 ND	7 ND	8 ND	11 ND
Old design [Hz]	603,3	608,1	609,1	610,1	611,4	617	620,6
New design [Hz]	550,8	553,1	555,5	556,5	557,2	557,6	558,2
Rel. diff. [%]	8,7	9,0	8,8	8,8	8,9	9,6	10,1

It can be concluded that for prototypes with the same hydrodynamic characteristics, only the disk-dominated modes can be expected to be similar. The bucket-dominated modes change due to a variation of the rear design, and with the less supported buckets of new designs, the bucket-dominated modes can be reduced significantly.

3.3. Influence of hydraulic design

In this section, a Pelton turbine with different features (hydraulic and mechanical design) will be studied experimentally and the results will be compared to the turbine of Arties.

3.3.1. Characteristics of the turbine

The machine studied is a horizontal Pelton turbine with one runner operated by two jets (Figure 3.16). The rotor is supported by three bearings. The main characteristics of the runner are listed in Table 3.6.

Table 3.6. Characteristics of Moncabril Pelton turbine

Name	Moncabril	**Pitch diameter D_1**	1500 mm
Head	555,5 m	**Jet diameter d_0**	185 mm
Output	12 MW	**Bucket width b**	464 mm
Speed	600 min^{-1}	**Nozzles**	2
N_s	17	**Buckets**	21

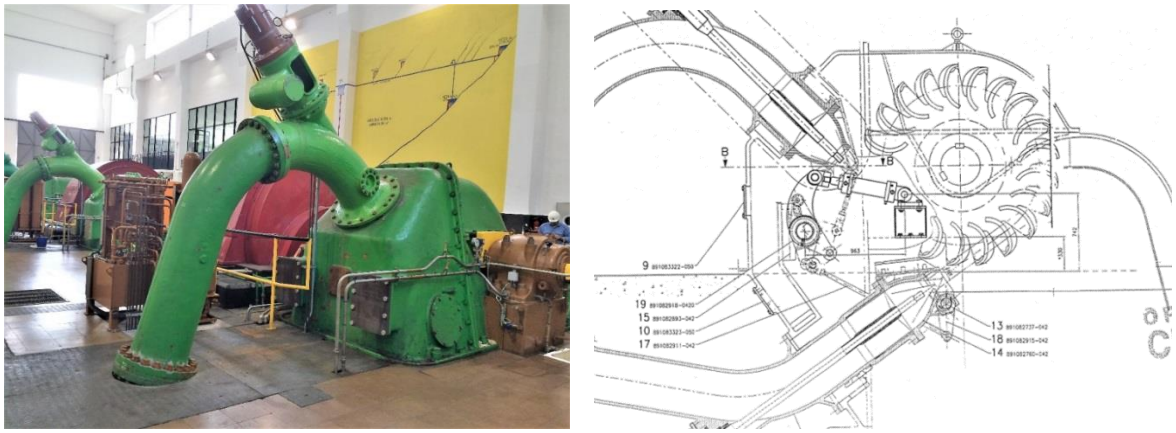

Figure 3.16. Views of Moncabril Pelton unit

3.3.2. Impact tests

In the on-site tests, accelerometers were placed on the bearings in the radial and axial direction, as displayed in Figure 3.17 and Figure 3.18. At the time of the impacts, it was possible to access the runner from underneath the casing. To detect the response of the bucket, first an accelerometer was placed in the tangential direction and impacts were performed in the same direction. Then the accelerometer was put in the axial direction and a series of axial impacts on the bucket rim were done.

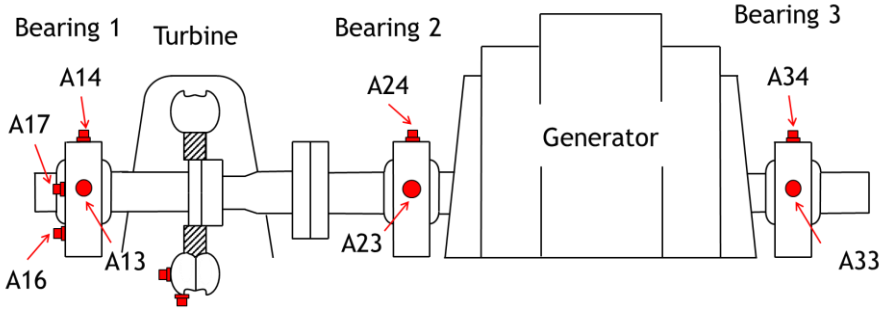

Figure 3.17. Distribution of accelerometers

Figure 3.18. Accelerometer position on machine bearings 1 (left), 2 (middle) and 3 (right)

3.3.3. Results

The runner modes excited during tangential and axial impacts to the bucket and the coherence between the accelerometers and the hammer are shown in Figure 3.19. As seen in the measurements in other machines, the location of the axial in-phase and counter-phase modes is clearly identified because of their large response to the axial impacts. In blue, the tangential modes are also spotted.

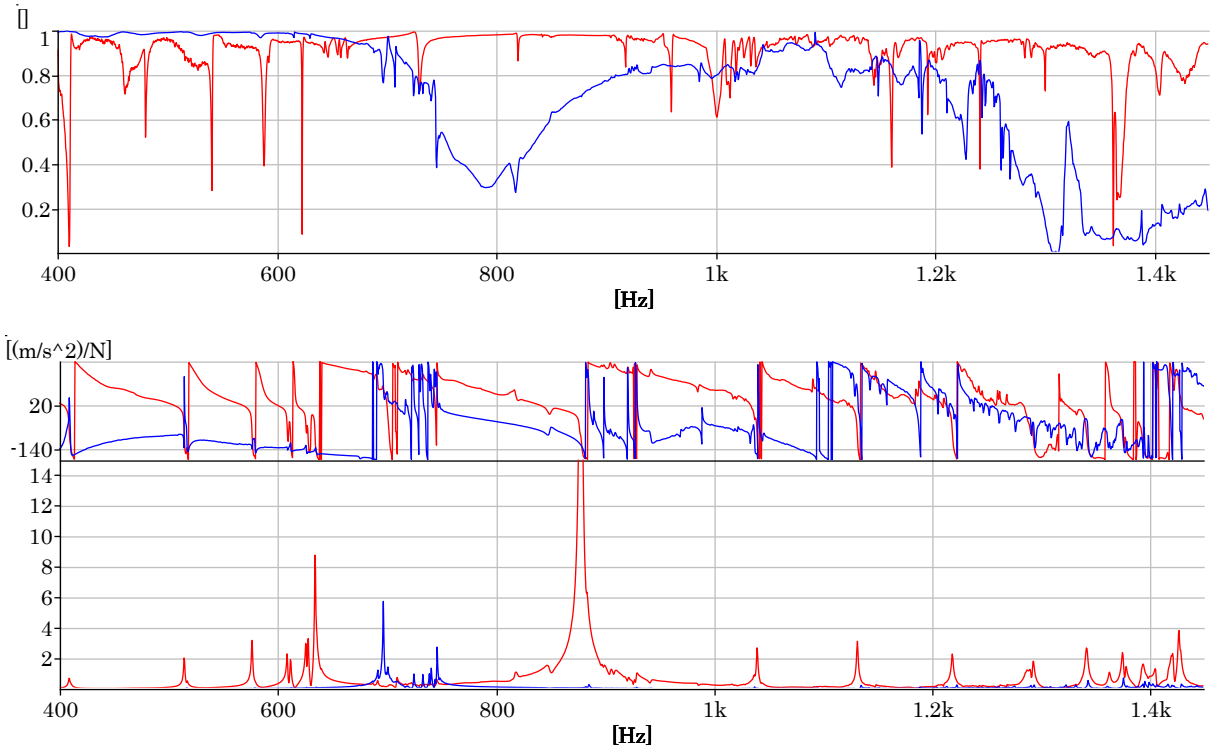

Figure 3.19. FRF (bottom) and coherence (top) between accelerometer and hammer signal to axial (red) and tangential (blue) impacts

The distribution of the modes of turbine Moncabril is displayed in Figure 3.20. It can be seen that, though the frequencies are different, the distribution is very similar to the turbine previously studied. The axial modes and radial modes, which are strongly affected by the disk

stiffness, show an asymptotic behavior and are spread. Tangential and axial counter-phase modes are gathered in a narrow frequency range. Tangential and torsional modes are very close to each other, so it is difficult to discern between them.

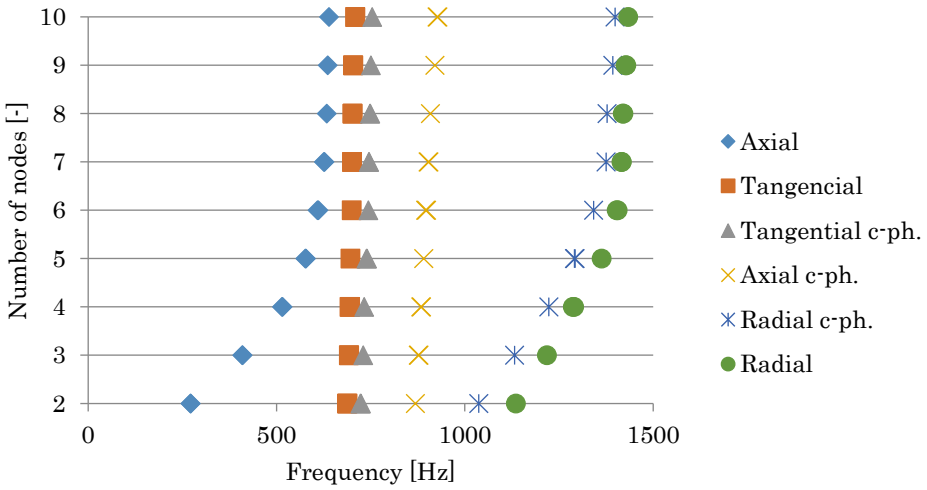

Figure 3.20. Distribution of natural frequencies of Moncabril turbine

3.4. Influence of hydraulic design (different N_s)

To investigate the influence of the structural design, three new runner designs with different N_s have been included in the study. The geometries were provided by Voith GmbH and will be referred to as runner T (H=600m), K (H=800m) and A (H=1200m). The runner characteristics are listed in [44]. The geometries are shown in Figure 3.21.

Figure 3.21. Geometry of the runners T, K and A

To know the numerical frequencies of the different designs, the modal analysis was performed attaching a shaft to each runner and following the same procedure as the one described in Chapter 2. The model was fixed at the tip surface of the shaft to emulate the attachment to the rotor. The mesh of runner T and the numerical axial frequencies obtained after the simulation for the three designs are shown in Figure 3.22. It can be seen that the

distribution of the axial frequencies has a similar pattern to the previously studied runners. In all of them, the lower frequencies correspond to the disk-dominated modes and, as the number of nodes increases, so does the resemblance to the behavior of a single bucket. At highest number of nodal diameters, the difference between the frequencies is smaller. However, it can be clearly seen that the dimensions of the runner dictate where the frequencies appear and their distribution. For instance, the maximum bucket-dominated frequency of model A is much higher than model T. However, the disk-dominated frequencies with 2 ND, 3 ND and 4 ND are lower, for the frequencies of model T appear to be much more compacted than model A.

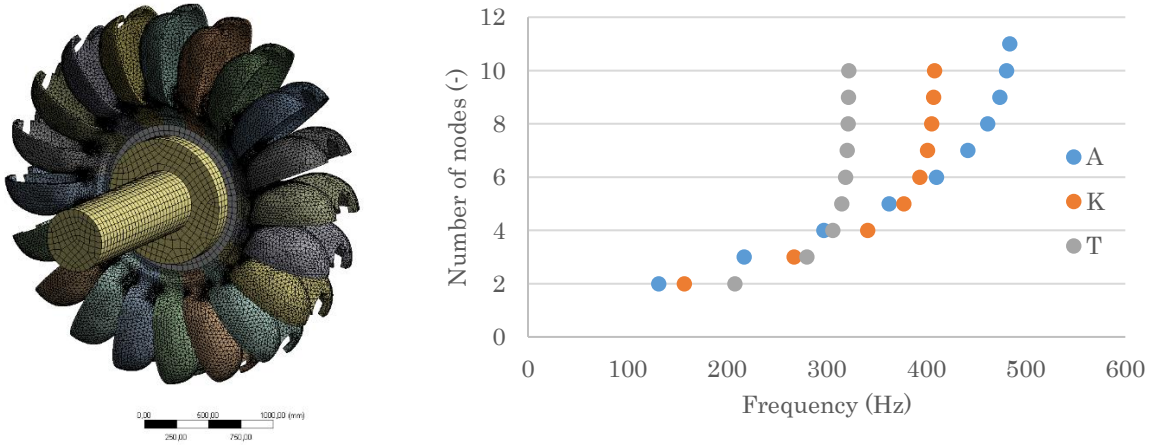

Figure 3.22. Left, mesh of runner T, and right, distribution of axial frequencies

3.5. General trends in modal behavior of PT

The features of the design cause the differences in the modal behavior between the runners. In Pelton turbines, these are ruled by two principal dimensions, which are the pitch diameter of the runner (D_1) and the jet diameter (d_0). The bucket width b is proportional to the jet diameter. The rest of the dimensions of the runner are related to these values. Therefore, if two different runners have the same diameter and bucket width, one should expect to have a similar modal behavior. Some error should always be expected due to differences in design and to factors such as the year of construction and the manufacturer.

D_1 and b are associated to the design characteristics of the turbine, such as the head H, the rotational speed N and discharge Q at the best efficiency point. Combining these parameters, we obtain the specific speed N_s. With N_s it is possible to obtain a trend in the design and dimensions of the runners, from the largest diameters and smallest buckets to the smallest diameters and widest buckets. In reference [39], a statistical relationship with non-dimensional parameters to obtain the main turbine dimensions is presented.

Since b and D_1 define the modal behavior of the structure, it would be viable to relate design parameters to the modal behavior of the runner. Finally, a common trend in the structural frequencies of Pelton turbines is to be found.

Apart from the data available from the previously analyzed cases, other Pelton turbines have been added to the study in order to find a trend that relates the dimensions of the runner to the design parameters. All the available power plants and their basic features are listed in Table 3.7.

Table 3.7. Main features of Pelton turbines available

Name	H [m]	Q [m³/s]	N [min⁻¹]	D_1 [mm]	b [mm]	Name	H [m]	Q [m³/s]	N [min⁻¹]	D_1 [mm]	b [mm]
Arties	770,5	5	600	1900	547	**Pampan.**	539,2	-	600	1580	495
Cabdella	836	5	500	2200	-	**Poqueira**	575	1,025	750	1320	413
Caldes	483	4	500	1640	533,1	**Sant Maurici**	532,7	1,12	750	1320	410
Duque	490	3	600	1500	522	**Toran**	518	3	600	1500	427
Dúrcal	708	0,26	1000	1050	-	**V - A**	1200	-	-	-	-
Lasarra	617	1,5	750	1320	-	**V - K**	800	-	-	-	-
Moncab.	550,5	2,8	600	1500	427	**V - T**	600	-	-	-	-

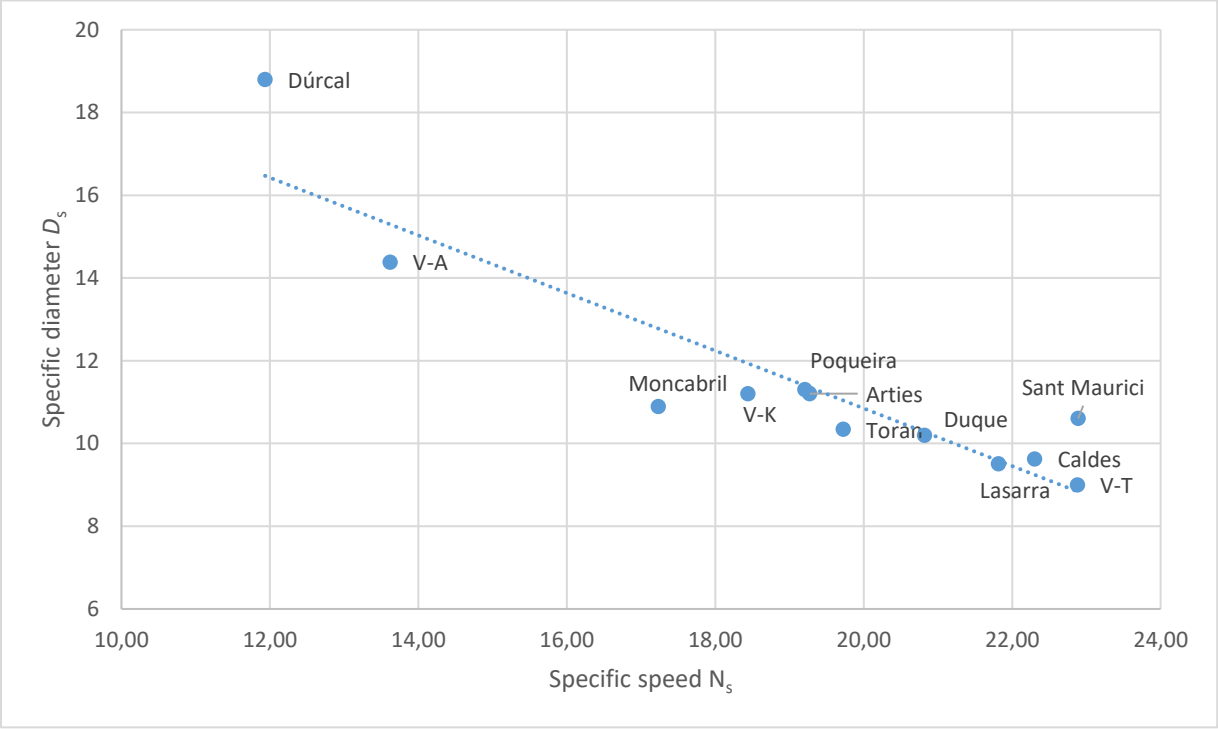

Figure 3.23. Plot of D_s against N_s

One way to estimate the D_1 is to calculate the specific diameter D_s from the N_s. The specific diameter is defined as

$$D_s = \frac{D_1 (gH)^{0,25}}{Q^{0.5}} \qquad \text{Eq. 3.2}$$

Several Pelton turbines available have been represented in Figure 3.23. The scattering is important and another type of presentation would be convenient.

The speed factor k_u and the discharge factor or loss coefficient k_{Cm} are defined in Eq. 3.3 and Eq. 3.4 and, as seen in Chapter 2, they can be considered as constants for simplicity purposes. Their value depends on the turbine design features of the manufacturer.

$$k_u = \frac{\omega D_1/2}{\sqrt{2gH}} \approx 0{,}5 \qquad \text{Eq. 3.3}$$

$$k_{Cm} = \frac{4 \cdot Q/\pi d_0^2}{\sqrt{2gH}} \approx 1 \qquad \text{Eq. 3.4}$$

Where ω is the rotational speed in rad/s, D_1 is the pitch diameter in m, Q is the discharge in m^3/s, d_0 is the diameter of the nozzle in m, H the head in m and g is the gravitational acceleration in m/s^2.

The bucket width b is proportional to the nozzle diameter by α times, which also depends on the particular design characteristics. Using this relationship, Eq. 3.4 can written as seen in Eq. 3.9.

$$b = \alpha \cdot d_0 \quad \text{with} \quad 3 \leq \alpha \leq 3{,}4 \qquad \text{Eq. 3.5}$$

$$k_{Cm} = \frac{4\alpha^2 \cdot Q/\pi b^2}{\sqrt{2gH}} = \frac{4\alpha^2 D_1^2/\pi b^2}{\sqrt{2g}} \cdot \frac{Q}{D_1^2\sqrt{H}} \approx 1 \qquad \text{Eq. 3.6}$$

Where b is expressed in m. Next, we will introduce the concepts of unit speed N_{11} and unit discharge Q_{11}. N_{11} and Q_{11} are, respectively, the velocity and the discharge of a geometrically similar runner with a diameter of 1 m which works under a head of 1 m. These are defined by Eq. 3.7 and Eq. 3.8.

$$N_{11} = \frac{N \cdot D_1}{\sqrt{H}} \qquad \text{Eq. 3.7}$$

$$Q_{11} = \frac{Q}{D_1^2\sqrt{H}} \qquad \text{Eq. 3.8}$$

Where N is the rotational speed in min^{-1}, D_1 is in m, H in m and Q in m^3/s.

Therefore, the speed factor k_u can be expressed as shown in Eq. 3.9, considering that $\omega = 2\pi N/60$

$$k_u = \frac{2\pi \cdot N \cdot D_1}{2 \cdot 60\sqrt{2gH}} = \frac{\pi}{60\sqrt{2g}}\frac{N \cdot D_1}{\sqrt{H}} = \frac{\pi}{60\sqrt{2g}}N_{11} \approx 0{,}5 \qquad \text{Eq. 3.9}$$

The unit speed factor can thus be regarded as constant:

$$N_{11} = const. \approx 42{,}3 \qquad \text{Eq. 3.10}$$

Finally, the pitch diameter of the runner D_1 can be related to the rotational speed N and the head H with the following expression

$$D_1 \approx 42{,}3\frac{\sqrt{H}}{N} \qquad \text{Eq. 3.11}$$

The discharge factor k_{Cm} can be expressed with respect to the unit discharge factor Q_{11}

$$k_{Cm} = \frac{4\alpha^2 D_1^2/\pi b^2}{\sqrt{2g}} \cdot \frac{Q}{D_1^2\sqrt{H}} = \frac{4\alpha^2 D_1^2/\pi b^2}{\sqrt{2g}} \cdot Q_{11} \approx 1 \qquad \text{Eq. 3.12}$$

Which yields

$$\left(\frac{b}{D_1}\right)^2 = \frac{1}{k_{Cm}}\frac{4\alpha^2/\pi}{\sqrt{2g}} \cdot \frac{Q}{D_1^2\sqrt{H}} = \frac{1}{k_{Cm}}\frac{4\alpha^2/\pi}{\sqrt{2g}} \cdot Q_{11} \qquad \text{Eq. 3.13}$$

Considering that $k_{Cm} \approx 1$ and $3 \leq \alpha \leq 3{,}4$ the following relation is found

$$\left(\frac{b}{D_1}\right)^2 = \frac{4\alpha^2/\pi}{\sqrt{2g}} \cdot \frac{Q}{D_1^2\sqrt{H}} = 0{,}29\alpha^2\frac{Q}{D_1^2\sqrt{H}} \qquad \text{Eq. 3.14}$$

In Figure 3.24, the diameters of all the available turbines have been plotted with respect to its defining operating parameters $\sqrt{H}$ and N^{-1}. The trend is clear and with small data scattering. However, the ratio is found to be smaller than the one found in Eq. 3.11. This is due to the approximation of $k_u \approx 0{,}5$, which in actual turbines is commonly found in the range $0{,}44 \leq k_u \leq 0{,}46$.

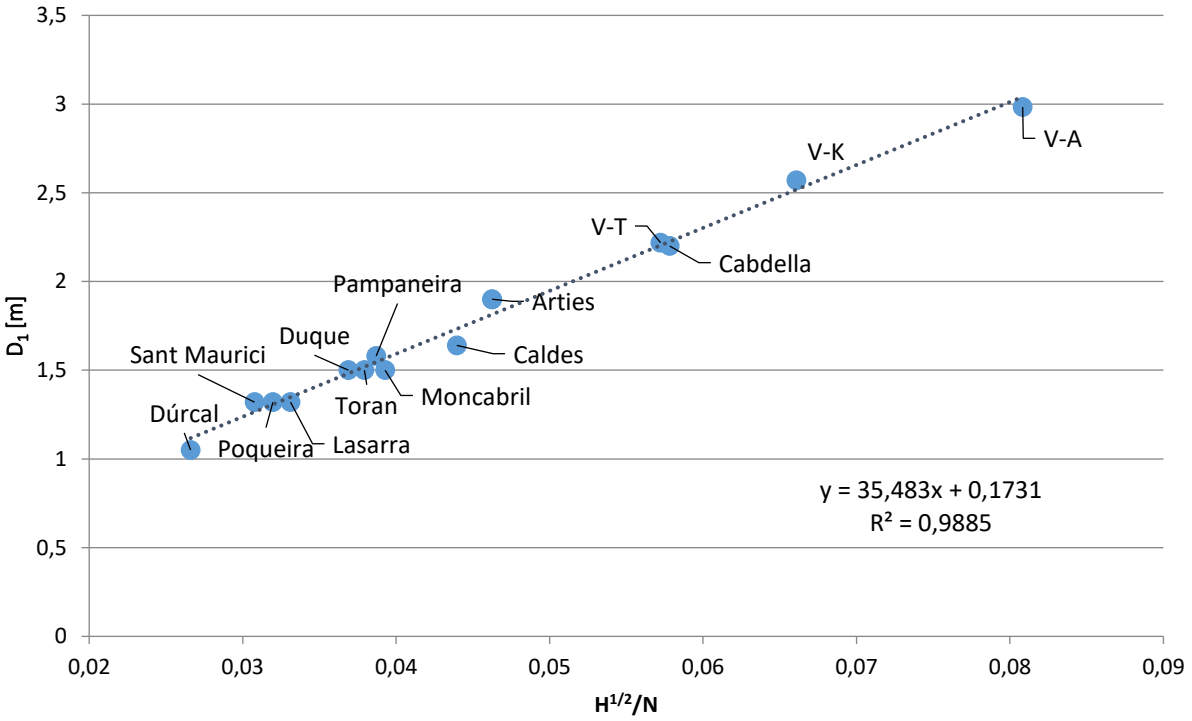

Figure 3.24. Runner pitch diameter trend

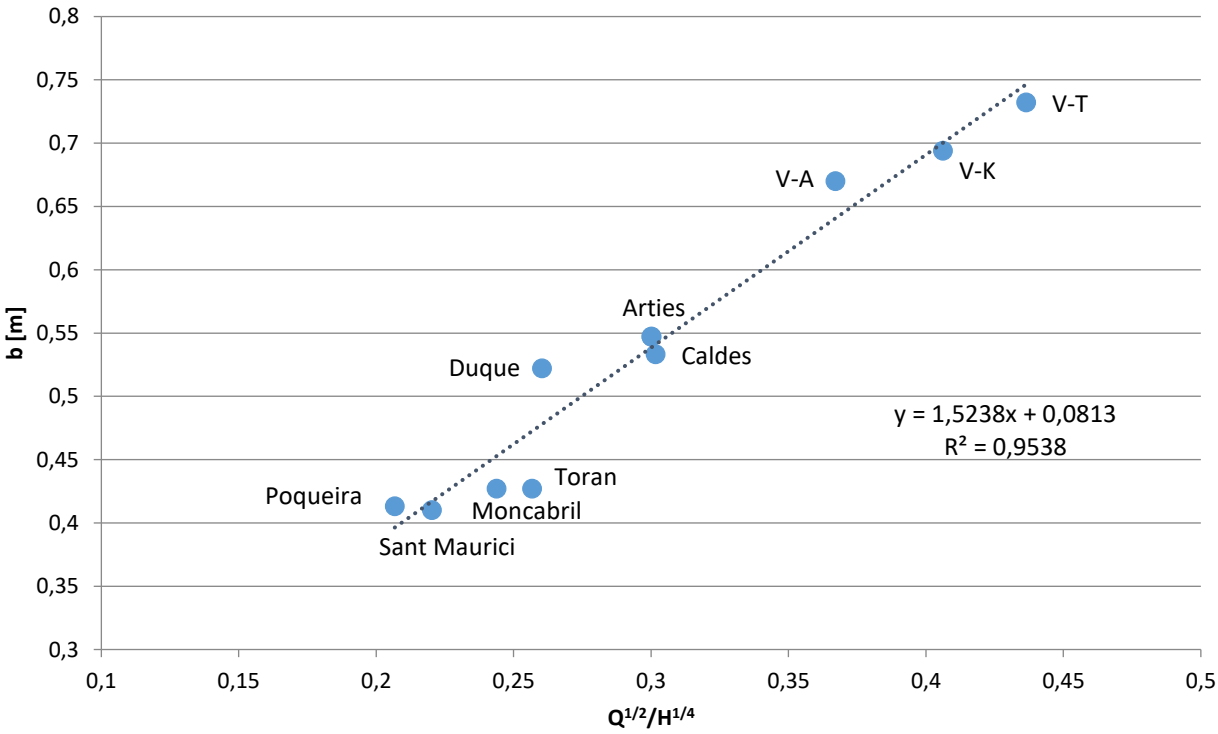

Figure 3.25. Bucket width trend

In Figure 3.25, the bucket width b has been plotted against $\sqrt{Q}$ and $H^{-1/4}$. A trend is made apparent with more scattering than the previous representation due to the wider range of the α values.

The main dimensions of the runner have been associated to the operating parameters of head H, discharge Q and rotational speed N. With this information, the main dimensions of Pelton runners can be characterized and, thus, the modal behavior can be approximated. The natural frequencies are related to the ratio b/D_1 and the global dimension of the structure. The runners with maximum head, minimum rotational speed and minimum discharge will be slimmer, with the largest diameter and the smallest bucket size. Hence the bucket dominated frequencies will be the largest, due to the reduced mass. On the other side, runners with minimum head, maximum rotational speed and maximum discharge will have the lowest frequencies.

To check the relation between the natural frequencies and the aforementioned parameters, the results obtained in the experimental tests and with the numerical models have been used. The maximum bucket-dominated frequencies of the axial and tangential modes of each model have been represented in Figure 3.26. The frequencies show a growing trend. The deviation of the points can be due to the differences in the material properties, in the design of the buckets (as seen in the previous section) and so on. Nevertheless, it is proved that the modal behavior can be approximated with the main operating parameters of the turbine. The trend lines of the axial and tangential frequencies have a similar slope, what means they increase at the same rate. However, the slope of the axial counter-phase modes is much steeper. As the bucket dimension shrinks, the frequencies increase more rapidly than the axial and the tangential modes. This may be caused by the fact that the buckets need more mass, especially at the rear side, with increasing head, what makes the axial and tangential modes not to increase as fast as the axial c-ph. modes, which are mainly affected by the mass of the rim. These modes are more difficult to predict due to their large sensitivity to the mass difference between the buckets.

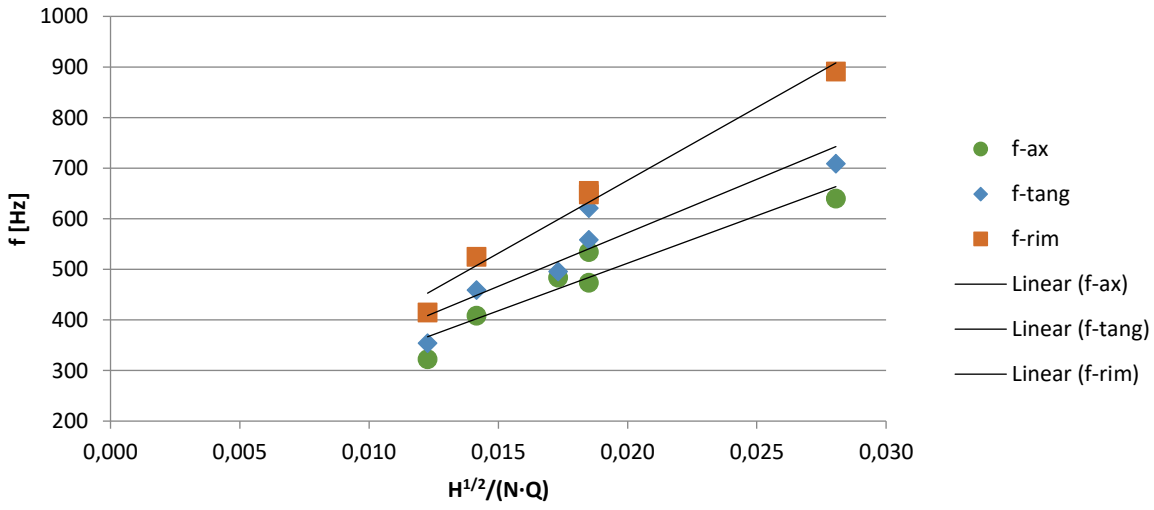

Figure 3.26. Trend between the design of Pelton runners and the natural frequencies

The design of the runner not only affects the maximum bucket-dominated frequencies. As seen before, the runners with higher head showed a larger distance between the axial frequencies. On the contrary, runners designed for lower heads had more compactness between the axial frequencies. It is widely known that the head is related to the ratio b/D_1, so the axial frequencies of the studied runners have been represented as a function of it in Figure 3.27. To be able to compare the different models, the frequencies have been scaled with respect with respect to the maximum bucket-dominated frequency in a non-dimensional way.

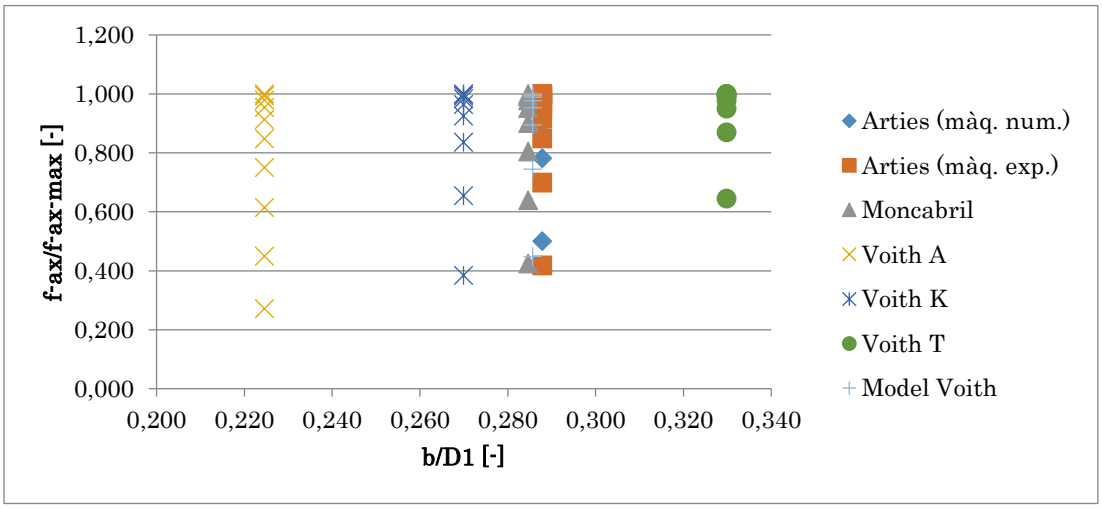

Figure 3.27. Axial natural frequencies of several runners in a non-dimensional form

According to the similarity laws, natural frequencies are scalable from model to prototype by using the geometric scale (λ_L), the density (λ_ρ) and Young modulus scale (λ_Y). For the same material between model and prototype, something usual in the case of Pelton turbines, the natural frequencies are λ_l times smaller in prototype than in the model. Furthermore, the mode shapes are exactly the same in both model and prototypes, while in theory the damping ratio should be also the same. The relationship between natural frequencies is

$$\lambda_\omega = \frac{1}{\lambda_L}\sqrt{\frac{\lambda_\rho}{\lambda_Y}} \qquad \text{Eq. 3.15}$$

where, λ_L is the geometric scale, defined as $\lambda_L = \frac{L_P}{L_M}$. Scaling the natural frequencies of the turbines analyzed to a turbine with the same bucket width (taking turbine 1-A as the reference) all the axial frequencies are in the range of 500 to 540 Hz and the tangential 560 to 620 Hz.

3.6. Conclusions

In this chapter, the modal behavior of the whole turbine has been investigated numerically and experimentally. The main turbine modes were identified with their natural frequencies and mode shapes.

Modes can be separated into two groups, one as rotor modes and another as runner modes.

Rotor modes cover the lower frequency range from 2,5-3,5 times the rotating frequency to around 300 Hz. Runner modes cover a higher frequency range from 300 to more than 1 kHz

The effect of the runner connection to the rotor has been found. The research shows that only some runner modes are slightly affected because of the added stiffness provided by the attachment. The first disk modes are affected but the bucket modes no so much

To check if this behavior was similar in other turbines of different mechanical and hydraulic design, other turbines were investigated.

The effect of the mechanical design has been studied first. Two runners with the same hydraulic design but with structural differences were investigated. Tangential modes are the ones more affected because they are very dependent on the rear bucket structure. However, the mode distribution and trends are very similar.

The effect of the hydraulic design has also been studied. Significant changes in the modal behavior has been found. For higher heads the runner is large and the width small. In this case the disk dominated modes have lower frequency while the bucket modes have higher frequencies. The opposite occurs for low head runners.

The method to estimate the diameters and widths of the runner depending on design operating parameters is proposed. Another important matter is to know if there is any relationship between the design parameters and the natural frequencies. A correlation has been found that can be useful for a preliminary estimation of the runner frequency ranges.

In this study the machine was still. When in operation, other effects like the added mass and centrifugal stresses appear in the runner what may change the modal characteristics. To determine that, more tests have to be done with the machine in operation.

Because no sensors can be placed on the runner when the machine is in operation, the feasibility to detect runner vibrations from outside has to be investigated.

Chapter 4 Transmissibility of runner vibrations

During operation, the water jet impinges on the runner buckets generating large vibrations and deformations on it. Damage in the runner depends on the amplitude and deformations generated, therefore their monitoring is of paramount importance for the turbine surveillance. Because sensors cannot be located directly on the runner, the feasibility to detect runner vibrations in the monitoring positions has been addressed in this chapter.

First the propagation of the runner vibrations to the shaft and then to the bearing has been investigated. Second the best monitoring positions to detect specific mode shapes have been selected. The effects of bucket construction and location have been also investigated.

4.1. Experimental study of Arties machine

4.1.1. Equipment and procedure

To test the transmissibility of the bucket vibrations to the monitoring positions, accelerometers were placed on the buckets (in the same way represented in Figure 3.13), on the shaft and on both turbine bearings (as shown in Figure 3.1). The turbine runner was accessible because the casing was removed. The accelerometers used were the same as in the impact tests. The setup is shown in Figure 4.1.

The procedure consisted in impacting all the accessible buckets (from 21 to 11) in the axial, tangential and radial direction. Also one bucket was impacted from underneath the wheel.

Figure 4.1. View of experimental setup

4.1.2. Transmissibility of vibrations

To investigate the transmission of vibrations from the buckets to the monitoring locations, two series of tests were performed. Two accelerometers were placed on bucket 6 in the axial and tangential directions and two other accelerometers were placed on the same line, one vertically on the shaft between the bearing and the turbine, and another in the vertical monitoring location A34. The first test consisted in performing axial impacts to the bucket and calculating the FRF. In Figure 4.2 and Figure 4.3, the FRF's of all these points have been represented in the low frequency range (lower modes). As to be expected, the axial modes and the radial modes are much more excited by the impingements than the tangential modes, as seen in Figure 4.2. In Figure 4.3, it can be observed that the vibrations are transmitted to the shaft and the bearing, even though the amplitude is smaller.

First point to see is that the transmission of the vibration from the bucket to the shaft and from the shaft to the monitoring location varies with the type of mode. It can be seen that, although the axial in-phase modes are the most excited in the bucket, the tangential and axial counter-phase modes are comparatively better detected in the shaft and the bearing. Thus, the transmission of these modes is better than for axial in-phase modes. In addition, the transmission from shaft to bearing also varies with the mode, being the axial in-phase modes the better transmitted.

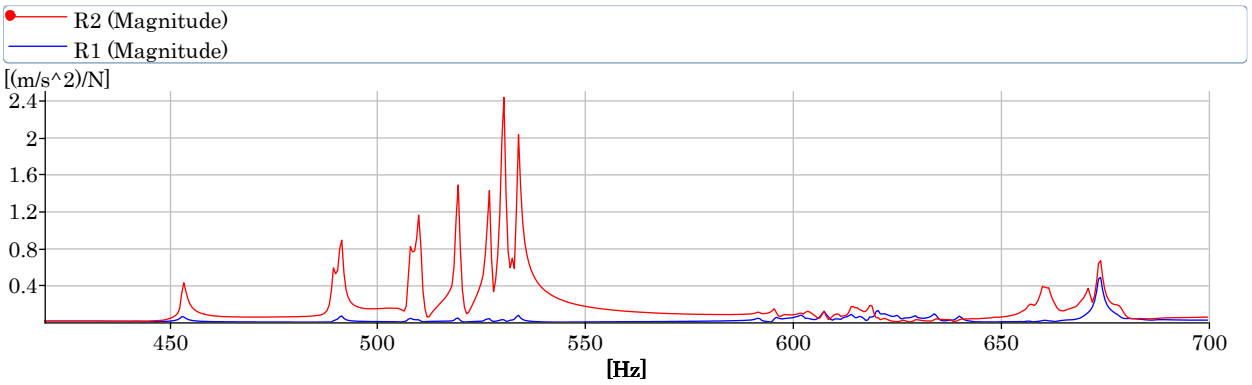

Figure 4.2. FRF of the response of axial (red) and tangential (blue) accelerometers placed on bucket 6 to axial impacts on the bucket

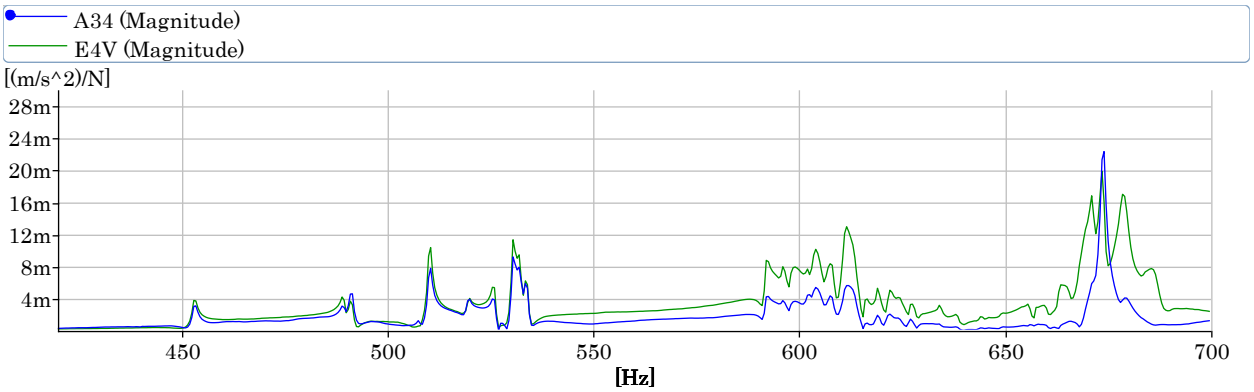

Figure 4.3. FRF of the response of A34 (blue) and E4V (green) accelerometers to axial impacts on the bucket

In Figure 4.4 and Figure 4.5, the same FRF's are represented, but for the frequency range of the higher modes (700-1300 Hz). The analysis of the higher natural frequencies shows that the transmission of the radial modes is similar to the axial in-phase modes. Sometimes the transmission is better in the bearing than in the shaft.

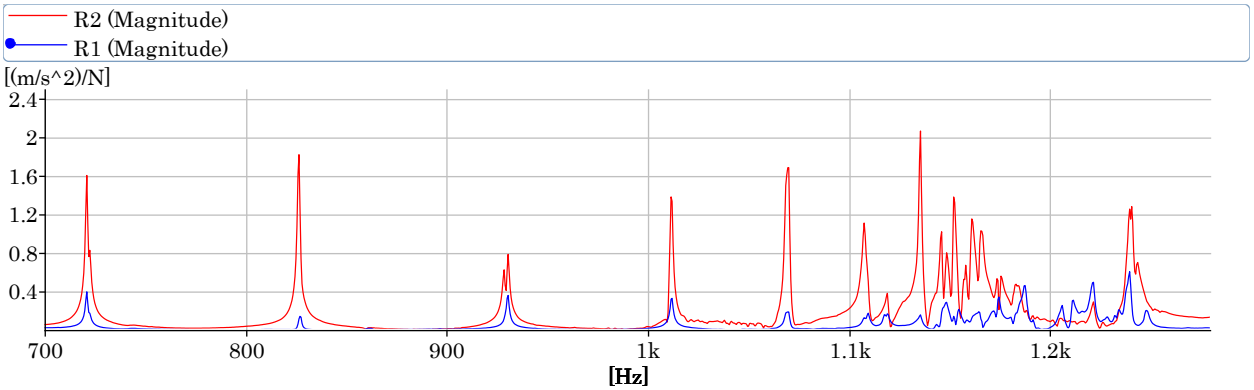

Figure 4.4. FRF of the response of axial (red) and tangential (blue) accelerometers placed on bucket 6 to axial impacts on the bucket

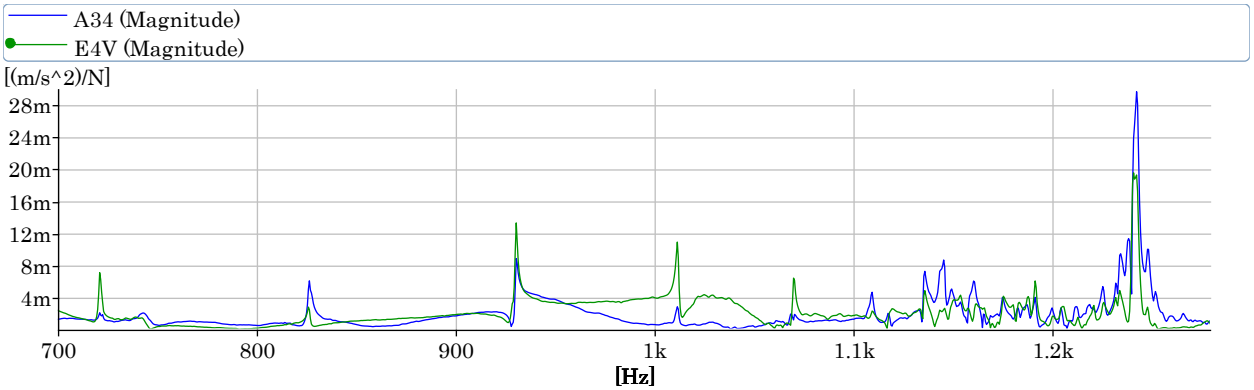

Figure 4.5. FRF of the response of A34 (blue) and E4V (green) accelerometers to axial impacts on the bucket

The second test consisted in performing tangential impacts, with the accelerometers placed tangentially in two different buckets. It is to be seen that there is a good transmission of the

tangential modes, especially on the shaft. The axial in-phase modes also show a good transmission ratio. Figure 4.6 and Figure 4.7 are for the low frequency range, and Figure 4.8 and Figure 4.9 for the high frequency range.

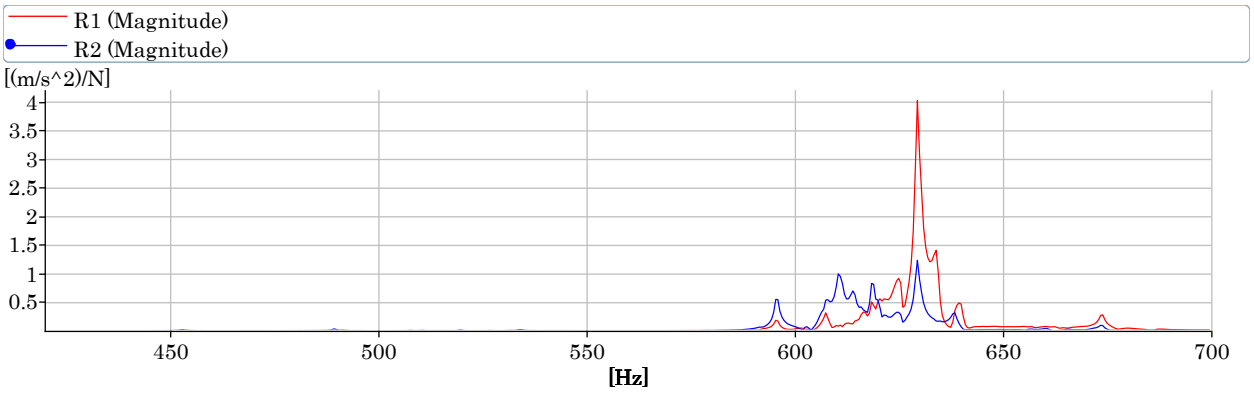

Figure 4.6. FRF of the response of tangential accelerometers placed on bucket 6 to tangential impacts on the bucket

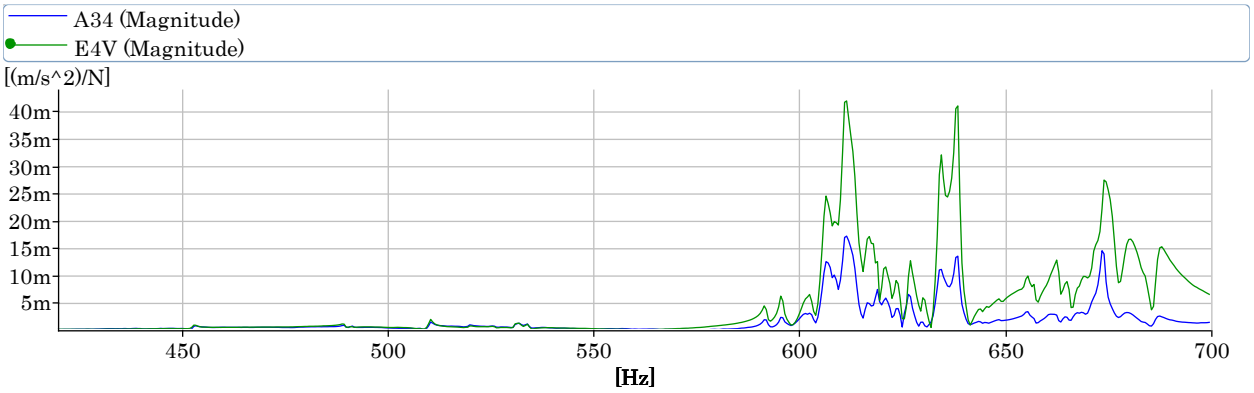

Figure 4.7. FRF of the response of A34 (blue) and E4V (green) accelerometers to tangential impacts on the bucket

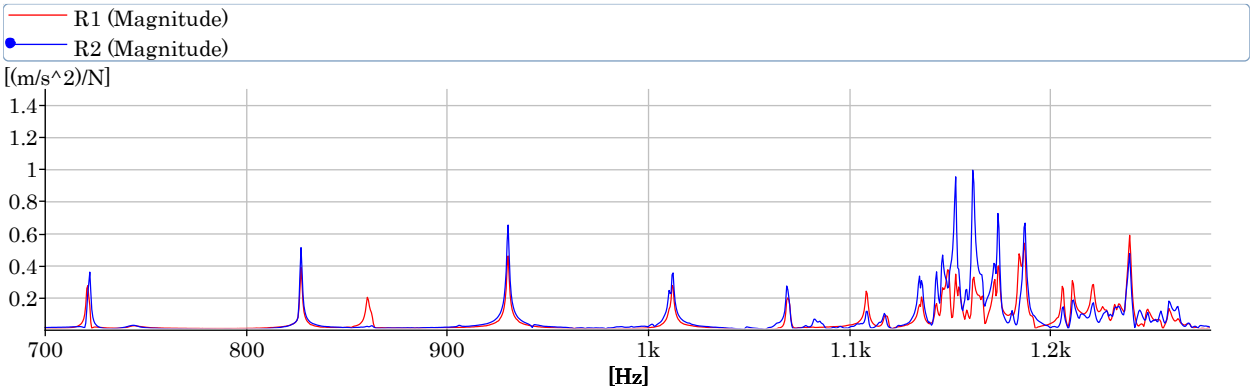

Figure 4.8. FRF of the response of tangential accelerometers placed on bucket 6 to tangential impacts on the bucket

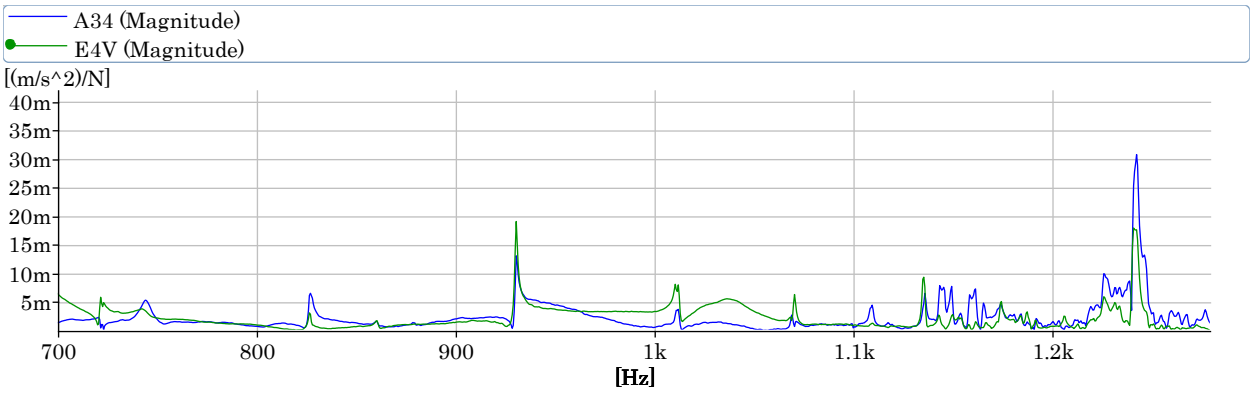

Figure 4.9. FRF of the response of A34 (blue) and E4V (green) accelerometers to tangential impacts on the bucket

4.1.3. Detection from monitoring positions

In this part the transmission of the bucket vibration to the different bearing locations has been studied. The objective is to determine which one is better to detect the different modes. The procedure used was to perform impacts to the same bucket in the axial, tangential and radial directions to excite the different types of modes and to evaluate which monitoring locations (A31, A34, A35 and A38) are more suitable for mode detection. Since a horizontal Pelton turbine is not a completely symmetric machine in terms of stiffness and transmission, the tests were performed in three different buckets, which were located 90 degrees from each other.

The results are showed in the following figures. The first test was performed in the bucket 21, which was located in the horizontal line of the turbine (same direction of the jet) and 180 degrees from the monitoring location A31. Three different frequency ranges have been selected for the display of the results [0-550 Hz], [550-700 Hz] and [700-1300 Hz].

In Figure 4.10 and Figure 4.11, the FRF's of the responses transmitted to the monitoring locations A31, A34, A35 and A38 after impacting the bucket axially are represented, respectively, in the range of 0-550 Hz. The lower frequencies, corresponding to the rotor modes, show a better detection from the axial monitoring locations A35 and A38. For example, the rotor modes at 163,5 Hz and 178,5 Hz are very well transmitted, especially to A38, and the rotor mode at 50 Hz is better detected from A35. The runner axial modes with less number of nodes (disk-dominated) are also better transmitted to the axial locations: the 1-ND, 2-ND and 3-ND axial in-phase modes are mostly seen from A35 and A38. Nevertheless, the axial modes with more number of nodes (bucket-dominated modes), though they can be detected from any position, have their best transmission ratio to the radial vertical monitoring location A34.

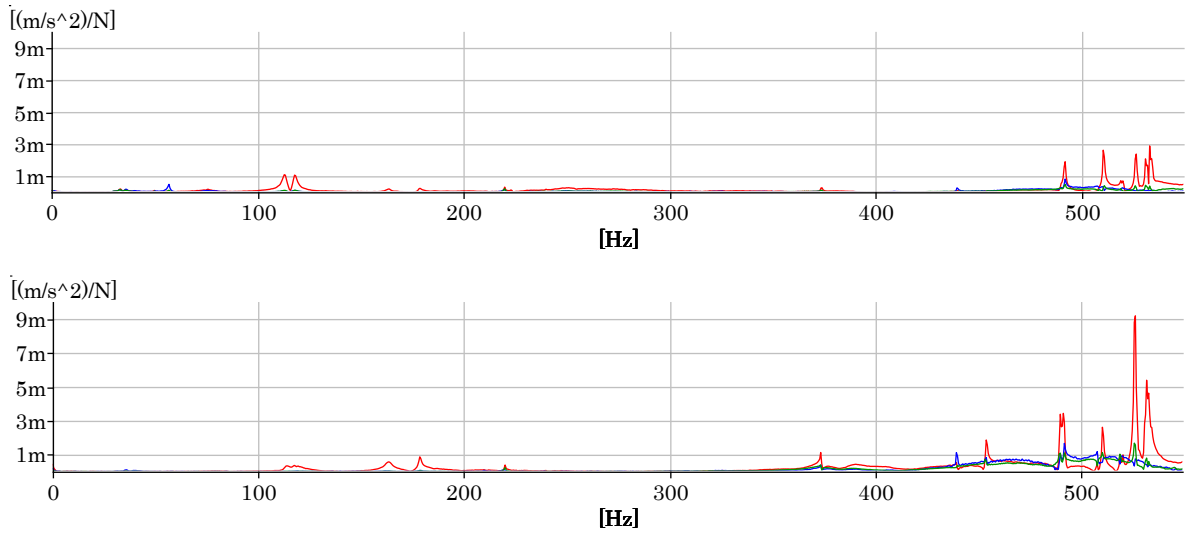

Figure 4.10. FRF's of the response from bearing position A31 (top) and A34 (bottom) to impacts on bucket 21 in axial (red), tangential (blue) and radial (green) directions

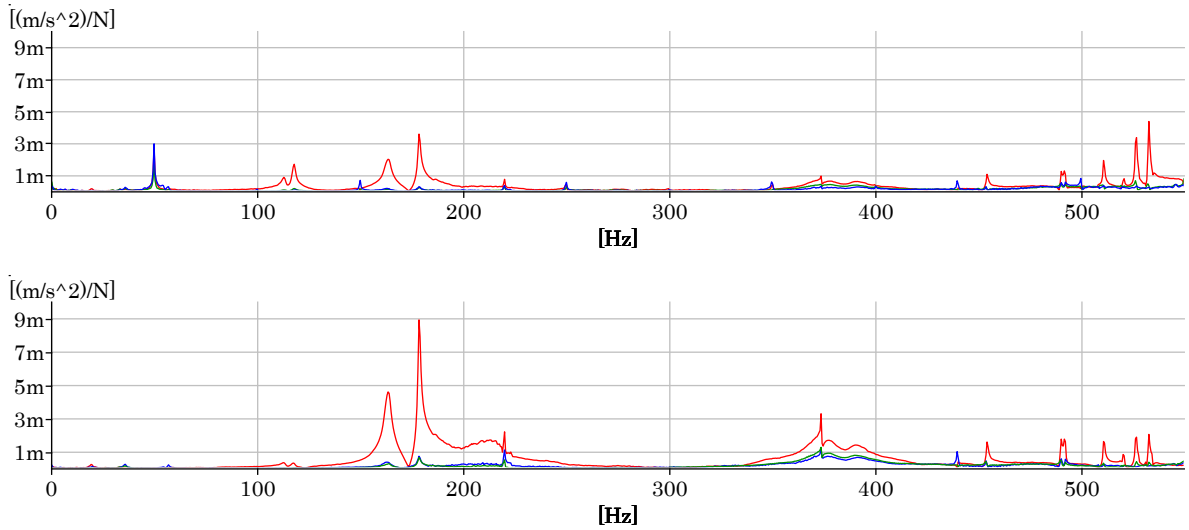

Figure 4.11. FRF's of the response from bearing positions A35 (top) and A38 (bottom) to impacts on bucket 21 in axial (red), tangential (blue) and radial (green) directions

To check that the vibration measured from the sensors placed on the bearings is the same as the vibration of the bucket, the coherence between both signals has been evaluated in the range of the axial in-phase modes (420-550 Hz). According to the signals previously analyzed, the vertical position A34 is more sensitive to these modes, so this has been analyzed in Figure 4.12. The same peaks are clearly discerned in both FFT signals, but with very different amplitudes. The peak axial vibration of the bucket is around x200 times the peak vibration transmitted to the bearings. It is worth noting that, even for the same type of modes, every natural frequency has a different transmission ratio. Analyzing the coherence in the bottom graph, it can be seen that this reaches the value of 1 in almost all the peaks. Therefore, it can be confirmed that the vibration from both signals is of the same origin. The only exception is the peak at the highest frequency, which has a very low coherence.

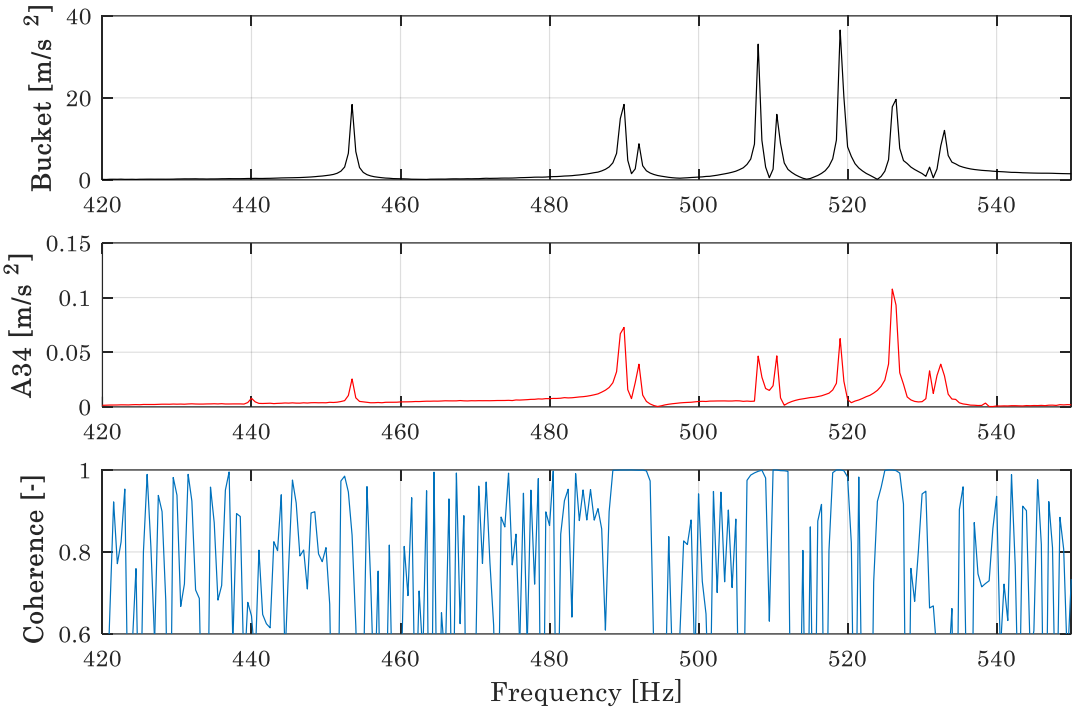

Figure 4.12. FFT and coherence between axial accelerometer on the bucket and vertical position A34

The transmission of the axial modes to the monitoring positions has been evaluated calculating the RMS acceleration values of the frequency band [420-550 Hz] from all the positions (see Table 4.1). The ratio between the vibration of the bearing positions with respect to the axial bucket acceleration has been calculated. As expected, the accelerometer on the axial position has the highest vibration levels. The percentage of energy sensed by the accelerometers on the bearings is about 0,3% the value of AA. The best position for this modes is the vertical radial.

Table 4.1. Axial RMS acceleration values between bucket 21 and monitoring positions

Location	Acceleration RMS [m/s²]	Ratio [%]
Bucket AA	29,89	
Bucket TA	1,111	
Bucket RA	3,24	
A31	0,03109	0,1040
A34	**0,09449**	**0,3161**
A35	0,04045	0,1353
A38	0,04328	0,1448

In Figure 4.13 and Figure 4.14, the FRF's are represented in the range 550-700 Hz. The tangential modes are excited by the impacts in the tangential and radial directions and have a similar transmission in all the monitoring points. It can be said, though, that A38 receives most part of the vibration, especially for the mode at 602,5 Hz, which corresponds to the natural frequency of the tangential mode of bucket 21. For the case of the axial counter-phase

mode, only the frequency of the impacted bucket is excited, and thus received in the monitoring positions. The accelerometer in the radial horizontal position A31 is the one that best detects the vibration of the bucket.

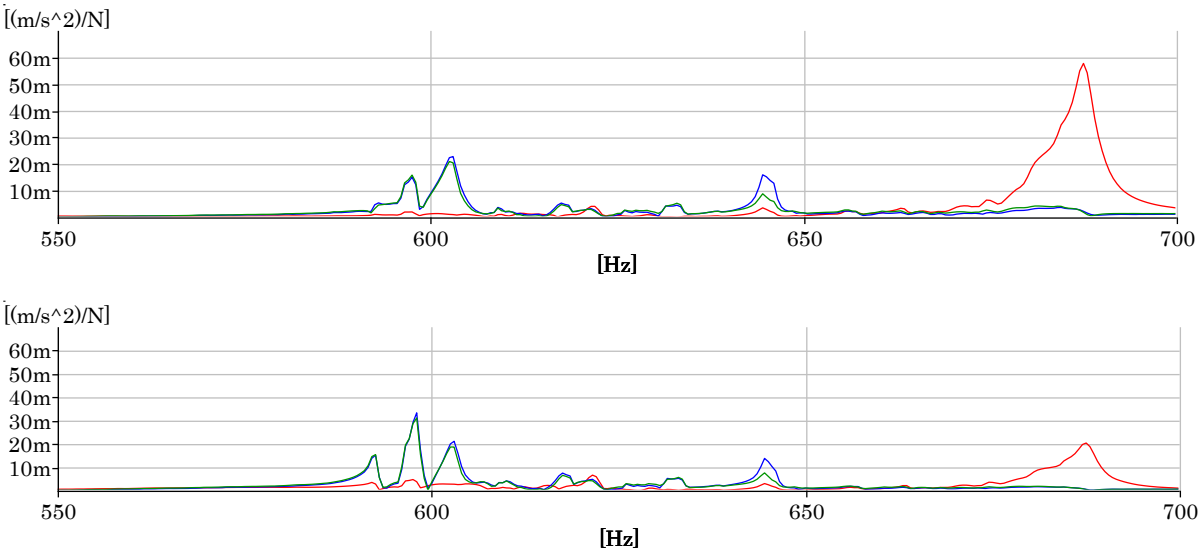

Figure 4.13. FRF's of the response from bearing position A31 (top) and A34 (bottom) to impacts on bucket 21 in axial (red), tangential (blue) and radial (green) directions

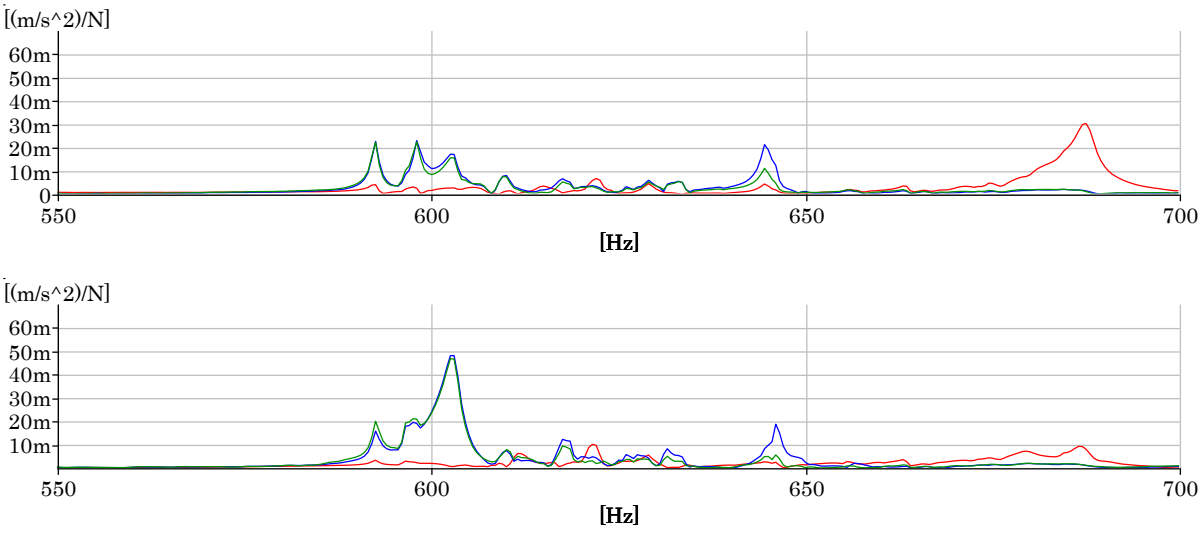

Figure 4.14. FRF's of the response from bearing position A35 (top) and A38 (bottom) to impacts on bucket 21 in axial (red), tangential (blue) and radial (green) directions

The coherence between the signal of the accelerometer installed tangentially on bucket 21 and the bearing location A38 is represented in Figure 4.15. As seen in the axial impacts, the same peaks can be found in both signals, with good coherence for most of them, but the relative magnitudes vary.

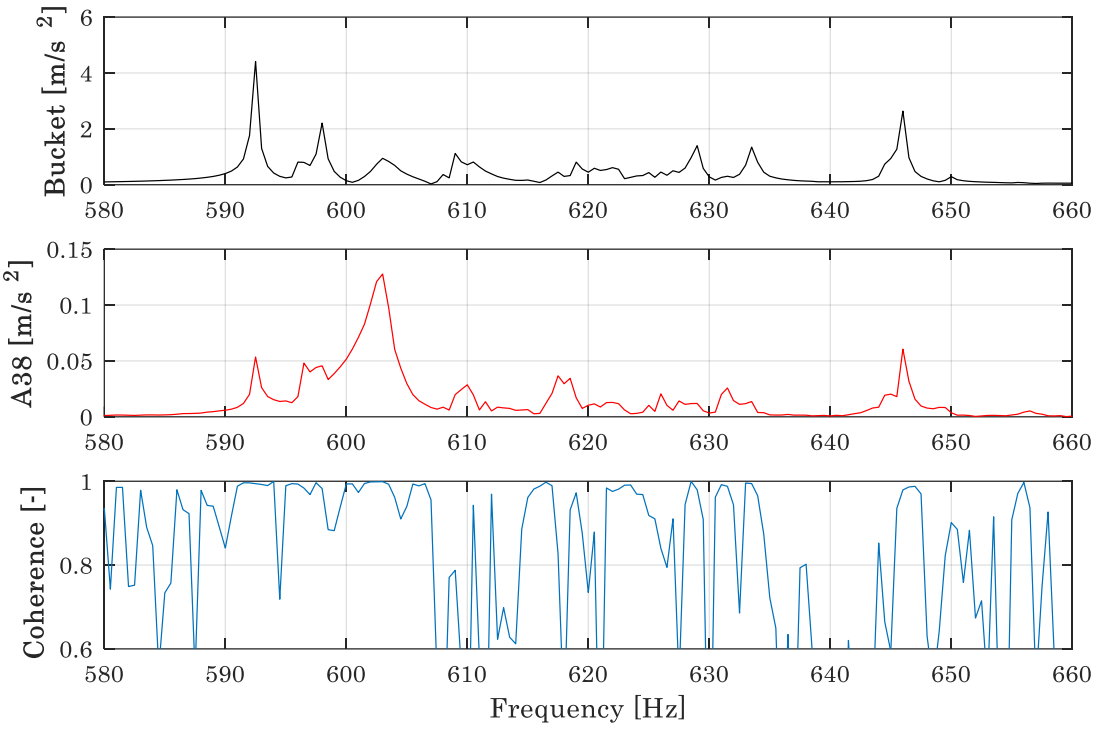

Figure 4.15. FFT and coherence between tangential accelerometer on the bucket and position A38

The range of the tangential [590-620 Hz] and torsional modes [620-635 Hz] has been evaluated in Table 4.2. At first sight, it is noticeable that for both kinds of modes, the accelerometer in radial direction RA vibrates more than the others. The tangential modes have very good transmission, and especially to the axial position A38.

Table 4.2. Tangential RMS acceleration values between bucket 21 and monitoring positions

Location	Acceleration RMS [m/s²]	Ratio [%]	Acceleration RMS [m/s²]	Ratio [%]
Bucket AA	3,898	-	2,923	-
Bucket TA	3,154	-	1,925	-
Bucket RA	7,737	-	6,477	-
A31	0,0865	2,743	0,01706	0,886
A34	0,111	3,519	0,02157	1,121
A35	0,1007	3,193	0,0244	1,268
A38	**0,1854**	**5,878**	**0,03035**	**1,577**

The rim modes are located in the range [640-690 Hz], for the RMS acceleration values have been calculated and listed in Table 4.3. The transmission is not as good as in the other cases, although the reference value is the vibration from the axial accelerometer AA, which is very high here. In this type of mode, the vibration is located almost completely in the bucket's rim, where the accelerometer is placed, so the sensitivity is very high. The best transmission ratio is from A35, but the difference with the other locations is not high.

Table 4.3. Axial RMS acceleration values between bucket 21 and monitoring positions

Location	Acceleration RMS [m/s²]	Ratio [%]
Bucket AA	114,2	-
Bucket TA	9,612	-
Bucket RA	45	-
A31	0,2171	0,190
A34	0,1664	0,146
A35	**0,2443**	**0,214**
A38	0,2235	0,196

The results for the last range of frequencies 700-1300 Hz are showed in Figure 4.16 and Figure 4.17. The radial counter-phase modes are mostly excited by the tangential impacts and their transmission is similar to all the monitoring locations. However, the radial in-phase modes (1120-1200 Hz) and the radial-axial counter-phase modes (1200-1300 Hz), which are mostly excited by the radial impacts, have clearly the best transmission to the axial vertical monitoring location A38.

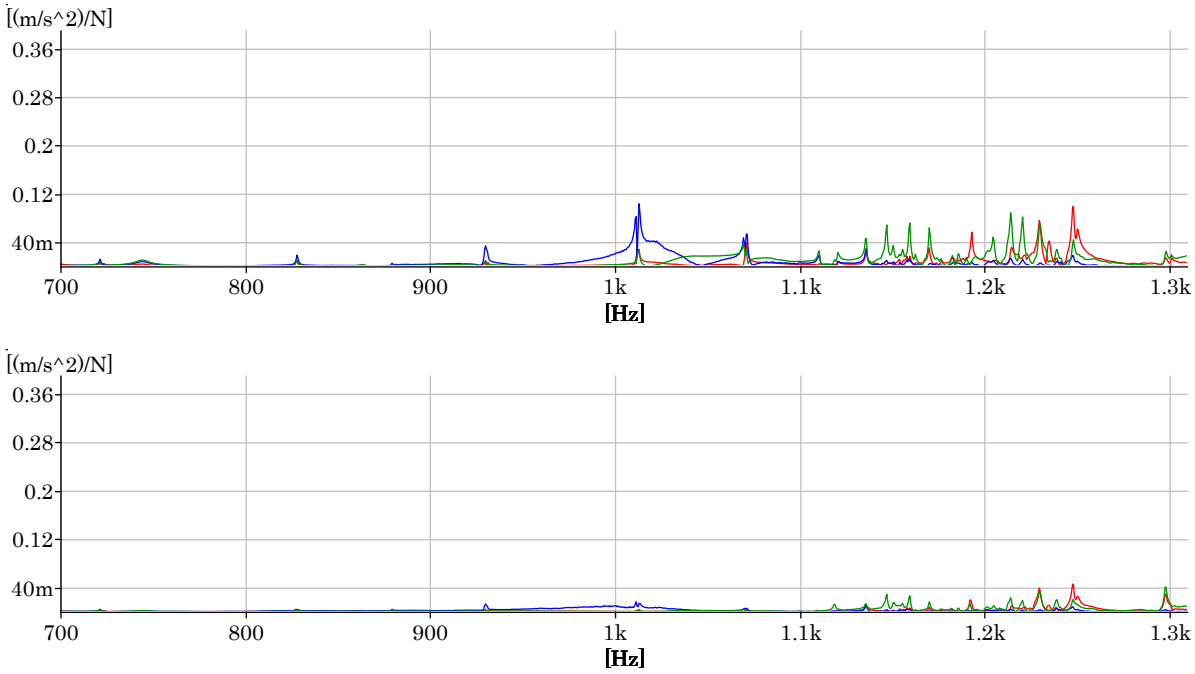

Figure 4.16. FRF of the response of bearing positions A31 (top) and A34 (bottom) to impacts in bucket 21 in axial (red), tangential (blue) and radial (green) directions

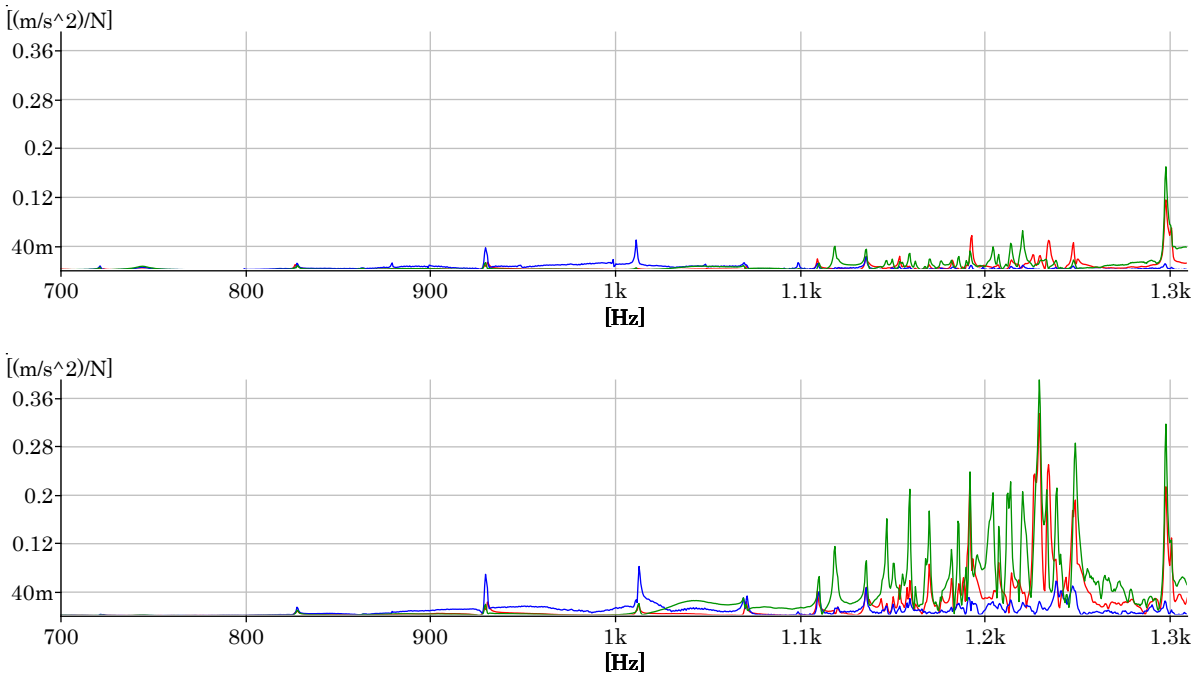

Figure 4.17. FRF of the response of bearing positions A35 (top) and A38 (bottom) to impacts in bucket 21 in axial (red), tangential (blue) and radial (green) directions

The RMS values of the radial modes (Table 4.4) show that, as seen in the plots, the axial location A38 is by far the most sensitive. The ratio has been calculated with respect to the radial accelerometer RA, which captures best the radial motion of the bucket.

Table 4.4. Radial RMS acceleration values between bucket 21 and monitoring positions

Location	Acceleration RMS [m/s²]	Ratio [%]
Bucket AA	33,06	-
Bucket TA	10,82	-
Bucket RA	58,8	-
A31	0,3292	0,5599
A34	0,09604	0,1633
A35	0,1877	0,3192
A38	**0,9662**	**1,6432**

Another series of tests were performed but impacting another bucket (bucket 16) which was located in the vertical plane of the turbine, which is the same as the monitoring position A34.

The results showed in the following pictures were obtained by performing axial, tangential and radial impacts to bucket 16. In Figure 4.18, the resulting FRF's are showed in the range 0-550 Hz. As seen in the previous tests, the frequencies corresponding to the rotor modes of the turbines are better detected from the axial monitoring positions. The choice between the vertical and the horizontal positions depends on the mode. The axial bucket-dominated runner modes also have the best transmission to the monitoring location A34.

In Figure 4.19, the FRF's in the range between 550 and 700 Hz are represented. The range of tangential modes is similarly detected by the four accelerometers, except the tangential mode corresponding to the bucket excited, which clearly outstands in the axial vertical sensor A38. When it comes to the axial counter-phase mode excited by the impact, in this case at 649 Hz since we are impacting a different bucket, there is a slight better detection from A31. Thus, the features of the transmission are the same as for the previous impacts to bucket 21.

Finally, the range between 700 and 1300 Hz is displayed in Figure 4.20. It is once again clear that radial in-phase and radial-axial counter-phase modes are by far best detected from position A38, unlike the radial counter-phase modes, which shows similar transmission to all four points.

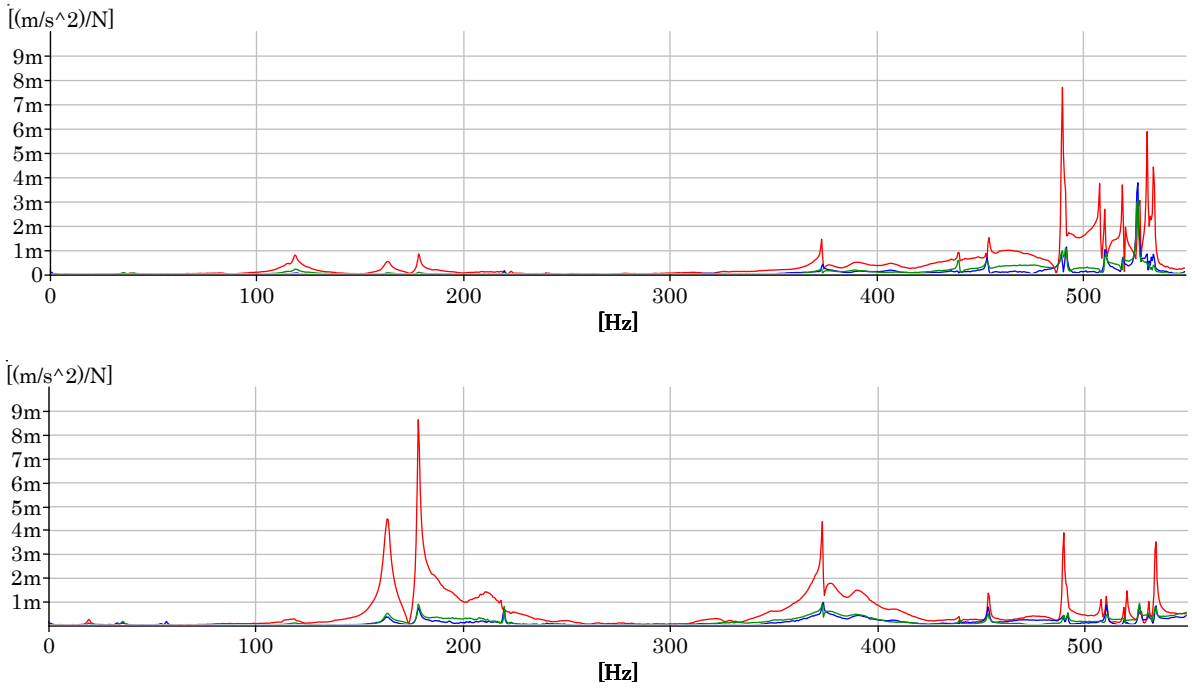

Figure 4.18. FRF's of the response from bearing position A34 (top) and A38 (bottom) to impacts on bucket 16 in axial (red), tangential (blue) and radial (green) directions

The transmission has been calculated in the same way as the impact in bucket 21. This time, the RMS acceleration value of the axial frequency band is evaluated with respect to the accelerometer in bucket 16. The response of the bucket is very similar to the impacts in bucket 21, as well as the transmission ratios. Again, position A34 is proved to be the most sensitive one.

Table 4.5. Axial RMS acceleration values between bucket 16 and monitoring positions

Location	Acceleration RMS [m/s²]	Ratio [%]
Bucket 16AA	29,32	-
A31	0,04649	0,1586
A34	**0,1129**	**0,3851**
A35	0,04657	0,1588
A38	0,04638	0,1582

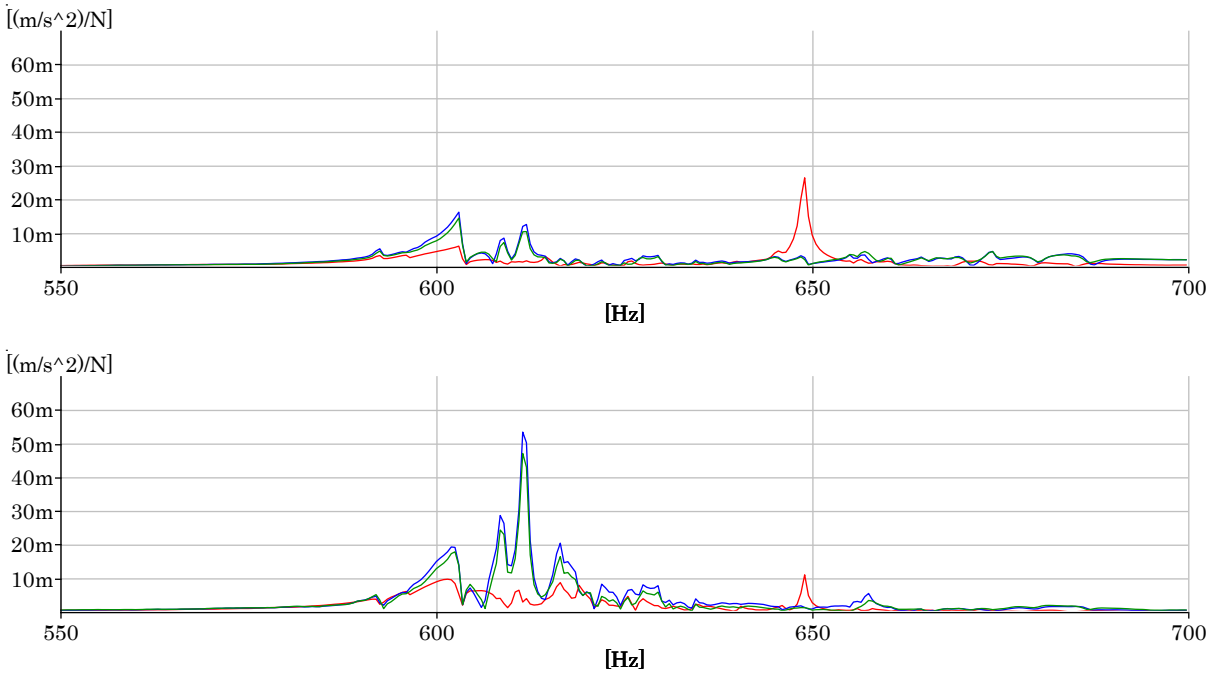

Figure 4.19. FRF's of the response to impacts on bucket 16 in axial (red), tangential (blue) and radial (green) direction from bearing positions A31 (top) and A38 (bottom)

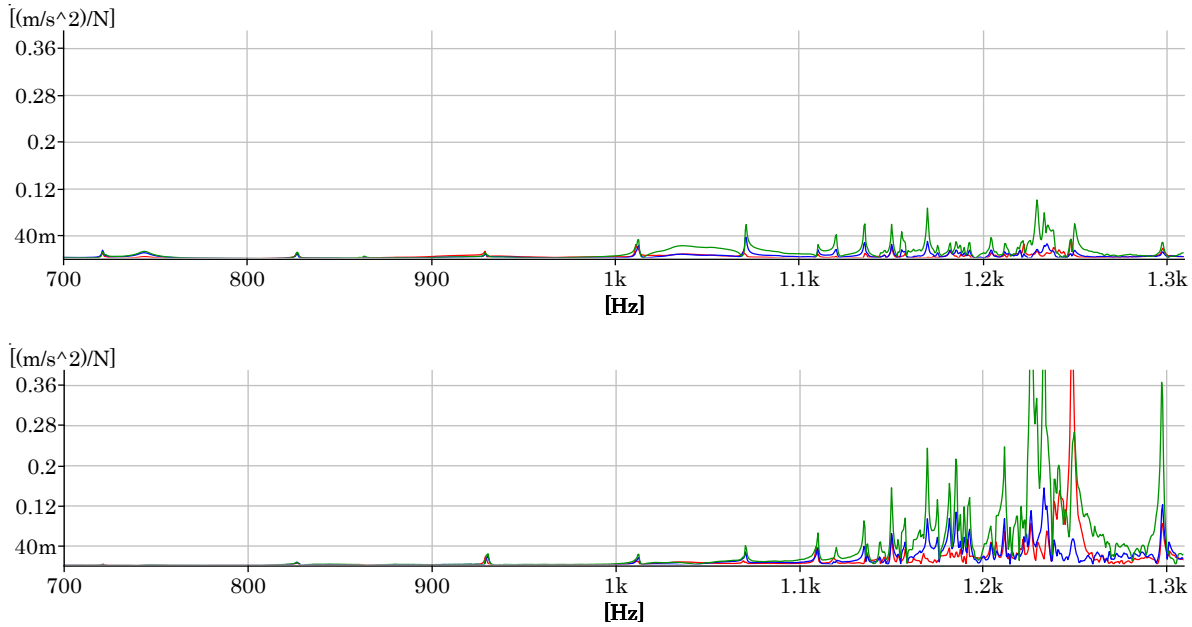

Figure 4.20. FRF's of the response from bearing position A31 (top) and A38 (bottom) to impacts on bucket 16 in axial (red), tangential (blue) and radial (green) directions

Lastly, a test similar to the previous ones was performed to the bucket near the location where the jet impacts the runner (bucket 6). This time, accelerometers were placed on positions A31 and A34. In Figure 4.21, the FRF's obtained are showed in the range 0-550 Hz. It can be seen that axial bucket-dominated modes are better transmitted to A34, like observed in the previous tests.

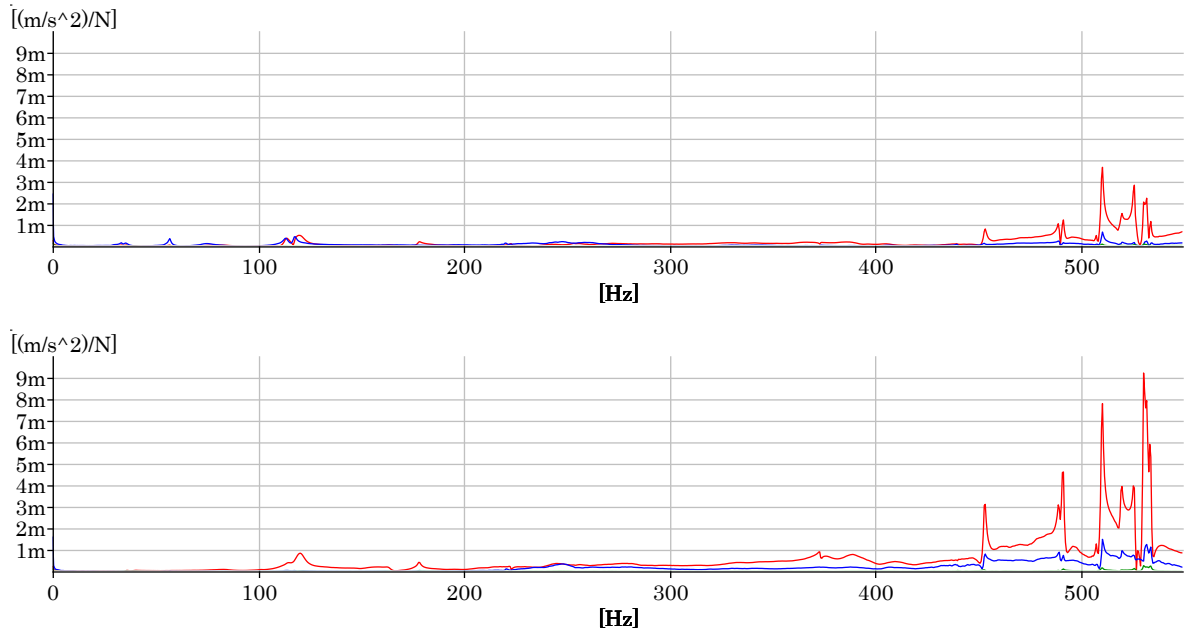

Figure 4.21. FRF of the response of bearing positions A31 (top) and A34 (bottom) to impacts in bucket 6 in axial (red) and tangential (blue) directions

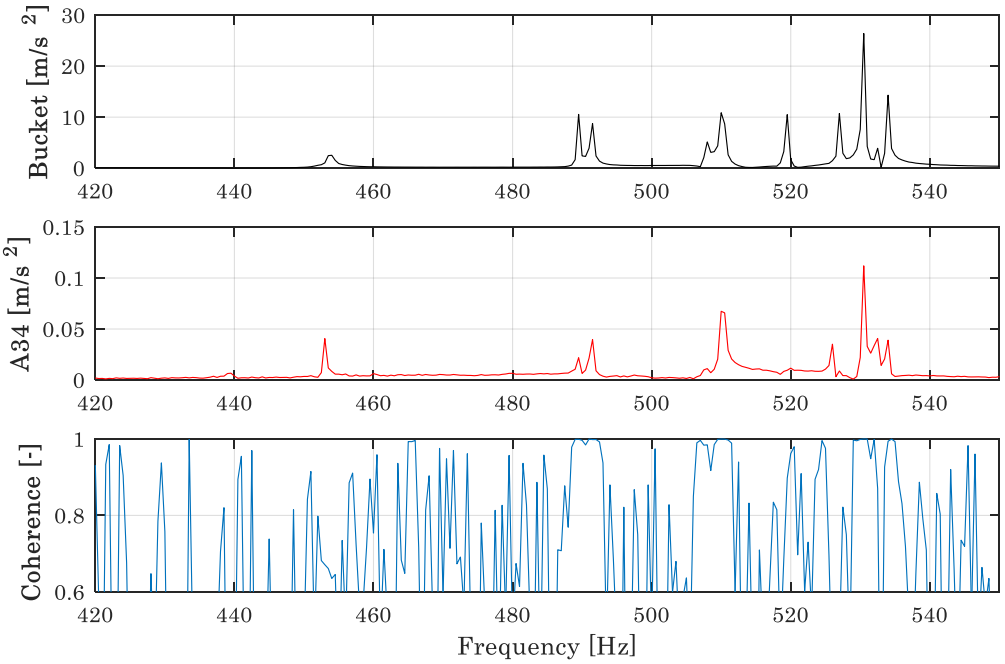

Figure 4.22. Coherence between bearing acc. A34 and bucket 6 acc.

Again, in Table 4.6 it is proved that the vertical position has the best sensitivity to the axial modes.

Table 4.6. Axial RMS acceleration values between bucket 6 and monitoring positions

Location	Acceleration RMS [m/s²]	Ratio[%]
R4 axial	8,031	-
R2 radial	7,204	-
A31	0,01457	0,1814
A34	**0,04395**	**0,5473**
E4V	0,05564	0,6928

The FRF's from A31 and A34 are showed in the range 550-700 Hz in Figure 4.23. Tangential modes have similar transmissibility between both locations. However, the axial counter-phase mode for this bucket at 674 Hz have almost twice better transmission in position A31 than A34. This confirms the behavior identified in the previous tests.

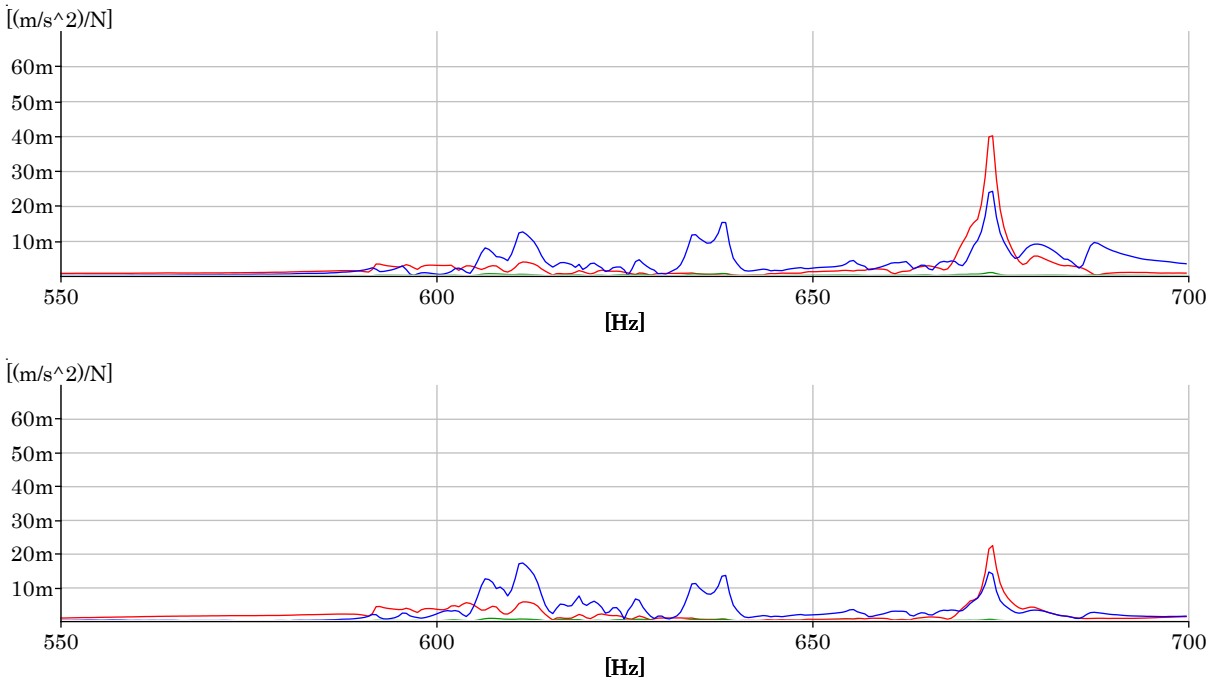

Figure 4.23. FRF of the response of bearing positions A31 (top) and A34 (bottom) to impacts in bucket 6 in axial (red) and tangential (blue) directions

All the tests have been used to determine which locations are the most suitable to identify the turbine modes. In general terms, the vertical positions provide a better transmission ratio than horizontal positions. This can be associated to the fact that the shaft has a closer contact to the bearing ring in the vertical positions due to the effect of the weight load.

To quantify the transmission, the energy bands corresponding to the different bucket modes have been filtered and calculated. For almost all bands the best detection position is the vertical location A34.

4.1.4. Scattering of runner frequencies

To check the scattering of the natural frequencies of each bucket, transmission tests for all the buckets were carried out. The results are indicated in Figure 4.24 and Figure 4.25, where the tangential and axial counter-phase frequencies measured from the bearings after impacting all the accessible buckets have been represented together. It can be seen that the rim modes are more local than tangential modes, since every bucket has its own natural frequency, which doesn't affect the other buckets. The scattering is quite important in both cases. A difference of about 7% (~50 Hz) can be found in these modes due to mechanical inaccuracies and/or different erosion between buckets. It is also worth noting that the transmission is different for every frequency.

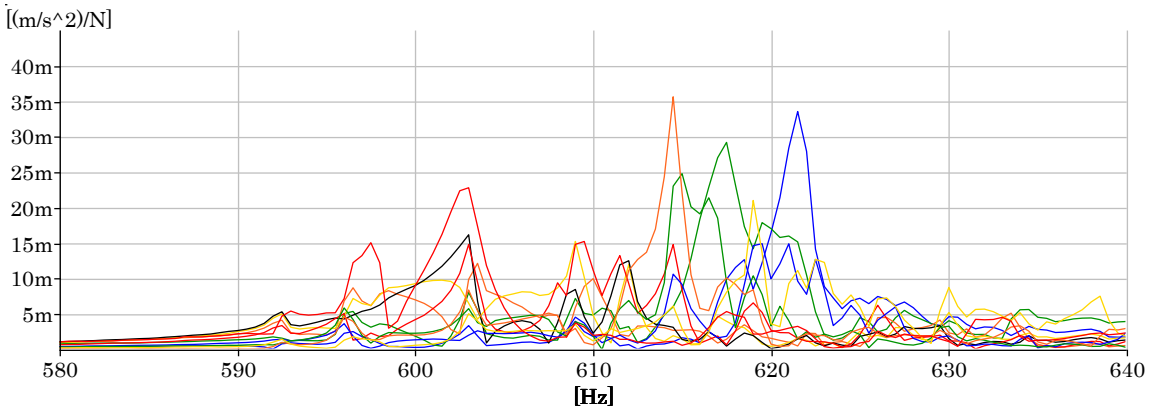

Figure 4.24. Frequencies of the tangential mode for different buckets

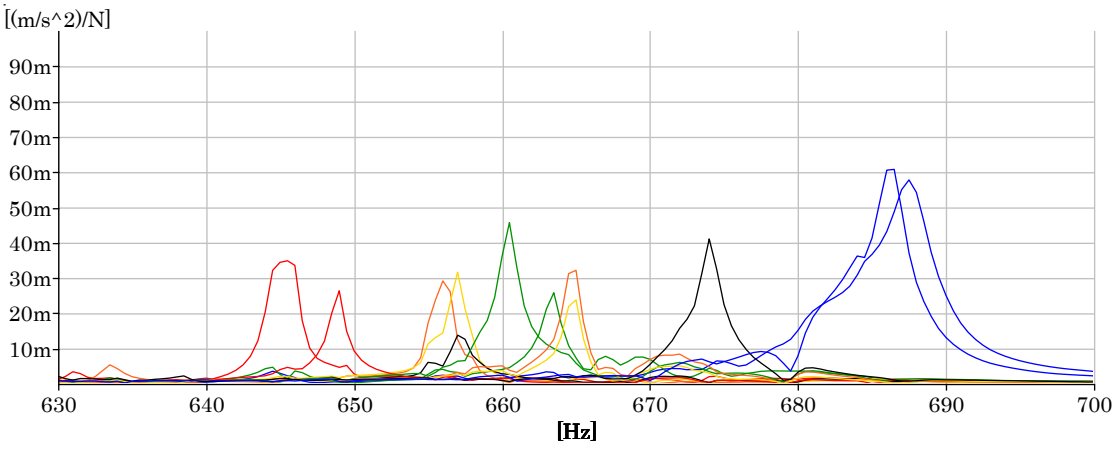

Figure 4.25. Frequencies of the rim mode for different buckets

4.2. Experimental study of Moncabril machine

The transmissibility of vibrations between the runner and the monitoring locations has been also studied for the Pelton turbine of Moncabril power plant. The same setup used for the impact tests (Figure 3.17) was used to study the transmissibility of this machine.

4.2.1. Choice of best monitoring positions

In this case only the turbine bearing has been studied, due to its proximity to the runner. Two accelerometers were placed in the horizontal and vertical direction of bearing 1, and axial and tangential impacts were performed to the buckets which were accessible from underneath the turbine. In Figure 4.26, it can be seen that the rotor modes are detected from both directions, but the horizontal position has a slight better transmission.

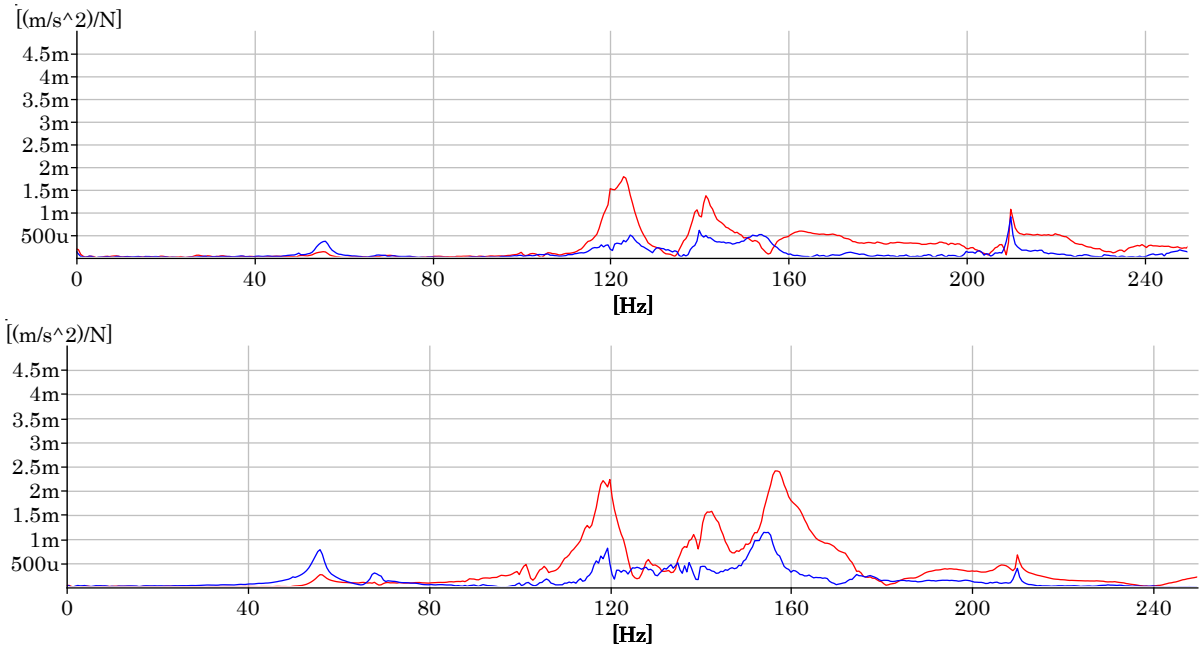

Figure 4.26. FRF's of the response from bearing positions A13 (top) and A14 (bottom) to impacts in axial (red) and tangential (blue) directions

The axial modes are excited by the axial impacts and, as seen in the previous section, are better detected from the vertical monitoring position A14. It can be seen that the transmission is better for high modes.

The vertical position also shows the better detection of the tangential and the axial counter-phase modes.

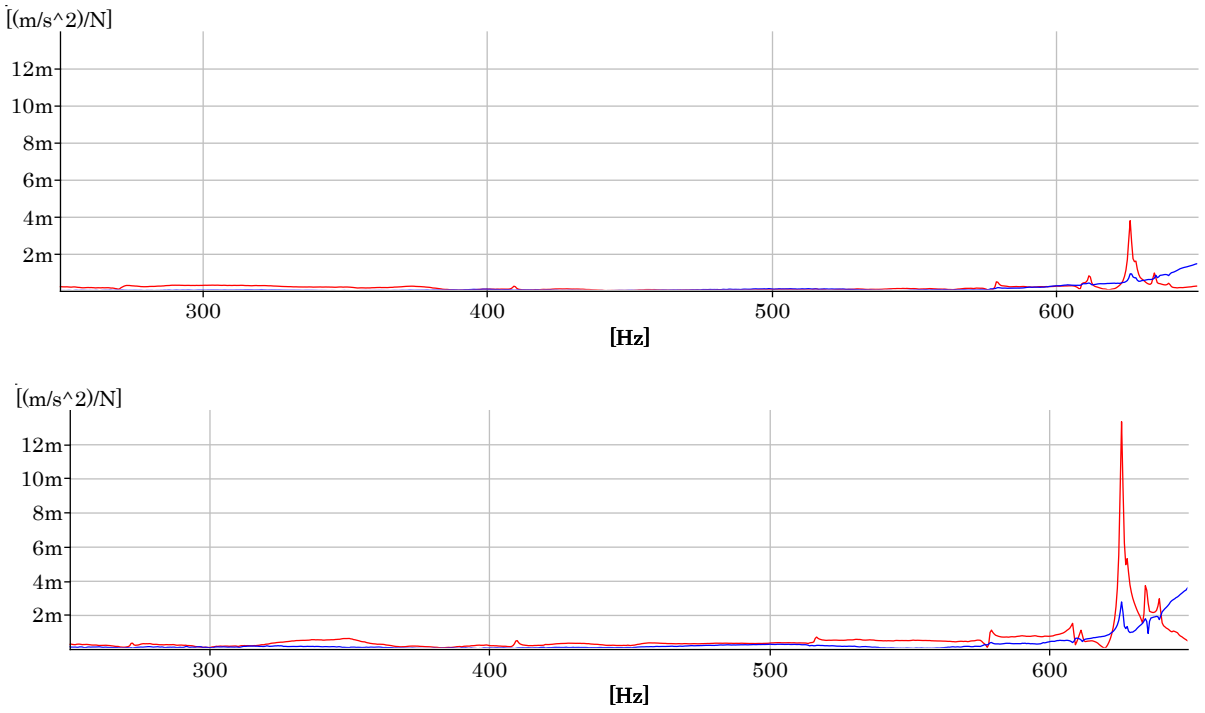

Figure 4.27. FRF of the response of bearing positions A13 (top) and A14 (bottom) to impacts in axial (red) and tangential (blue) directions

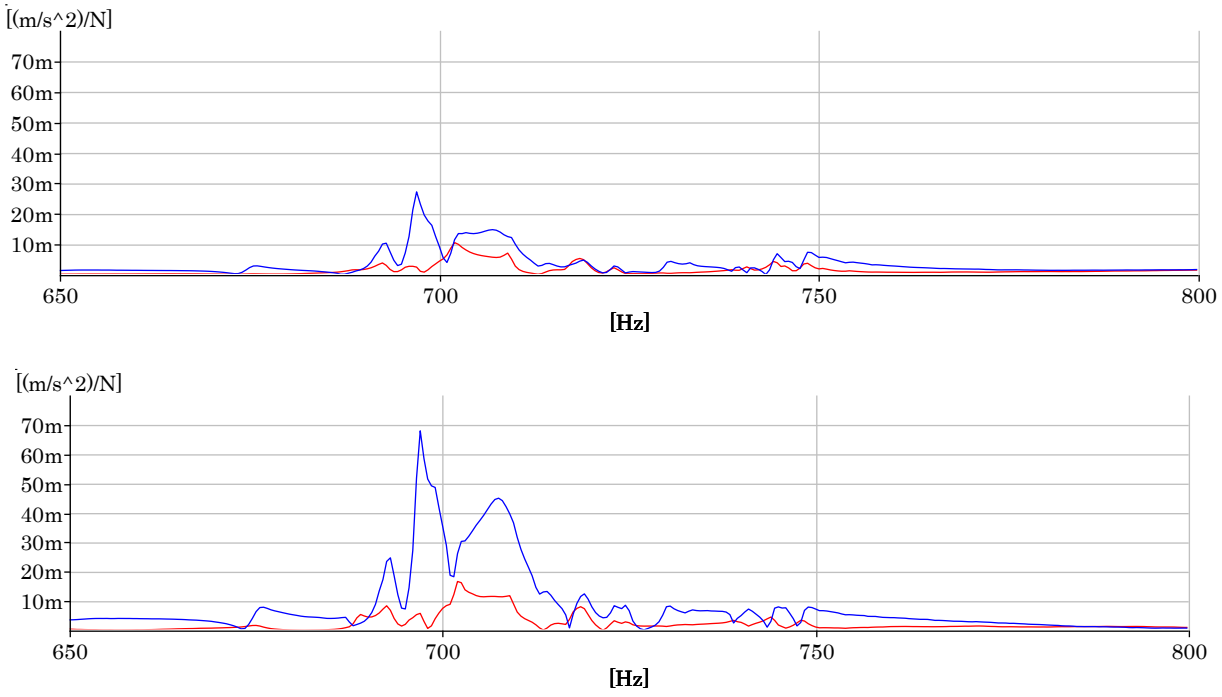

Figure 4.28. FRF of the response of bearing positions A13 (top) and A14 (bottom) to impacts in axial (red) and tangential (blue) directions

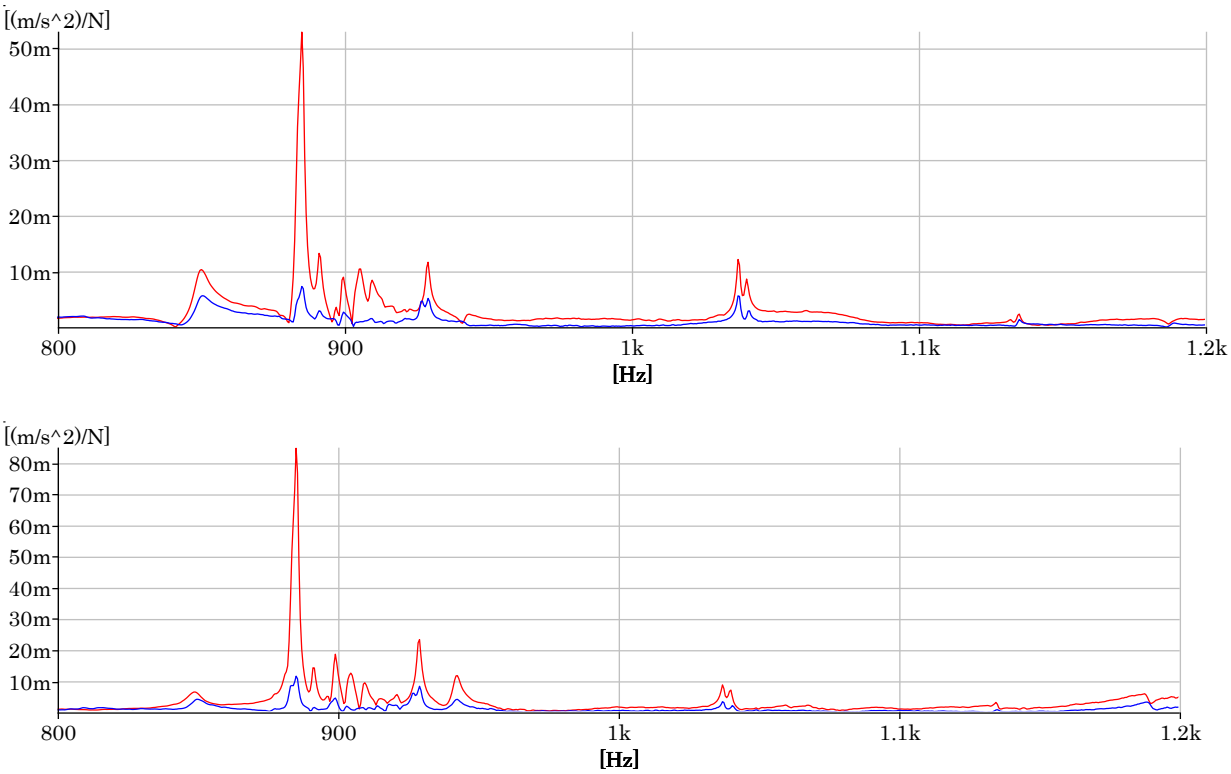

Figure 4.29. FRF of the response of bearing positions A13 (top) and A14 (bottom) to impacts in axial (red) and tangential (blue) directions

4.3. Conclusions

The propagation of vibrations from runner to bearings in two different turbines was investigated. The experimental investigation shows that all the runner vibrations are transmitted and detected on the bearing. High coherence values are found between runner and bearing vibrations. Anyway, the amplitudes seen in the bearing are much smaller than the amplitudes in the runner.

The propagation of the runner natural frequencies to each monitoring position depends on the mode shapes. The tangential modes are better propagated than axial modes

In general, tangential modes are better propagated than axial modes

In general terms, vertical positions have better transmissibility than horizontal positions. The only exception are the axial counter-phase modes, which are better transmitted to horizontal positions.

In addition, rotor modes and disk-dominated modes are generally better detected from axial bearing locations, while bucket dominated modes transmit their vibration better to the radial positions.

The best monitoring positions for the machines studied are the vertical position in the turbine bearing.

A detailed analysis shows that there are small differences between the natural frequencies of each bucket.

So far, the turbine has been studied still. In operation some effects like the centrifugal forces and the added mass, can modify the natural frequencies. Moreover, the modes excited during operation have to be determined.

For that and with the knowledge obtained with the previous studies, the dynamic behavior of a Pelton turbine in operation has been performed and presented in the next chapter.

Chapter 5 Dynamic analysis of Pelton turbines

In the previous chapter, it was proved that the vibration of the runner buckets can be detected from the bearings, and that the transmission depends on the bucket mode and on the monitoring location and direction. However, the dynamics of a Pelton turbine in operation are more complex, due to the effect of the rotational forces, the electrical excitation and the water jets.

In this chapter, the dynamic behavior of two different Pelton turbines, Arties and Moncabril, has been investigated at different operating conditions. The first analysis consists in identifying the modes excited during the start-up transient of the turbine. Second, the vibration of the machine under steady operating conditions has been analyzed with the purpose of identifying which modes are excited in normal operating conditions. Finally, the frequency bands where the different runner modes are found and their RMS vibration values have been determined.

5.1. Dynamic behavior of Arties PT

5.1.1. On-site measurements

The instrumentation used for the measurements in the power plant of Arties consisted of nine accelerometers and one strain gauge. The sensors were disposed as shown on the sketch in Figure 5.1. Eight accelerometers were placed on both bearings in the same positions as the impact tests (A11, A14, A15, and A18 on turbine bearing one, and A31, A34, A35 and A38 on turbine bearing two).

In addition, an onboard system with one accelerometer and one strain gauge was installed on the shaft between turbine 2 and bearing 2 (Figure 5.2 left). A strain gauge is a sensor whose resistance varies with the applied force. The one used for the tests was a pre-wired gauge HBM K-CDY4-0030-1-350-3-005 with a grid length of 3 mm, a nominal resistance of 350 Ohm and cable length of 0,5 m.

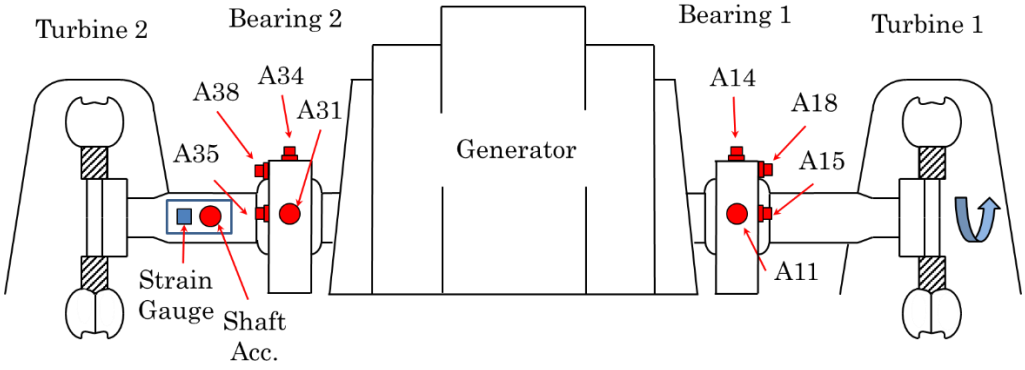

Figure 5.1. Sketch of the position of the sensors during on-site measurements

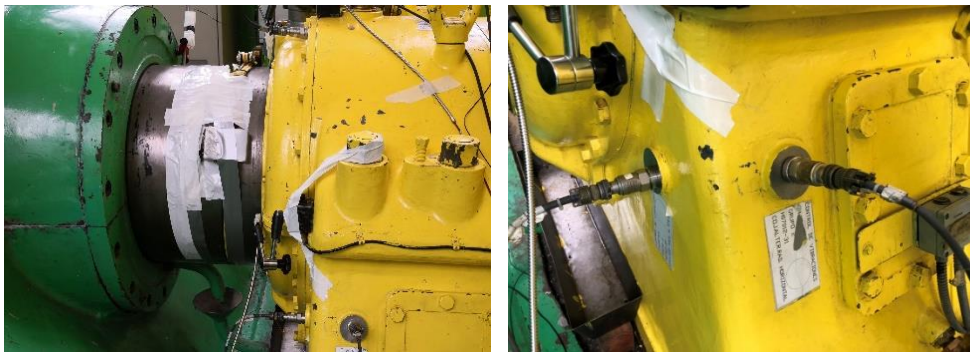

Figure 5.2. On the left, onboard system installed on the shaft and on the right, horizontal accelerometers placed on the turbine bearing

The test performed consisted in recording the vibration of the machine during a whole operating cycle, from the machine being still to operating at maximum load. The operating parameters of the turbine at every instant were known thanks to the software SCADA (Supervisory Control and Data Acquisition), which is used by the power plant operators to control and monitor the operation of the turbine. Figure 5.3 shows a screenshot of the program when the turbine is operating at minimum load. Among other parameters, one can see the rotational speed, the opening degree of the nozzles and the overall vibration levels.

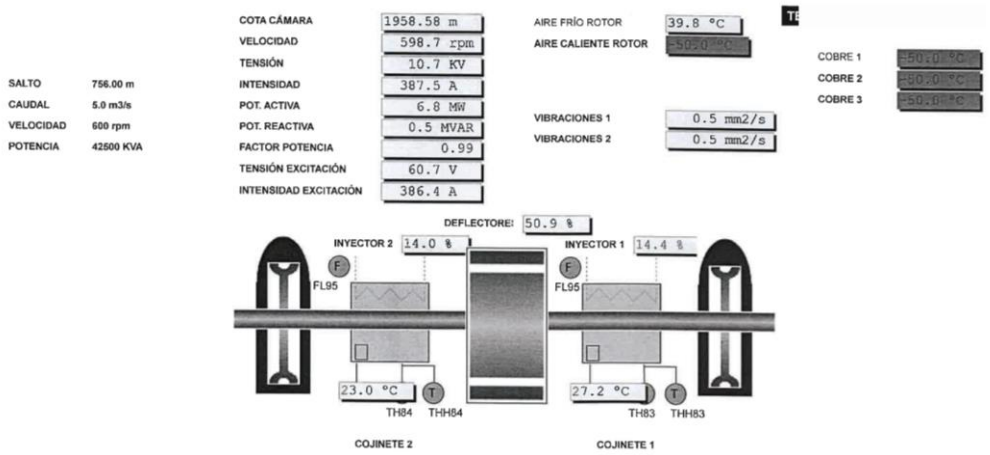

Figure 5.3. Screenshot of the SCADA software at minimum load of the turbine

The time signal of the vibrations obtained from monitoring location A34 during the whole test is shown in Figure 5.4 in acceleration (m/s^2). Four different operating states can be discerned: the first one is the startup transient, which comprises the time between the first collision of the water particles (1) on the buckets and the turbine reaching nominal speed (2). The jet from runner 2 is opened at 3.6% to set the turbine in motion. During this time, the vibration levels are very high due to the resonances of the jet excitation with the modes of the turbine. The second operating state of the turbine is called Speed no load, which is the time when the rotor runs at nominal speed but the alternator is not yet connected to the electrical grid. The vibrations during Speed no load are low because the velocity is constant and the jet load is small. After that time, the alternator is excited by a magnetic field (3).

In the third operating state, the machine operates at minimum load (10 MW). Before doing so, the nozzle of runner 1 is opened, causing a small excitation (4), and the alternator is connected to the electrical grid. Since the resistant torque is higher, both nozzles increase the opening degree to 14% to keep the rotational speed constant. This is translated into an increase in the vibrations (5). After some minutes, the power plant operators start to increase the turbine load (6). In a short time, the turbine is operating at the maximum load of 35,8 MW (7), with the nozzles opened at 99,8%. In this stage, the vibration amplitudes are high.

In the following sections, the dynamic behavior of the machine will be studied in detail during the startup transient, the operation at minimum load and at maximum load.

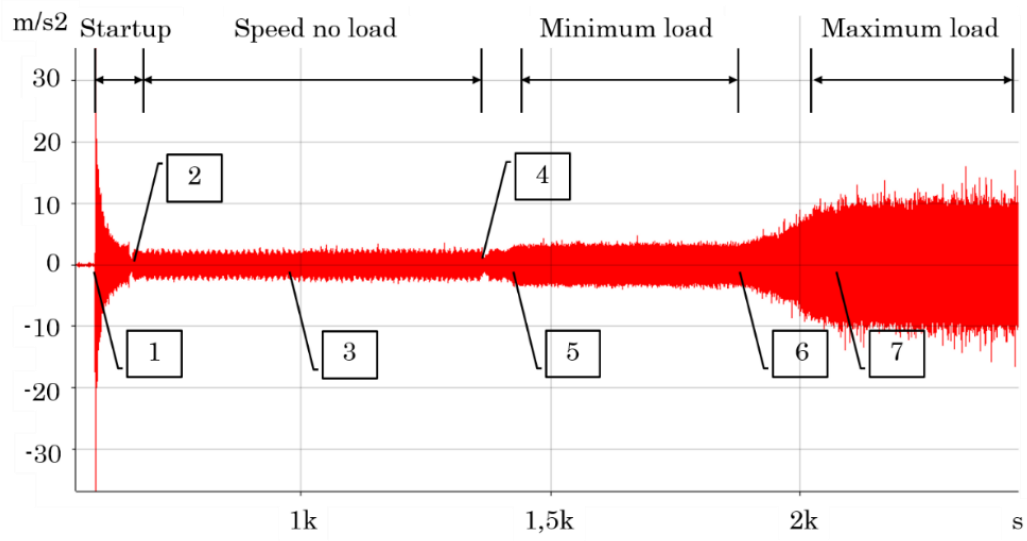

Figure 5.4. Time signal during the tests from position A34

5.1.2. Startup transient

The startup transient comprises the time that it takes to bring the machine to nominal speed. The vibrations during this time can be dangerous for the machine and need to be studied. The opening degree of the nozzle must be kept small during startup so that the load applied on the buckets is not too strong. However, it is also important that the transient doesn't last too much for regulation purposes.

The time signal recorded from A34 during the startup transient has been represented in Figure 5.5. This has been divided into two stages. In the first one, the runner buckets are excited by the collision of the first water particles coming out of the nozzle. The vibrational response to this impingement is very high because the velocity of the buckets is zero. The second stage takes place when the runner starts rotating and lasts until it reaches its nominal speed. At the beginning of this period, the vibration levels go up and down due to several resonances with the natural frequencies of the turbine. However, as the machine approaches its nominal speed, the vibration decreases steadily.

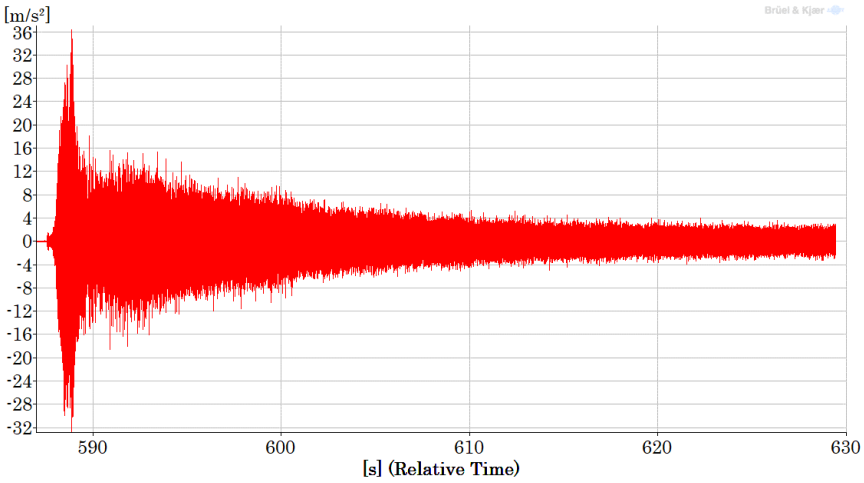

Figure 5.5. Time signal during startup transient from A34

The time signal recorded from position A34 has been represented in Figure 5.6 in the frequency domain. This representation is known as waterfall and shows the change in the vibration spectrum over time. In the figure, the first impact and the speedup of the turbine can be clearly identified. Before the runner starts rotating, different frequency bands are excited by the first collision of the jet. These correspond to the modes of the turbine, which can be divided into rotor modes (0-400 Hz) and runner modes (>400 Hz). After that, the runner starts accelerating (Speed-up). The rotation of the machine and the force of the jet are clearly detected at every instant. The frequency of rotation f_f can be expressed as

$$f_f = N/60 \qquad \text{Eq. 5.1}$$

Where N is the rotational speed in min^{-1}. At nominal speed (600 min^{-1}) the f_f is 10 Hz. The bucket passing frequency f_b determines the rate at which the jet impinges the runner buckets and can be written as

$$f_b = z_b f_f \qquad \text{Eq. 5.2}$$

Where z_b is the number of buckets. At nominal speed, the bucket passing frequency is 220 Hz. During the speed-up, the turbine enters into resonance with the turbine modes every time the f_b is the same as a natural frequency of the structure (Campbell diagram). It is worth noting that the vibration is higher at the beginning of the speed-up than at the end because the velocity of the runner is still much lower than nominal speed, and this causes the jet to impinge the buckets with very high velocity. After the machine has reached its nominal speed, the vibration levels diminish considerably and mainly the f_f, the f_b and their harmonics are noticeable.

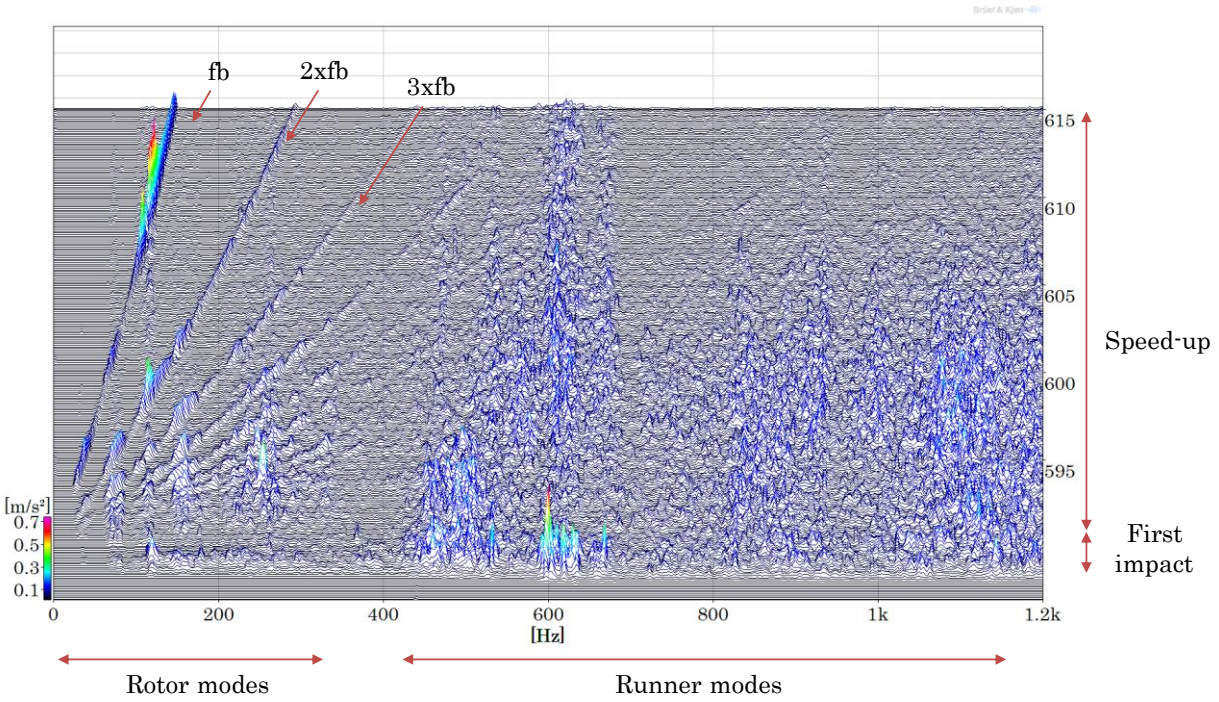

Figure 5.6. Acceleration waterfall of the startup transient from A34

The signals obtained from the different positions have been analyzed to detect which rotor modes (low frequencies) and runner modes (high frequencies) are excited during startup. At low frequencies, the vibration of the system is ruled by velocity and, at high frequencies, it is dominated by the acceleration. This can be clearly seen in Figure 5.7, where the same vibration signal obtained from A31 during startup has been represented in acceleration (top image) and in velocity (bottom image). Therefore, the vibration of the runner modes will be studied using the signal in acceleration and the rotor modes will be studied using it in velocity.

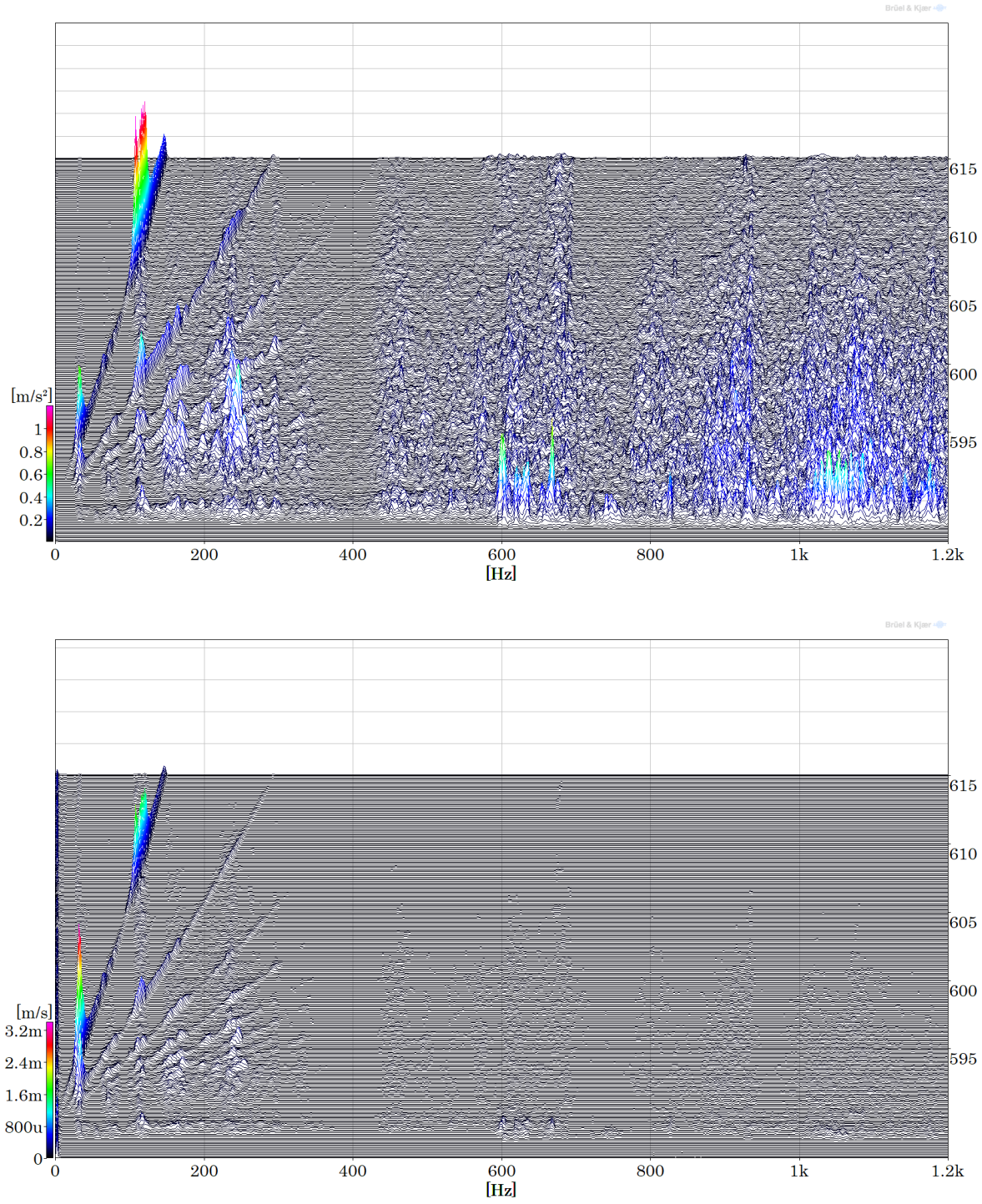

Figure 5.7. Waterfall of the startup transient from A31 in acceleration m/s2 (top) and velocity mm/s (bottom)

The collision of the first water particles coming out of the nozzle induces a large vibration on the turbine. This is attributed to the fact that with the runner still, the jet enters the buckets at a relative velocity that doubles that from steady operation. This aggravates the effects of

the transient inside the buckets and makes it more prone to excite the natural modes of the runner. In addition, the water can also show some deviations with respect to the optimal jet shape, due to the small transitory that takes place inside the nozzle after the displacement of the needle. In order to minimize the harmful effects on the structure, the opening degree of the nozzle is kept small during startup.

The study of the initial jet impact is of interest due to its similarity with the impact tests. The runner is still not affected by rotational or electrical forces, and, moreover, only one or two buckets are impinged, for the vibration is not mixed between all the buckets like in steady operation. The dynamic behavior of the turbine during the initial instant is thus less complex than for the rest of the operating cycle, and the characteristics of the jet and the transmissibility of the vibrations can be analyzed more accurately.

Observing Figure 5.7 top, it can be seen that the runner modes are more excited than the rotor modes in the initial seconds of the transient. These require much less energy to oscillate, for the mass displaced is much lower. Since the excitation of the rotor modes is more significant during the speedup of the turbine, only the runner modes will be studied in the initial impact. These will be identified from the different monitoring locations and the results will be compared to the impact tests performed on the still machine. In addition, the transmissibility of the vibrations to the shaft will also be checked with the measurements from the on-board system.

The vibration recorded from the accelerometer in position A31 is shown in Figure 5.8. According to the information obtained in the impact tests, four different types of runner modes are found between 500 and 700 Hz: axial modes, tangential modes (in phase and in counter-phase) and axial counter-phase modes. The frequency ranges corresponding to each mode type have been delimited in red to be compared with the peaks detected at the start of the transient. Observing the figure, it is clear that the frequencies excited by the initial jet collision are very similar to the ones obtained in the impact tests. The most outstanding frequencies correspond to the tangential and the axial counter-phase modes, which is to be expected, for the jet impinges the buckets tangentially and the water is deflected by the buckets' rim. The most prominent peak is located at 668 Hz in the range of the axial counter-phase modes, which corresponds to the natural frequency of the impacted bucket.

The vibration in the axial frequencies is low comparatively to other modes. However, it should be remembered that, as seen in Chapter 4, their transmission to the bearings is lower, what means that the vibration of the runner is higher.

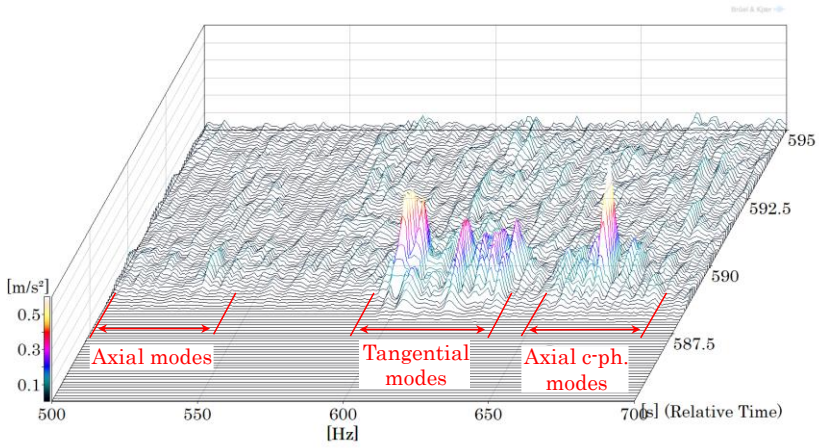

Figure 5.8. Runner modes excited in the initial impact detected from A31

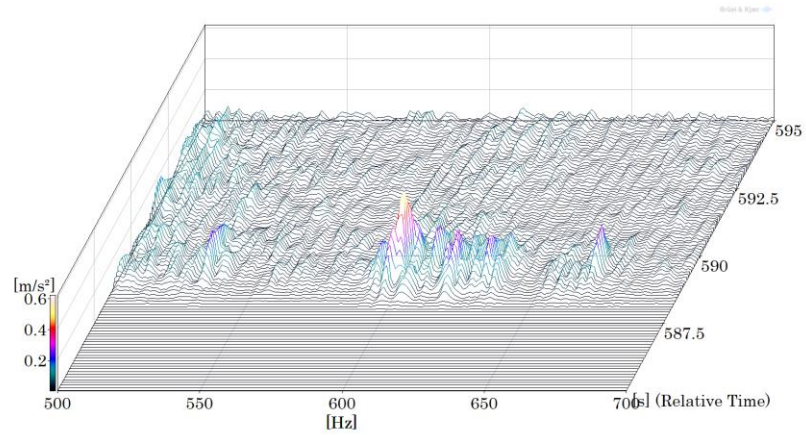

Figure 5.9. Runner modes excited in the initial impact detected from A34

The signals from the axial positions A35 and A38 are represented in Figure 5.10. The axial modes and the tangential modes are better detected from the vertical position, what also confirms the conclusions from the impacts on the still machine.

With this, it is proved that the runner modes are excited in the first impact, and that they can be detected from the bearings. The transmission has been compared between different locations and the results agree with the impact tests, being the vertical positions A34 and A38 the best to detect the axial modes and A31 the best to detect axial c-ph. modes. The transmissibility of the tangential modes is good for all the directions, except A35.

The transmissibility of the runner modes has been studied with the accelerometer and the strain gauge installed on the shaft. In Figure 5.11 the spectrum waterfall recorded from the accelerometer is represented in the range of the axial and tangential frequencies and compared to bearing position A34. It is seen that the same frequencies detected in the bearings are found in the shaft, but the transmission is different depending on the mode. The transmissibility of the axial in phase and the tangential modes is better than the axial counter-phase modes.

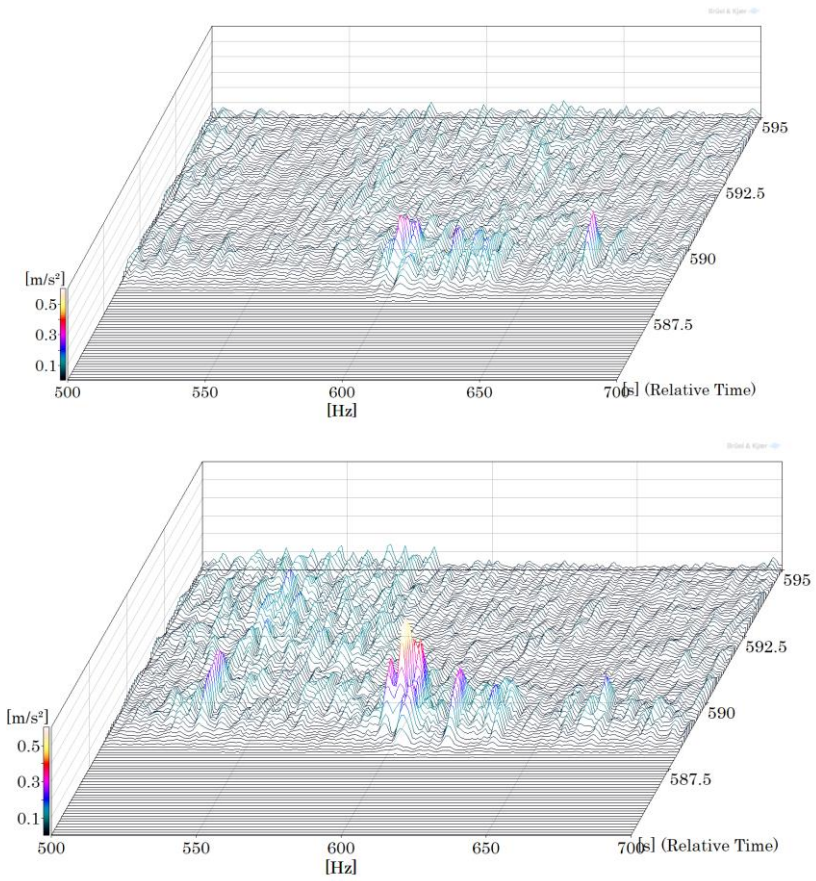

Figure 5.10. Runner modes from A35 (top) and A38 (bottom) in the initial impact

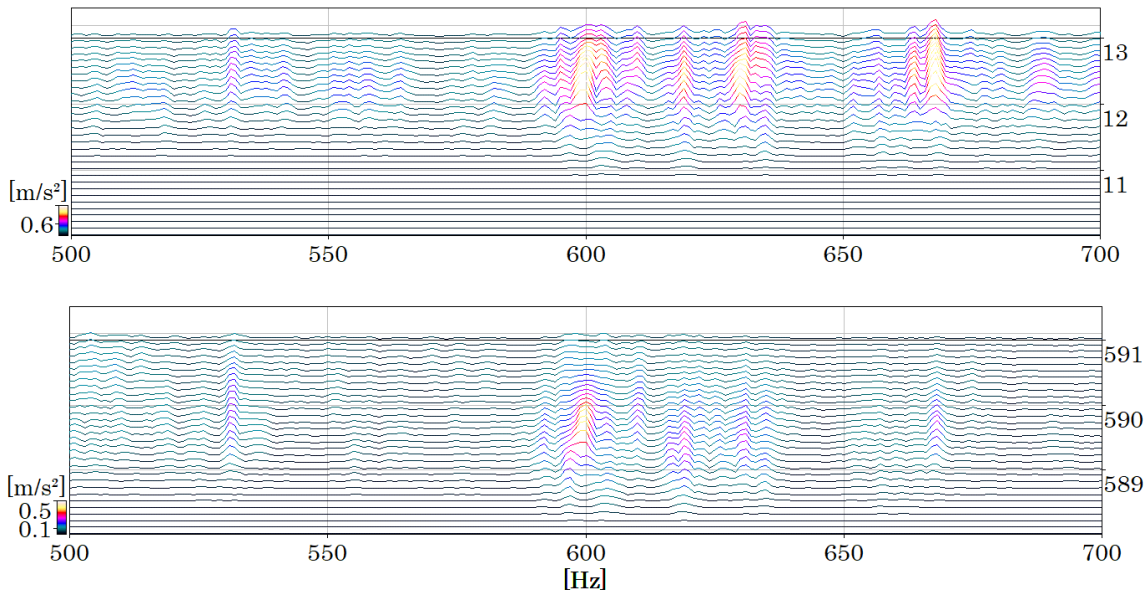

Figure 5.11. Transient from shaft accelerometers A2 (top) and A34 (bottom)

The signal obtained from the strain gauge has also been analyzed and it has been proved that the runner modes also perform a strain on the shaft. The same range of frequencies is represented in Figure 5.12 from the strain gauge and the shaft accelerometer. The tangential modes are well detected by the gauge and have good coherence with respect to the accelerometer. The axial in-phase and counter-phase perform a lower strain on the shaft, but also can be distinguished.

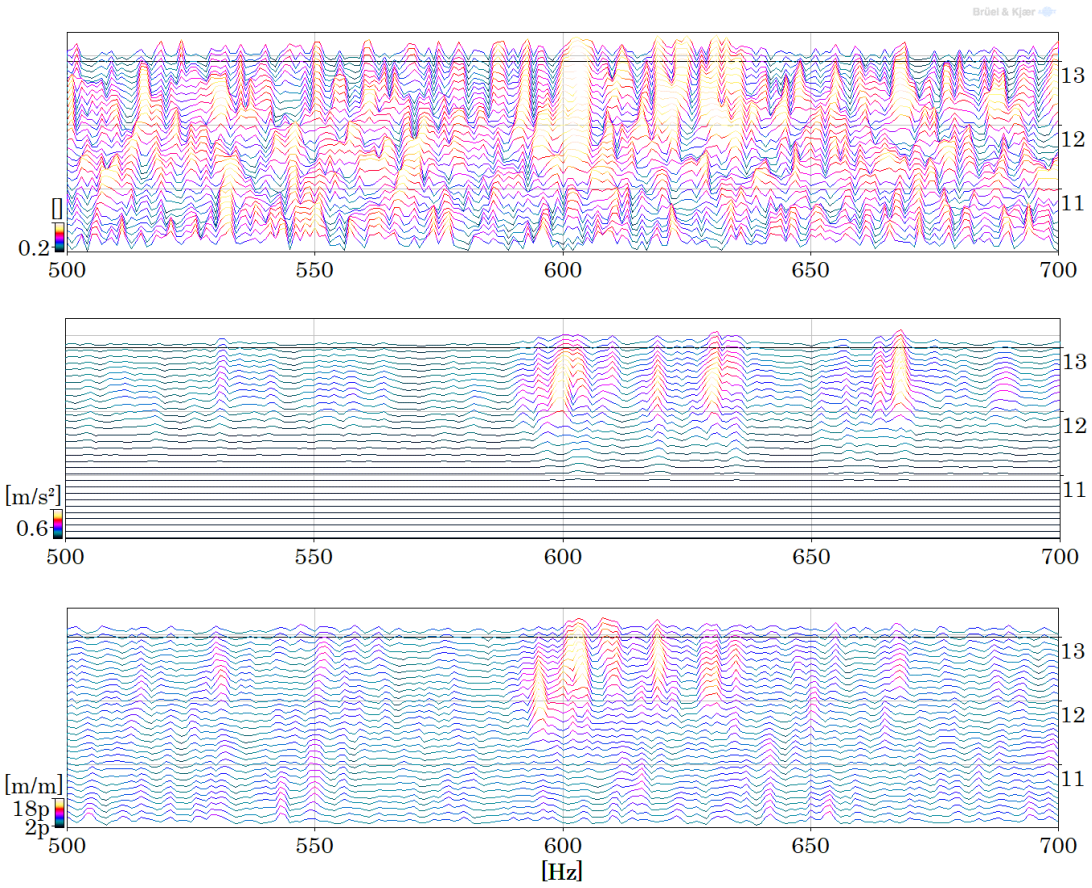

Figure 5.12. Spectra waterfall from strain gauge (bottom), from shaft accelerometer (middle) and coherence between both signals (top)

After the first impact, the turbine starts to increase its velocity and the water jet is converted into a periodic load applied to all of the buckets. The structure is then affected by the centrifugal forces, which increase its stiffness and vary its natural frequencies. With the increment of the frequency of rotation, the load of the jet enters into resonance with the natural frequencies of the turbine, especially with modes of the rotor, which are found below the 300 Hz. To understand the effect of the new operating conditions on the dynamic behavior of the machine, the speed-up has been divided into two periods. The first one covers the behavior of the machine at the beginning of the speed-up, when the velocity of the runner is low and the vibration is high due to resonances with rotor and runner modes. The second period comprises the end of the startup, when the runner is near its nominal speed. The vibrations are then considerably lower, and mainly resonances with the lowest harmonics of the excitation take place.

In the initial stage of the speed up, first the rotor modes have been studied. The frequencies excited between 0 and 250 Hz detected from A38 are shown in Figure 5.13. Many peaks can be observed due to the resonance of the turbine modes with the excitation frequency f_b and its harmonics. Four frequency bands are identified, which correspond to different bending modes of the rotor. Some excitations haven't been identified in the impact tests, which can be due to resonances with the system frequencies.

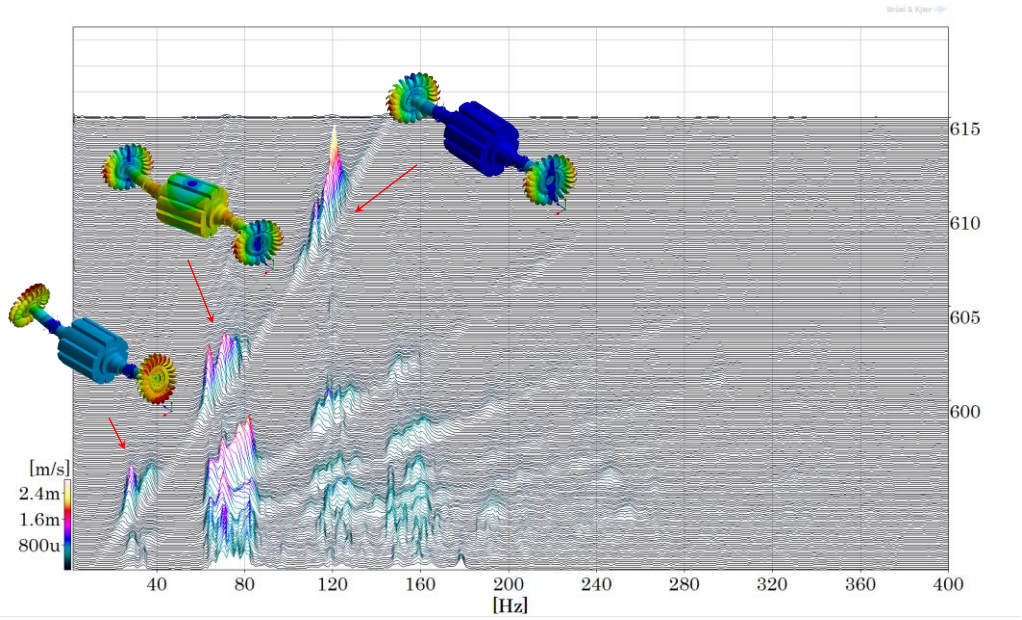

Figure 5.13. Startup from position A38

The strain gauge cannot detect as well the bending modes of the rotor as the accelerometers on the bearings, but provides a clear evidence of the excitation of the torsional modes at 54 Hz, what is difficult to find for any other sensor.

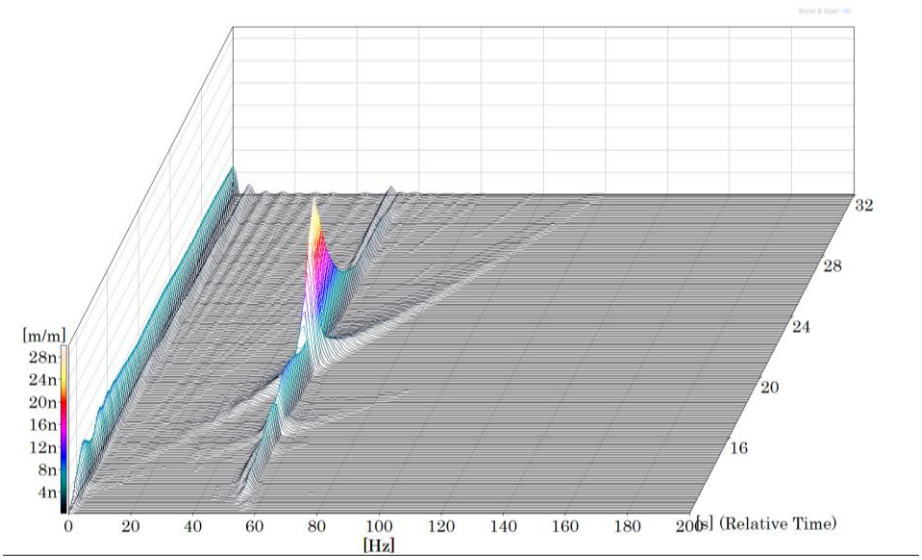

Figure 5.14. Torsional rotor mode detected with the strain gage

The excitation of the runner modes during the speedup is analyzed in this section. The range of frequencies 500-700 Hz has been analyzed from position A34, just after the first collision of the jet (Figure 5.15) and at the end of the transient, when the machine is almost rotating at nominal speed (Figure 5.16). In both figures, the ranges of the axial in phase, tangential (phase and counter-phase) and the axial counter-phase modes have been delimited after the results obtained in the impact tests. In the beginning of the speedup many peaks can be discerned, due to the mixed vibration from different buckets. As seen in Chapter 4, each bucket has its own natural frequency, which is different from the others. These still have still very low velocity and the jet excitation has an important random component. Just after the first impact, the range of the axial modes is the most excited by the jet forces. As the runner increases its velocity, the main excitation forces increase their frequency, exciting the tangential modes between 600 and 605 seconds. With this, the main frequency ranges can be discerned and compared to the results for the still machine. Comparing both, it is seen that the natural frequencies are very similar.

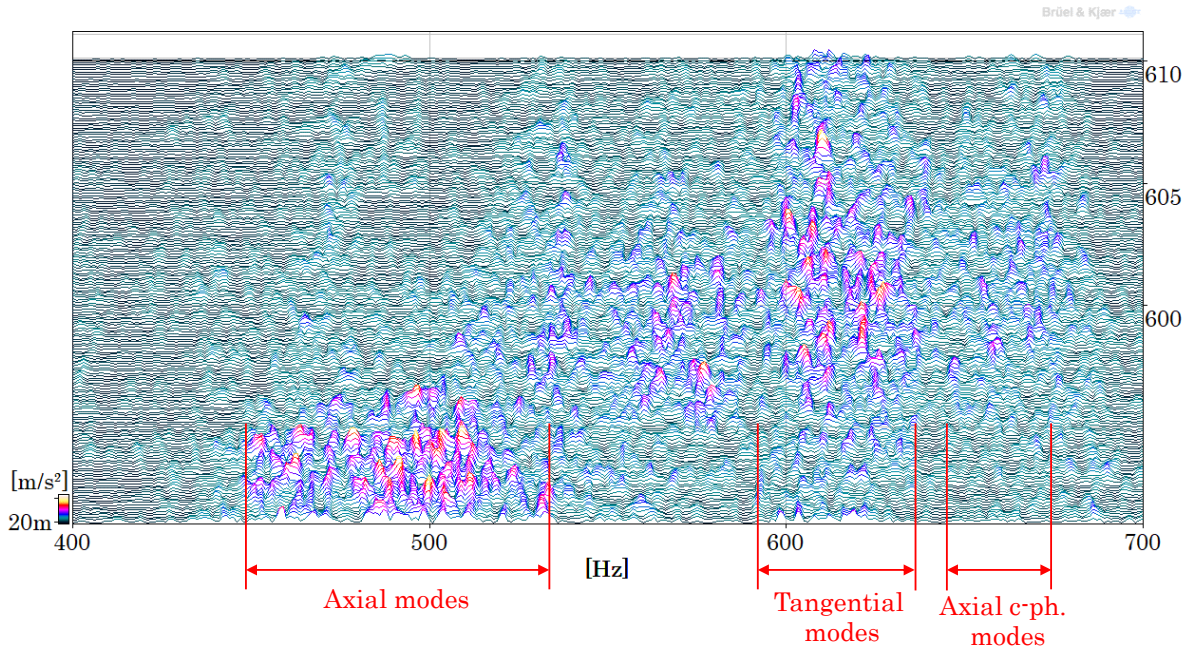

Figure 5.15. Axial and tangential modes from positon A34 at the start of the speed-up

At the end of the transient, the velocity of the runner is adjusted to meet its nominal speed (600 min^{-1}). Due to the resonance of the runner modes with the harmonics of the f_f and f_b, different peaks stick out. In the range of the axial modes the most excited frequencies correspond to the bucket-dominated modes. It can be seen that some of the frequencies have increased with respect to the still machine, which is due to the higher stiffness of the structure caused by the rotational velocity. The tangential modes aren't as much excited as the axial modes. Some frequencies in the range of the axial counter-phase modes are excited by the 3rd harmonic of f_b (660 Hz).

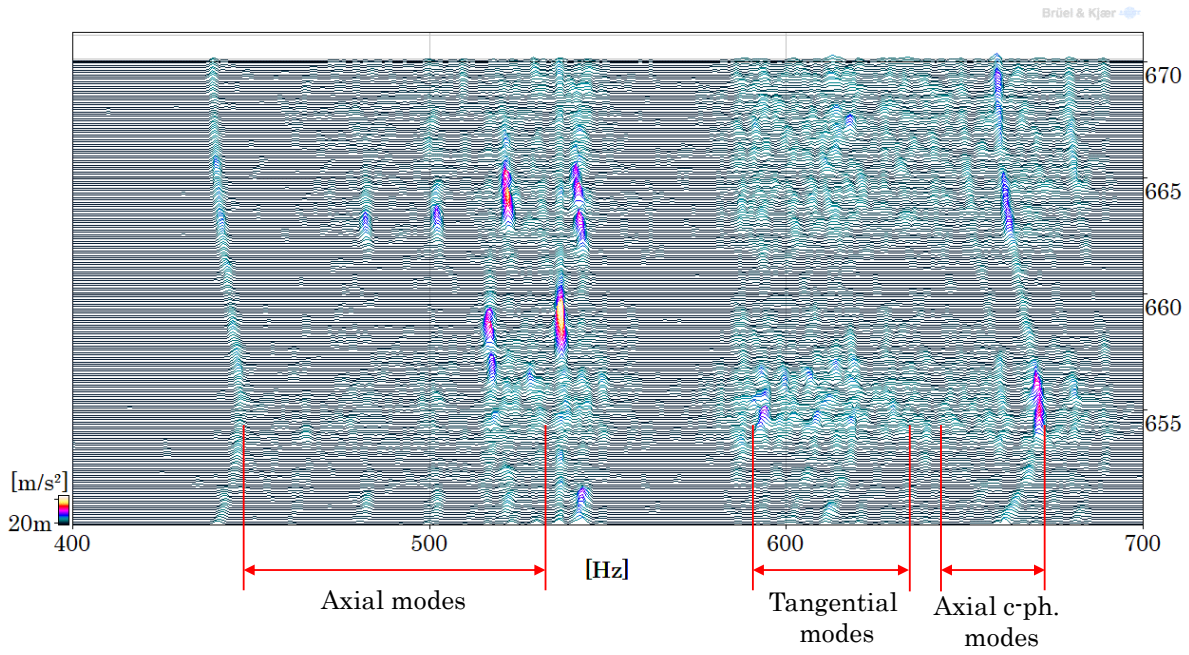

Figure 5.16. Axial and tangential modes from positon A34 at the end of the speed-up

During the startup transient, large vibrations occur due to the resonance of the modes of the turbine with the excitation coming from the water jet. Since the main excitation frequencies f_f and f_b are below 300 Hz, the largest resonances come from the rotor modes. Therefore, to assess the effect of these resonances on the structure of the turbine, the vibration has been studied in velocity form. In Figure 5.17, the time signal from A34 and A31 has been represented, respectively, as velocity. It can be seen that the vibration is higher from the horizontal position than from the vertical, which can be explained by the fact that the stiffness of the bearings is lower in the horizontal direction. In addition, the water jet impinges the machine horizontally.

According to standards, the vibration value of a rotating machine must not exceed 3,1 mm/s rms to avoid big damage. In the horizontal direction A31, this value is surpassed during the startup in one occasion, as seen in Figure 5.18. The highest oscillation velocity takes place when the blade passing frequency enters into resonance with a horizontal bending mode at 33 Hz. In this case, the peak-to-peak vibration exceeds 14 mm/s.

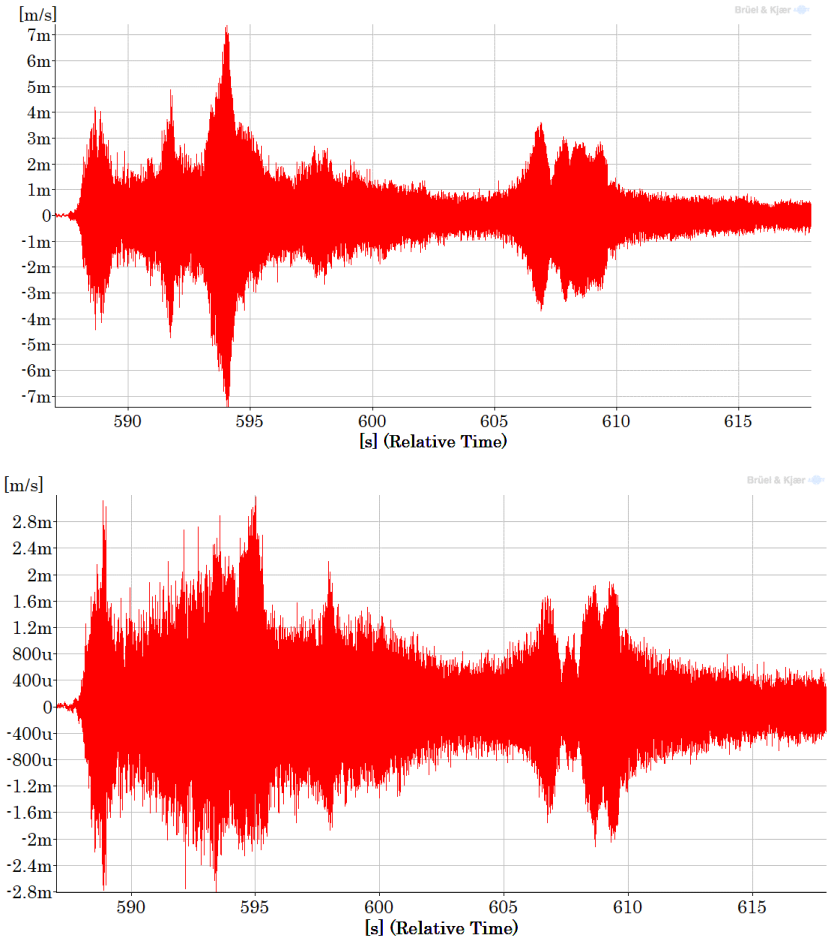

Figure 5.17. Velocity time signal from A31(top) and A34 (bottom)

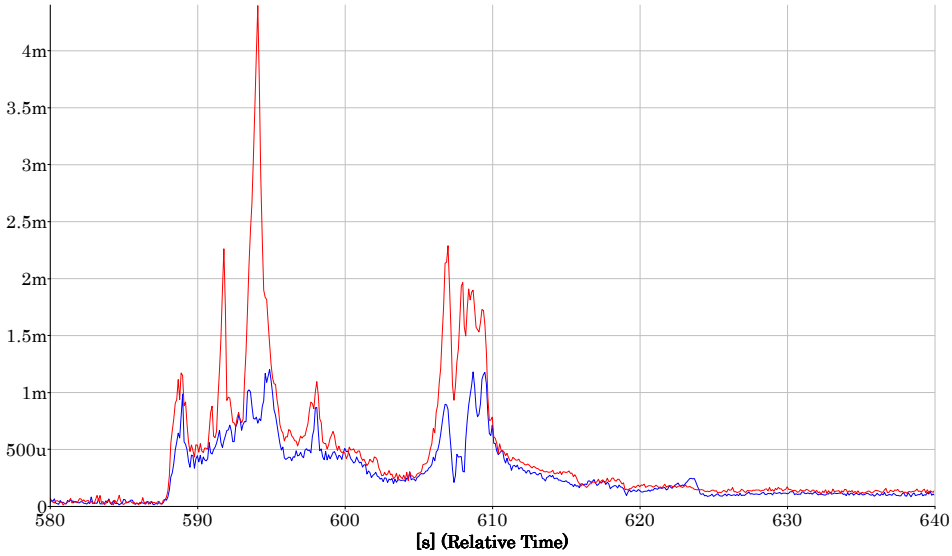

Figure 5.18. Overall vibration values during startup from A31 (red) and A34 (blue)

5.1.3. Steady operation

The dynamic behavior of the turbine under load conditions will be studied in this section. To do so, the excitation of the runner modes will be identified and analyzed from the bearings and compared between partial load and maximum load. After that, the frequency ranges corresponding to the different runner modes will be determined. The overall vibration levels of every frequency band will be obtained to see how the excitation of the runner modes changes with the power delivered by the turbine. These will be analyzed to understand the characteristics of the jet excitation and its repercussion on the structural integrity of the turbine.

The waterfall of the spectra at partial load from position A34 is showed in Figure 5.19. In the lower range of frequencies, typical excitations from the electrical grid can be seen at 100 Hz and harmonics. The main excitation comes from the jet impingement at the bucket passing frequency (220 Hz) and its first harmonic at 440 Hz.

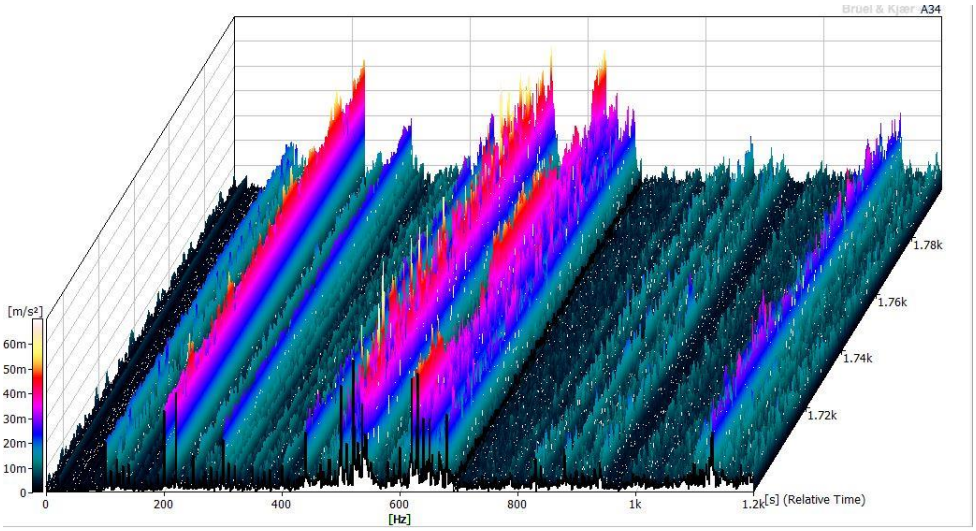

Figure 5.19. Spectra waterfall from position A34 of Arties at minimum load

The frequencies between 10 and 300 Hz have been studied as velocity from position A31 at partial and full load, as seen in Figure 5.20. Looking at the top image it can be seen that the vibration is dominated by the constant excitation at the frequency of rotation f_f (10 Hz), the bucket passing frequency f_b (220 Hz), the pole passing frequency f_p (100 Hz) and the corresponding harmonics. Moreover, the periodic excitation of the rotor bending modes can be seen between 100 and 130 Hz. This vibration fluctuates over time, what means a different frequency is excited at every instant, corresponding to the different variants of the same bending mode.

When working at full load (bottom image), the vibration levels increase. The frequencies excited are the same as the partial load operation, but the magnitudes of each one of them vary in different ways. The unbalance force at f_f doesn't increase, since its value only depends on the velocity and the unbalanced mass in rotation, which are the same as in partial load.

However, the frequencies that are related to the force of the jet (bucket passing frequency and turbine modes) are higher. The frequencies around 30 and 120 Hz stand out due to the excitation of two types of rotor bending modes, which have more vibration for the increased force of the jet. The bucket passing frequency also increases at full load operation.

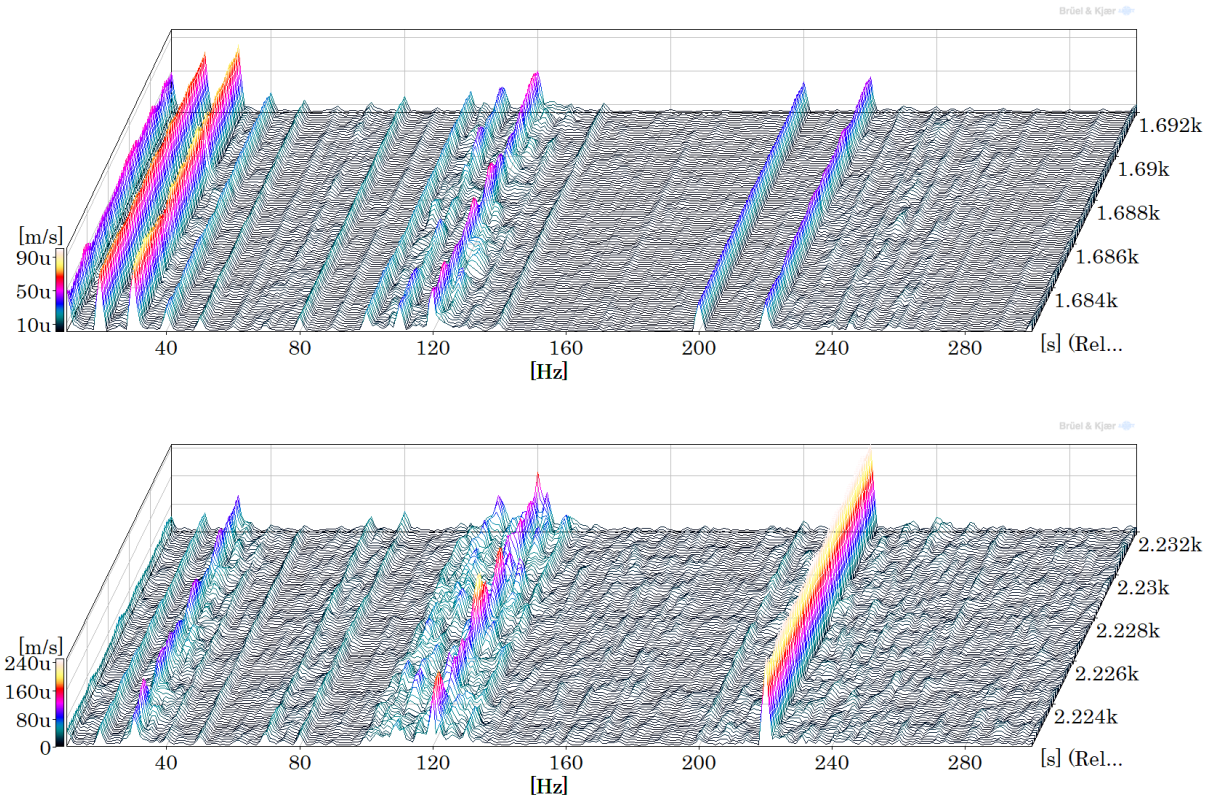

Figure 5.20. Spectra waterfall from position A31. Top, partial load and bottom, full load

The vibration in the range between 10 and 400 Hz has been represented as acceleration in Figure 5.21 as a wavelet. Wavelets provide a high resolution in the time domain and are useful to detect the pulses of an excitation at a certain frequency, what cannot be seen with FFT. In the figure, it is clearly seen that the main excitations at 120 and 220 Hz are not constant over time and have a pulsating frequency. Demodulating the ranges 119-121 Hz and 219-221 Hz, pulses at 10 and 20 Hz are obtained, respectively. Since these can be related to the rotational speed of the turbine, this means that at every turn some parts of the runner vibrate more than others, what causes the vibration to increase.

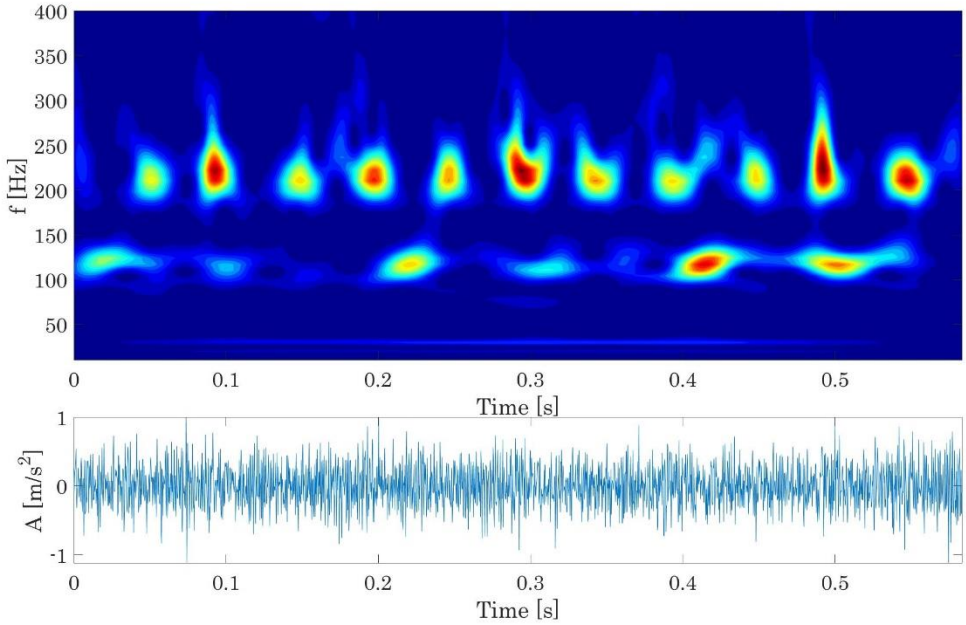

Figure 5.21. Wavelet representation of the signal from A31 at partial load

Next, the modes of the runner excited during operation are discussed. To do so, the waterfall from position A31 has been represented in acceleration for the different frequency bands.

The range of the axial modes has been studied from position A31 at partial load and full load (Figure 5.22). A periodic excitation can be seen at 440 Hz, which corresponds to the second harmonic of f_b. The range of the axial modes is clearly identified in the picture between 460 and 550 Hz. The largest vibration amplitude, though, is gathered between 500 and 550 Hz, where the bucket dominated modes are located. Comparing these values to the natural frequencies of the still machine, it can be seen that the frequencies have increased around 2% when in operation. What can also be observed from the waterfall is that the frequencies don't have any significant change with the increase of load.

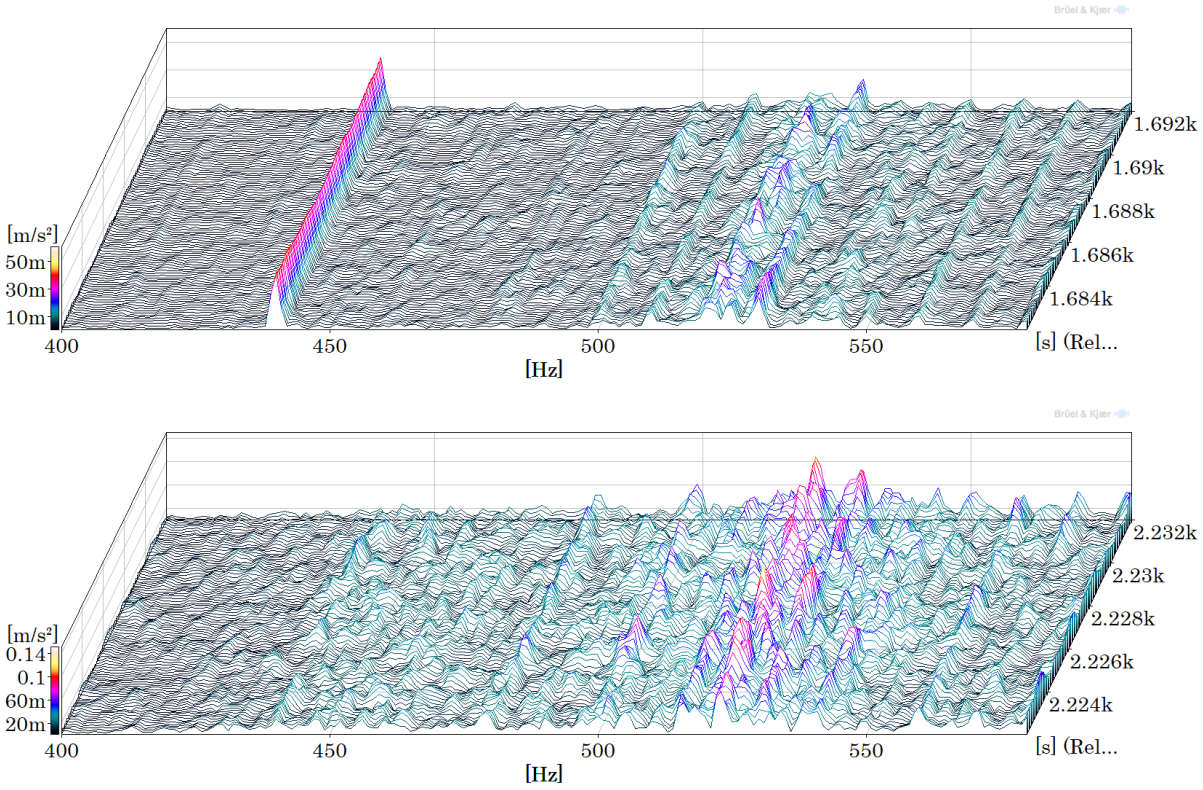

Figure 5.22. Waterfall in the band of the axial modes at minimum (top) and maximum (bottom) load from position A31

The axial frequencies excited during operation have been compared to the frequencies obtained from the impact tests in the still machine, as shown in Figure 5.23. It can be seen that, as during the impact tests, higher frequencies are more excited by the water jet than lower frequencies. This is because the energy required to excite the bucket-dominated modes is lower than disk-dominated modes. The maximum natural frequency when the machine is running is found at 544,5 Hz in partial-load operation and at 543,5 Hz in full-load operation. This suggests that the increase in the discharge increases the added mass in the buckets, and this leads to a small decrease in the frequencies. When compared to the still machine, it is clear that the maximum frequency, which is found at 534,5 Hz, has increased due to the effect of rotation.

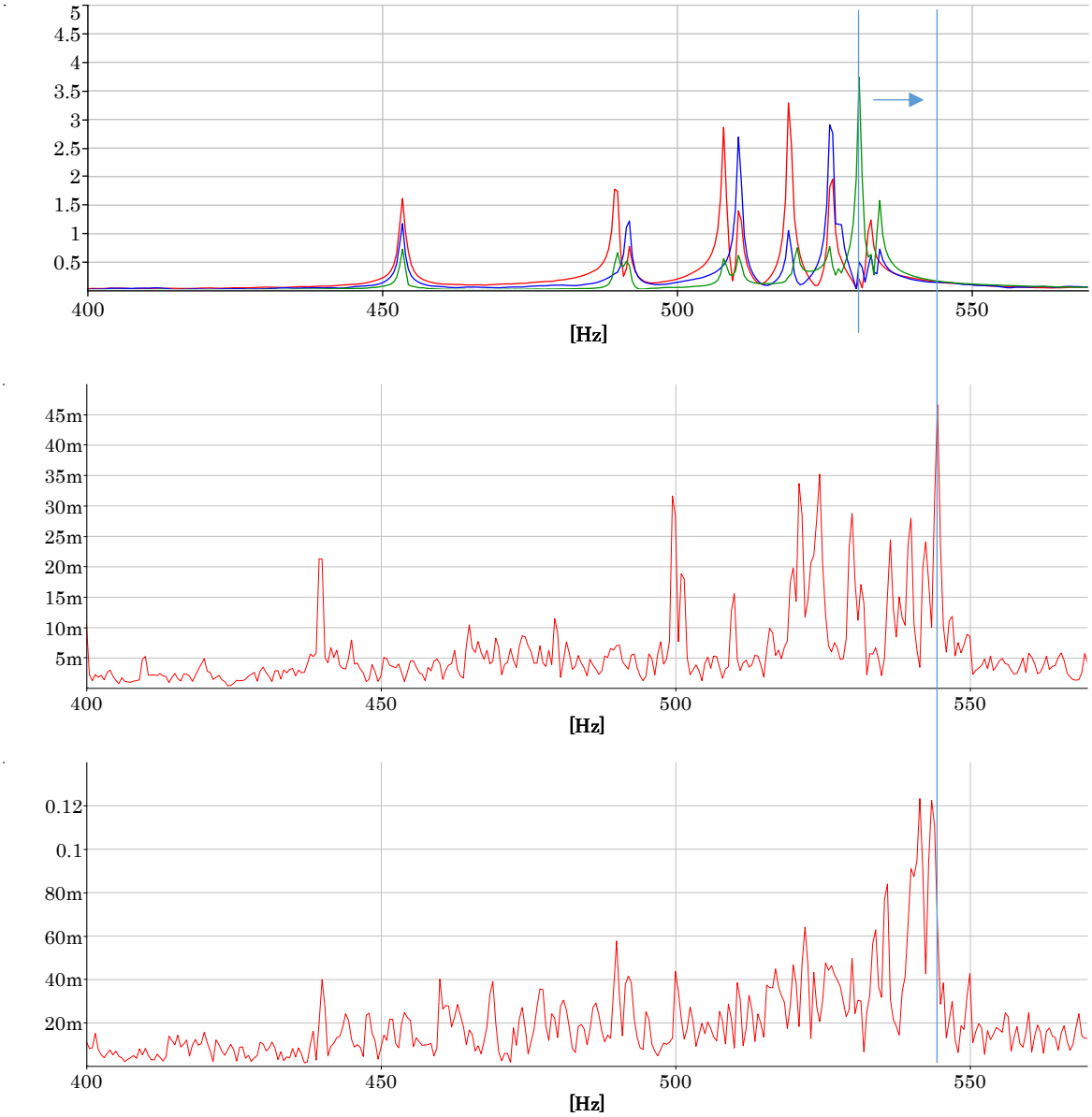

Figure 5.23. Comparison between axial frequencies in the machine still (top), during part-load operation (middle) and full-load operation (bottom)

The tangential modes and the axial c-ph. modes have been analyzed from position A31 and represented in Figure 4.25. These are clearly excited between 600 and 700 Hz. Even though the main excitations are found in the harmonics of the frequency of rotation, the frequencies excited at every instant are different. In this case, it is difficult to discern the limits between the different types of modes. Thus, it is not possible to quantify the variation of the frequencies due to rotation and added mass.

The range of the tangential modes has been represented as a wavelet waterfall in Figure 5.25. As seen previously, the excitation is not constant and shows many fluctuations, possibly due to differences in the excitability of the buckets.

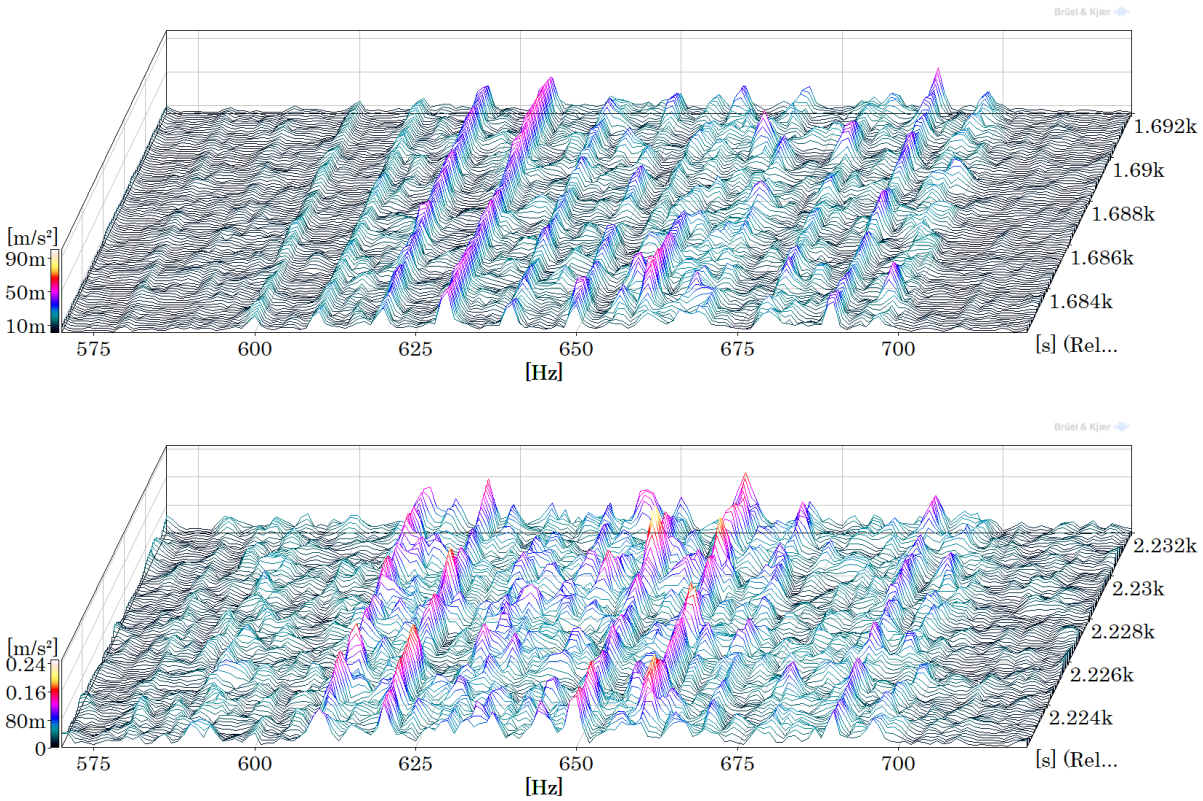

Figure 5.24. Excitation of tangential and axial c-ph. modes at minimum (top) and maximum (bottom) load from position A31

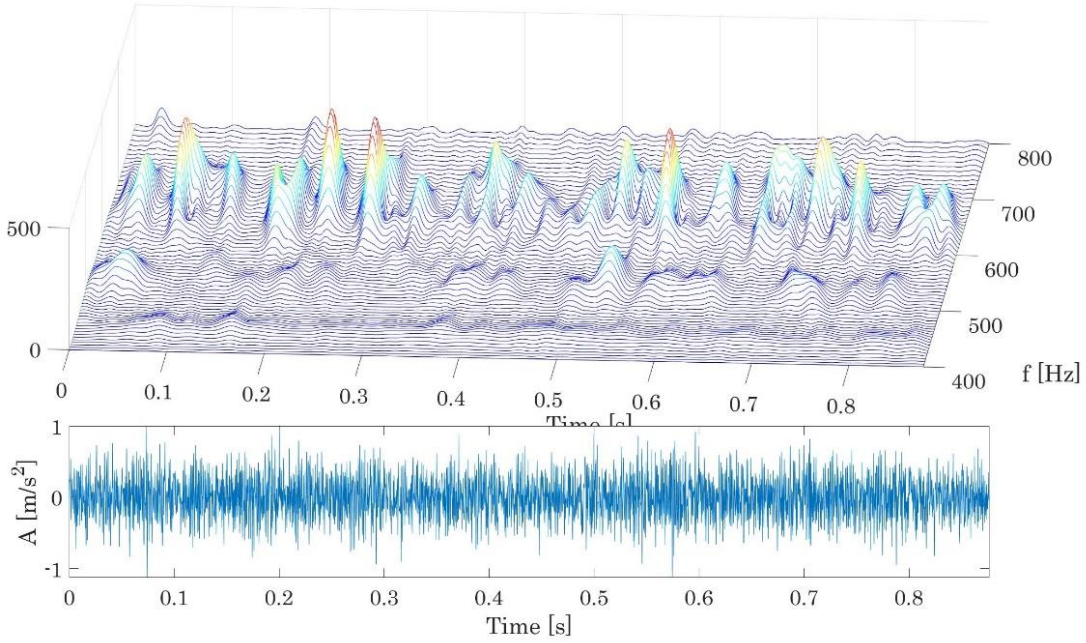

Figure 5.25. Wavelet representation of the tangential modes excited from A31

To analyze the excitation of the radial modes, the signal has been represented between 900 and 1300 Hz in Figure 5.26. The vibration in this range is lower than for other modes. It is worth noting, though, that at full load there is a large excitation at 1100 Hz, which corresponds to the fifth harmonic of the bucket passing frequency. The amplitude of vibration stands out considerably more in comparison to the part load operation. Considering that some radial natural modes are near this frequency, it can be said that the harmonic of the jet is exciting one mode, which due to the effect of added mass, has changed its value.

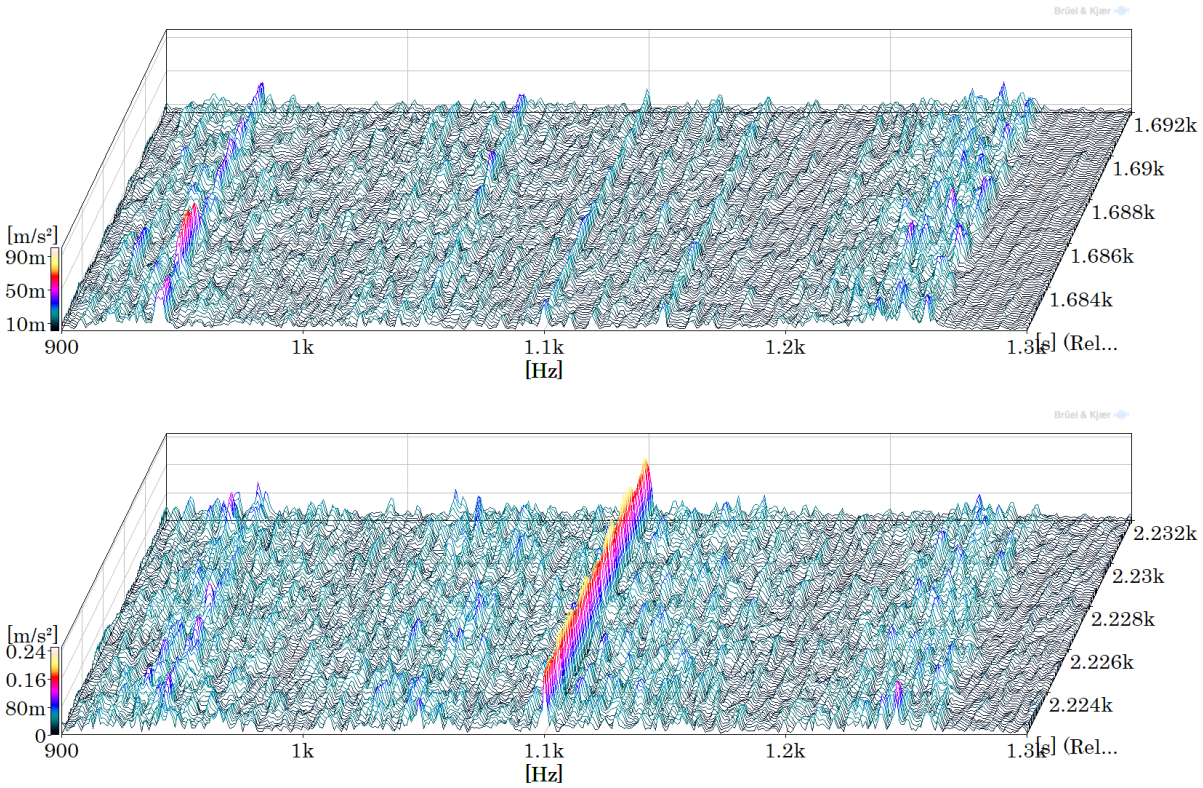

Figure 5.26. Excitation of radial modes at minimum (top) and maximum (bottom) load from position A31

According to Standards, RMS velocity values between 2 and 100 Hz must be used to evaluate the vibration of a machine. The overall RMS velocity levels of the turbine at part load and full load have been represented from each monitoring location in Figure 5.27. The values have been obtained every 100 ms. At both operating conditions the vibration is larger from axial monitoring positions than from radial positions. Also the fluctuation is higher. The average values from each position have been listed in Table 5.1. At full load, the vibration values and the fluctuation increase, especially from axial vertical position A38.

Table 5.1. Overall RMS velocity values of Arties from different monitoring positions

Location	RMS Partial load [mm/s]	RMS Full load [mm/s]	Ratio
A31	0,170	0,430	2,53
A34	0,112	0,402	3,6
A35	0,235	0,710	3,02
A38	0,430	1,020	2,37

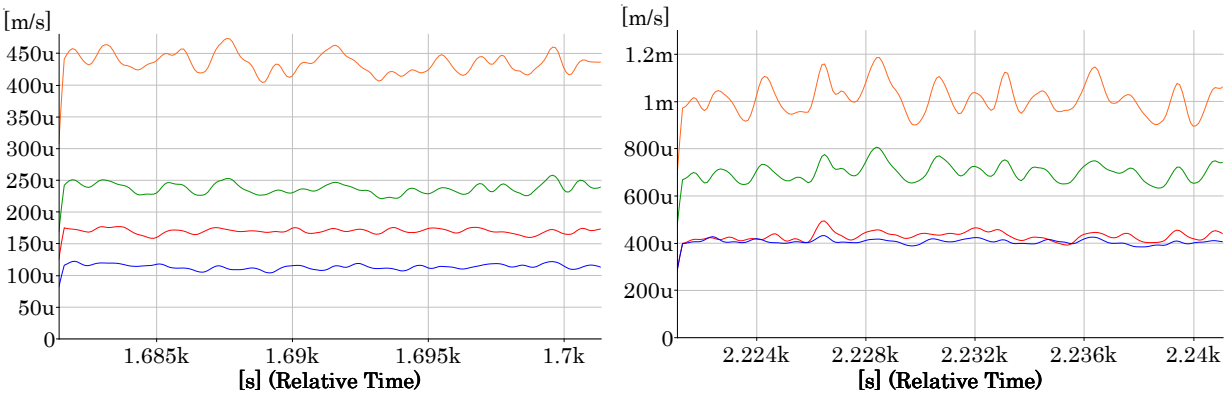

Figure 5.27. Overall RMS velocity values from positions A31 (red), A34 (blue), A35 (green) and A38 (orange) at partial load (left) and full load (right)

Two frequency bands have been selected to see the energy used to excite each type of turbine mode, according to the information obtained from the spectra. The RMS velocity values have been obtained. They have been represented for the band of the axial modes [480-540 Hz] in Figure 5.28 and for the band of the tangential modes [600-670 Hz] in Figure 5.29. Operation at partial load and at maximum load can be compared. The RMS average values are listed in Table 5.2 and Table 5.3, respectively. It is interesting to see that, even if the global RMS values are low comparatively to other positions, A34 has the best sensitivity to both axial modes and tangential modes.

Table 5.2. Averaged RMS values for the axial modes from every position at partial and full load

Location	RMS Partial load [mm/s]	Ratio to total energy	RMS Full load [mm/s]	Ratio to total energy
A31	0,014	8,2%	0,060	14%
A34	0,032	28,6%	0,084	21%
A35	0,008	3,4%	0,028	4%
A38	0,017	4%	0,070	6,9%

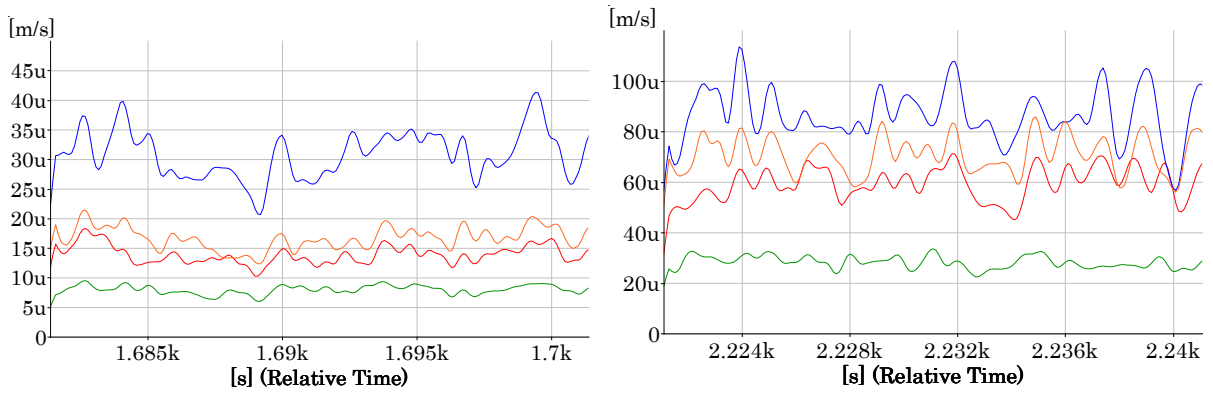

Figure 5.28. Overall RMS velocity values in the band of axial modes from positions A31 (red), A34 (blue), A35 (green) and A38 (orange) at partial load (left) and full load (right)

Table 5.3. Averaged RMS values for the tangential modes from every position at partial and full load

Location	RMS Partial load [mm/s]	Ratio to total energy	RMS Full load [mm/s]	Ratio to total energy
A31	0,028	16,5%	0,108	25%
A34	0,028	25%	0,128	31,8%
A35	0,028	11,9%	0,092	13%
A38	0,016	3,7%	0,062	6%

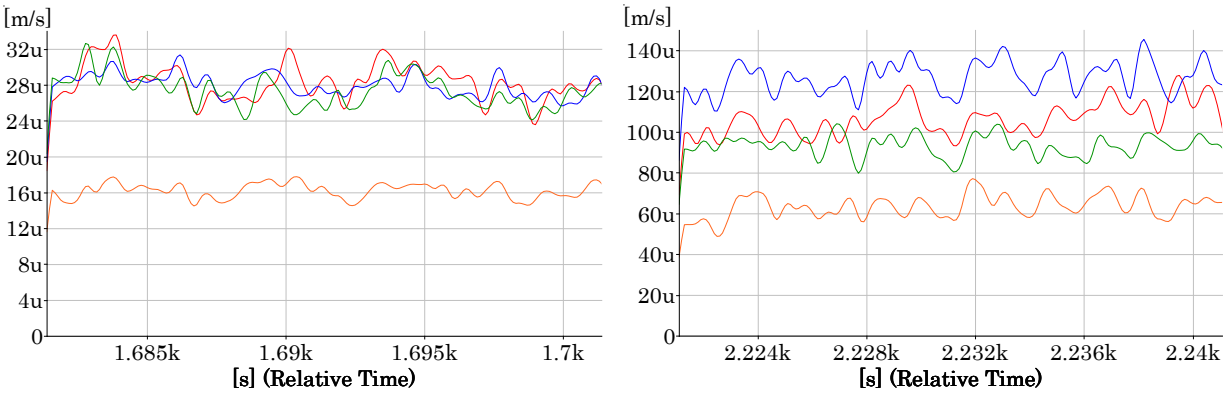

Figure 5.29. Overall RMS velocity values in the band of tangential modes from positions A31 (red), A34 (blue), A35 (green) and A38 (orange) at partial load (left) and full load (right)

5.2. Dynamic behavior of Moncabril PT

In this section the operation of the Pelton turbine of Moncabril has been studied. The setup of this machine is different from Arties because there is only one runner and this is operated by two nozzles. Moreover, the directions of the jets are different. The vibrations of the machine were recorded during the startup and at different operating loads, from minimum to maximum. In this case, two transients take place, one from the entrance of the first jet and one for the second jet. Both transients will be studied to see the effect they have on the vibration of the buckets. After that, the vibration at minimum and maximum load will be analyzed to check the effects of the load on the runner modes and the vibration.

5.2.1. On-site measurements

The instrumentation used in the Pelton turbine of Moncabril was the same used in the impact tests, described in Chapter 3. To carry out the tests in operation, four accelerometers were placed on the turbine bearing in two radial positions and two axial positions: A13, A14, A16 and A17. The vibration recorded by accelerometer A14 during the whole test is showed in Figure 5.30. The turbine was set in motion by opening one of the nozzles (1). After achieving the nominal speed of 600 min^{-1}, the machine was operated at Speed No load during approximately 5 minutes. During this time, the generator was excited magnetically (2). At (3), the machine was connected to the electrical grid and operated at the minimum load of 1 MW. After a period of time, the load was increased to 3 MW, and then to 4,8 MW. Before increasing the load to 6 MW, the second nozzle was opened. This can be seen in the time signal by the increase of the vibration levels (4). After that, the load was increased to 9 MW, and, finally, to maximum load, 12 MW.

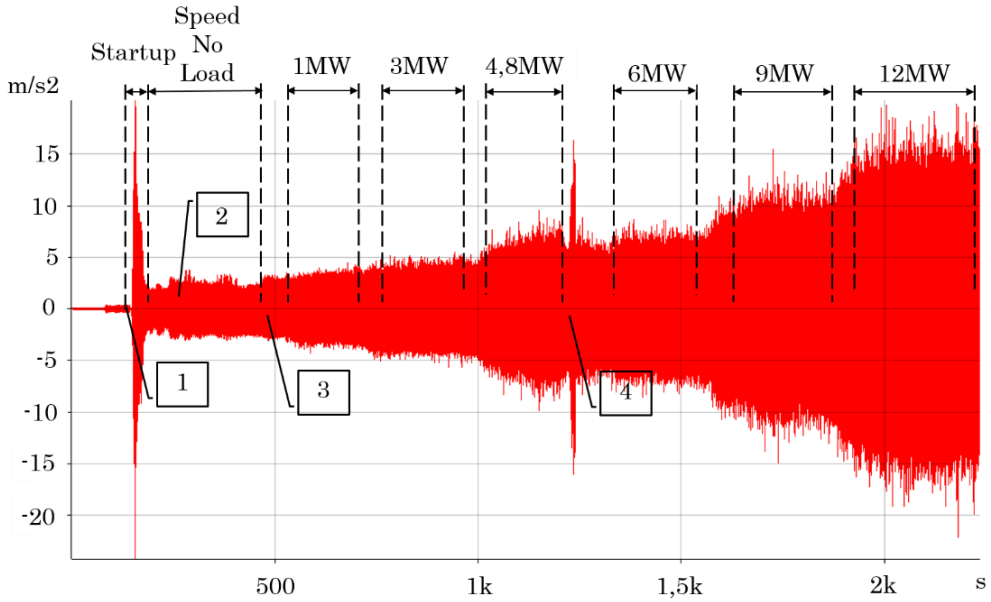

Figure 5.30. Time signal of the whole test from position A14

5.2.2. Startup transient

The acceleration time signal of the startup transient measured from position A14 is showed in Figure 5.31. At the start of the excitation, the first impact of the water particles can be identified. The levels increase when the machine starts rotating due to the resonance with different turbine modes, and then decreases as it approaches its nominal speed. The spectra waterfall from the same position is in Figure 5.32. The range of the rotor modes (lower frequencies) and the runner modes (higher frequencies) can be discerned.

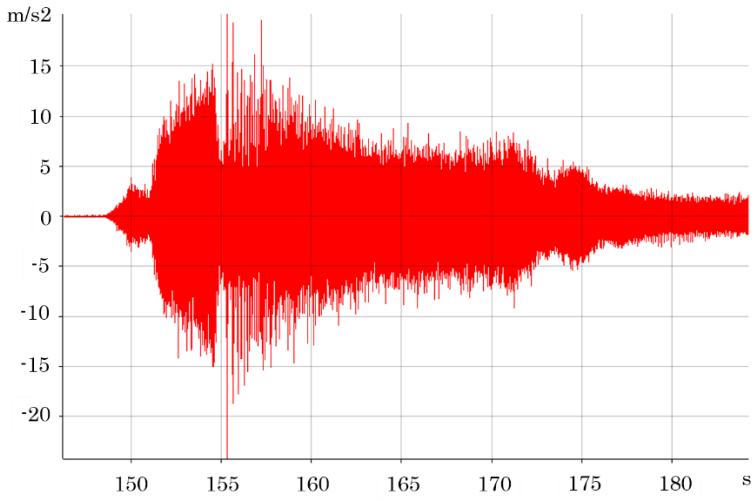

Figure 5.31. Time signal during the startup transient from A14

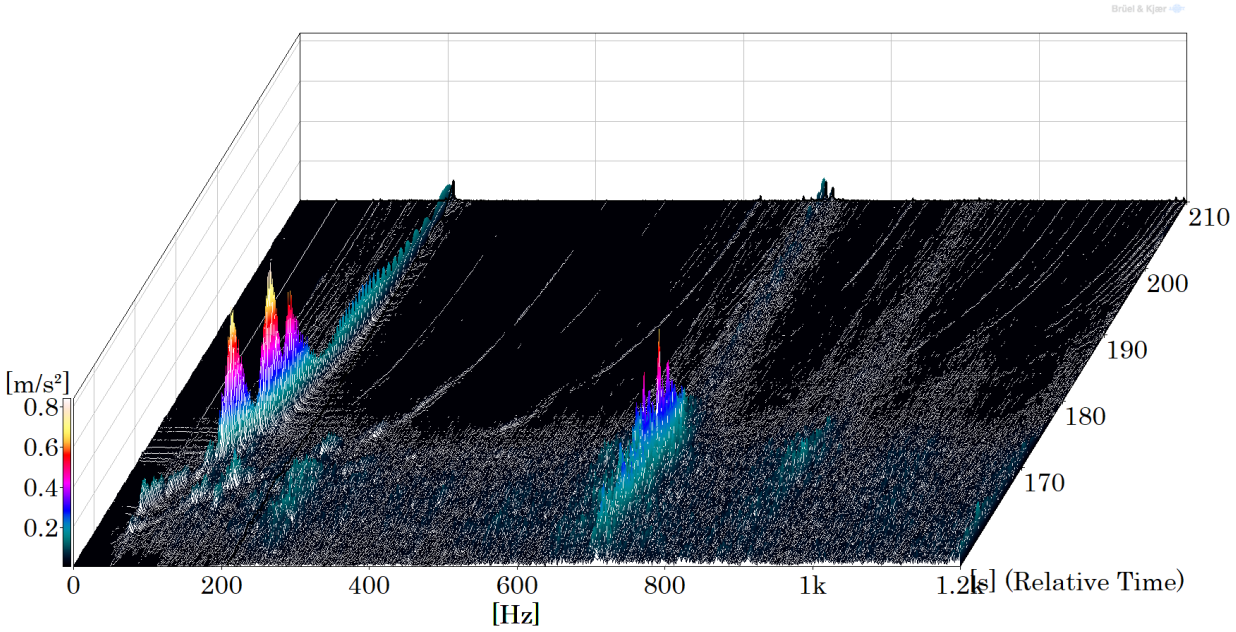

Figure 5.32. Waterfall of the startup transient from position A14

First, the initial impact of the water particles will be studied in the range of the runner modes. This is the first and purest excitation of the runner modes during operation, and from this, the modes of the buckets can be identified.

In Moncabril Pelton turbine, the most excited frequencies are found in the range of the tangential modes, as seen in Figure 5.32. The axial modes, unlike the case of the machine in Arties, don't show a large excitation after the first impact. Taking a closer look at the first seconds between 680 and 770 Hz, several peaks can be identified (Figure 5.33), which correspond to the tangential modes in phase and in counter-phase of the runner. The values of the frequencies are very similar to the still machine, and the highest peaks are detected from the radial vertical position A14, which was proved to be the best monitoring location during the impact tests. It can also be seen that the tangential in phase modes are more excited than the torsional modes.

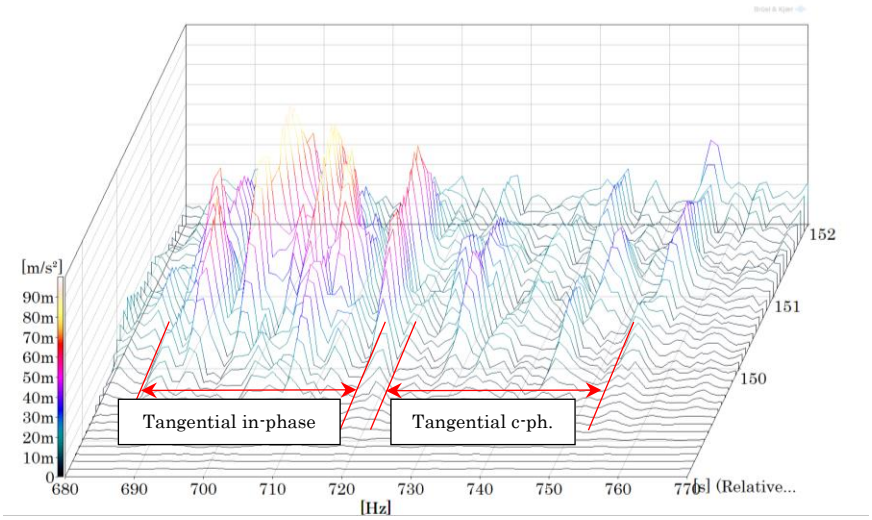

Figure 5.33. Tangential modes excited after the first impact

Compared to the Pelton turbine in Arties, the axial counter-phase modes in Moncabril appear at much higher frequencies than the tangential modes, and thus the limits can be more easily discerned. In Figure 5.34, the range between 860 and 940 Hz is showed. It is proved that the axial counter-phase modes are excited in the first impact, and that the frequencies are the same as the still machine. Two main frequencies are excited at 903 and 910 Hz, which correspond to the frequencies of the buckets impinged by the jet. The radial vertical position A14 has the highest sensitivity to that vibration.

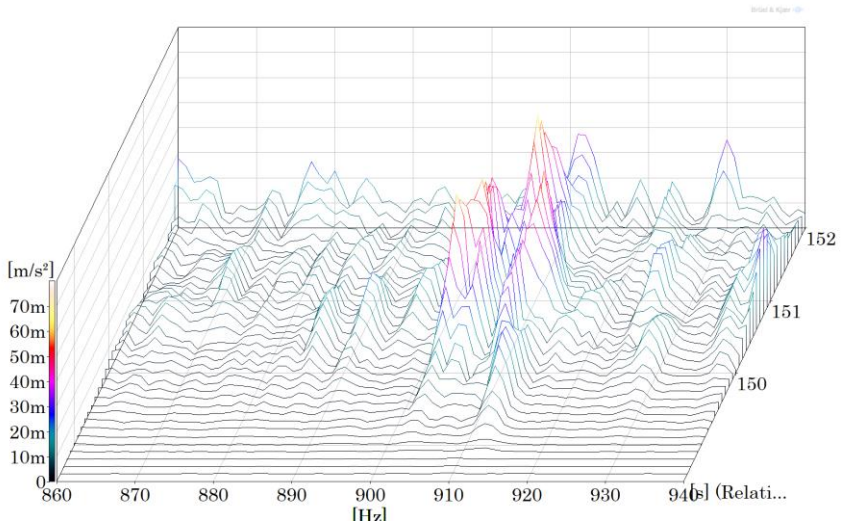

Figure 5.34. Axial counter-phase modes after initial impact

During the first seconds of the machine speed-up, the load applied on the buckets excites many modes. Since the rotational speed is much lower than the nominal speed, the jet enters the buckets with a relative velocity that is still too fast, and the load applied is high. During this time, the vibration is also mixed between the different buckets.

The lower range of frequencies during startup has been analyzed from position A13 (Figure 5.35). The increasing bucket passing frequency can be clearly seen. Rotor modes are excited by the f_b at 40 Hz, 70 Hz, 120 Hz and 155 Hz.

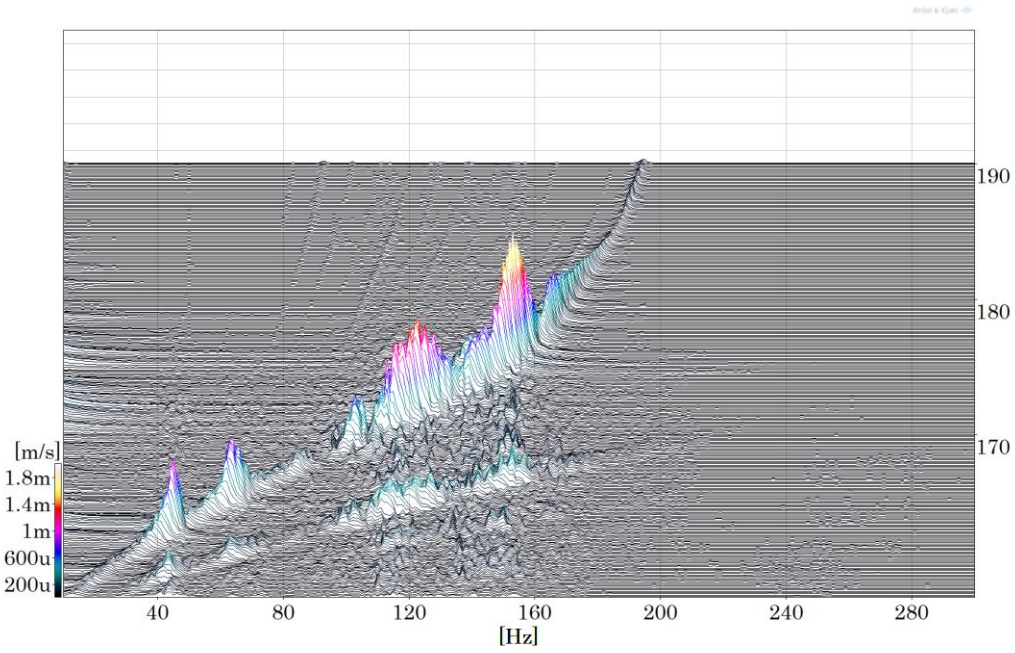

Figure 5.35. Startup from position A13

Next, the higher range of frequencies is evaluated. The most excited runner modes are the tangential. These have been investigated from the monitoring position A14 (Figure 5.36) because of their better transmission. The vibration is mixed between many different frequencies that correspond to the natural frequencies of every bucket. The largest excitation takes place during approximately 10 seconds and then decreased considerably.

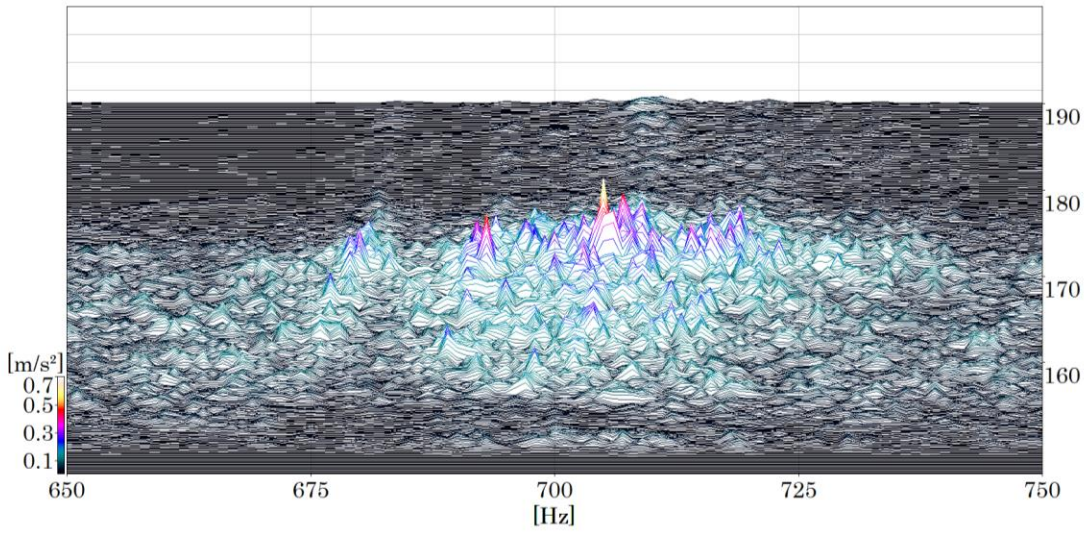

Figure 5.36. Tangential modes from position A14. Bottom, start of speed-up

At the end of the transient, the vibration is considerably reduced, but due to the harmonics of the rotation frequency, some tangential modes are still lightly excited, as seen in Figure 5.37. The axial modes have also been investigated from position A14 (Figure 5.38). The range of axial frequencies can be seen at the end of the transient between 613 and 627 Hz, which is similar to the results obtained in the still machine.

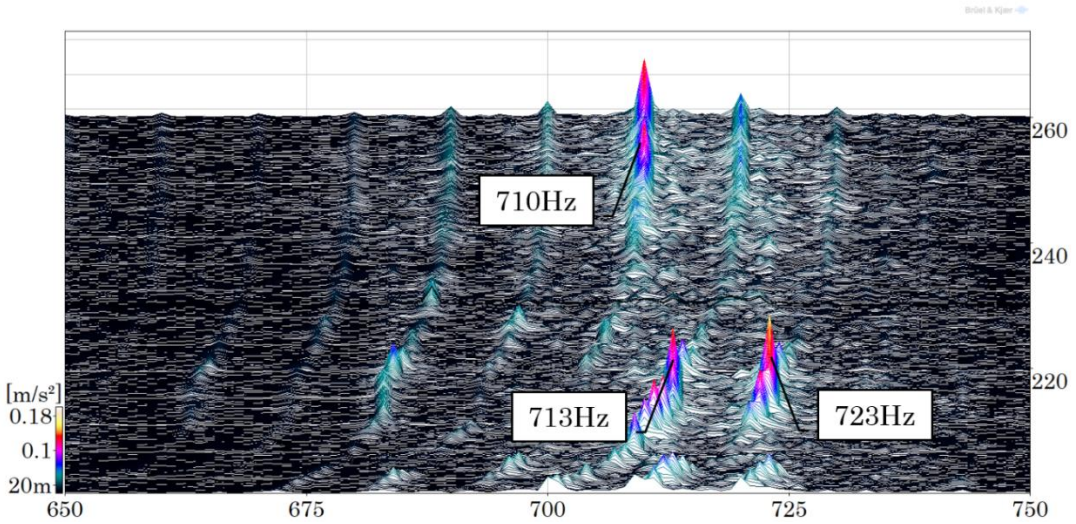

Figure 5.37. Tangential modes at the end of the transient

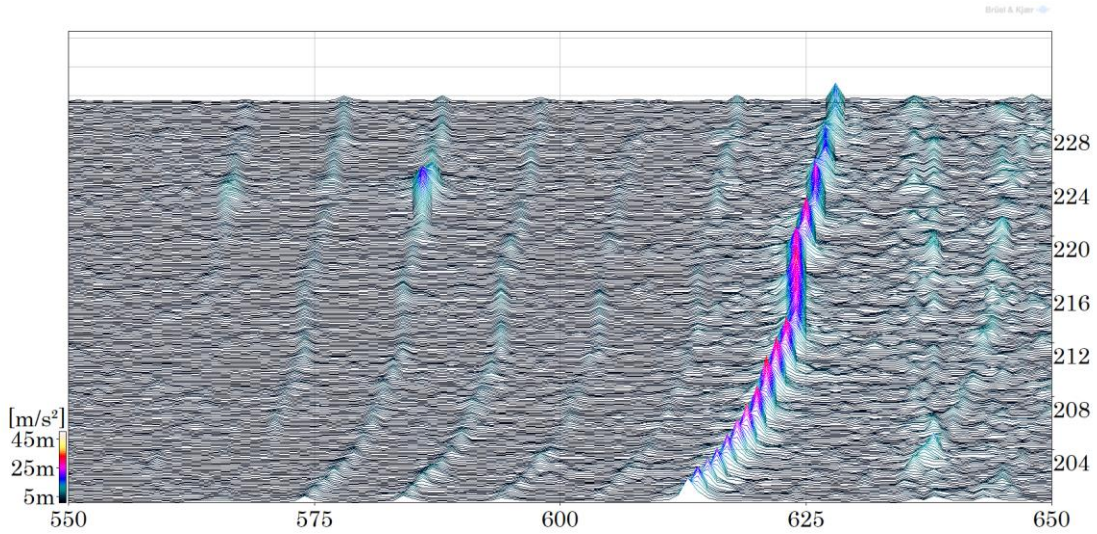

Figure 5.38. Axial modes at the end of the transient

The effect of the transient on the structure can be evaluated from the velocity values of the vibration (see Figure 5.39). The horizontal radial position A13 shows the largest vibration levels. The maximum peak-to-peak velocities reach the value of 14 mm/s. In these instants, rotor bending modes are excited by the bucket passing frequency. To assess the peril of this situation on the structure, the stress distribution must be studied by numerical models and the most affected zones must be determined.

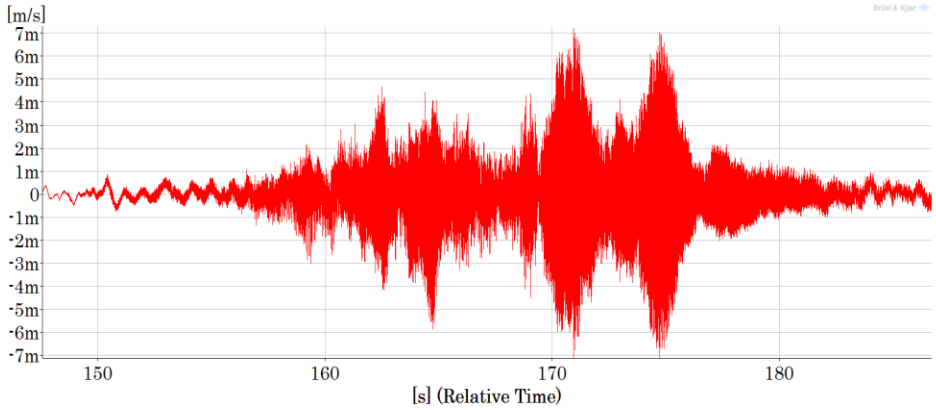

Figure 5.39. Overall velocity vibration levels from A13

5.2.3. Second jet transient

When the machine goes from 4,8 to 6 MW, the second nozzle is opened. This causes a small transient that will be evaluated in this section. The spectra waterfall from position A14 is represented in Figure 5.40. The top figure encompasses the lower frequency range [10-300 Hz] and the bottom figure the higher frequency [600-950 Hz]. After the impingement, all the rotor modes found during the startup transient are excited, especially around 120 and 155 Hz. Above 600 Hz, all the runner modes are excited, especially the tangential modes.

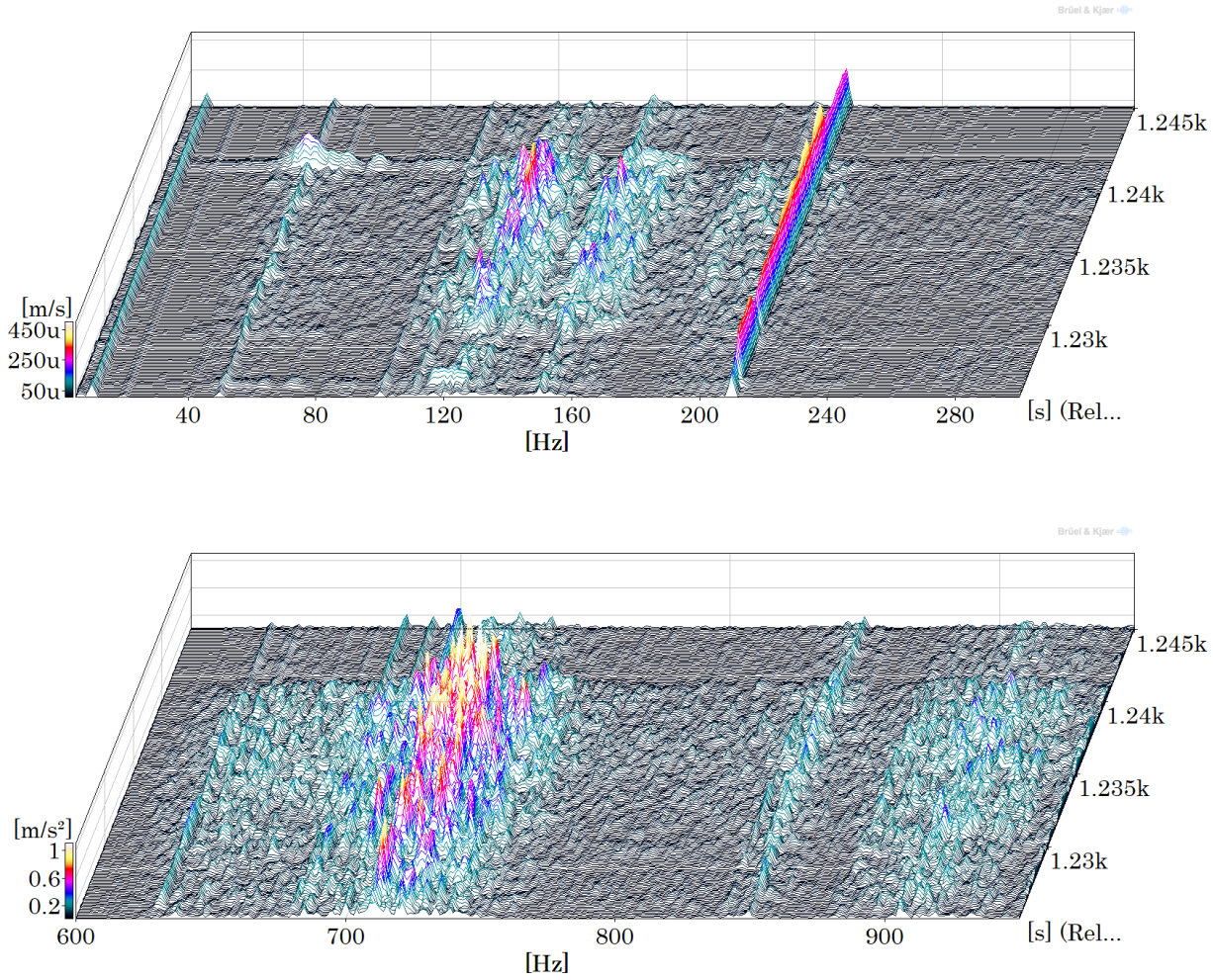

Figure 5.40. Spectra waterfall from A14 after the impingement of the second jet

The RMS velocity values during the second jet transient have been represented in Figure 5.41. The water causes a large increase in the vibration, what is especially sensed by the vertical radial A14 accelerometer. However, the values don't surpass the standardized limits of 3,1 mm/s. Even so, it would be good to analyze the effect of this transient due to the excitation of the tangential modes excitation. Another interesting thing to see in the figure is that the overall values are lower when both jets are operating at 6 MW than when a single

jet is operating at 4,5 MW. The machine is thus more balanced with both jets operating and this causes less vibration, even if the load is larger.

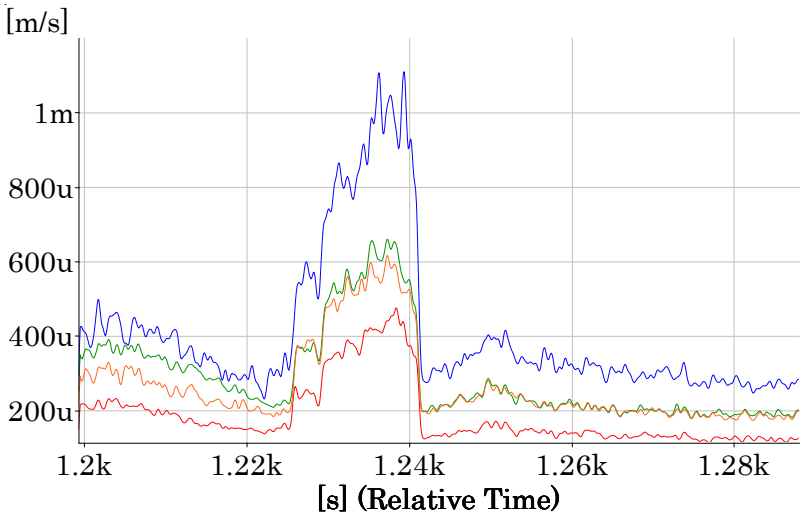

Figure 5.41. Overall RMS velocity values during second jet transient

5.2.4. Steady operation

The dynamic behavior of a Pelton turbine is ruled by the modal behavior of the structure and by the excitation coming from the various forces that are applied to them. These are difficult to predict, especially the ones coming from the jet. In this section, the steady operation of the Moncabril turbine has been studied. The vibration while operating at minimum load (1 MW) and maximum load (12 MW) has been analyzed.

First, the lower frequency range has been evaluated. In Figure 5.42, the spectra waterfall between 10 and 300 Hz is represented for both operating conditions. The main excitations are to be seen at the rotating frequency (f_f=10 Hz) and at the bucket passing frequency (f_b=210 Hz). The corresponding harmonics can also be seen. At minimum load, the excitation of the rotor modes is not large compared to the force of the jet. However, when operating at maximum load, the rotor modes are comparatively more excited and the vibration fluctuates more than the minimum load operation.

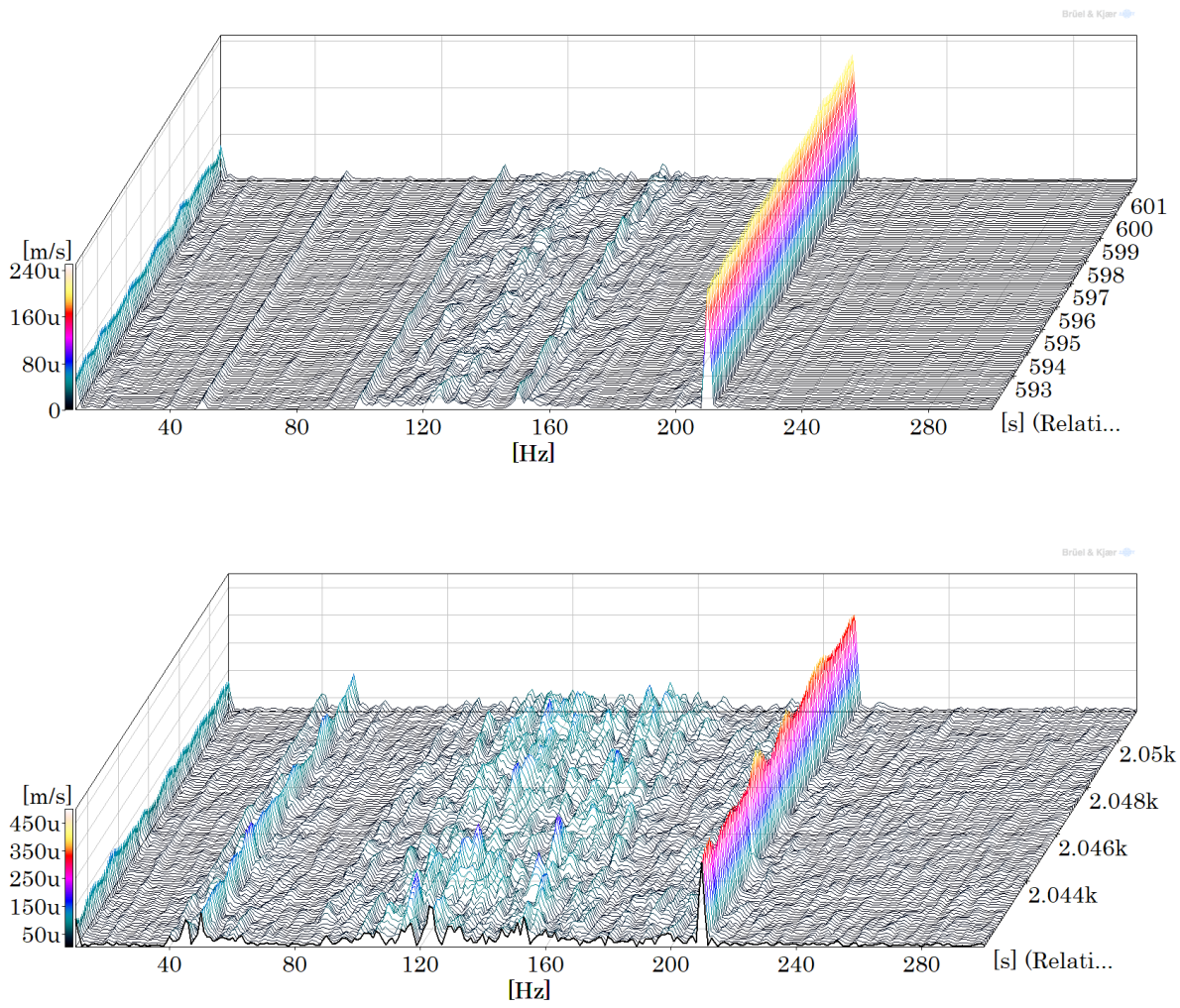

Figure 5.42. Spectra waterfall at minimum (top) and maximum load (bottom) from position A14

Representing the wavelet at the f_b, the vibration certainly has a pulsating behavior, as seen in Figure 5.43. For every turn of the runner (every 0,1 s) there are seven pulses. Doing the representation as a waterfall wavelet from A13 for eight turns of the runner, it is apparent that the fluctuation has a repeating pattern, there being two outstanding pulsations every 0,1 s.

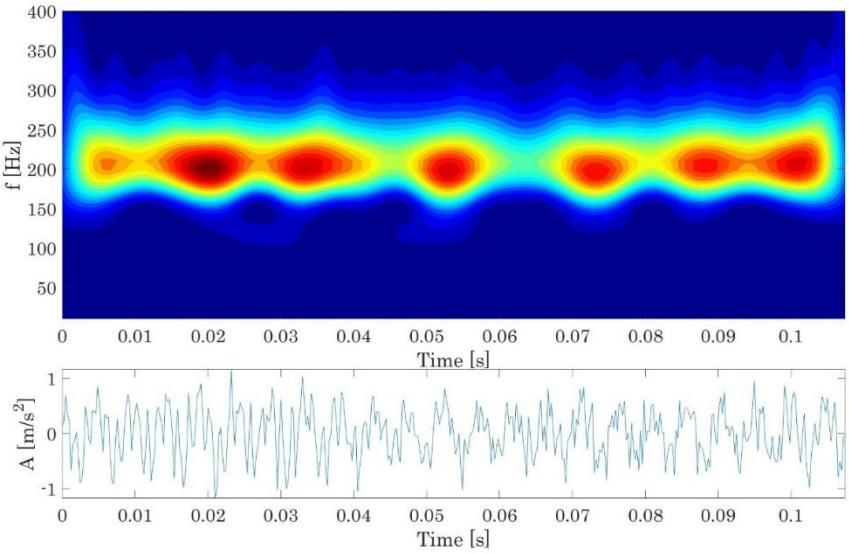

Figure 5.43. Wavelet of the vibration from A14 at the lower frequency range

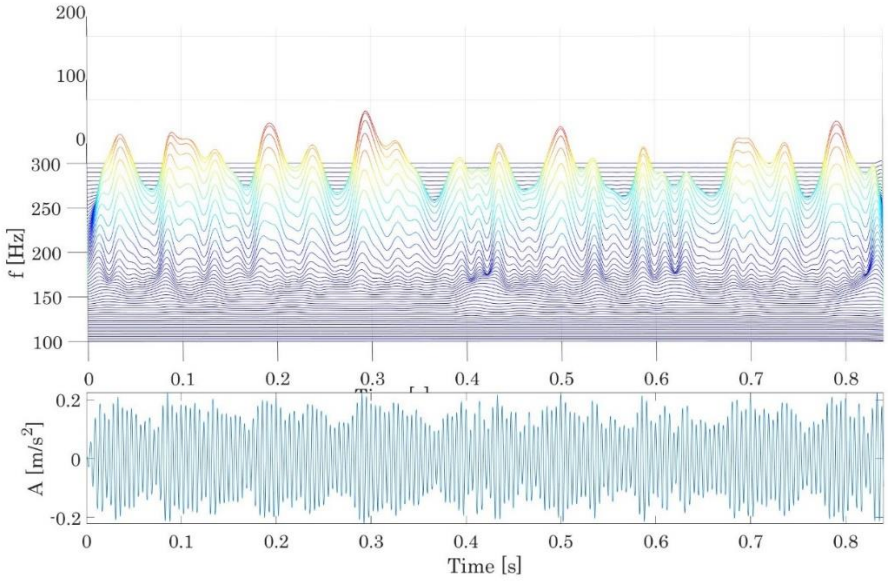

Figure 5.44. Wavelet waterfall of the vibration from A13 at the lower frequency range

Next, the higher frequency range has been represented to evaluate the runner modes. The spectra waterfalls in the ranges of the axial, tangential and axial in-phase modes are illustrated in Figure 5.45, Figure 5.46 and Figure 5.48, respectively. In the range between 400 and 660 Hz, the second harmonic of the bucket passing frequency at 420 Hz and the axial modes are seen. However, the excitation is low and cannot be considered important.

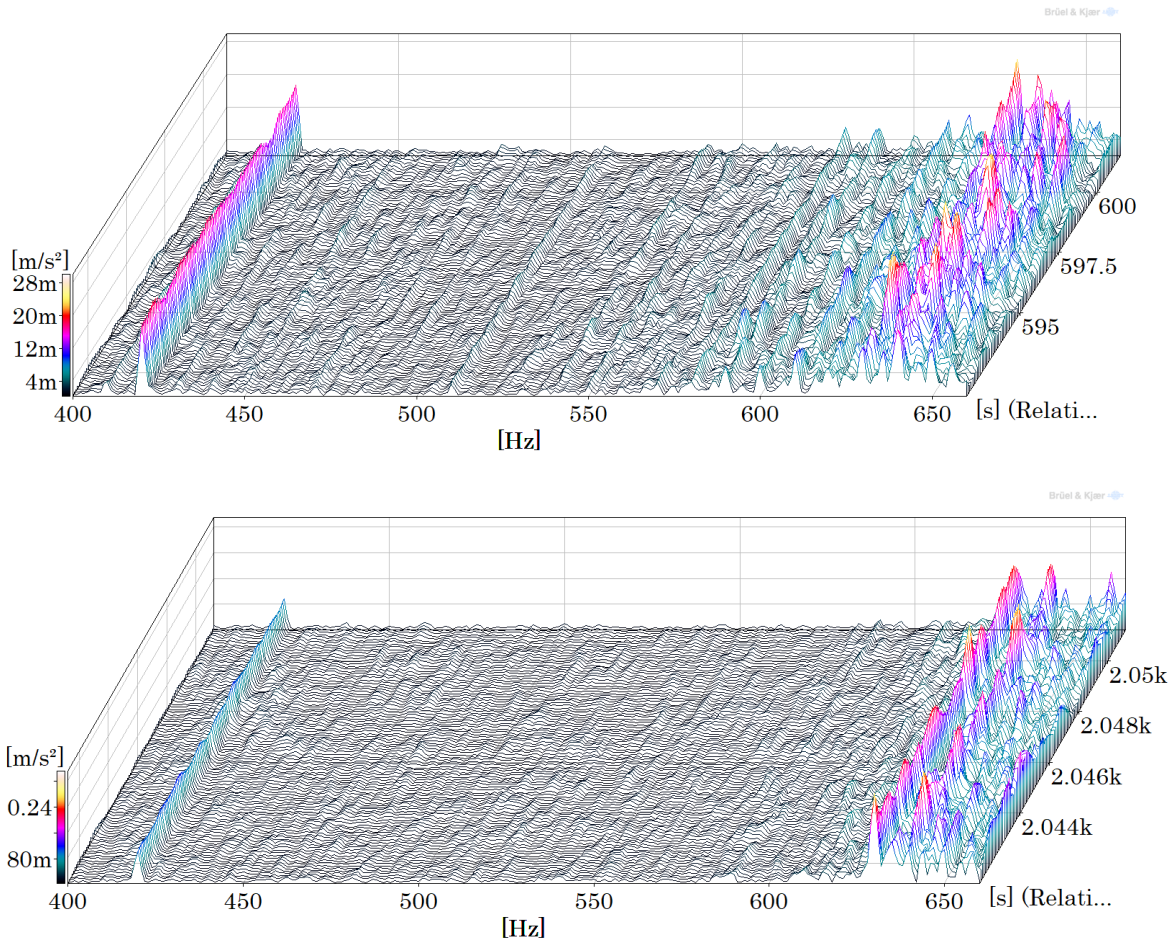

Figure 5.45. Range of runner axial modes at minimum (top) and maximum load (bottom)

The tangential modes are, as expected, the most excited frequencies. At minimum load, one frequency at 710 Hz outstands, but at maximum load the vibration is more spread. Because the range of the tangential modes is close to the tangential counter-phase modes, it is difficult to evaluate if the natural frequencies have increased or decreased with respect to the still machine.

In Figure 5.47, the signal has been filtered between 800 and 100 Hz. It should be pointed out that, apart from the fact that the vibration has a large fluctuation in the range of the axial counter-phase modes, the peaks of vibration appear every three turns of the runner (every 0,3 s).

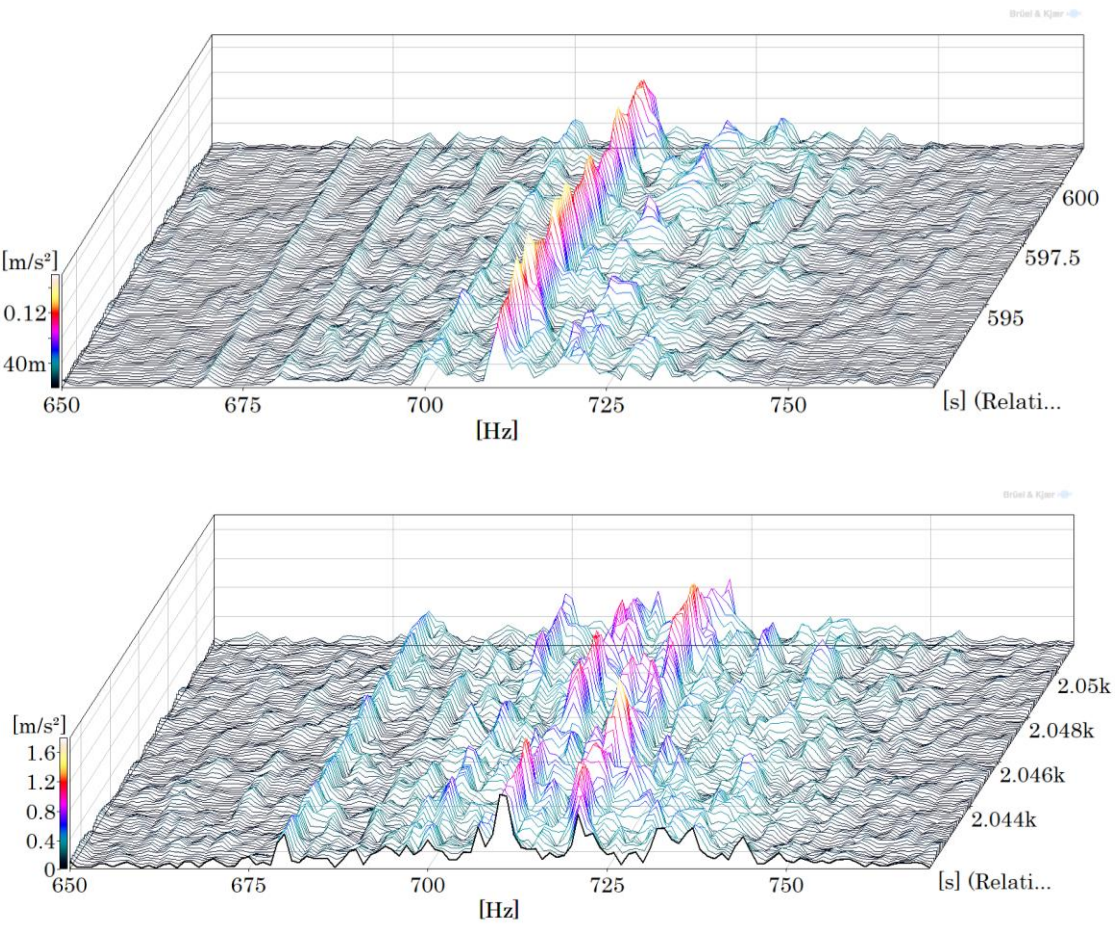

Figure 5.46. Range of the tangential modes at minimum (top) and maximum load (bottom)

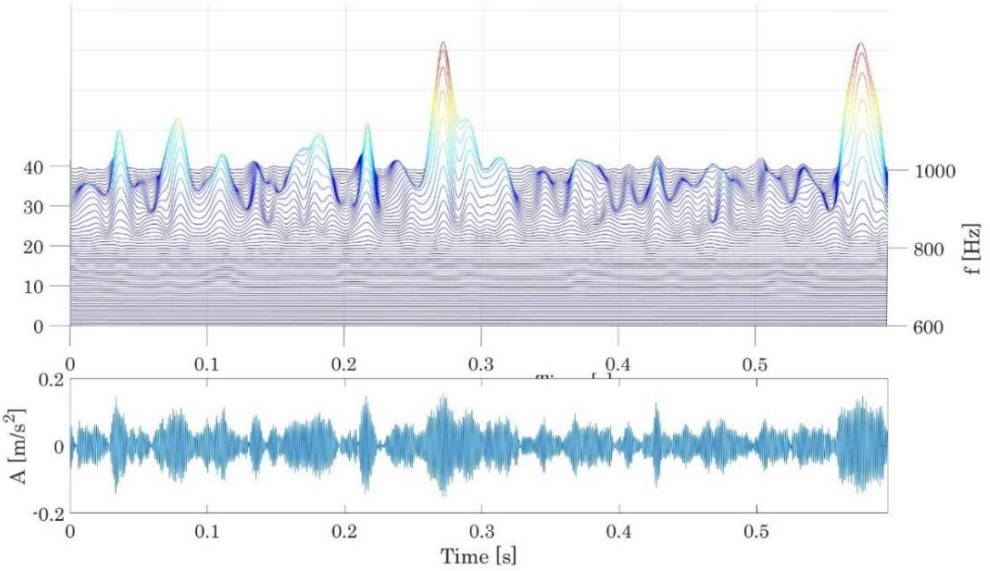

Figure 5.47. Wavelet waterfall in the range 800-1000Hz

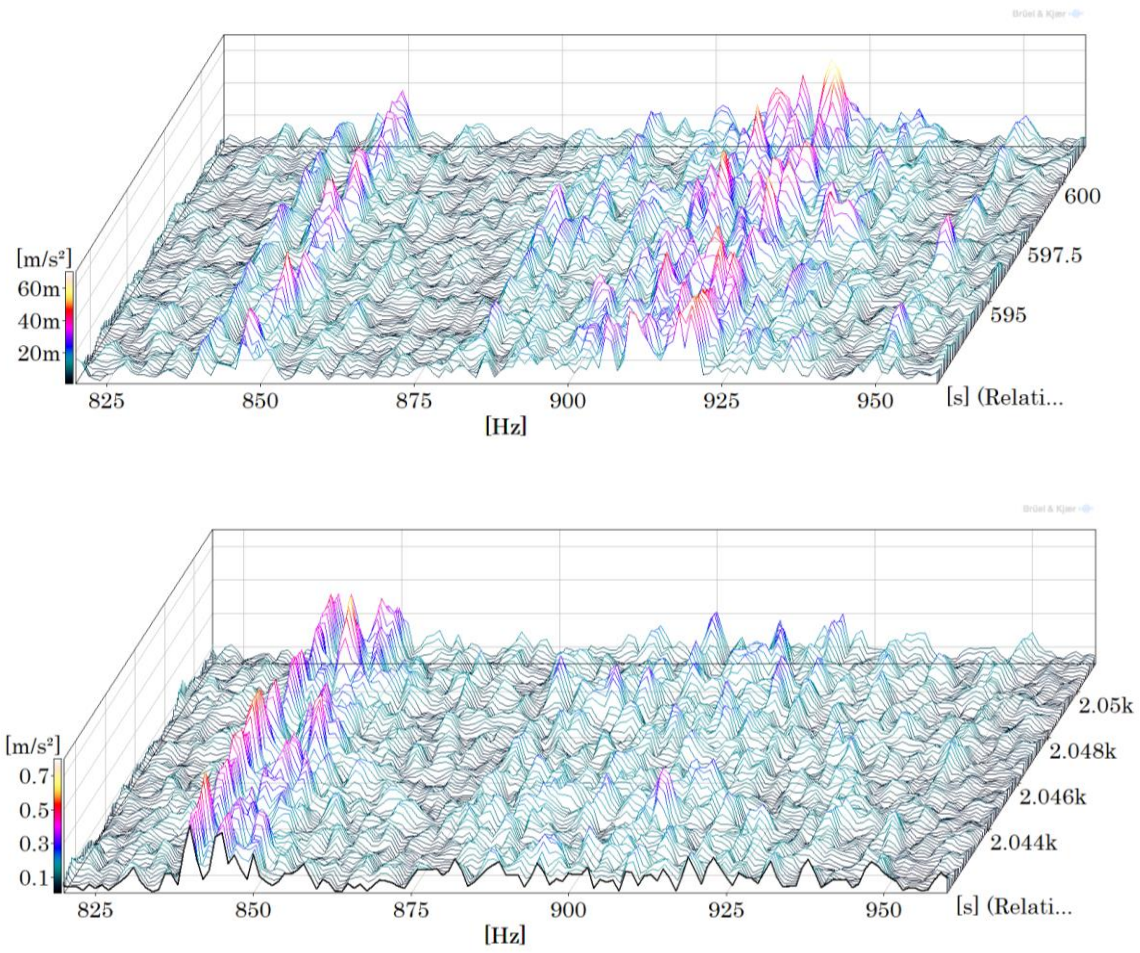

Figure 5.48. Range of the axial c.-phase modes at minimum (top) and maximum load (bottom)

The overall vibration levels are listed in Table 5.4 and are represented in Figure 5.49. The vibration levels in this machine are higher in the vertical position A14, especially when the load is increased and the machine is working with both jets.

Table 5.4. Overall RMS velocity levels from different monitoring positions at minimum and maximum load

Location	RMS 1MW [mm/s]	RMS 12MW [mm/s]	Ratio
A13	0,065	0,316	4,86
A14	0,120	0,920	7,67
A17	0,124	0,486	3,92
A16	0,114	0,436	3,82

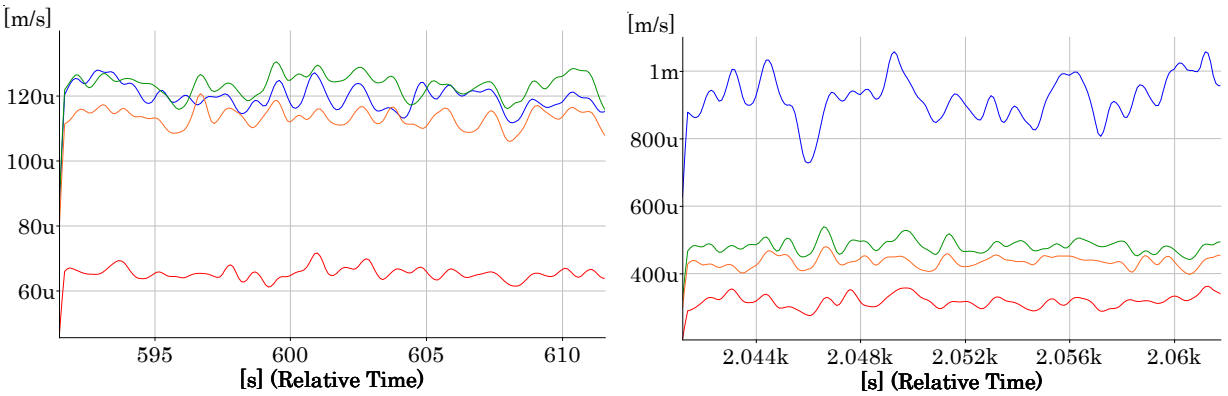

Figure 5.49. Overall RMS levels for different monitoring locations. Left, at minimum load and right, at maximum load

5.3. Conclusions

The dynamic behavior of two prototype horizontal shaft Pelton turbines in operation has been investigated. The structural disposition was different, one machine has two bearings at both sides of the generator and the other has three bearings. A simultaneous measurement of vibrations from different positions and strains on the shaft was performed. The sensors were located on bearings and the shaft. The operating conditions were taken from the Scada system. First the start-up and second the steady operating conditions were analyzed.

In the beginning of the start-up, vibrations are generated by the excitation of the runner natural frequencies by the impact of the jet. The tangential modes and rim modes are especially excited by the impact of the water jet on the buckets. In this moment, acceleration amplitudes are larger than when the machine is at full load.

The onboard system showed that the transmission from shaft to the bearing varies with the runner mode. In addition, strain gauge proved to be capable of detecting runner modes, especially tangential modes.

After that moment, when the runner increases the rotating speed, the main vibration amplitudes are due to the match between the blade passing frequency f_b and the natural frequencies of the rotor. The vibration amplitude depends on the mode shape and damping characteristics. The amplitudes of the more global mode shapes where all the rotor masses are deformed have the lowest amplitude. The response in the axial direction also depends on the mode shape characteristics.

The strain measurement indicates that the torsion stress fluctuates at the rotation frequency with low amplitudes and at the blade passing frequency. The maximum amplitude occurs when the blade passing frequency equals the torsion natural frequency.

Vibrations in the horizontal direction are higher than in the vertical direction because the stiffness of the bearing is lower in horizontal direction. Amplitudes of 4.5 mm/s rms are reached, what is ten times larger than ones obtained at maximum load. The maximum

response is with the mode with axial motion of the runner producing large stresses in the coupling zone between shaft and runner.

It is proved that with the machine in operation, the runner natural frequencies can be detected in the monitoring positions. The best positions for the best detection of them have been assessed.

Another important topic is the variation of the runner frequencies when the turbine is in operation due to added mass and stiffness due to centrifugal forces. In the cases studied, the changes observed are not significant and are in the range of the scattering of natural frequencies due to lack of precision during the runner machining.

Finally, the evolution of the band level related to each mode shape have been calculated.

In the next chapter all the knowledge obtained will be used for an upgrading of the monitoring systems.

Chapter 6 Monitoring of Pelton turbines

Due to the massive entrance of new renewable energies (NRE), the electricity market has changed completely. Today, hydropower plants are of paramount importance due to their capability to absorb and supply a variable quantity of energy, depending on the electrical grid needs. By 2030 the market share of NRE is forecast to be higher than 30% in Europe. To cope with this increase, more flexibility is demanded to hydropower plants so that they can respond faster to any change in demand and supply. Because the price of energy depends much on the rapidity of hydropower plants to provide or take energy from the grid, operators can obtain more revenues by increasing the flexibility of the turbines. However, this is translated into the turbines operating longer in off-design conditions and increasing the start/stop sequences. This usually means stronger excitation forces on the structure and a faster deterioration, what may reduce the maintenance intervals and increase the costs.

In this new competitive market, managers demand more control on their assets and require more tools to weigh the economic benefits of flexibility with the increased cost of maintenance. Remaining useful life (RUL) estimations that are based on present and future operational conditions (input commands, environment and loads) have to be introduced in the current monitoring systems. It is about operation decision making according to the cost of maintenance and price of energy. To achieve this goal, an upgrading of the actual condition monitoring systems has to be done, so that the consequences of machine of flexibility can be estimated.

In this chapter, the extensive structural and dynamic analysis of Pelton turbines carried out in the other chapters will be used for an optimization of the existing condition monitoring systems.

An advanced condition monitoring system has to be able to identify situations of abnormal turbine operation that may lead to failure and to detect incipient damage in real time. As indicated in the beginning, the runner is the component more prone to have damage. Therefore, the feasibility to detect, evaluate and follow up the runner vibrations constitutes the main challenge.

The strategy to implement an advanced condition monitoring system is discussed in this chapter. First step is to analyze typical vibration signatures of Pelton turbines and to determine how they change with the most common types of damage. Knowing the dynamic behavior of the machine, two methods are possible; one is through the analysis of field data (if available) and the other generating synthetic damage in calibrated models. Field data analysis of vibration signatures before and after maintenance results very useful to extract symptoms of damage in vibration signatures. The historic of several machines have been studied for that. Second step is to select the condition indicators. In this thesis, the choice of spectral bands associated to the runner vibration will be discussed with some examples.

6.1. General approach to CM of hydro turbines

The goal for a condition monitoring system is:

- Identification of operating condition with abnormal situations that can lead to damage.

- Detection and diagnosis of (incipient) damage.

- Prognosis. The ultimate objective is to calculate the residual useful time (RUL) depending on the operating conditions so that the cost of operation can be estimated.

An advanced condition monitoring system has to be able to detect in real-time incipient damage and abnormal operation that can lead to failure and estimate the RUL according to the possible future operating conditions. With this information the operating conditions and/or maintenance tasks can be decided. All this process has to be done in “real time”, simulating different scenarios of operation each one with a degradation model.

In Figure 6.1 a general sketch of an ideal monitoring system has been represented.

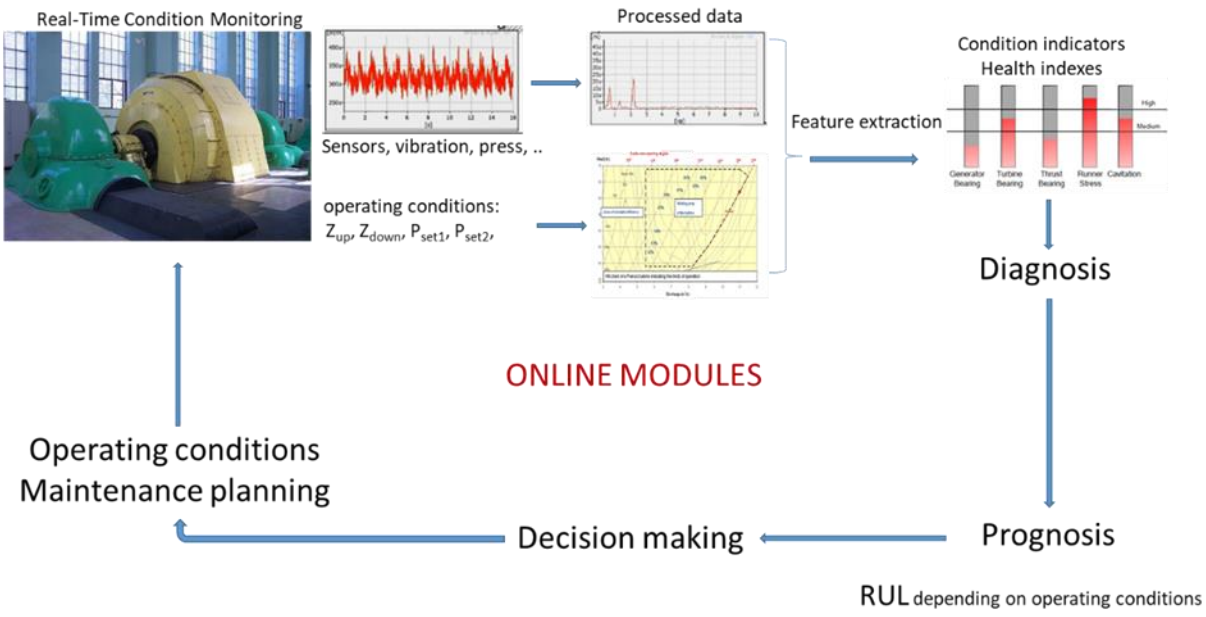

Figure 6.1. Sketch of a monitoring system

The first stage of the monitoring process consists in measuring all the relevant dynamic variables of the turbine (e.g. vibrations) and in collecting the parameters related to its operating conditions, like the head and the output. Typically, vibrations are measured from the bearings with accelerometers and/or proximity probes and recorded as raw signals by the acquisition system. Nevertheless, due to the complexity of the vibration signals and the insufficient knowledge regarding the dynamics of the system, assessing the state of the turbine runner is a challenging task.

In an advanced monitoring system, the dynamic variables to be measured in the machine, as well as the monitoring locations and the measuring sensors, are selected according to its sensitivity to runner vibrations. For every characteristic vibration of the turbine (modes and frequencies), the optimal measuring location and direction, as well as its corresponding transmission function, are to be determined. With this, the signals collected from the monitoring locations can be associated to the vibration in the runner. In case of abnormal operation or incipient damage, the change in the vibration will be identified by the sensors and its gravity assessed.

The suitability and sensitivity of each monitoring location to detect vibrations and the most common types of damage can be studied with validated dynamic models. In Figure 6.2, a FEM numerical model of a Pelton turbine is shown. The excitation force can be introduced in the model and the response in each bearing computed through a harmonic analysis. In some cases, the typical monitoring locations are not always effective to detect abnormal operation and damage, especially in the runner. Thus, a deep understanding of the dynamic behavior of the turbine is mandatory.

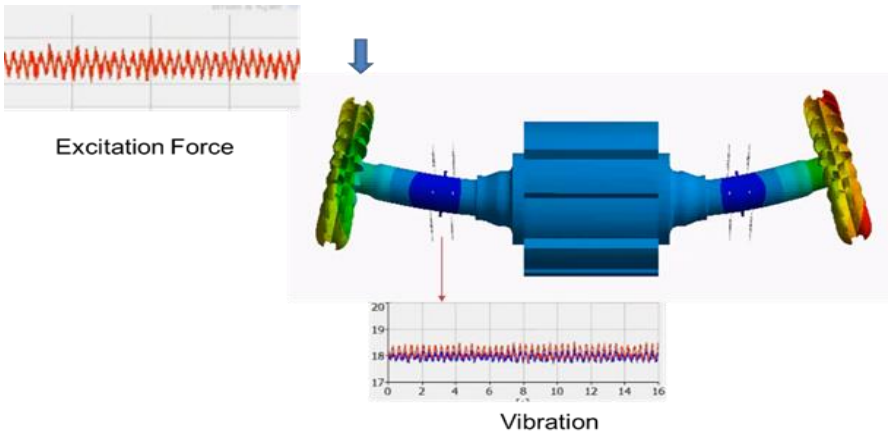

Figure 6.2. Dynamic model to determine the response in the monitoring positions to the excitation generated during the operation of the machine

The acquired raw signals are processed to extract basic features that indicate fault growth or damage. Typical signal processing uses time-domain and frequency-domain techniques like Fast Fourier Transforms (FFT) algorithms and other signal processing methods, like time-frequency transforms or Frequency Response Functions (FRF). Overall RMS amplitudes, spectral bands, statistical factors and time-domain parameters are extracted. With the vibration features, condition indicators can be calculated, which can be effective to detect incipient damage. These indicators are trended and compared to some alarm and trip levels (Figure 6.3). After overpassing the alarm threshold, the diagnostics have to be done.

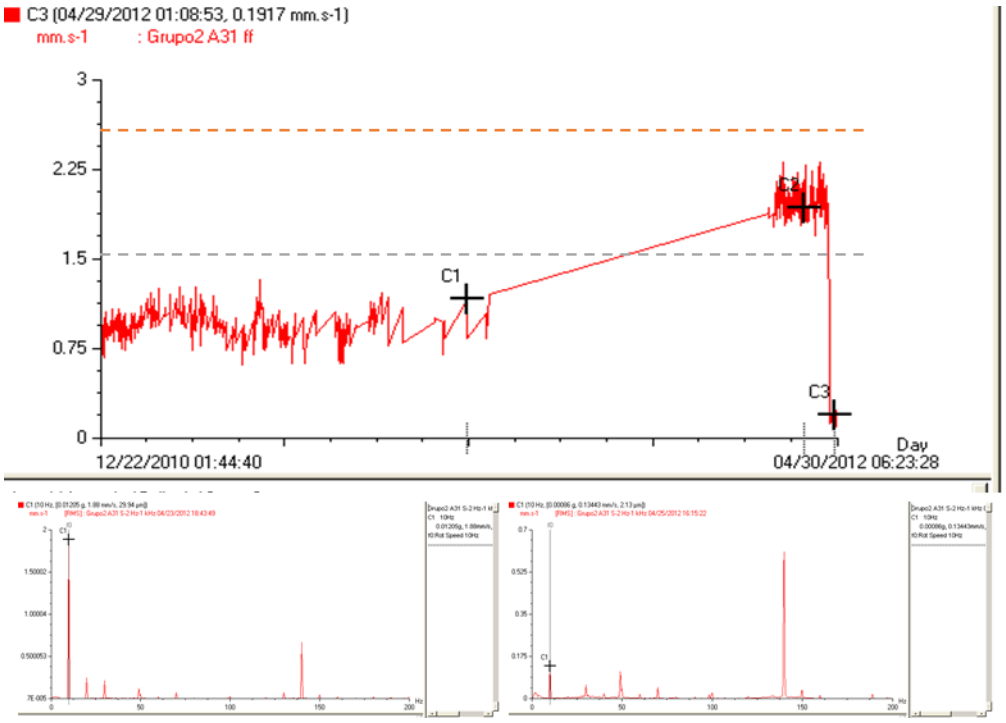

Figure 6.3. Trend analysis of a spectral band detecting damage, the diagnostic and the repair

Selecting alarm and trip levels able to identify incipient damage in the runner is a complex task. First, the levels of each indicator must be mapped for all operating conditions with the machine in good condition (Figure 6.4). Second, a mapping of the evolution of these condition indicators under a damage situation should also be represented. Machine learning techniques can be used for such purpose, but they need large amounts of historic data that encompass the evolution of the machine vibration from good condition to failure. Since machines are never allowed to operate until the end of their useful life, one of the limitations in condition monitoring of hydropower plants is the lack of data. These shortcomings can be partially overcome with the use of sophisticated numerical simulation models where synthetic damage can be simulated.

Regarding the setting of alarm and trip levels, the point is how to select them. The point is how soon is too soon and how late is too late for the trigger of alarms. If the alarm levels are set too high, the monitoring will be able to detect when the system is healthy with few false alarms, but may miss incipient faults. If the alarm levels are set too low, the monitoring will be able to trigger an alarm signalling when the system is no longer in good condition, but may give false alarms regarding healthy states. In remotely located hydropower plants with unmanned operation, the false alarms should be avoided but critical damage should be detected.

The last stage is the prognosis. Prognosis is the estimation of the remaining life of a component conditional on future load and environmental exposure. It estimates when the component will no longer operate within its stated specifications. Prognosis can be carried out in many ways, like approaching historical time to failure data to model the failure distribution (Weibull Analysis), calculating the component degradation (Cumulative Damage Model) and so on. There are many uncertainties from a variety of sources like measurement, modeling and preprocessing.

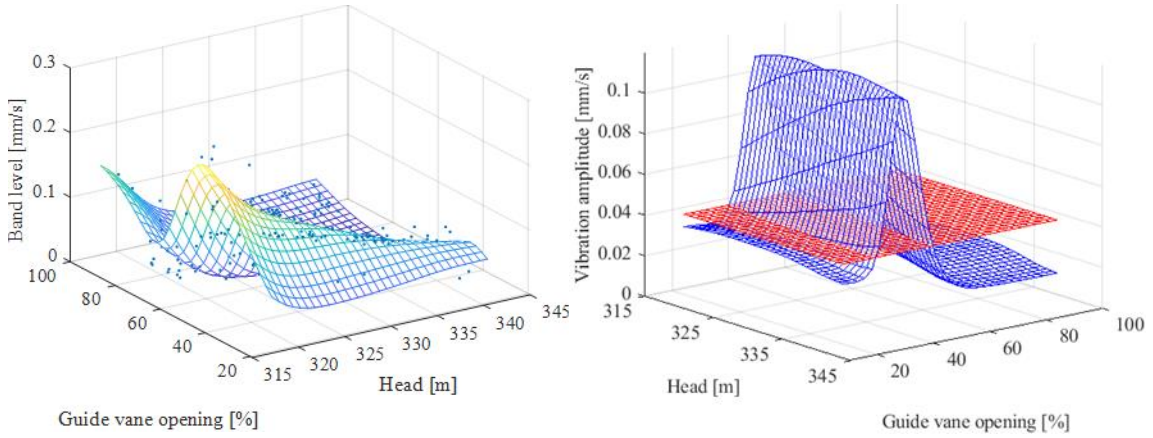

Figure 6.4. Mapping showing the evolution of condition indicator levels with operating conditions (power and head) in a pump-turbine

Extended operating conditions complicate a lot the monitoring. Turbines may operate in rough zones with high turbulence and vibration levels. When operating off-design, the levels of the extracted features can be more responsive to the operating conditions than to incipient

damage. These abnormal operating conditions have to be identified and the effects on the machine components estimated.

Fortunately, Pelton turbines have a broad operating range (between 20 and 100%) with good efficiency. Unless they are working at very low load when the jet may be asymmetric or at very high load where the force is very large, the behavior is quite good. In the next section the monitoring of Pelton turbines is analyzed.

6.2. Condition monitoring of Pelton turbines

First step is to analyze typical vibration signatures of Pelton turbines and to determine how these signatures change with the most common types of damage. The vibration generated depends on the excitation forces and on the structural response (Figure 6.5).

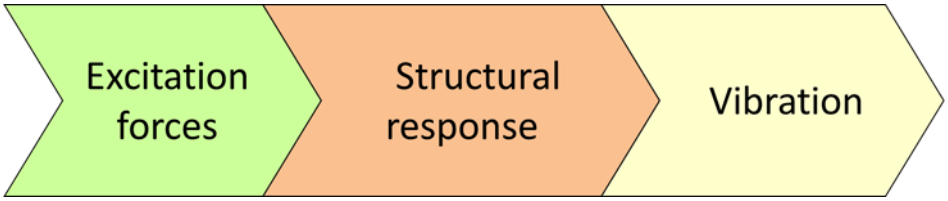

Figure 6.5. Vibration generation sketch

In Figure 6.6, a typical spectral signature of a Pelton turbine rotating at 600 min^{-1}, with 22 buckets has been represented. Different types of excitation forces are generated during the operation of the turbine, which can be classified depending on their origin as mechanical, hydraulic or electromagnetic. Mechanical excitations are produced by unbalance and misalignment and are found at the frequency of rotation f_f. This is defined as

$$f_f = \frac{N}{60} = 10 \text{ Hz} \qquad \text{Eq. 6.1}$$

Where N is the rotating speed in min^{-1}. Vibrations of hydraulic origin are also identified in the spectrum. Unlike reaction turbines, Pelton turbines are not subjected to pressure changes, as they are set up in an open casing. Instead, the main forces affecting the structure are the ones coming from the water jet impacts on the runner. The frequency at which the jet impinges the structure depends on the rotating speed of the wheel and on the number of buckets. It can be defined by the following equation

$$f_b = n \cdot z_b \cdot f_f = 220n \text{ Hz} \qquad \text{Eq. 6.2}$$

where f_b is the frequency of the vibration generated on the wheel by the impact of the jet (bucket passing frequency), z_b is the number of the wheel buckets and f is the shaft rotating frequency. n stands for the harmonics of the exciting force (n =1,2,3…). Other vibrations

identified are the ones related to the structural response, like rotor eigenfrequencies. At higher frequencies, some broadband vibrations can also be seen.

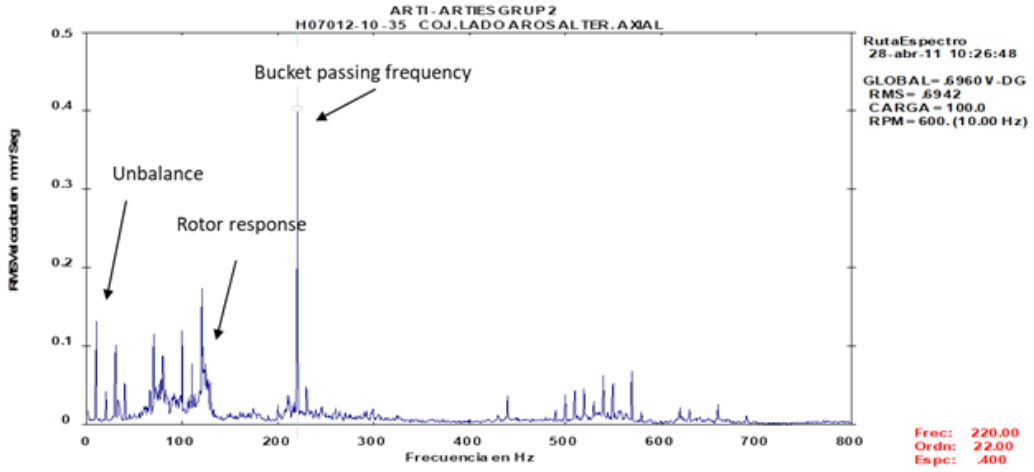

Figure 6.6. Typical spectral vibration signature in a Pelton turbine

From these signals some features can be extracted and used for monitoring purposes, like spectral bands amplitudes and peak to peak values. Overall vibration levels are not sensitive enough to detect incipient damage. Potentially serious problems can develop within the turbine and have a negligible effect on the level of the overall vibration. Anyway, they are a reference to be considered when setting vibration monitoring. In Figure 6.7, the vibration limits recommended by ISO Standards are indicated.

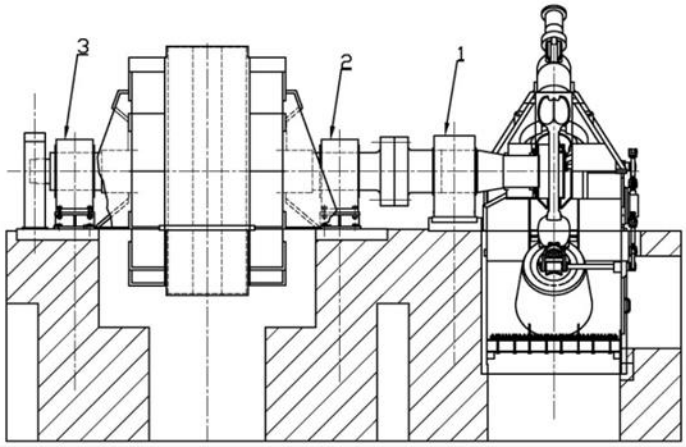

Machine type:	Shaft vibration Sp-p, µm			Bearing vibration Vrms, mm/s		
Pelton Horizontal	T1	GE-DE	GE-NDE	T1	GE-DE	GE-NDE
Action limit 1 (A-B/C)	120	140	100	2,0		1,1
Action limit 2 (C/D)	190	210	160	3,1		1,8

Normal operating range for Pelton horizontal: from 10 % to 100 % of rated power

Figure 6.7. ISO 10816-5. Group 1 horizontal machines with vibration limits

With properly specified spectral bands, incipient problems and abnormal operation can be detected. There are many indictors but spectral bands are one of the most powerful basic indicators in predictive maintenance. The spectrum is divided into several individual bands, where each one of them is representative of an excitation force or a structural response. Two different types of spectral alarm bands can be defined, energy (or power) bands and threshold bands. Threshold bands will trigger the alert when any peak in the band reaches the alarm value. Typical spectral bands are established around the main excitations produced by the machine and around the symptoms of damage that can be detected by vibration analysis. The analysis of a typical spectrum should reveal which frequencies are present in the spectrum and how they are related to the rotating speed and how to one another. Phase is important to differentiate between problems with the same frequency components. Typical spectrum bands are described in the following list:

- Sub-synchronous bands to detect bearing problems and oil whirl
- f_f to detect mass unbalance
- First harmonics of f_f for misalignment,
- Higher harmonics of f_f for mechanical looseness and bearing problems,
- Higher frequencies for natural frequencies

Although there are many publications and studies related to the analysis of excitations/problems of mechanical origin, but this is not the case for hydraulic excitations in hydropower turbines. For Pelton turbines, where the vibrations are generated by the runner/jet interaction, bands around the bucket passing frequency and harmonics are selected. The choice of the alarm levels is mainly based on expertise. If this is not available, setting the alarms levels between three and four times the standard deviation is an initial possibility.

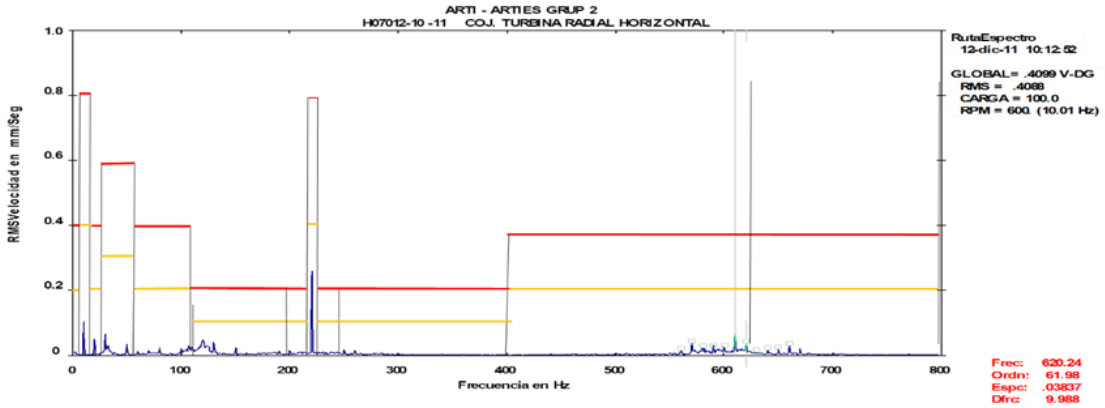

Figure 6.8. Spectral bands in a Pelton turbine spectrum

In Figure 6.8, typical monitoring bands for a Pelton turbine are indicated. High frequency bands are selected for the detection of natural frequencies. Spectral bands have to be complemented with other time-domain indicators. Other processing methods can be also used for the detection of specific problems.

For diagnosis and prognosis, the change of the aforementioned indicators with the most common types of damage is necessary. This information should be obtained from the monitoring of actual machines. For that purpose, a systematic analysis before and after repair comparing the changes and knowing the damage found during the outage is very informative. Usually this information is difficult to obtain and is not complete enough to describe all types of damage. Apart from that, power plants are not allowed to operate beyond their maintenance limit, what makes it difficult to know how the monitoring parameters change when the turbine is in an advanced degradation state.

As indicated above, another possibility to complement the field data is to have a numerical model that simulates the dynamic behavior of the whole machine. The structural response (deformations, vibrations, strains) to the variable dynamic forces acting on the machine during operation can be calculated. Physics-based numerical model can be used to simulate types of damage not found in the machine (synthetic damage generation). This analysis enables determining how all the components of the machine are deforming when the turbine is in operation, and, at the end, allows seeing which locations of the wheel are more prone to suffer fatigue problems. However, developing models is not trivial and refined models may be computationally expensive to run. CFD computation of the jet and its application to the FEM model is not an easy task and impractical for real-time applications. Moreover, models have to be tuned with field data.

A critical issue when monitoring a Pelton turbine is the detection of runner problems. The runner is receiving directly the high speed jet of water and is the turbine component more prone to have damage. In the previous chapters, the feasibility to detect runner vibrations from the monitoring positions has been proved. Moreover, the best sensor type and location has been checked. This information will be used to upgrade the monitoring system.

Once proved that the runner can be monitored from the bearings, the next step consists in knowing which are the most common types of damage. For that purpose, the monitoring information and data obtained after more than twenty years of monitoring have been analyzed. The main types of damage that have occurred in several Pelton turbine units in Spain and Chile are described in chapter 6.3. With this information, it can be determined what types of damage to go for and how critical they are.

6.3. Types of damage

Pelton turbines can suffer from different types of damage. Most of the cases are due to sand erosion, fatigue or cavitation [10], [16]. Erosion problems are very common in some areas like the Andes, where the water carries a large amount of sand particles [33], [45]–[50]. In these cases, the most affected locations are the surfaces where the water velocity and/or the acceleration are high. Nozzles, needles and the inner surface of the buckets are usually the most eroded areas. In Figure 6.9, the erosion produced by solid particles in a Pelton turbine located in Chile is shown. Deflector, nozzle ring and runner show important erosion.
Sediment erosion reduces the efficiency and increases the risk of operation. These problems are overcome by welding repair. The runner geometry after repair should be checked with

design templates to avoid increased operating stress at bucket root. Welding repair could be advantageous due to lower cost but quality control is necessary.

Figure 6.9. Particle erosion in Pelton turbine components

Cavitation can produce pitting on the buckets, especially on the tip and on the cutout lips [51]. Sand erosion enhances the possibility of cavitation because the waviness of the eroded surfaces increases wall turbulence, thus reducing the local pressure. Nevertheless, damage caused by the fatigue of the material is proved to be the most dangerous one [9], [33]. The periodic impacts of the water jet lead to a large concentration of stresses at the root of the buckets. After long operation times, these stresses result in cracking the material and destroying the runner buckets [17]. To minimize the effect of fatigue, the design and manufacture of the turbine has to be optimized. At present, reliable runners are constructed using forged blocks of stainless steel due to its improved mechanical properties compared with cast steel, such as fatigue strength and fracture toughness [52]. Even so, mounting and operating conditions can modify the stress distribution in actual runners, thus leading to unexpected failures.

Hooped runners have a different structural design. According to literature, they achieve a reduction in the stresses on the most stressed zone [21]. The transformation of the jet force into torque is carried out by rings, on which the buckets rest. Measurements made in situ on runners in operation, show that the level of vibratory stresses is statistically of the order of 40 per cent. In our study no hooped Pelton runners were available and only conventional runners could be investigated.

From the database, a few history cases have been analyzed determining which are the symptoms for each type of damage and how they can be detected. In Figure 6.10, some examples of the fatigue damage in runners are shown. Fatigue cracks in the root and in the tip of a runner bucket can be observed. Cracks like those seen in the pictures can spread quickly and, if unnoticed, can result in a bucket rupture with potentially disastrous results.

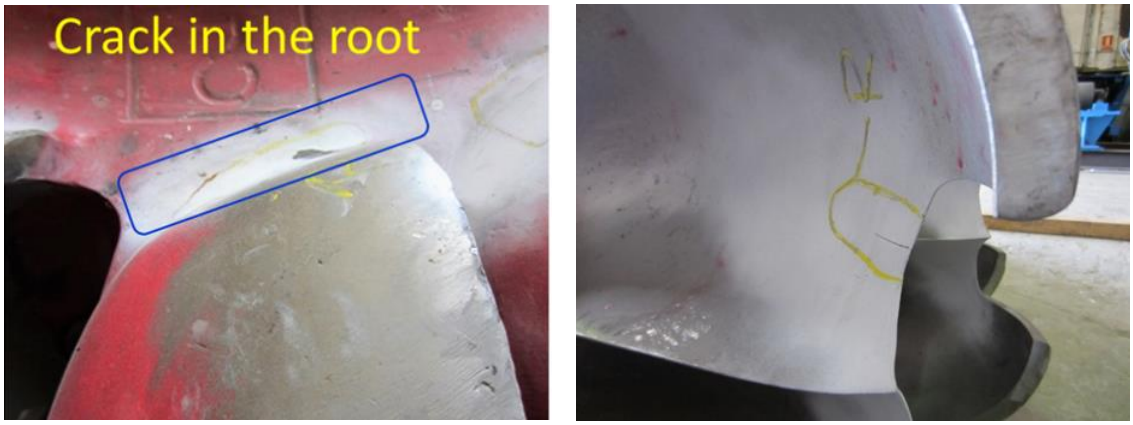

Figure 6.10. Typical fatigue cracks in Pelton runners

In the following pictures, damage found in the injectors during maintenance of turbines are shown. In Figure 6.11, needles with particle erosion and with cavitation damage can be observed. In Figure 6.12, a broken needle is also shown.

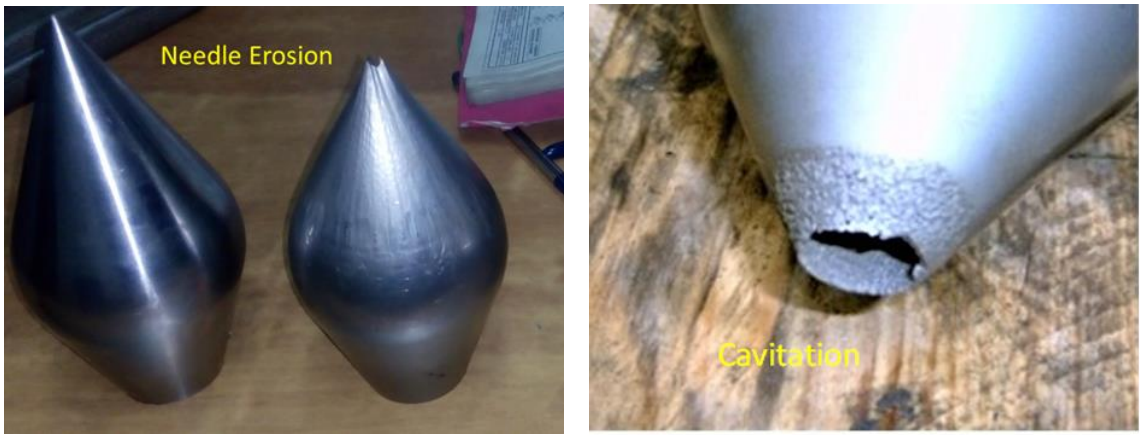

Figure 6.11. Injector needle damage by erosion (left) and cavitation (right)

Figure 6.12. Injector damage in Pelton turbine

Another typical problem in injectors is due to ingested bodies [53]–[55]. They are not uncommon and produce blockage in the waterways, especially at the end of the nozzle. There are losses due to unbalanced velocity profiles and turbulent fluctuation causing "bad jet quality" in the form of jet deviation or jet dispersion, producing abnormal operation of the turbines. In Figure 6.13, a couple of cases with blockage can be seen. In the first one, a piece of wood was stuck inside the nozzle, and in the second one, leaves and branches were found inside the nozzle during an inspection.

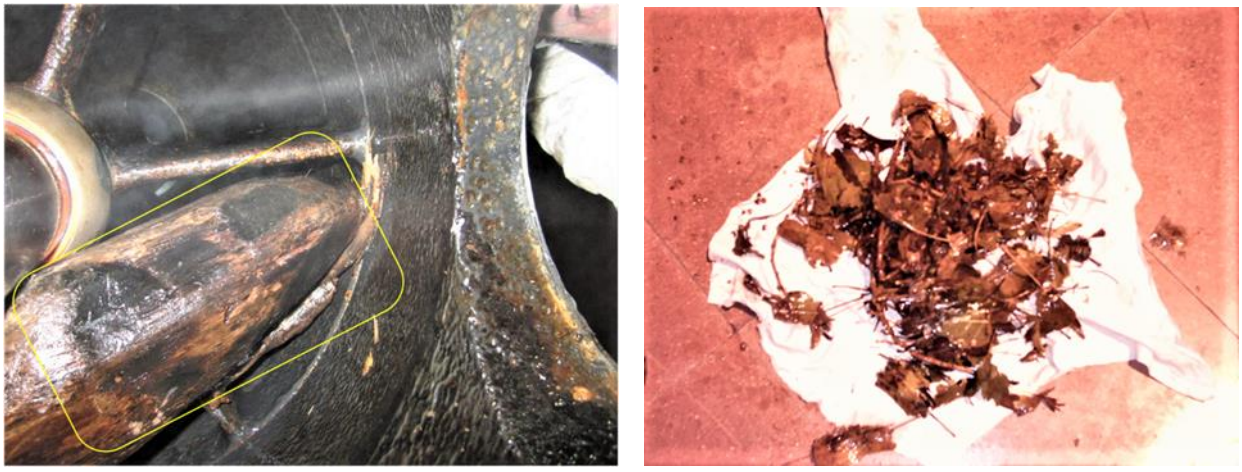

Figure 6.13. Examples of blockage in Pelton turbine injectors

Figure 6.14. Examples of weld repair

In Figure 6.14, examples of poor repair in a Pelton runner are shown. Their geometry after repair can deviate from the original design profile [56], [57]. This causes some scatter of the bucket geometries that can modify the natural frequencies of the buckets. Deviation in the bucket splitters and other small changes can modify the force distribution on the bucket.

According to the field data analysis, the damage found can be summarized as follows:

- Damage in runners:
  - Particle erosion
  - Cavitation pitting
  - Cracks in the root and in the tip
  - Broken parts (due to fatigue)

Poor construction and, especially, poor repair enhance damage. Combined phenomena like particle and cavitation erosion enhance each other effects.

- Damage in injectors
  - Broken injectors
  - Particle erosion
  - Cavitation
  - Blockage

Bends and bifurcations in the distributor of the Pelton turbine can result in jet dispersion and deviation, what can generate abnormal operation in the turbine, increase the risk of cavitation and thus reduce its remaining useful life [58]–[62]. Poor mounting of the runner can also lead to jet misalignment, as well as axial generator thrust if generator rotor and stator are not centered.

The analysis of signatures before and after damage (if available) have been used to extract the best vibration features and condition indicators for the diagnosis. An example is shown in Figure 6.15, where the vibration signatures before and after the change of the runner can be observed.

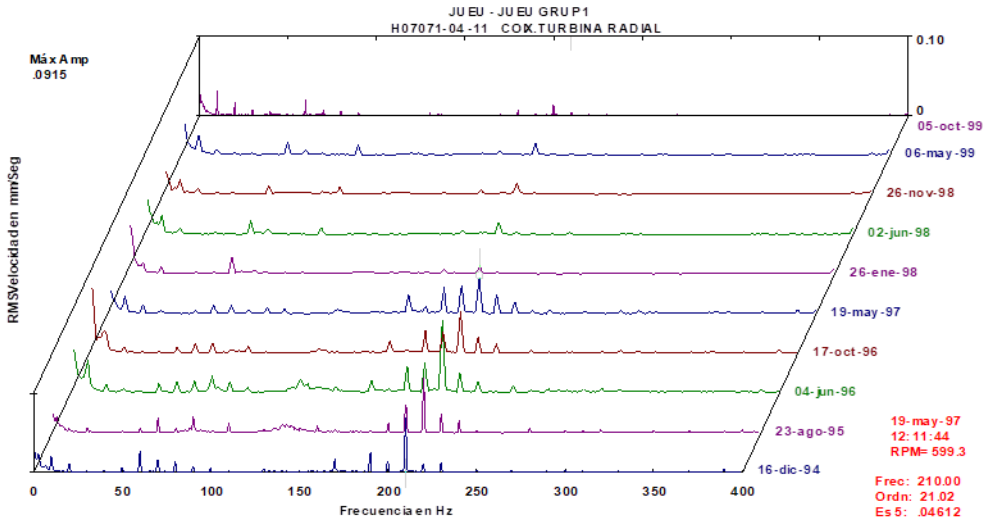

Figure 6.15. Change of a worn runner

6.4. Upgrading of the monitoring system

The bands usually selected for the monitoring are not refined enough to detect some incipient problems. One way to upgrade existing monitoring systems is to "follow" the way the runner vibrates and select the best condition indicators.

The runner vibration modes excited during operation depends on the jet force direction and on the runner. In Pelton runners, from the rotational reference system perspective, the jet force is applied to each one of the buckets with a phase shift. In the course of the excitation, the force on the bucket changes its value and direction. In Figure 6.16, the force variation induced in a bucket by the jet is shown (taken from [30]). The components of the force F_x, F_y and F_z correspond to the axial, radial and tangential directions of the wheel, respectively. As it can be seen in the graph, the most important component is in the perpendicular direction of the bucket (tangential to the wheel), thus the bending modes are more prone to be excited. Forces in axial and in radial direction are very small.

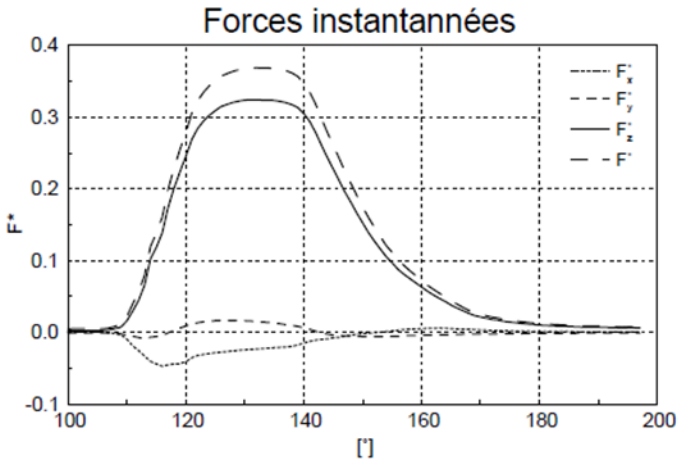

Figure 6.16. Distribution of the forces produced by the jet on a bucket (image taken from [30])

Therefore, in normal operating conditions, with the runner and injector in good state and the jet aligned, the runner vibrates mainly in the tangential direction. With the tangential force, the tangential modes and other modes with tangential deformation are the ones to be excited. In an aligned turbine, axial forces should be very small and so the axial deformations and vibrations. Because the tangential force of the jet depends on the jet discharge, the amplitude of these modes will increase with load.

Damage and abnormal operation can modify the runner vibration due to the excitation of other runner modes. Changes in these vibrations can be generated by problems in the jet or by damage in the runner. Both of them can produce changes in amplitude or in the distribution of the runner modes.

The most common types of damage change the components of the jet force on the runner. Axial components of the jet force on the bucket may be not zero if the jet centerline is not coincident with bucket centerline. An axial force may also appear if the stator magnetic field

center is not aligned with the rotor magnetic field. In some occasions an axial force are due to problems in the injector or in the runner.

The analysis of the historic data shows that most of the damage found produces a change in the jet alignment and jet quality exciting axials modes. A change in jet quality may increase the turbulent excitation. The effect of jet misalignment can be checked with a simulation of the harmonic response including the axial component of the jet force.

One possible way to detect these types of damage is by stablishing properly specified spectral bands after the natural frequencies of rotor and runner has been identified. Spectral bands around the axial, tangential, rim, radial and other modes can be stablished.

Any change in the state or excitation of the runner will modify these bands. Because the band energy for the different operating conditions can change with the machine power and with damage, the mapping of all bands from minimum to maximum power has to be calculated with ML methods (part 5.6). Mapping for the most common types of damage should be also included. A history case will be analysed with this method.

The potentiality of each spectral bands levels depend on the machine power but also on the position and direction. This has been discussed in the last chapters, where the best monitoring positions have been studied.

6.5. History case

The case reported here corresponds to a Pelton turbine analyzed with a head of 770 m and a maximum power of 34 MW. It is a horizontal shaft machine composed by a wheel with 22 buckets with a diameter of 1930 mm and one injector.

Periodically, a monitoring analysis is carried out in the machine. Vibrations are measured on the bearings in the axial and radial directions, in order to monitor the turbine condition. This procedure allows the surveillance of the machine detecting abnormal vibrational behavior, and, in some cases, detecting incipient damage. In one of the measurements, the vibration monitoring system detected an increase in the vibration levels and a change in the signatures (see Figure 6.17). The RMS velocity values overpassed the alarm level, and the machine was stopped and inspected. In Figure 6.18, the spectra measured by the vibration based monitoring system days before, during and after the damage can be observed.

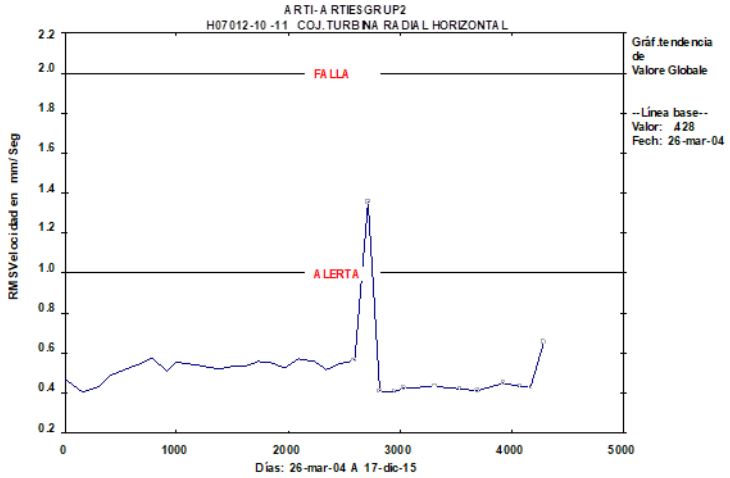

Figure 6.17. Trend plot of the overall vibration values measured in the turbine bearing

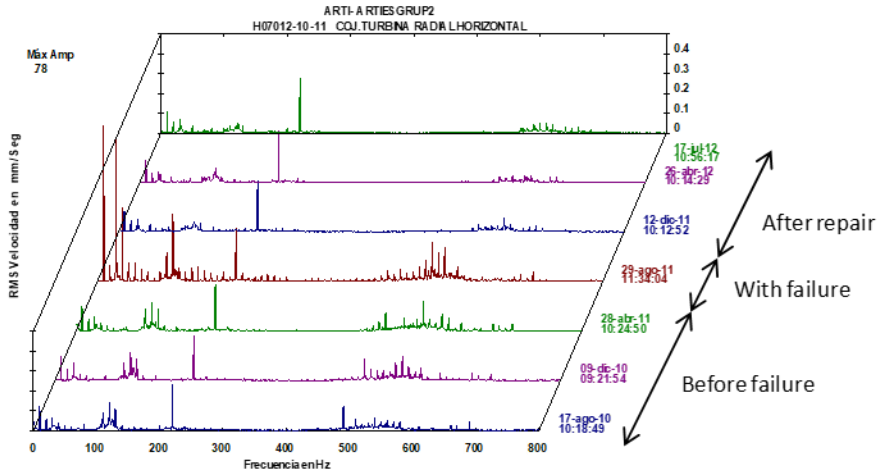

Figure 6.18. Frequencies acquired by the monitoring system in the turbine bearing

The inspection of the Pelton wheel showed an important damage in one of the buckets: a fragment was detached from the outer part of the bucket's rim. In addition to that, several buckets showed cracks in the same location. It is important to remark that all damage appeared in the same side of the wheel. Figure 6.19 shows how the broken bucket looked like after the failure and the segment of bucket blown off. The analysis of the fragment revealed that the failure took place due to a fatigue problem. This can be claimed because of the beach marks, which can easily be identified in the crack.

Fatigue problems appear when a structure is subjected to cyclic loads, which lead to a concentration of stresses that end up weakening the material. In general, all the studies reporting Pelton turbine failures evidenced that the main stresses affecting the structure appear in the bucket's root.

Figure 6.19. Pictures of the wheel with damage. Left, view of the broken bucket and right, detached bucket part

In order to check how a misaligned water jet influences on the stress distribution of the bucket, the numerical model of the turbine was subjected to the jet impingement. The excitation characteristics of the water jet were simulated according to the pressure map taken from [30]. After that, the same values were shifted to one side of the bucket in order to simulate the influence of the asymmetric jet. The results can be observed in Figure 6.20, where an asymmetric distribution of stresses is shown.

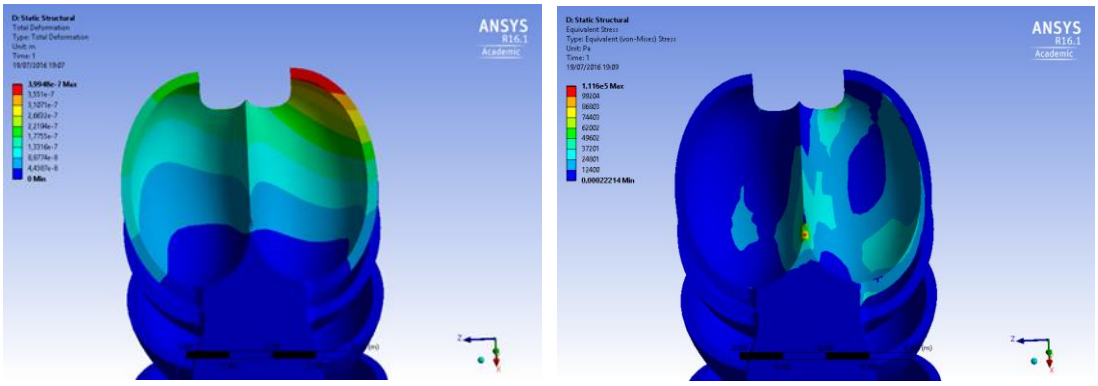

Figure 6.20. Displacement and distribution of stresses on the bucket with a misaligned jet

The results show that a stress concentration area appears at the base of the splitter and at the tip of the bucket. This last location corresponds to the area where cracks appeared in the real turbine, what proves that the origin of the failure was a misaligned jet. Since these areas are usually the most prone to have cracks, the effect of jet deviation would be to accelerate the deterioration of the buckets. Taking a look at Figure 6.18 again, it is seen that before damage occurred, the axial modes of the runner were excited, indicating the existence of an axial force (dates before 29 August 2011). When the failure occurred, there was an increase in unbalance and the natural rotor frequencies were more excited. After repair, the signature changed completely and no axial frequencies were identified anymore.

Analysing this case with the correct bands, a better diagnosis could have been made and the breaking of the runner would have been avoided. For two years before the failure, there is a patent abnormal vibration in the runner. From the dynamic analysis it can be deduced that the axial bucket frequencies were excited, what means that an axial force is acting on the

runner. This is an abnormal situation, which should have been checked before reaching the damage level. Under these conditions, as shown in the FEM analysis, the stress distribution is modified.

In the trend graphs of the next figures, the variation of the selected spectral bands with abnormal operation and damage can be observed. In Figure 6.21, Figure 6.22 and Figure 6.23 the evolution of the new spectral bands has been represented. At the beginning, there are the levels with abnormal operation, then the levels with damage and last the levels after repair.

The classical spectral bands like f_f and f_b show a large alteration only when the failure occurs, not before. The same happens with the rotor natural frequencies. Only the axial runner band shows a big change in abnormal operation before damage took place.

AI techniques can be used to correlate all the bands for a better accuracy in the monitoring. This can be considered a hybrid approach where physics-based models can be used to understand the dynamic behavior of the machine. Further processing can be carried out with new techniques.

With this approach incipient damage like the one indicated in Figure 6.24 could have been detected and trended.

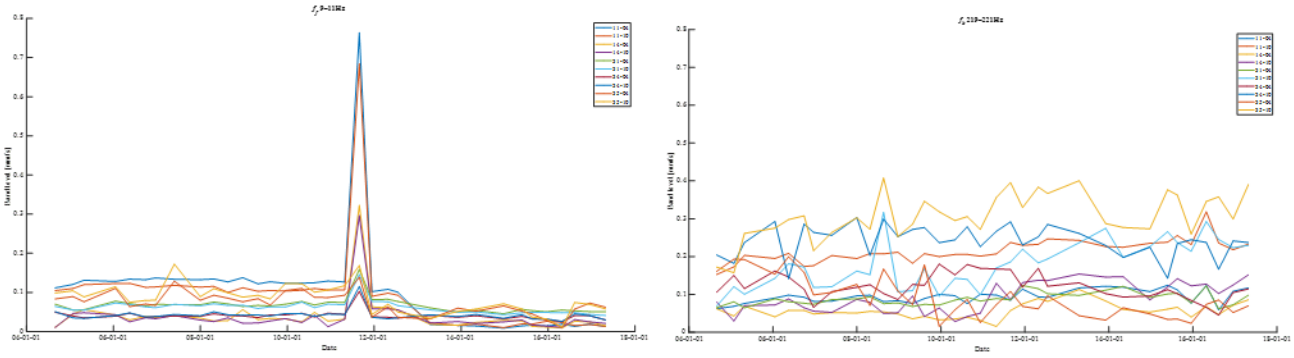

Figure 6.21. Variation in the runner f_f band and f_b band levels with time

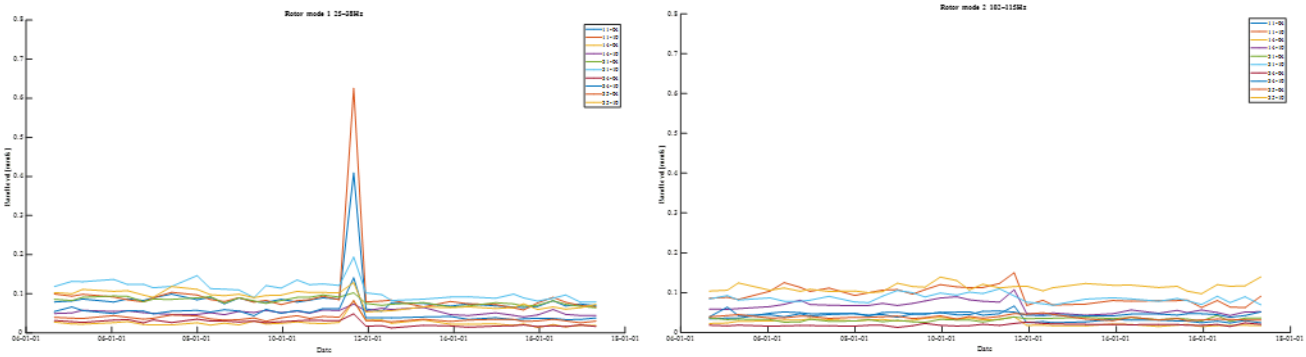

Figure 6.22. Variation in one of the rotor natural frequencies band levels with time

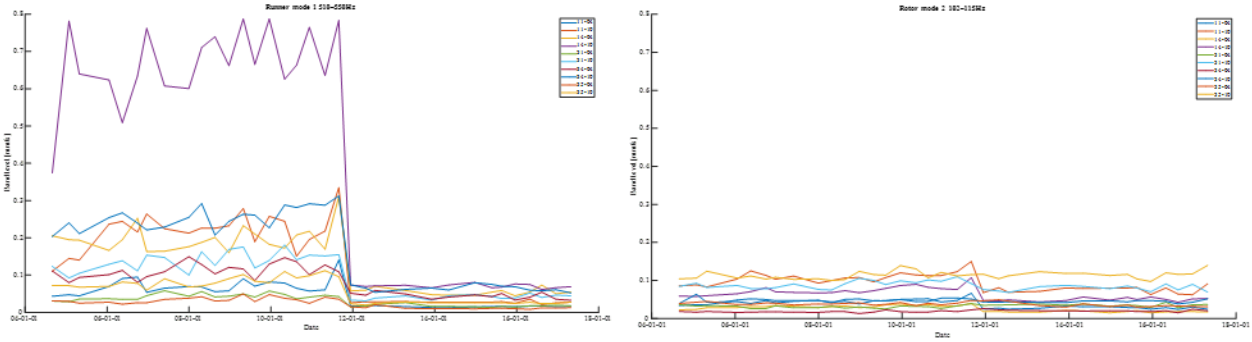

Figure 6.23. Variation in one of the runner axial and tangential frequency band levels with time

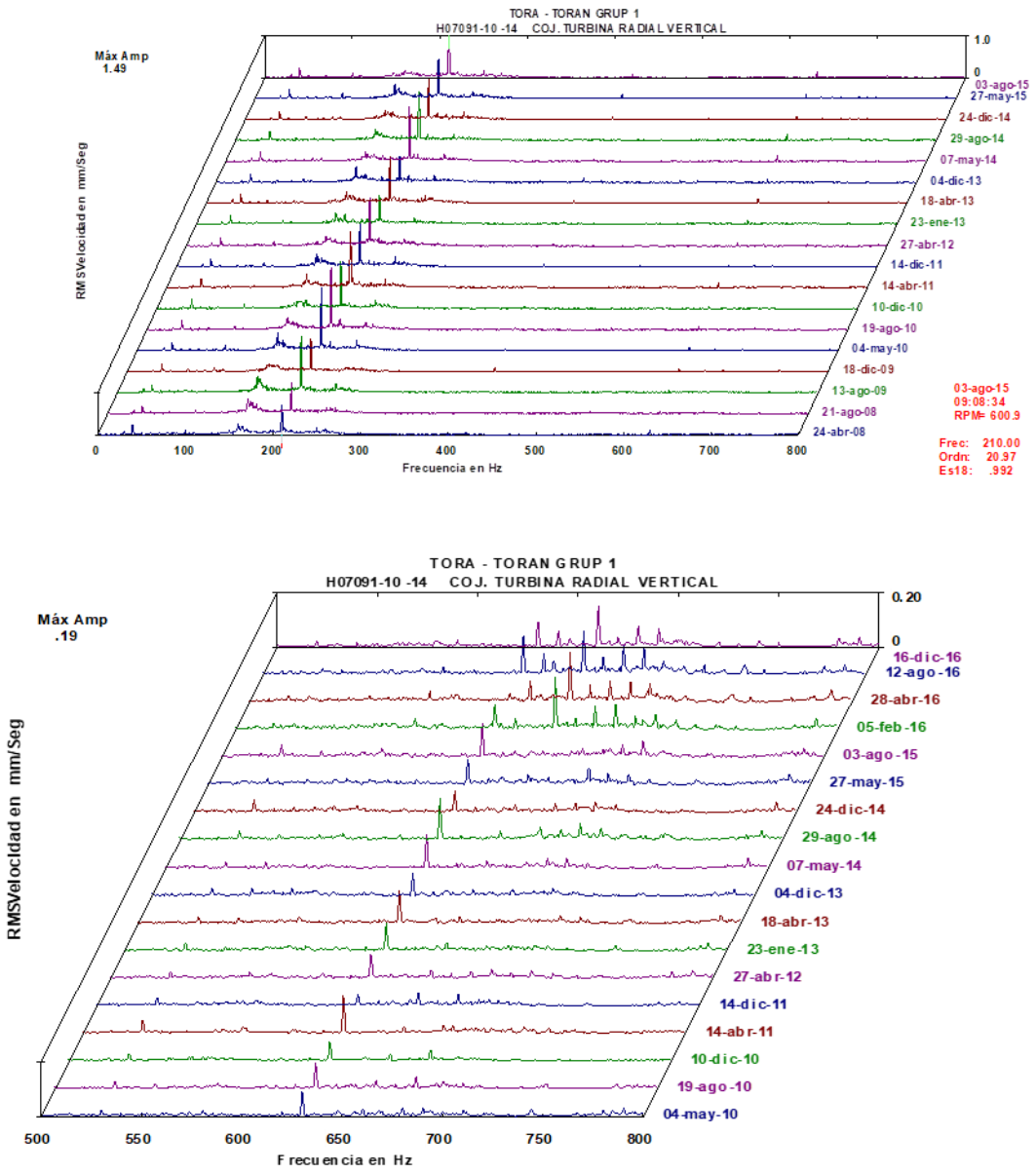

Figure 6.24. Incipient detection

6.6. Data-driven diagnostic methods

Another possibility is to use only data-driven methods. Condition monitoring using machine learning and cloud solutions is a future application in hydro power plants. Machine learning is a field of computer science where models are trained on data to predict an output given a set of input values. These methods train models with historical monitoring data measured in hydro power plants to predict abnormal operation and damage. If a component breaks down, the AI methods can identify similar patterns in future. The most common machine learning methods need data with machine in good condition and with different levels of damage till

the end of life. Mappings relating features and the damage state have to be created but hydropower plants are never operated until the end of life. This information is very difficult to obtain.

Another important disadvantage is that physical cause-effect relationship is not used and lessons learned analysing what happened to several units may not be good enough to predict for another unit. Example are Neural Networks (NN).

In Figure 6.25, the three different time-domain signals of the Pelton turbine vibration discussed before are analyzed here using AI techniques [63]. The signals correspond to the machine in good condition, with abnormal operation and with damage. Applying Convolutional Neural Networks, the three situations are learned and identified. The accuracy of the identification is tested with another segment of the same signal. The identification is perfect.

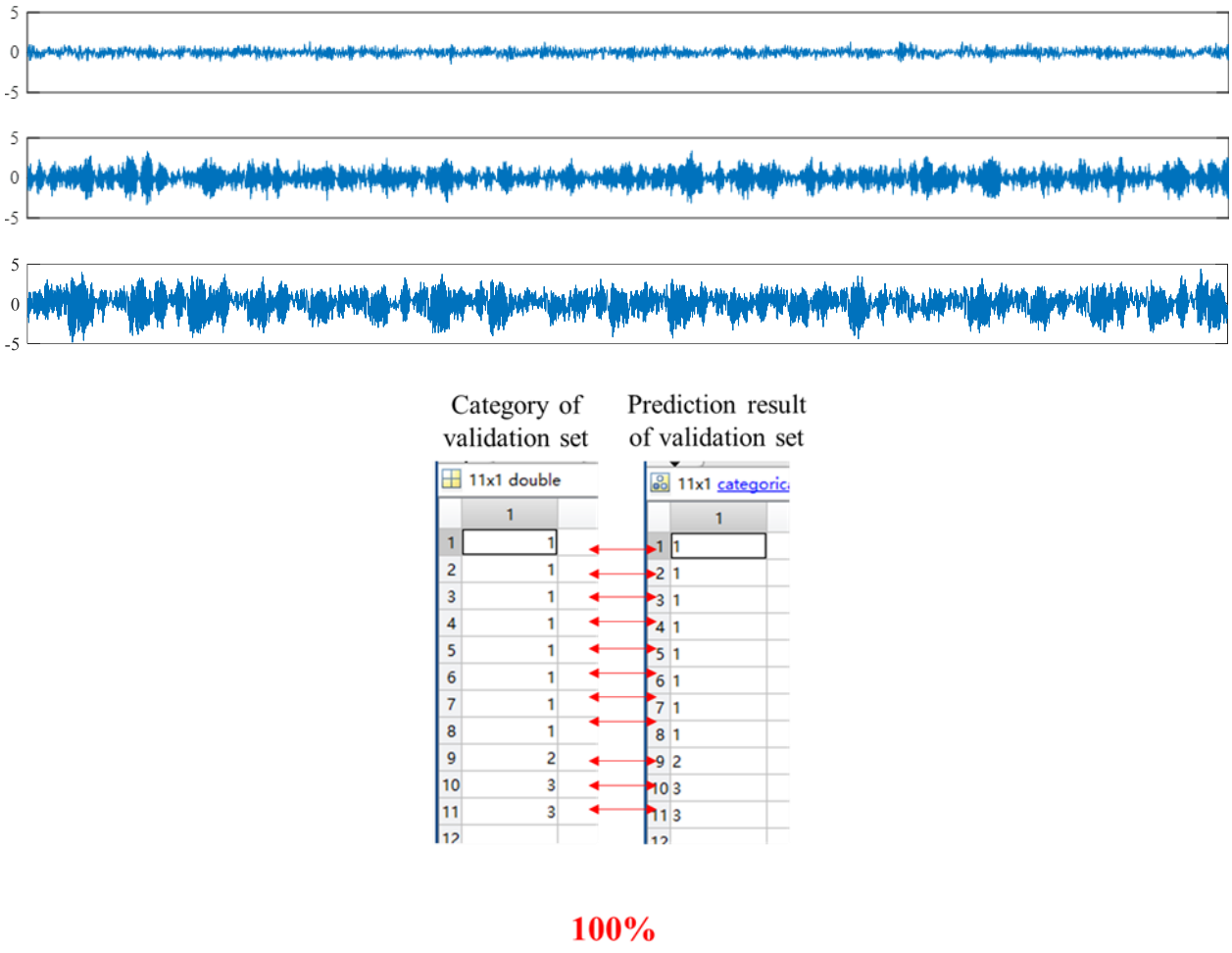

Figure 6.25. Data driven approach

6.7. Conclusions

In this chapter the condition monitoring procedures for hydraulic turbines in general including new trends are introduced.

It follows the application to Pelton turbines, with an analysis of the vibration signatures and the explanation of actual monitoring procedures.

Once proved that the runner can be monitored from the bearings, the next step has consisted in knowing the most common types of damage and their symptoms. For that purpose, the monitoring information and data obtained after more than twenty years of monitoring have been analyzed. The main types of damage that have occurred in several Pelton turbine units are described.

A new spectral band distribution is proposed so that the excitation of the different runner modes can be monitored. An analysis about which of these modes can be excited in normal an abnormal operation is performed.

The proposed procedure is check with a history case where the evolution of the vibration signatures with a fatigue induced damage was available. The proposed method is more sensitive to detect damage and for the diagnostic of damage.

Chapter 7 Conclusions and future work

In this thesis the dynamic behavior of horizontal shaft Pelton turbine prototypes has been investigated. For this purpose, several prototype turbines have been investigated using numerical models and on-site tests.

Vibrations generated during turbine operation depend on the excitation force produced by the jet and especially on the modal response of the turbine. In the first part of the thesis, a detailed analysis of the modal response has been used carried out in a systematic way. First a single runner suspended and second with the runner attached to the shaft (Chapters 2 and 3)

Modal behavior of Pelton runners

In this chapter, a study of an existing turbine runner (suspended) has been done with a numerical simulation and with a comprehensive experimental investigation.

First, assuming that the buckets are rigidly connected (to disregard the effect of the disk) the bucket modes have been studied. In this way, the bucket modes were identified and classified as axial, tangential and radial. Depending on the phase between the bucket halves, these modes were in-phase or counter-phase. The first modes found are axial in-phase followed by tangential in and in counter-phase. After them axial in counter-phase and radials appeared.

Second, the analysis of the complete runner was performed. The results showed that for every type of basic bucket mode, the runner has several multiples, which are coupled to the modes of the disk (n nodal diameters). For each group of bucket modes, the frequencies increase with the number of nodal diameters of the disk. It was noticed that in lower frequencies the vibration is global to all the runner (behaves like a disk) and in higher frequencies the vibration is more restricted and is dominated by the vibration of the buckets. In addition, some bucket modes are more affected by the stiffness of the disk than others are and this affects the distribution of frequencies. For example, tangential modes gather in a small frequency range, while axial modes are more spread. The natural frequencies of the whole runner are lower than the ones obtained with a fixed single bucket.

Because runners are attached to the turbine rotor the influence of this connection is analyzed in the next chapter.

Modal behavior of Pelton machines

In this chapter, the modal behavior of the whole turbine has been investigated numerically and experimentally. The main turbine modes were identified with their natural frequencies and mode shapes.

Modes can be separated into two groups, one as rotor modes and another as runner modes.

Rotor modes cover the lower frequency range from 2,5-3,5 times the rotating frequency to around 300Hz. Runner modes cover a higher frequency range from 300 to more than 1kHz.

The effect of the runner connection to the rotor has been found. The research shows that only some runner modes are slightly affected because of the added stiffness provided by the attachment. The first disk modes are affected but the bucket modes not so much.

To check if this behavior was similar in other turbines of different mechanical and hydraulic design, other turbines were investigated.

The effect of the mechanical design has been studied first. Two runners with the same hydraulic design but with structural differences were investigated. Tangential modes are the ones more affected because they are very dependent on the rear bucket structure. However, the mode distribution and trends are very similar.

The effect of the hydraulic design has also been studied. Significant changes in the modal behavior have been found. For higher heads the runner is large and the width small. In this case, the disk dominated modes have lower frequency while the bucket modes have higher frequencies. The opposite occurs for low head runners.

The method to estimate the diameters and widths of the runner depending on design operating parameters is proposed. Another important matter is to know if there is any relationship between the design parameters and the natural frequencies. A correlation has been found that can be useful for a preliminary estimation of the runner frequency ranges.

In this study the machine was still. When in operation, other effects like the added mass and centrifugal stresses appear in the runner what may change the modal characteristics. To determine that, more tests have to be done with the machine in operation.

Because no sensors can be placed on the runner when the machine is in operation, the feasibility to detect runner vibrations from outside has to be investigated.

Transmissibility of runner vibrations

The transmissibility of runner vibrations to the monitoring positions has been investigated in this chapter. On-site tests were done in two different turbines.

The investigation shows that all the runner vibrations are transmitted and detected on the bearings. High coherence values are found between runner and bearing vibrations. Anyway, the amplitudes seen in the bearing are much smaller than the amplitudes in the runner.

The propagation of the runner natural frequencies to each monitoring position depends on the mode shapes. The tangential modes are better propagated than axial modes

In general terms, vertical positions have better transmissibility than horizontal positions. The only exception are the axial counter-phase modes, which are better transmitted to horizontal positions.

In addition, rotor modes and disk-dominated modes are generally better detected from axial bearing locations, while bucket dominated modes transmit their vibration better to the radial positions.

It has been proved that the propagation depends on the runner mode shape. A detailed study to determine which are the best positions to detect each mode was carried out. By doing that, the best monitoring positions to detect each mode were found. Tangential modes are better transmitted and better detected in vertical monitoring positions.

So far, the turbine has been studied still. In operation some effects like the centrifugal forces and the added mass, can modify the natural frequencies. Moreover, the modes excited during operation have to be determined

For that and with the knowledge obtained with the previous studies, the dynamic behavior of a Pelton turbine in operation can be performed.

Dynamic behavior of Pelton turbines

The dynamic behavior of two prototype horizontal shaft Pelton turbines in operation has been investigated. The structural disposition was different, one machine had two bearings at both sides of the generator and the other three bearings. A simultaneous measurement of vibrations, noise and strains on the shaft was performed. The sensors were located on bearings and shaft. The operating conditions were taken from the Scada system. First the start-up and second the steady operating conditions were analyzed.

The study of the start-up transient gives important information. In the beginning of the start-up, when the runner is still, vibrations are generated by the excitation of the runner natural frequencies from the initial impact of the jet. The tangential modes and rim modes are especially excited by the impact of the water jet on the buckets. In this moment acceleration amplitudes are larger than when the machine is at full load.

The onboard system showed that the transmission from shaft to the bearing varies with the runner mode. In addition, strain gauge proved to be capable of detecting runner modes, especially tangential modes.

After that moment, when the runner increases the rotating speed, the main vibration amplitudes are due to the match between the blade passing frequency f_b and the natural frequencies of the rotor. The vibration amplitude depends on the mode shape and damping characteristics. The amplitudes of the more global mode shapes where all the rotor masses are deformed have the lowest amplitude. The response in the axial direction also depends on the mode shape characteristics.

The strain measurement indicates that the torsion stress fluctuates at the rotation frequency with low amplitudes and at the blade passing frequency. The maximum amplitude occurs when the blade passing frequency equals the torsion natural frequency.

Vibrations in the horizontal direction are higher than in the vertical direction because the stiffness of the bearing is lower in horizontal direction. Amplitudes of 4.5mm/s rms are reached what are ten times larger than ones obtained at maximum load. The maximum response is with the mode with axial motion of the runner producing large stresses in the coupling zone between shaft and runner.

It is proved that with the machine in operation, the runner natural frequencies can be detected in the monitoring positions. The best positions for the best detection of them have been assessed.

Another important topic is the variation of the runner frequencies when the turbine is in operation due to added mass and stiffness due to centrifugal forces. In the cases studied, the changes observed are not significant and are in the range of the scattering of natural frequencies due to lack of precision during the runner machining.

Finally, the evolution of the band level related to each mode shape was calculated.

Monitoring of Pelton turbines

An advanced condition monitoring system has to be able to detect in real-time abnormal operation that can lead to failure and incipient damage. The strategy to implement an advanced condition monitoring system in hydraulic turbines is introduced. It follows the application to Pelton turbines, with an analysis of the vibration signatures and the explanation of actual monitoring procedures.

Once proved that the runner can be monitored from the bearings, the next step has consisted in knowing the most common types of damage and their symptoms. For that purpose, the monitoring information and data obtained after more than twenty years of monitoring have been analyzed. The main types of damage that have occurred in several Pelton turbine units are described.

A new spectral band distribution is proposed so that the excitation of the different runner modes can be monitored. An analysis about which of these modes can be excited in normal an abnormal operation is performed.

The proposed procedure is checked with a history case where the evolution of the vibration signatures with a fatigue induced damage was available. The proposed method is more sensitive to detect damage and for the diagnostic of damage.

Future work

To improve the upgraded monitoring procedure, AI methods can be used. The data coming from different locations, sensors could be correlated using Neural Networks and other methods. Moreover, better condition indicators can be obtained with the combination of the new spectral bands and other vibration features.

The data of continuous monitoring could be used for the mapping of the condition indicators in different operating conditions. Historical data can be used to map the change of these conditions indicators with the most common types of damage.

Regarding the transmission of vibrations from the runner to te monitoring positions, other on-site tests should be done with an on-board system measuring runner vibrations so that the changes in the FRF between runner and bearing could be improved.

References

[1] L. Gaudard and F. Romerio, "The future of hydropower in Europe: Interconnecting climate, markets and policies," *Environ. Sci. Policy*, pp. 1–10, 2013.

[2] "International Renewable Energy Agency (IRENA)." [Online]. Available: https://www.irena.org/hydropower. [Accessed: 10-Jul-2019].

[3] Z. Zhang, *Pelton turbines*. 2016.

[4] H. Keck, G. Vullioud, and P. Joye, "Commissioning and Operation Experience with the World's largest Pelton turbines Bieudron," pp. 1–16, 2004.

[5] A. Bezinge and P. Loth, "Cleuson-Dixence extension sets world records," *Hydropower Dams*, no. March, pp. 29–34, 1994.

[6] A. A. Fulton, "Present Tendencies in Water Turbine Machinery," *Proc. Inst. Mech. Eng.*, vol. 135, no. 1, pp. 387–444, 1937.

[7] A. B. Winterbottom, "Cracking of Bucket Lugs in Pelton Turbines," vol. 127, 1951.

[8] M. Nechleba, *Hydraulic Turbines. Their Design and Equipment*. 1957.

[9] H. Grein, R. Angehrn, M. Lorenz, and A. Bezinge, "Inspection periods of Pelton runners."

[10] H. Brekke, "State of the art in Pelton turbine design," *Hydropower Dams*, no. March, pp. 21–28, 1994.

[11] M. Bjerke, H. Brekke, and K. I. Berg, "Modern design and manufacturing of multijet Pelton turbines," in *Proceedings of the 15th IAHR Symposium on Hydraulic Machinery and Systems*, 1990, vol. 2.

[12] H. Brekke, "A discussion on operational problems," *Proc. 24th Symp. Hydraul. Mach. Syst.*, no. 7026, pp. 1–12.

[13] J. Mañanés, A. Mirasso, and A. Antunez, "Manufacture of the Pelton runners of Pykara, India," *Hydropower Dams*, no. 6, pp. 58–59, 1999.

[14] J. Vesely, J. Mikulasek, and P. Vesely, "Modern technologies for producing Pelton runners," *Hydropower Dams*, no. 2, pp. 113–117, 2006.

[15] J. Veselý and M. Varner, "A Case Study of Upgrading of 62.5MW Pelton Turbine."

[16] R. Angehrn, H. Grein, W. Keiser, and H. Kloter, "The maintenance of Pelton turbine runners," *Hydropower Dams*, no. March, pp. 35–40, 1994.

[17] J. C. Chávez, J. A. Valencia, G. A. Jaramillo, J. J. Coronado, and S. A. Rodríguez, "Failure analysis of a Pelton impeller," *Eng. Fail. Anal.*, vol. 48, pp. 297–307, 2015.

[18] L. Chapuis and K. Froschl, "Optimized fabrication of Pelton turbine runners," *International Journal on Hydropower and Dams*, vol. 5, no. 2. pp. 30–32, 1998.

[19] C. Calderaro and J. Mañanes, "Recent trends in the manufacture of Pelton runners,"

Hydropower Dams, pp. 109–110, 1997.

[20] A. Kalberer and M. Krause, "A review of experience with MicroCast Pelton wheels," *Hydropower Dams*, no. 1, pp. 22–24, 1996.

[21] F. Linet, G. Rossi, B. Michel, and P.-Y. Lowys, "Hooped runner design offers advantages for Pelton units," *Hydropower Dams*, no. 6, pp. 60–62, 1999.

[22] G. C. Chaudhari and S. P. Shah, "GT2011-46052," pp. 1–9, 2016.

[23] M. Sick, H. Keck, G. Vullioud, and E. Parkinson, "New Challenges in Pelton Research," in *Proceedings oh Hydro 2000 Conference*, 2000.

[24] J. Schmied, T. Weiss, and R. Angehrn, "Detuning of Pelton Runners," *Proc. 7th IFToMM Conf. Rotor Dyn.*, no. September, pp. 25–28, 2006.

[25] M. Sick, W. Michler, T. Weiss, and H. Keck, "Recent developments in the dynamic analysis of water turbines," *Proc. Inst. Mech. Eng. Part A J. Power Energy*, vol. 223, no. 4, pp. 415–427, 2009.

[26] R. Mack and C. Probst, "Evaluation of the dynamic behavior of a Pelton runner based on strain gauge measurements," *IOP Conf. Ser. Earth Environ. Sci.*, 2016.

[27] R. Angehrn and M. Dubas, "Experimental stress analysis on a 260MW Pelton runner," in *Proceedings of the 11th IAHR Symposium*, 1982.

[28] R. Angehrn, J. Rettich, and C. Schärer, "Pelton runner design based on measured unsteady pressure distributions in the bucket," *Hydropower Dams*, no. 6, pp. 53–57, 1999.

[29] B. Zoppé, C. Pellone, T. Maitre, and P. Leroy, "Flow Analysis Inside a Pelton Turbine Bucket," *J. Turbomach.*, vol. 128, no. 3, p. 500, 2006.

[30] S. Kvicinsky, "Méthode d'analyse des écoulements 3D à surface libre: application aux turbines Pelton," École Polytechnique Fédérale de Lausanne, 2002.

[31] F. Avellan, P. Dupont, S. Kvicinsky, L. Chapuis, E. Parkinson, and G. Vullioud, "Flow calculations in Pelton turbines. Part 2 : Free Surface Flows," in *Proceedings of the 19th IAHR Symposium on Hydraulic Machinery and Systems*, 1998, vol. 1.

[32] A. Perrig, "Hydrodynamics of the free surface flow in Pelton turbine buckets," ÉCOLE POLYTECHNIQUE FÉDÉRALE DE LAUSANNE, 2007.

[33] H. Brekke, "A review on dynamic problems in Francis and Pelton Turbines," *IOP Conf. Ser. Earth Environ. Sci.*, vol. 22, pp. 1–10, 2014.

[34] M. Sanvito, L. Coscarelli, E. Pesatori, G. Turozzi, and P. Pennacchi, "A New Method for the Dynamic Analysis of Pelton Runners Using CFD/FEM Interaction," *Proc. ASME 2009 Int. Des. Eng. Tech. Conf. Comput. Inf. Eng. Conf.*, pp. 1–5, 2009.

[35] E. Pesatori, G. Turozzi, P. Pennacchi, and A. Tosi, "Dynamic Investigation on a Pelton Runner: FEM Calculations and Experimental Results," *Proc. ASME 2007 Int. Des. Eng. Tech. Conf. Comput. Inf. Eng. Conf.*, pp. 3–7, 2007.

[36] P. Dörfler, M. Sick, and A. Coutu, *Flow-Induced Pulsation and Vibration in*

Hydroelectric Machinery. Springer, 2013.

[37] A. Karakolcu, J. Erhard, and B. Wittwer, "Best practice in rehabilitation of Pelton turbines as applied at Vermuntwerk M5," *Proc. 17th Int. Semin. Hydropower Plants*, pp. 1–20, 2012.

[38] E. Egusquiza, *Comportament dinàmic de màquines hidràuliques*. 2003.

[39] F. De Siervo and A. Lugaresi, "Modern trends in selecting and designing Pelton turbines," *Water Power & Dam Construction*, vol. pp. 40–48, 1978.

[40] P. Heckbert, "Fourier Transforms and the Fast Fourier Transform (FFT) Algorithm," *Notes Comput. Graph.*, vol. 3, no. 2, pp. 15–463, 1995.

[41] T. Irvine, "An Introduction to Frequency Response Functions." pp. 1–29, 2000.

[42] M. A. Kramer, "An introduction to field analysis techniques: the power spectrum and coherence," *Soc. Neurosci.*, pp. 18–25, 2013.

[43] P. Loth, H. Sprysl, and G. Ebi, "Bearing stiffness determination through vibration analysis of shaft line of Bieudron Hydro Powerplant," *Int. J. Hydro Power Dams*, pp. 427–447, 1998.

[44] M. Egusquiza, "Study of the axial modes of Pelton turbines," 2017.

[45] B. Thapa and H. Brekke, "Effect of sand particle size and surface curvature in erosion of hydraulic turbine," *22nd IAHR Symp. Hydraul. Mach. Syst. Stock. Sweden, June 29 - July 2, 2004*, vol. 1, no. 11, pp. 1–11, 2004.

[46] M. K. Padhy and R. P. Saini, "A review on silt erosion in hydro turbines," *Renew. Sustain. Energy Rev.*, vol. 12, no. 7, pp. 1974–1987, 2008.

[47] M. K. Padhy and R. P. Saini, "Study of silt erosion mechanism in Pelton turbine buckets," *Energy*, vol. 39, no. 1, pp. 286–293, 2012.

[48] T. R. Bajracharya, B. Acharya, C. B. Joshi, R. P. Saini, and O. G. Dahlhaug, "Sand erosion of Pelton turbine nozzles and buckets: A case study of Chilime Hydropower Plant," *Wear*, vol. 264, no. 3–4, pp. 177–184, 2008.

[49] O. G. Dahlhaug and T. Nielsen, "Efficiency loss in Pelton buckets due to sediment erosion," in *Proceedings of the 23rd IAHR Symposium on Hydraulic Machinery and Systems*, 2006, vol. 1, no. October, pp. 2–7.

[50] A. K. Rai, A. Kumar, and T. Staubli, "Hydro-abrasive erosion in Pelton buckets : Classification and field study," *Wear*, vol. 393, no. August, pp. 8–20, 2017.

[51] H. Grein, "Cavitation Pitting and Rain Erosion on Pelton Turbines," in *Proceedings of the 15th IAHR Symposium on Hydraulic Machinery and Systems*, 1990, vol. 1.

[52] M. Pradel, "Pelton runner manufacture from forged stainless steel," *Hydropower Dams*, no. January, pp. 25–26, 1995.

[53] K. Stevanovic, "Damage of the Pelton turbine wheel," *Proc. Int. Conf. CSHS03*, pp. 219–226, 2003.

[54] E. Egusquiza, C. Valero, A. Estévez, A. Guardo, and M. Coussirat, "Failures due to

ingested bodies in hydraulic turbines," *Eng. Fail. Anal.*, 2011.

[55] X. Liu, Y. Luo, and Z. Wang, "A review on fatigue damage mechanism in hydro turbines," *Renew. Sustain. Energy Rev.*, vol. 54, no. FEBRUARY, pp. 1–14, 2016.

[56] M. Mione and G. Mazza, "Repairing cast Pelton runners: Problems and modern solutions," *International Journal on Hydropower and Dams*, vol. 6, no. 6. pp. 63–65, 1999.

[57] A. Panthee, B. Thapa, and H. P. Neopane, "Quality control in welding repair of Pelton runner," *Renew. Energy*, vol. 79, no. 1, pp. 96–102, 2015.

[58] Z. Zhang and M. Casey, "Experimental studies of the jet of a Pelton turbine," *Proc. Inst. Mech. Eng. Part A J. Power Energy*, vol. 221, no. 8, pp. 1181–1192, 2007.

[59] E. Parkinson, R. Lestriez, and L. Chapuis, "Flow calculations in Pelton Turbines - Part 1 Repartitor and injector numerical analysis," *Proc. 19th IAHR Symp. Hydraul. Mach. Syst.*, pp. 285–293, 1998.

[60] M. Peron, E. Parkinson, L. Geppert, and T. Staubli, "Importance of jet quality on Pelton efficiency and cavitation," in *International Conference on Hydraulic Efficiency Measurements*, 2008, pp. 1–9.

[61] T. Staubli *et al.*, "Jet quality and Pelton efficiency," *Hydro 2009 Prog. - Potential – Plans, Lyon, Fr.*, 2009.

[62] B. W. Solemslie and O. G. Dahlhaug, "Studying the effects of jet alignment in Pelton units," *Int. J. Hydropower Dams*, vol. 22, no. 3, pp. 78–83, 2015.

[63] W. Zhao and M. Egusquiza, "Application of CNN to Pelton machine diagnostics," 2019.